# Reviews of Plasma Physics

# 21

Edited by
B. B. Kadomtsev and V. D. Shafranov

# Reviews of Plasma Physics

Edited by B. B. Kadomtsev
(deceased)
and
V. D. Shafranov

Volume 21

CONSULTANTS BUREAU
NEW YORK · BOSTON · DORDRECHT · LONDON · MOSCOW

**Camera-ready copy prepared in Russia by:**
**V. D. Pustovitov and K. A. Postnov** (translators)
**G. G. Michael** (language editor)
**and Alexei Yaremchuk** (desk editor) **of**
*Uspekhi Fizicheskikh Nauk*

ISBN 0-306-11064-4


Consultants Bureau
233 Spring Street, New York, N.Y. 10013

http://www.wkap.nl/

10 9 8 7 6 5 4 3 2 1

A C.I.P. record for this book is available from the Library of Congress.



Printed in the United States of America

# CONTENTS

# THEORETICAL PRINCIPLES OF THE PLASMA-EQUILIBRIUM CONTROL IN STELLARATORS

**V. D. Pustovitov**

# FUNDAMENTALS OF STATIONARY PLASMA THRUSTER THEORY

**A. I. Morozov and V. V. Savelyev**

*To my teacher in plasma physics*
*Academician V. D. Shafranov*
*on his 70th birthday*

# THEORETICAL PRINCIPLES OF THE PLASMA-EQUILIBRIUM CONTROL IN STELLARATORS

V. D. Pustovitov

## Introduction

This review is devoted to the theory of plasma equilibrium in conventional stellarators with a plane circular axis and helical magnetic fields. Its primary objectives are the analysis of the conditions of finite-pressure plasma equilibrium in stellarators and the search for ways of increasing the achievable $\beta$ (ratio of kinetic to magnetic pressures).

In toroidal systems the maximal $\beta$ is limited by the necessary conditions for plasma equilibrium and stability. The optimization of a magnetic configuration with the purpose of increasing this limit has always been an important problem of the theory. In the last twenty years, this direction has acquired a special importance for conventional stellarators because progress in the development of plasma heating methods has removed the technical obstacles from the way to high $\beta$.

The transition to a qualitatively new stage of research on stellarators in the early 1980s led to new theoretical problems, which could not be resolved by old methods. The development

of more powerful self-consistent analytical approaches that are of high accuracy and sufficiently universal was required. It was necessary, at least, to "pull up" the theory of plasma equilibrium in stellarators to such a level that the theory could answer the questions already resolved for tokamaks.

On the whole, this was successfully done. The modern theory, whose basic principles are systematically described in the present review, allows the consideration of a wide scope of problems of plasma equilibrium in tokamaks and stellarators within the framework of a unified approach on the basis of a natural generalization of the methods of tokamak theory. Besides increasing the accuracy and reliability of theoretical predictions for stellarators, this also allows the possibility of a direct comparison with tokamaks, enabling us to reveal the latent general relations and leading, finally, to a physically simple and clear interpretation of the results. In the conceptual aspect, such a comparison facilitates the transfer of those ideas and principles to stellarators that have already been successfully cultivated in tokamaks but for different reasons have not yet been applied in stellarators. Among them was the problem of plasma-equilibrium control, which became urgent for stellarators because of the successful progress to high $\beta$ in experiments.

A distinctive feature of our time, noticeable even by comparing the first volumes of *Reviews of Plasma Physics* with recent volumes, is a much stronger orientation of the theory toward experiment than earlier. Furthermore, we should also mention the essential, sometimes even excessive, elaboration of minute details in theoretical problems, which partially reflects the accumulated experience and high level of experimental skill but to a much greater degree is due to the total penetration of numerical methods into plasma theory. The analytical theory presented in this review could be formally described without mentioning any experiment, either real or numerical. But such "purity" of theory is hardly good for physicists. We believe that some references and direct appeal to experimental results are quite pertinent even in a completely theoretical work. We would not only like to

present the methods and results of the theory, but also to show, at least in separate aspects, the history of the development and the interaction of key ideas and concepts. Such a general review is given in the first section.

The second section deals with the problem of theoretical description of plasma equilibrium in conventional stellarators. The contents and style of the second section were dictated by our desire to give an accurate self-consistent description of finite-pressure equilibrium plasma in stellarators. That is the basis for all further analysis. That is why we give a detailed substantiation of the general theoretical model here.

In Section 3, we explain which simplifications are allowable when a general theory is applied to particular problems. Actually, we discuss the choice of the simple, but reliable initial approximation for numerical or analytical modeling.

In the fourth section, which strongly draws upon the results of the previous two sections, the boundary conditions for the equilibrium equation are formulated. After that the problem of plasma-equilibrium control is considered. The main question is the control of the position of the plasma column in a stellarator with the help of a vertical magnetic field. In addition, the possibility of developing configurations that are not sensitive to the plasma pressure is discussed here.

In the fifth section, we discuss effects related to plasma-shape control in stellarators. In the first two subsections, the influence of the quadrupole field on the vacuum configuration is considered, with an analysis of the possibility of producing doublet-like configurations in stellarators in the second. An analytical theory of the control of the rotational-transform profile in stellarators by means of plasma elongation is given in the third subsection. Finally, in the fourth subsection, the physical mechanism of the increase of the equilibrium $\beta$ limit due to plasma elongation is explained.

Our intention was to present the material in a coherent and uniform way and to make the description complete and detailed but not overburdened by excessive algebra. Moreover, we would

like to show that the theory of stellarators, usually perceived as approximate, fragmentary, and overburdened by calculations, has a right to pretend to integrity, elegance, and harmony.

The review is based on results obtained over a long period. The author was fortunate enough to discuss them with a number of excellent specialists. Among them, first of all, I should mention my colleagues from the Kurchatov Institute. Numerous discussions with Yu. K. Kuznetsov, V. K. Pashnev, O. S. Pavlichenko and A. A. Shishkin from Kharkov gave a great impetus to this work. In various respects, this study was supported by B. A. Carreras, K. Matsuoka, M. Wakatani, Y. H. Ichikawa, and S. Besshou. It is a great pleasure to thank everyone who has been interested in this subject and has made it possible to complete this work.

Finally, I would like to take this opportunity to express my sincere gratitude to my scientific teacher and supervisor, Academician V. D. Shafranov. In December 1999, he will celebrate his 70th birthday. In honor of this occasion, I would like to extend my hearty personal greetings, kind regards, and best wishes.

# 1. History of the problem and a general review of the theory

## 1.1. The first problems of tokamaks and stellarators

To provide the conditions for plasma equilibrium is a prerequisite for successful operation with a plasma discharge in toroidal systems for controlled nuclear fusion. The solution of this problem implies the formation of a configuration of a magnetic field such that it would keep a plasma column in a given position, forcing it at the same time to acquire a desired shape. The changes in plasma parameters during the discharge should not result in a loss or deterioration of the equilibrium. Therefore, ideally, the configuration of the confining fields should be changeable so that at any moment the shape and position of the plasma should exactly correspond to the operational requirements.

Conceptually, the necessity of *plasma-equilibrium control* in fusion systems follows from the very designation of the final goal — controlled nuclear fusion. This problem revealed itself with the utmost urgency in tokamaks, where it was found in the very first experiments that the behavior of the current discharge in the toroidal chamber was greatly determined by its spontaneous motion along the major radius. This was due to a small external vertical field [1], which appeared as a secondary unforeseen result due to the large currents flowing in the electrical circuits of the device. It created an additional radial force pressing the plasma to the limiter, the interaction with which worsened the discharge. It might be possible to prevent such a development of events with the help of a special system creating its own transverse field of a proper magnitude. This proposal [1] implied a transition to active control of the plasma position, without which tokamaks were later inconceivable. The conclusions of Artsimovich and Kartashev [1] were reinforced by Shafranov's detailed theoretical analysis [2, 3].

Plasma equilibrium became a problem of paramount importance at the very beginning of tokamak research because the longitudinal magnetic field alone is not able to provide equilibrium of a current-carrying plasma ring [3]. An additional external vertical field is required. Furthermore, its strength should vary depending on variations in the plasma current, pressure, and their radial distributions [3]. In principle, a stationary vertical field could be sufficient for plasma equilibrium, but then the changes in plasma parameters would be accompanied by a significant shift of the plasma column along the major radius [2, 3], as was observed in experiments [1] and was extremely undesirable.

Plasma equilibrium remained one of the main research subjects on tokamaks in the 1960s, which can be seen from the review of the theory by Mukhovatov and Shafranov [4] and from the detailed description of the main experimental works of that period by Artsimovich [5, 6]. The theory of plasma equilibrium in tokamaks created by V. D. Shafranov was confirmed by experimental results, which was especially emphasized as a fact worthy

to be noted the first in the main conclusions of review [5]. The solution of the principal problem of plasma-position control has allowed the tokamak discharge parameters to be significantly improved and has pushed tokamaks to a leading position in fusion research [7]. The logical completion of all this work was the construction of the TO-1 tokamak [8], in which the control of the position of the plasma column was carried out by a system of automatic control.

For stellarators such systems were not needed. The reason is that in stellarators the problem of plasma equilibrium is resolved by the very formation of the magnetic configuration: the force lines of the vacuum magnetic field form a family of nested surfaces capable of resisting the plasma pressure [9]. That was the main idea of L. Spitzer in 1951, which laid the foundation for research on stellarators in Princeton, New Jersey [9, 10].

Irrespective of the particular realization of this idea, the main difference between stellarators and tokamaks is that in stellarators the necessary configuration of the magnetic field is created by currents in external conductors (Fig. 1.1) and there is no need to drive a current in the plasma to keep it in equilibrium. If there is no longitudinal current, there is no corresponding pushing force. Further, without the net current the external vertical fields, whose influence on plasma equilibrium appeared so essential in tokamaks, do not contribute to the integral force balance.

Unfortunately, this obvious advantage of stellarators, facilitating the problem of equilibrium, must be paid back in the struggle for high quality of *magnetic surfaces*. It turned out that they are very sensitive to perturbations [11–19]. The inevitable presence of "perturbing" fields (or actually, of undesirable small components of the magnetic field) in real systems manifests itself in the distortion and destruction of magnetic surfaces, which in the worst case can be catastrophic.

It is generally recognized that the creation of the nested magnetic surfaces necessary for plasma confinement is the key problem in the concept of a stellarator. Because of this it has been rather thoroughly studied. Besides the pioneering works

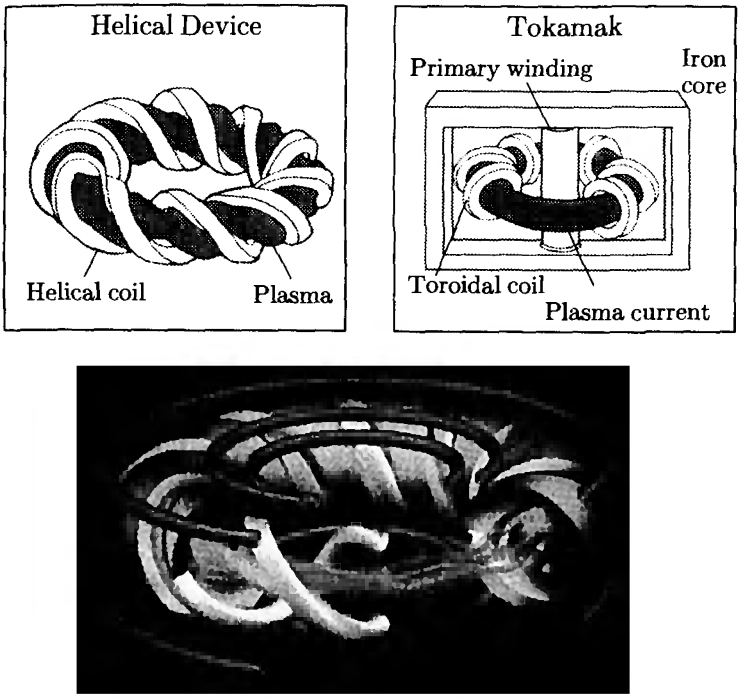


**Fig. 1.1.** Schematic view of a helical device, a tokamak, and the model of the Large Helical Device (LHD). [From the pamphlet of the National Institute for Fusion Science, 322-6 Oroshi-cho, Toki-shi, Gifu-ken 509-52, Japan].

mentioned above, a whole sequence of serious theoretical research (see [20, 21] and the extensive review in the monograph [22]) has been devoted to this problem; the existence of good magnetic surfaces for a proper choice of external currents in stellarators has been confirmed by direct experiments [23–37] and numerical simulations [38–59].

A separate mention is deserved for publications [60–67], where stellarator configurations with magnetic islands and stochastic behavior of the field lines were considered using the HINT code [60]. This code was especially developed for studying plasma in those conditions which, generally speaking, are typical for

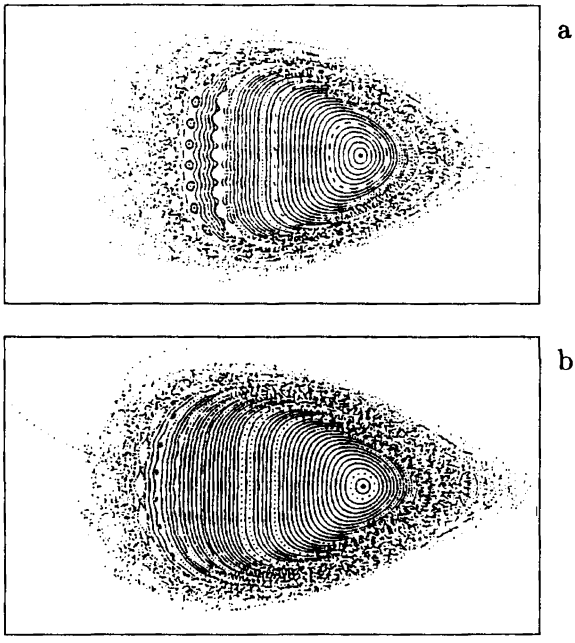


**Fig. 1.2.** Magnetic surfaces in an $\ell = 2$ torsatron with $m = 10$ before (a) and after (b) imposing the correcting field suppressing the magnetic islands [62].

stellarators. Papers [60–67] answer the old and very important question [5, 21, 68, 69] of whether the breaking of magnetic surfaces in stellarators becomes stronger under the action of a plasma, and if yes — to what extent. As was expected, in some cases such breaking can be inadmissibly strong even at small $\beta$ (the ratio of plasma to magnetic pressures) [60–64]. At the same time, it was shown by Hayashi et al. [61–64] that by using an additional control magnetic field it was possible to achieve appreciable reduction of this danger (Fig. 1.2). But most remarkable was an unexpected discovery of a surprising new effect: at finite $\beta$, the magnetic islands inside the plasma disappeared [65–67]. This happened by itself, allowing the effect to be called "self-healing" [65]. The possibility of such self-organization in a

plasma, when for imperfect initial conditions the restoration of good nested magnetic surfaces occurs with growing $\beta$, relieved some apprehensions and substantially improved the prospects of stellarators.

As soon as it was realized that the breaking of magnetic surfaces, the formation of magnetic islands, and the stochastization of the field lines are the inherent drawbacks of all stellarators, the problem of elimination or reduction of their most unpleasant manifestations immediately became urgent. The optimization of the magnetic configuration was under careful study in all stellarator centers [70–77, 22], which is also reflected in the publications mentioned above. The subject of optimization was the vacuum magnetic field. This essentially distinguishes stellarators from tokamaks: in tokamak research, from the very beginning the focus of the equilibrium problem was the behavior of the plasma column. The difference was reflected even in the terminology: in tokamaks, the external transverse fields are called control fields, but in stellarators they are called correcting or adjusting fields. The names correspond to the different purposes: in tokamaks they are used for control of the plasma position and shape, but in stellarators they are used for correction of the defects of a vacuum magnetic configuration.

A configuration optimized from the point of topology must, primarily, provide a good confinement of the plasma. In the first stellarator, Spitzer's figure-8, it was unsatisfactory, forcing a change to systems with helical windings, rejecting the idea of a stellarator with a spatial axis [9, 10]. The helical currents allow one to produce a magnetic field with force lines rotating around the magnetic axis with different rates of rotation at different distances from the axis. This property, called *shear*, appeared to be necessary for plasma stability [9, 10, 78]. In shearless systems like Spitzer's figure-8, as followed from the first theoretical evaluations, the plasma would be unstable against flute perturbations even at very low $\beta$ [9, 10, 78]. Soon after the discovery of the stabilizing role of shear, another means of suppressing instabilities in stellarators was found: a *magnetic well* [79–87].

This is a more subtle characteristic of the magnetic field than a shear. Creating a magnetic well is something of an art. As was shown by further development of the theory, systems without a magnetic well are not promising. In practice, this meant the application of tougher criteria to the selection of stellarator configurations. At the same time, researches appeared confident that with two stabilizing factors at once, both shear and a magnetic well, plasma stability in stellarators could be provided, at least for small $\beta$.

## 1.2. The problem of high $\beta$

At the initial stage of stellarator research, the development of the plasma-equilibrium theory was motivated primarily by the necessity of a reliable description of equilibrium for the analysis of its stability [78]. Further, since the stellarator, according to Spitzer's concept [9], should be a stationary current-free system, it was necessary to evaluate its potential in just this capacity, though the first Princeton experiments on stellarators were conducted with Ohmic heating of the plasma [9, 10, 74, 88–92].

Before the publication of [93] by Greene and Johnson in 1961, the equilibrium of plasmas in stellarators was considered in a cylindrical approximation [78], though the general properties of toroidal plasma equilibrium had already been discussed by Kruskal and Kulsrud [94]. Without exaggeration, the work by J. M. Greene and J. L. Johnson [93] can be noted as outstanding. At that time it was not properly appreciated, but in the 1980s Greene and Johnson's ideology [93] was conceived and widely used in the theory. It arose after the successful experiments on the Wendelstein VII-A stellarator [95], where a current-free plasma with impressive parameters ($T_i \sim 700\,\mathrm{eV}$, $T_e \sim 500\,\mathrm{eV}$, $n \sim 10^{14}\,\mathrm{cm}^{-3}$, $\tau_E \sim 20\,\mathrm{ms}$) was obtained using neutral beam injection.

Those results and later experiments in another large installation, Heliotron E [96], showed that stellarators may compete with tokamaks and, furthermore, in the current-free mode,

which is the most advantageous feature of stellarators. These achievements [95, 96] gave impetus to stellarator research and made it possible to expect high $\beta$ in installations of the following generation [38, 45, 70, 77, 97]. In the present work, we shall discuss the control of the plasma equilibrium, which should enable progress toward this goal.

The notion of a high $\beta$ requires a more precise definition. In stellarators, always $\beta \ll 1$. According to calculations, in the ATF torsatron (Oak Ridge, Tennessee) the maximal value of $\beta$ could be of the order of 8% [45]; in the Uragan-2M torsatron with an additional toroidal field (Kharkov, Ukraine) it could be about 7% [98]; in the torsatrons CHS [97, 99] and LHD [58, 100] (Nagoya, Toki, Japan) and also in the Wendelstein VII-X modular stellarator [57, 101] (Garching, Germany) about 5%; in the L-2/4 stellarator (Moscow, Russia) of the order of 4.5% [102]. These are the best values obtained in calculations under the careful optimization of the projects of real or realistic stellarators. In experiments such values of $\beta$ have not yet been reached: the world-record $\beta$ achieved in 1993 in the CHS torsatron was 2.1% [103, 104]. However, even at $\beta$ small on an absolute scale the effects of finite plasma pressure can be rather strong in stellarators. From a physical viewpoint, those $\beta$ at which the self fields of the equilibrium plasma currents can appreciably deform the initial vacuum configuration of a stellarator should be considered as large. This occurs at $\beta$ close to the theoretical limit on equilibrium, $\beta_{eq}$, which depends on the device parameters and may be relatively small. For example, in the Wendelstein VII-AS stellarator (Garching, Germany) $\beta_{eq}$ is only 2% [101]. Here and further, the symbol $\beta$ denotes the value averaged over the plasma cross section.

Each of the mentioned stellarator devices is unique in its own way, which is emphasized frequently in the very definition of the installation type: torsatron, modular stellarator, or Heliotron. The word *stellarator* is used here in the generally accepted wide meaning. This generic name, indicating that a system belongs to a certain class, covers stellarators in the narrow

sense of the word, torsatrons and Heliotrons when the physics is discussed, but not the design of the installation. "Conventional" stellarators (in contrast to more exotic systems with a spatial axis) are those with a plane circular axis and helical fields. They constitute the main group of stellarator systems, with such typical representatives as Liven'-2 [27], Uragan-3M [37] and Uragan-2M [98], Heliotron E [71, 96], ATF [45], CHS [97, 99, 105], and LHD [58, 100].

The history of stellarators is described in detail in a whole series of substantial reviews [10, 22, 70–77, 106–114]. To retell it could lead us too far from the main theme of our work. Therefore, we shall concentrate further on questions related only to the problem of plasma equilibrium at large (or as is sometimes said — at finite) $\beta$.

The aspiration to high $\beta$ is a natural tendency in controlled fusion: at a given magnetic field the specific fusion power in a reactor will be proportional to $\beta^2$. In toroidal systems the plasma interaction with the confining magnetic field is ensured due to the plasma-equilibrium currents. The larger the $\beta$, the stronger these currents. The magnetic field produced by them deforms the magnetic configuration, so the increase in $\beta$ is allowed only up to some critical value $\beta_{\rm eq}$, which is called the equilibrium limit.

The *optimization of the magnetic configuration* with the purpose of increasing this limit has always been an important problem of the theory. One of the solutions for conventional stellarators was offered in 1961: Greene and Johnson [93] showed numerically that in a particular $\ell = 3$ stellarator the configuration can be made independent of the plasma pressure at a certain value of the external vertical field $B_\perp$. However, the magnetic axis must then be strongly shifted inwards, into the region of stronger toroidal field where the plasma equilibrium is unstable.

Nevertheless, the main problem has been stated: in stellarators, the finite pressure of plasma shifts the magnetic axis outward, which does not allow $\beta$ to be increased above some limit. For the experiments of that time this was not dangerous,

hence the problem was rather of academic interest. This problem was mentioned again much later by Gibson [115], who proposed, though without calculations and proofs, that to get a higher $\beta_{eq}$ the axis shift (which already differed from the previous proposal [93]) should be suppressed by the external vertical field. The idea was then supported by Pyatov and Shishkin [116] in the discussion of the vertical-field effect on near-axis magnetic surfaces in an $\ell = 3$ stellarator. The model used was rather crude and inconsistent and some results [116] lie far outside the domain of its applicability, but one fact, nevertheless, deserves mentioning: the control field $B_\perp$ depending on $\beta$ was discussed (in contrast to the unchangeable value [93]).

Those discussions [115, 116] were about the magnetic axis and the control of its position. But in [117–121] the control vertical field was already offered as a means of suppressing the destruction of the outer magnetic surfaces produced by the plasma self-field at $\beta \neq 0$. As in [116], a vertical field $B_\perp$ depending on $\beta$ was necessary for this purpose. It should be used to suppress the plasma boundary shift (but not the shift of the axis, as in [116]).

Paper [118], where only $\ell = 3$ stellarators were considered, was concluded by a statement about the necessity of automatic control of the magnitude of this field. How it should be carried out remained unclear. For tokamaks, let us recall, such a proposal was stated back in 1962 [1]; by the 1970s, the theory developed [2–4] had already allowed a practical realization in the TO-1 tokamak [8], and by the time of publication of [118] the automatic systems of plasma-position control had become standard for tokamaks [7, 122–128]. This was not mentioned in [118], and, incidently, nothing in common between tokamaks and stellarators could be seen there. On the contrary, it was stressed by Danilkin [117] that the requirements for a system of plasma-equilibrium control in stellarators could hardly be more rigid than those for tokamaks.

The conclusion that a vertical field, suppressing the plasma shift and thus preventing the destruction of the external mag-

netic surfaces, may become useful at high $\beta$ was accompanied in [119–121] by the special reservation that, in principle, plasma equilibrium in a stellarator is also possible without such a field.

In [116–121], results were obtained in the approximation of small $\beta$. Therefore, in comparison with similar results of the tokamak theory, they may be considered only as preliminary estimates. The more so that these recommendations of general character, being fair on the whole, treated the high $\beta$ range.

By definition, as quoted above, those $\beta$ should be considered as small at which the magnetic surfaces are not strongly deformed, remaining almost the same as they were without plasma. Correspondingly, the calculation of equilibrium can then be done by iterations, assuming at the first step that the plasma pressure distribution is determined by the geometry of vacuum magnetic surfaces. Having calculated then the field of the equilibrium currents, it is possible to find the related change of the magnetic configuration [9, 21]. This approach is justified when the result does not contradict the initial assumption. If, as in some cases in [22, 116, 118], the configuration is strongly changed under the action of the "perturbing" field, the result should be considered as doubtful.

The approximation of small $\beta$ in the sense mentioned has been occasionally used up to now. From the outset, it limits the range of applicability of the results. But in a strict approach, as is clearly seen from [117, 119–121], it does not give a radical simplification of the problem, even if instead of being iterated the procedure is cut off after the first step.

Papers [116–121] and the status of the stellarator equilibrium theory before the 1980s merely reflected the level of experiments of that time: until 1980 the results of stellarator research were presented at IAEA conferences in the section "Low-Beta Toroidal Systems." In accuracy and potential, and according to the range of resolved problems, stellarator theory was significantly behind the theory of plasma equilibrium in tokamaks [3, 4, 129, 130] at the end of 1970s. Already it could not meet the new demands. The state of the theory of plasma equilibrium in

stellarators until 1980 is described in more detail in the reviews [106, 112, 131].

## 1.3. Development of the MHD theory of stellarators

The foundation of the *theory of plasma equilibrium in conventional stellarators* was laid in the article already mentioned [93], where an effective algorithm was proposed to solve three-dimensional equilibrium equations by an expansion method. Then the problem could be reduced to a two-dimensional equation of the same type as the known Grad–Shafranov equation [132–134]. In the framework of this approach [93], which was then also applied in problems of plasma stability [135–138], the magnetic configuration is described self-consistently, and the main equation can be solved using the methods of tokamak theory. All this could have brought about significant progress in the theory of stellarators, but for almost 20 years the ideas and results of Greene and Johnson [93] did not gain wide recognition and application, probably for two reasons. First, when experiments on stellarators were carried out with low-pressure plasmas and the main problem was the study of plasma heating and confinement, there was no urgent need for the exact analysis of finite-$\beta$ effects. Second, in [93], and later in [137], the final result was formulated as three separate equations [the first was written in [137] as $\nabla^2 A = -4\pi j_z(r,\theta)$], so the analogy between stellarators and tokamaks, where the equilibrium is described by the Grad–Shafranov equation

$$\operatorname{div} \frac{\nabla\psi}{r^2} = -4\pi^2 p'(\psi) - \frac{FF'(\psi)}{r^2}, \tag{1.1}$$

was not noticed even by the authors of [93, 135–138]. Moreover, when particular problems had been analyzed [135, 136], the calculations were too cumbersome, so one could not see any obvious merit of the method [93, 135–138]. It is curious, but there is no mention of Greene and Johnson's equation in the monograph *The Stellarator* [22]. Moreover, there was also no mention of it

in the articles [139, 140], which appeared in 1980, and in two subsequent series of publications [141–147] and [148–154], where a new formalism for the description of plasma equilibrium in conventional stellarators was developed.

With the obvious difference of techniques used in [139, 141–147, 140, 148–154], and also [155, 156] and [157], the common feature of these four different approaches is the diverse use of the so-called *stellarator expansion* [93]. Finally, as was shown in [158], all the two-dimensional equilibrium equations derived in different ways [140, 146, 155, 157] are physically equivalent, despite their different appearance or even incomparability. They either reduce (as, for example, the vector equations of Kovrizhnykh and Shchepetov [140]) to the equation [158]

$$\operatorname{div} \frac{\nabla(\psi - \psi_V)}{r^2} = -4\pi^2 p'(\psi)\left(1 + \Omega^0\right) - \frac{FF'(\psi)}{r^2}, \qquad (1.2)$$

generalizing the Grad–Shafranov equation (1.1) on stellarators, or can be derived from Eq. (1.2) with additional simplifying assumptions. In the limit of large aspect ratio they actually reproduce Greene and Johnson's equation [93]. The equivalence of the general equations, to which different authors have come in different ways, testified to the correctness of the calculations, which are not so simple to repeat in all details, removed any possible doubts about the advantages or disadvantages of one method or another, and indicated that there should be no contradiction in applications.

The outcome of the new approaches was not only the "rediscovery" of Greene and Johnson's equation [93] but also the derivation of more general two-dimensional equations describing the plasma dynamics [140, 153, 155, 156] and plasma equilibrium in stellarators with finite [157] and arbitrary [158] aspect ratios, and also the reduction of these equations to a form allowing a natural application of the methods already developed for tokamaks. It greatly expanded the possibilities of the theory and created the basis for subsequent more detailed research on plasma behavior in stellarators. The derivation of general

equations was made with the use of only "natural" expansion parameters and self-consistently, and so no principal restrictions of their applicability appeared at this stage.

The main goal was the development of adequate methods for solving problems of plasma equilibrium and stability in stellarators at finite plasma pressure with the intention of evaluating the real theoretical limits on $\beta$ (this can be seen even from the titles of [144, 150, 151, 156]). This goal was achieved, and the first results turned out to be optimistic: it was shown [141, 148] that the plasma stability in stellarators with shear should be improved with growing $\beta$ because of the axis shift into the region of a weaker toroidal field, which results in a deepening of the magnetic well.

This effect, called *plasma self-stabilization*, had already been described in [136], but, along with the two-dimensional equilibrium equation for a stellarator [93], was not noticed and was then even forgotten. In the 1980s, the attitude toward the problem of high $\beta$ was quite different, and the results published in [141] and [148] immediately attracted attention. They were confirmed and elaborated in a whole series of subsequent works [143, 149–153, 159]. Later, in reviews [154, 160, 161], the rediscovery of plasma self-stabilization in stellarators with shear was mentioned as one of the major achievements of stellarator theory.

Indeed, it seemed that there should be no serious problems with plasma equilibrium in stellarators, but there was no similar confidence with respect to stability. On the one hand, for shearless $\ell = 2$ stellarators with a magnetic well, the theory predicted plasma stability up to $\beta_{\rm st}$ of the order of 10% [162]. This conclusion was made on the basis of the necessary Mercier stability criterion [163–167], but the sufficient Solov'ev criterion [168, 169] also gave a smaller, but still finite value of $\beta_{\rm st}$ [170]. On the other hand, the estimates for stellarators with large shear gave a small $\beta_{\rm st}$ [117]. There was a thoroughly discouraging proposition [171] (fortunately, incorrect) that in $\ell = 2$ stellarators, irrespective of their parameters, the necessary and

sufficient stability criteria could not give $\beta_{st}$ higher than 0.66% and 0.22%, respectively.

The conclusion on plasma self-stabilization, which turned out to be stronger in stellarators with shear than that predicted earlier for shearless systems [172], gave rise to hopes for the achievement of high $\beta$ which could be limited only by the equilibrium limit $\beta_{eq}$ [140, 142–144, 148–154, 159–161] in the absence of dangerous instabilities. The problem of high $\beta$ should be addressed then to the optimization of stellarators on equilibrium, as mentioned above.

Closing the discussion of MHD stability, let us mention two important facts. First, the predictions of the analytical theory on plasma self-stabilization in stellarators with shear were confirmed by numerical calculations: at first within the framework of ideal magnetohydrodynamics [39, 41, 42, 51, 59, 159] and then with account of resistivity, diamagnetic effects, and plasma compressibility [173, 174]. The calculations of [39, 41, 42] were performed as part of the physical studies in the ATF torsatron project [45], which was to become the largest and most experimentally flexible stellarator installation (experiments began in January 1988 [175]). It was expected that in the ATF it would be possible to attain $\beta$ of the order of 8% [45]. The self-stabilization of the plasma was one of the factors with which these hopes were related. Second, these hopes partially came true. For a number of reasons, rather high $\beta$ were not achieved in the ATF, but the effect of self-stabilization was confirmed experimentally. In the ATF [36, 176–179] and later also in the CHS [103, 104], it was observed as a decrease in the level of fluctuations of the magnetic field at $\beta$ above some threshold value. For completeness, we should also mention [180], which expresses a lower level of optimism with respect to MHD plasma stability in the ATF. The results of [180] show, at least, that the problem of MHD plasma stability has not yet been completely resolved.

The construction of the ATF was a significant event in the stellarator world. It was preceded by extensive theoretical

work of a high level, mainly numerical modeling whose results are summarized in [45] and partially in [77].

Modern computers have already allowed the direct solution of the complete three-dimensional equilibrium problem, but the use of the two-dimensional Eq. (1.2) as the basis for calculations considerably facilitated and accelerated them [42]. However, strictly speaking, equation (1.2) is approximate. Though its derivation from the initial equations of equilibrium, sharpened by the efforts of several theorists from different laboratories, did guarantee its good accuracy, there was still not complete trust in the reduced equations. The fear of losing accuracy in aspiring to simplicity and speedy calculations was an incitement to careful comparison of the results of two-dimensional calculations on the basis of Eq. (1.2) with those obtained by numerical solution of the full three-dimensional equilibrium problem [39, 42, 59]. This comparison showed that for stellarators with large or even moderate aspect ratios ($A \geq 7$) Eq. (1.2) appears quite reliable, so that its accuracy was even characterized as unexpectedly high [53, 181]. For compact stellarators with $A \cong 4$ (such systems do not yet exist), the accuracy of Eq. (1.2) was found to be insufficient, but the results of two-dimensional simulations turned out to be qualitatively correct even in this case [51].

The main results of the present work are obtained within the framework of the model where Eq. (1.2) plays a central role. Thus, the conclusion of [39, 42, 59] regarding the reliability of Eq. (1.2) justifies its use beforehand.

The physical studies on the ATF project have substantially changed the look of the MHD theory of stellarators. First, by using numerical methods as the main (if not the only) tool for obtaining the desired information (see [45, 182]). The analytical models were necessary only for construction of the calculation algorithms. But the models already had to be self-consistent, so as not to introduce some serious initial restrictions. Second, by the scale and depth of the project elaboration at a high level of requirements on the accuracy of the results. It is enough to say that four three-dimensional and three two-dimensional numerical

codes were used only in equilibrium problems [45], covering all reasonable needs and practically excluding the chance of a casual error. Finally, by aiming at high $\beta$, up to $\beta = 8\%$ [45]. Before that such values were mentioned only as desirable, but they are now being discussed as actually achievable in the installation that was constructed.

## 1.4. High $\beta$ and the problem of plasma-equilibrium control

The main purpose of optimization of the ATF magnetic configuration was the capability of high $\beta$ operation. In addition, the ATF was initiated as a unique installation where a significant *variation of the magnetic configuration* would be possible. This should ensure the great experimental flexibility that was always mentioned as one of the advantages of the ATF [39, 42, 45, 81]. As was discovered [183], the possibility of changing (even during the discharge) the shape of the plasma appeared to be not only a useful additional degree of freedom in the ATF, but also absolutely necessary for achieving the desired high $\beta$.

In was shown [183] that in the ATF at the circular averaged plasma boundary an increase in $\beta$ is accompanied by a strong deformation of the rotational-transform profile. Because of this, the resistive modes, aggravating the energy confinement, could become unstable even at moderate $\beta$. The solution to the problem [183] appeared to be surprisingly simple: with increasing $\beta$ the profile of the rotational transform could be kept almost unchanged by properly varying the currents in the ATF poloidal-field coil system (three pairs of ring conductors). But this is accompanied by a change in the plasma shape. So *control of the rotational-transform profile* [183] actually required control of the plasma shape.

For stellarators this was new. The control of the plasma position in stellarators had been discussed earlier at the level of general considerations and analytical estimates [115–121, 184, 185]. The effect of the vertical field on the current-carrying

plasma position (at $\beta = 0$) was even studied experimentally in the Liven'-2 stellarator [186]. But control of the plasma shape was never considered earlier as necessary or, at least, desirable for conventional stellarators.

The proposal was new only where stellarators were concerned. However, *control of the plasma shape* was already a natural element in tokamak operation. It is enough to say that JET, the largest tokamak completed in the middle of 1983, had a non-circular vacuum chamber, a system of plasma-shape control, and from the very beginning operated with a non-circular plasma [187].

The plasma shape came into the circle of main concepts of tokamak physics after the publication by Artsimovich and Shafranov [188] in 1972, where a tokamak with a vertically elongated cross section (the so-called finger-ring) was proposed. Theoretically, the elongation of the plasma should increase the maximal achievable $\beta$ and simultaneously reduce the transport coefficients. The idea of a "non-circular" tokamak immediately became popular [189–198], also promoted by studies of doublet (strongly elongated three-axial) configurations [199–202]. Both experiment and the theory confirmed the advantages of tokamaks with non-circular plasmas [7, 167, 203–207]. In tokamaks, the art of plasma-shape control has reached a high level [208–213]. Only "non-circular" tokamaks are considered in modern projects for new devices or future reactors [214–219].

All this has left stellarators almost untouched. The ATF torsatron was a unique installation where the plasma-shape control was scheduled at the design stage [45, 183] and then tested in experiments [220]. It is known that the ATF was operated under substantial budget restrictions [221] and as a result was completely shut down in 1994. This did not allow the experiments to proceed with high $\beta$. The possibility of changing the plasma shape was used in the ATF only as an effective means of bootstrap current control [220].

However, even this result shows that the plasma-shape control in stellarators may be useful at least. Calculations [42,

183] did not leave any doubts of the unconditional necessity of such a control for the achievement of high $\beta$ in the ATF. From these and other numerical calculations [39, 51, 59, 64, 81, 98, 102, 155, 181, 222–225] it is clear that the maximum value of $\beta$ could be just of the order of 5% (in typical realistic situations). Actually, this means that conventional stellarators, working traditionally without control of the plasma shape and position, do not have an excess in $\beta$ because 5% is the lowest level for the reactor requirements [77]. The problem of high $\beta$ also remains urgent for Helias-type systems [226, 227] ($\beta_{st} \leq 5\%$), which were incarnated in the grand Wendelstein 7-X project in Germany [101, 228]. Stellarators have already proceeded to the $\beta > 2\%$ area [103, 104, 229] and the technical possibilities allow further progress. Thus, the actuality and practical importance of the problem of plasma-equilibrium control in stellarators are obvious.

In stellarators, a lot of attention has always been paid to the vacuum configuration. Its quality was evaluated by the size of the last closed magnetic surface, by the value of the rotational transform and shear, and by the depth of the magnetic well. This was sufficient for experiments with plasma at $\beta \ll \beta_{eq}$. But will the configuration optimized in the best way for a plasma with $\beta \ll \beta_{eq}$ also be so good at $\beta$ close to $\beta_{eq}$? And what is the limit $\beta_{eq}$? What does it depend on and how can it be increased? These questions inevitably arise when the transition to high $\beta$ becomes the real goal, and equilibrium theory must answer them. These very questions actually determine the subject of the present work.

We are going to discuss the *control of plasma equilibrium in stellarators* as a means of increasing the achievable $\beta$. To analyze the finite pressure effects, it was necessary, first of all, to develop a self-consistent analytical approach of high accuracy and enabling us to embrace a wide range of problems of plasma equilibrium in stellarators.

Plasma-equilibrium control means the *control of the position and shape of the plasma column* with the help of external

magnetic fields. The control fields enter the problem of equilibrium through the boundary conditions. Therefore, a part of our article must be devoted to general formulations of the problems of free-boundary plasma equilibrium and to reduction of the boundary conditions when the general theory is applied to particular problems.

Control of the plasma position is carried out by means of an external vertical field, and the strongest means of plasma-shape control is the quadrupole field. Both problems are discussed below. This is the intrinsic logic of the article. Thus, we continue now with a brief discussion of the results on the problems of free-boundary plasma equilibrium and plasma-shape control in toroidal systems.

## 1.5. Free-boundary plasma equilibrium

The theory of *free-boundary* plasma equilibrium should answer two basic questions:

— What external fields are necessary for creating the desired shape of the plasma column and for keeping it at a given position?

— What will be the plasma shape and position in a given magnetic field?

Accordingly, direct (because the choice of plasma shape and position is primary) and inverse problems of equilibrium can be distinguished [129].

In both cases, not only the plasma itself but the external vacuum area should be considered. Calculation of the magnetic field in a vacuum is a classical problem of electrodynamics. When it is "matched" with a calculation of the magnetic field inside the plasma, the key element of the problem is the matching of the solutions at the boundary plasma-vacuum. The magnetic field $\mathbf{B}$ has no normal component at the plasma boundary: $\mathbf{B}\cdot\mathbf{n} = 0$, where $\mathbf{n}$ is the normal to the plasma surface. Therefore, irrespective of the geometry of a system, all sources of the external

field can be formally replaced by the surface current [20, 130, 230]

$$\mathbf{i} = [\mathbf{n} \times \mathbf{B}]. \tag{1.3}$$

Because of this, in order to solve a full direct equilibrium problem, it is enough after solving the internal problem at a given plasma boundary to calculate the field produced by the current (1.3).

The method based on using Eq. (1.3) and enabling us to proceed naturally from the solution of the internal problem to a complete description of the plasma in the magnetic field is known in equilibrium theory as the *virtual casing principle* [230, 130]. If we leave the physical analogies aside, this is the classical method of the Green's function or the surface potential. Its application in two-dimensional problems of plasma equilibrium appears to be rather effective [130, 205, 207]. The attempt to apply it to stellarators was undertaken for the first time by Fielding and Hitchon [119–121] in developing an analytical approach based on a multistep (up to the sixth order!) expansion in equilibrium equations. This expansion, actually not admitting the asymptotic transition to infinity (necessary to account for the regularity conditions), and also essential initial restrictions of the model [119–121] have not allowed the authors to reveal any advantage of the virtual casing principle in application to stellarators or obtain any reliable general result.

The absence of a regular method for matching the internal and external solutions for the magnetic field at the plasma boundary manifested itself in the fact that whenever the problem of the influence of the vertical field on plasma equilibrium in stellarators was considered, assumptions compensating for a missing equation were required (see [22, 116, 118, 137, 184, 185, 231]). In the majority of cases they were introduced implicitly, but always toward a radical simplification of the problem. As a consequence, the results of different authors were practically incomparable. Moreover, even the highly natural transition to the limit of axial symmetry (tokamak) was impossible. This can be illustrated, for example, by expressions for the plasma shift

under the action of a vertical field in a stellarator presented in relatively recent papers [184, 231].

It is difficult to use expression (1.3) directly for finding the external confining field in a stellarator because the problem is three-dimensional. However, the equations of plasma equilibrium in conventional stellarators can be reduced in a general form to two-dimensional equation (1.2). This necessarily requires the appropriate reduction of boundary conditions and, at the same time, suggests the following logic of actions: it is necessary to obtain the analogue of Eq. (1.3) but for the "averaged" boundary, just where the boundary condition to Eq. (1.2) must be formulated. The nontrivial moment essentially distinguishing this problem from that for tokamaks is the presence of a nonzero normal component of the averaged "effective poloidal field" on the "averaged" boundary. Nevertheless, it became possible to join the virtual casing principle with the classical stellarator approximation [232]. More details will be presented in the Section four.

The general formulation of the reduced *two-dimensional virtual casing principle for stellarators* [232] turned out to be extremely convenient in free-boundary plasma equilibrium problems [233–235]. With its help the axially symmetric component of the plasma's own magnetic field or external confining field may be calculated through contour integrals over the boundary of the plasma "averaged" cross section with the two-dimensional Green's function. It is essential from a theoretical standpoint that then the obstacles for the direct transfer of ideas and methods of tokamak theory onto stellarators completely disappear. Certainly, we do not mean the literal analogies, which are faulty in the majority of cases, but the fundamental possibility of formulating the problems mathematically correctly and solving those already resolved for tokamaks. It should also be possible to make an exact asymptotic transition to a tokamak at any stage of the calculations or reproduce known results of the tokamak theory with a desired accuracy (at least, to check the calculations) in the limit of a vanishing helical field.

The main conclusion following from consideration of the free-boundary plasma equilibrium in conventional stellarators was that the plasma column could move strongly outward with increasing $\beta$. The larger the $\beta$, the stronger this effect. An external vertical field $B_\perp \sim \beta$ is needed to suppress this undesirable plasma shift.

In the preceding papers only suppositions [115, 118] or estimates [21, 116, 117, 119–121, 184, 185] were suggested within the framework of excessively simplified models and for $\beta \ll \beta_{eq}$. Analytical calculations [233] performed self-consistently and with an accuracy typical of recognized methods of the tokamak theory [4, 130, 236, 237] have removed the uncertainty from the subject.

The conclusion of [233] can be formulated as a statement about the unconditional necessity of the vertical control field for achievement of high values of $\beta$ in stellarators. Though this conclusion was relevant to a greater degree to stellarators of the next generation such as LHD, its validity was already convincingly manifested in the preparation of experiments on achievement of high $\beta$ in the relatively small CHS device [103]. Three-dimensional numerical calculations of equilibrium have shown that, in agreement with estimates by expressions from [233], with $\beta$ increasing up to 2% at a stationary unchanged vertical field the plasma column in CHS should move outward by one centimeter. Indeed, this was observed in experiments [103]. At the same time, use of the vertical control field, varied during the discharge with increasing $\beta$, allowed suppression of this shift, which promoted progress toward the $\beta$ that are the highest obtained thus far in stellarators [104].

In CHS experiments [104], the plasma position was detected by two independent diagnostics: by density-profile measurements using a lithium-beam probe and by measurements of the emission profiles in the vacuum ultraviolet range. This reflected the fact that for stellarators the control of the plasma position was a new matter. If the tokamak experience is taken for guidance, first of all it should be necessary to generalize the

method based on magnetic measurements described for tokamaks by Zakharov and Shafranov [130] on stellarators.

This was done in [234]. Before this only particular cases were considered [184, 186, 231, 238], and either the transition to a current-free plasma was impossible (and inexact even in the tokamak limit) or the result greatly depended on the accepted assumptions (for example, on the assumed pressure profile). But the analysis in [234] was conducted in the spirit of Zakharov and Shafranov [130], which guaranteed the accuracy, and the result of [234] allowed both asymptotic transitions and also did not require knowledge of the profiles of plasma current or pressure. The proposed *method of measurement of the plasma-column position* [234] was successfully tested in the Heliotron E helical device [239–241] and indeed appeared to be quite accurate: it was possible to measure the plasma shift at a level of 0.5% of the minor radius. The measured shift was within the limits of analytical predictions [235], so, in general, the experiments [239–241] both demonstrated the efficiency of the method [234] (which was natural because it was actually the generalization of the classical method [130]) and confirmed the conclusions of [233–235].

The development of computers and the wide use of numerical methods in plasma physics now allows solution of the complete three-dimensional problem of free-boundary plasma equilibrium in formulations most adequate to the conditions of a real experiment and with high accuracy. The results of calculations of the plasma-column shift with increasing $\beta$ and of the influence of the vertical field on the plasma-column position in stellarators [242–244] confirm the conclusions of [233, 235]. Moreover, we should also mention the good quantitative agreement of numerical simulation and the results of analytical theory. This agreement is not the outcome of "adjustment" or casual coincidence. Within the correct approach it is predetermined by two basic circumstances. First, calculation of the external field is a purely magnetostatic problem, for the solution of which powerful methods of mathematical physics have been developed. Second, the plasma-column shift is an integral effect. The former means that

after adequate formulation of the boundary conditions (what is mainly required here from the physics) there remain only technical difficulties in the solution, and no further errors related to the inaccuracy of the physical models appear at this stage. The latter guarantees that the final result appears to be insensitive to the description of the plasma "interior": the integration smooths the distinctions enhancing the reliability of the results for physically reasonable analytical modeling. This is merely a general comment to the strategy of the construction of analytical models [232–235]. Its actual realization and results are described in Sections 3 and 4.

## 1.6. Plasma-shape control in stellarators

Optimization of the shape of the magnetic surface in stellarator systems was discussed in the theory long ago as a means of creation of the magnetic well [21]. Further, soon after the publication of the finger-ring tokamak concept [188], a finger-ring stellarator ("stellatron") was also proposed [245, 246], in which a significant reduction of transport coefficients could be expected because of the very large elongation of the magnetic surfaces. This new and, from a theoretical standpoint, interesting proposal definitely led away from customary notions of stellarators, since elongations of the order of the aspect ratio and multiaxial configurations were discussed [245, 246]. Perhaps because of this the proposal was not realized, though it was supported by [247, 248], where similar structures were considered.

Before the work on the ATF project, rather exotic stellarator configurations were discussed in connection with the shaping problem. Only vacuum configurations were the object of optimization. Because of this, the proposal to control the rotational-transform profile [183] was doubly new: it was applied to the "conventional" $\ell = 2$ torsatron ATF, and it recommended changing the plasma shape depending on the $\beta$ variation. Conceptually, the fact that the results of Carreras et al. [183] demonstrated

not only the desirability but also the necessity of plasma-shape control in the ATF was also new.

The theory was not ready to explain the results of numerical simulations [183]. The physical mechanism of the control of the rotational-transform profile was not completely clear, and it was also impossible to understand why modest changes in the plasma shape in the ATF gave an unexpectedly strong effect. At the same time, it was beyond doubt that a very important problem, requiring detailed study, had been touched upon by Carreras et al. [183].

If we recall tokamaks, where the advantages of a noncircular plasma were generally recognized long ago, the problem can be briefly formulated as a question: what benefit could be attained if in conventional stellarators the plasma shape were modified in the same manner as in tokamaks? Drawing parallels with a tokamak, it is natural to ask by analogy with Artsimovich and Shafranov [188]: what can be obtained by elongation of the plasma in stellarators? However not with elongation up to the unusually large values proposed by Danilkin and Kovrizhnykh [245, 246], but, primarily, in the range mastered in tokamaks. Let us say, at elongations of 1.5–2. One answer was given by Carreras et al. [183]: it is possible to get rid of the undesirable change of the rotational-transform profile with increasing $\beta$. This result [183] was obtained numerically and was found in calculations by changing the currents in three pairs of independently powered ring coils serving as a poloidal field system in the ATF. It is known, however, that the rotational transform in stellarators is a purely geometrical characteristic dependent only on the shape and position of the magnetic surfaces. Therefore, it was natural to consider this problem in a direct and more general physical formulation. This was done in [249–251], where the explicit dependence of the rotational transform on the shift and ellipticity of magnetic surfaces was found.

In the analytical theory of plasma equilibrium, the ellipticity of magnetic surfaces is introduced as a small value [130, 150, 172, 252, 253] when its radial dependence is essential. But

no restrictions were imposed on the value of the ellipticity in [249, 251], and the formulas derived allowed an explanation of the behavior of the rotational transform from the axis up to the plasma boundary since the ellipticity of the magnetic surfaces turned out to be larger at the center than at the plasma boundary in stellarators with shear [249, 250].

This fact was discovered in numerical calculations made with the help of a code generalizing the code of L. E. Zakharov for tokamaks [254] to stellarators [255]. In this code, the equilibrium equation (1.1) or (1.2) is reduced to a chain of one-dimensional equations for shift, ellipticity, triangularity, etc., which are the parameters used to describe the shape of the magnetic surfaces (the so-called moment method). The code was simple, flexible, reliable, fast, and had good convergence. However, attempts to calculate a configuration with a plasma elongation $K_b$ of the order of 1.5 (which is a quite moderate value for tokamaks) appeared unsuccessful for stellarators with shear. No problem arose for small ellipticity of the plasma boundary $K_b$, which was prescribed in the calculations. But increasing it finally resulted in a large elongation of the near-axis magnetic surfaces, which terminated the calculations.

At the center the elongation was always larger than at the boundary. In tokamaks the situation is the opposite: the inner surfaces remain more circular even for strong elongation of the plasma column (see, for example, [207, 211, 213, 214, 218, 219]). This difference is related to the different mechanisms of rotational-transform creation in these systems. In the final analysis, the most essential fact is that in tokamaks the rotational transform is maximal at the center and minimal at the edge, but in stellarators it grows from the center to the edge. The large values of elongation of near-axis surfaces in stellarators with shear at rather small $K_b$ [256] are explained exactly by this property. As follows from analysis [249–251], it is only due to this fact that the control of the rotational-transform profile proposed for the ATF [183] is possible in any stellarator with shear.

The role of shear should be especially emphasized. In the shearless case, the ellipticity of the magnetic surfaces elongated

by the external quadrupole field appears to be constant over the whole cross section [256], and the undesirable deformations, related with finite $\beta$, of the rotational-transform profile cannot be suppressed [249].

The fast growth of the elongation of internal magnetic surfaces with increasing $K_b$ in shear systems allows a twofold increase in $\beta_{eq}$ to be reached even at small (by tokamak standards) $K_b$ of the order of 1.2–1.4 [250]. This is one more essential benefit enabling us to speak confidently about the undoubted advantages of plasma elongation in stellarators.

Certainly, this rather obvious positive effect of elongation tempts us to use it as much as possible in increasing $K_b$, at least up to the standard tokamak values 1.5–2. But this is hindered by the formation of the internal separatrix. Analysis of the influence of the quadrupole field on the stellarator configuration [256] has shown that with $K_b$ approaching some critical value $E$ the elongation of the near-axis magnetic surfaces grows unlimitedly. Then the magnetic axis becomes split at $K_b > E$ and, instead of single-axial nested magnetic surfaces, a *three-axial doublet-like structure* appears whose size increases quickly with growing $K_b$.

An analytical treatment [256] uncovered the mechanism of formation of the internal figure-eight separatrix in numerical calculations of possible operational regimes of the ATF [41, 42, 45, 183]. It was also explained why the formation of such structures in the central area of $\ell = 3$ stellarators and torsatrons [16, 17, 22, 37, 257, 258] is inevitable: in these systems the rotational transform goes to zero at the axis, and even an infinitely small quadrupole field is sufficient for splitting it.

The general theory of the splitting of magnetic surfaces in a stellarator under the action of external perturbations is described in detail in [11–21]. In [256], the additional axially-symmetric quadrupole field was not assumed to be small, hence the results of [256] remained valid even in the case where the separatrix "grew" to the size of the initial configuration. The appearance of the separatrix at the center of a plasma is, generally speaking, undesirable. But when its size is large, already not the external but rather the internal area of the separatrix can be

considered as the useful volume for plasma confinement. Three facts are driving us toward such a proposal. First, the doublet-like configurations appearing under the action of the quadrupole field in stellarators [256] look very similar to the configurations studied in Doublet tokamaks [198–202, 259, 260]. Second, it is possible even to achieve a quantitative similarity in the main parameters [261, 262]. Finally, it is not difficult to create a large doublet-like structure in stellarators.

The fact that three-axial doublet configurations could be created in stellarators was actually known earlier: some particular examples were presented in [247, 248, 263]. All these results were obtained in numerical calculations with fixed parameters.

The authors of [247], developing the ideas of Danilkin and Kovrizhnykh [245, 246], calculated the magnetic field created by currents in $\ell = 2$ and $\ell = 3$ helical windings wound on the surface of an elliptical torus. The doublets were obtained for $\ell = 3$ only. The reasons for their formation in this case and the absence for $\ell = 2$ or any functional dependence were not discussed.

In [247], the three-axial doublet configuration was the result of a casual coincidence of circumstances, but in [248] the search for such configurations was the purpose of the analysis. The construction of the magnetic system was also different because the prototype was the already mentioned Doublet. This was the development of the concept of T. Ohkawa [264, 265]: Wang and Jensen [248] proposed creating doublets by superposition of the toroidal, helical, and additional quadrupole fields. The proposals of T. Ohkawa [264, 265] were of a rather general nature. Therefore, as was mentioned in [248], even the search for doublet configurations in the space of parameters appeared to be a complicated problem. Finally, they have been found only in stellarators with helical fields of very high multipolarity, $\ell = 7-9$. Satisfied with the demonstration of this result, the authors of [248] once again especially emphasized in their conclusions that the problem involved a large number of parameters, which did not allow a complete optimization to be carried out.

Later on it was shown that actually the situation is much simpler [261, 262]. It is enough to say that $\ell = 2$ stellarators [261] and stellarators with arbitrary $\ell$ [262] have been considered analytically, and the role of the relevant parameters has been clearly shown.

One interesting example was presented by Chodura and Schlüter [263] using the $\ell = 3$ stellarator as a basis (compare with $\ell = 7-9$ in [248]). Further, the calculation was done for a doublet configuration with a finite-pressure plasma. Some similar calculations were also reported later [41, 266].

Summarizing this brief discussion, let us conclude that *control of the plasma shape* is still an unused potential enabling us to significantly expand the possibilities of stellarators. The shut-down of the ATF has postponed the practical verification of corresponding theoretical predictions. But the idea of the "non-circular" stellarator is becoming more and more popular and is more often discussed by theorists (see [267–273]). In the opinion of the leaders of stellarator centers [274], stellarators lag behind tokamaks by one-to-two generations of installations, and the search for the optimal stellarator configuration still remains one of the problems whose solution should help to overcome this backlog. Control of the plasma position and shape is the logical and natural step forward in this direction.

## 2. General equations of the theory of plasma equilibrium in conventional stellarators

The MHD theory of plasma equilibrium in toroidal systems is based on the equations

$$\nabla p = [\mathbf{j} \times \mathbf{B}], \tag{2.1a}$$

$$\operatorname{div} \mathbf{B} = 0, \quad \mathbf{j} = \operatorname{rot} \mathbf{B}. \tag{2.1b}$$

Here $p$ is the plasma pressure, $\mathbf{j}$ is the current density, and $\mathbf{B}$ is the magnetic field. A detailed substantiation of the applicability

of Eq. (2.1a) for the description of even a nonideal plasma can be found in [130].

All subsequent discussion is based on Eqs. (2.1a) and (2.1b). Stellarators are three-dimensional systems, which greatly hinders the solution of these equations. However, the complexity of the problem is partly compensated by the presence of small parameters. The use of expansion in small parameters is the key element of all analytical methods in stellarator theory. Consequently, the choice of the minimal number of expansion parameters and the realization of calculations with minimal restrictions is an important problem. The success in the reduction of the main system of equations (2.1a) and (2.1b) will determine the circle of problems that may potentially be solved, the accuracy of solutions, and, in the final analysis, the ease and degree of completeness of integration of this branch of the theory into the general theory of plasma equilibrium in toroidal fusion devices. The purpose of the present section is the construction of the necessary mathematical technique to describe plasma equilibrium in conventional stellarators on the basis of Eqs. (2.1a) and (2.1b).

## 2.1. Stellarator approximation and the magnetic differential equation

The stellarator approximation or stellarator expansion is the method proposed by Greene and Johnson [93] to solve the equilibrium equations for stellarators. It is based on the principle known in physics as the Bogolyubov–Mitropolskii averaging method [275] (see also [20, 276]).

In a conventional stellarator with a plane circular axis the magnetic field has two components: the axially symmetric one $\bar{\mathbf{B}} = \bar{\mathbf{B}}(r, z)$, whose main part is the longitudinal field $B_t \mathbf{e}_\zeta$, and the "helical" field $\tilde{\mathbf{B}}$ oscillating rapidly in the longitudinal coordinate $\zeta$:

$$\mathbf{B} = \bar{\mathbf{B}} + \tilde{\mathbf{B}}. \tag{2.2}$$

Formally, the difference between conventional stellarators and tokamaks is related only to the field $\tilde{\mathbf{B}}$, which makes the config-

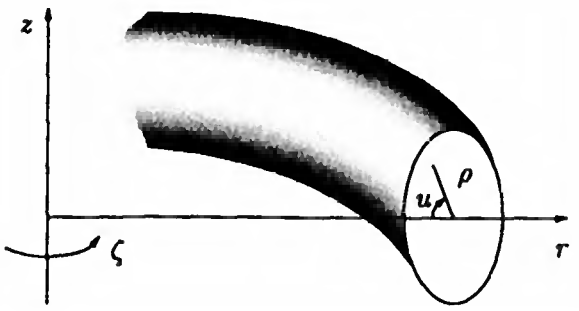


**Fig. 2.1.** Cylindrical coordinates $r, \zeta, z$ and polar coordinates $\rho, u$ in the transverse cross section $\zeta =$ const.

uration three-dimensional. But the value $\tilde{\mathbf{B}}$ is small in Eq. (2.2), which allows the use of an expansion in the parameter $\tilde{B}/\bar{B}$ when Eqs. (2.1) are solved. Here and in what follows, $r, \zeta, z$ are the usual cylindrical coordinates, and $\rho, u, \zeta$ are the quasi-cylindrical coordinates associated with the geometrical axis $r = R$ of the device (Fig. 2.1).

Greene and Johnson proposed [93] to consider the system in the lowest "zero"-order approximation as a straight configuration with a uniform longitudinal field and to consider the helical field as the main first-order perturbation and the toroidicity, an axially symmetric poloidal field, and the field of equilibrium currents as values of the second order. It was assumed that the parameters of the expansion thus determined are subject to the ordering

$$\frac{\tilde{\mathbf{B}}^2}{B_0^2} \sim \frac{B_J}{B_0} \sim \beta \sim \frac{b}{R} \ll 1, \tag{2.3}$$

where $B_0$ is the vacuum longitudinal field at the geometrical axis $r = R$, $B_J$ is the field of the longitudinal current, and $b$ is the characteristic transverse size of the plasma column (average minor radius of the plasma).

It was mentioned in the first section that an expansion in these and sometimes in even more parameters was later used

explicitly and implicitly in a number of works on the theory of plasma equilibrium and stability in stellarators [117, 135–156, 160, 161, 222, 223, 277–279]. Physically this approach is quite correct and effective, so it was natural to try to expand its domain of applicability by getting rid of some of the restrictions expressed by (2.3). This possibility was analyzed in [158] and was then developed in [131] and [280].

The idea of improving the Greene and Johnson approach arises when we try to establish the correspondence between the results of stellarator and tokamak theories. It is clear that under conditions (2.3) the asymptotic transition to a tokamak could not be complete. Indeed, the Grad–Shafranov equation (1.1) is derived from the equilibrium equations (2.1) under the single condition that the system is axially symmetric. But for vanishingly small helical field $\tilde{\mathbf{B}}$ the restrictions on the three parameters $B_J/B_0$, $\beta$, and $b/R$ still remain in (2.3), whereas, in general, they are not needed for tokamaks.

It is clear that assumptions (2.3), though acceptable in the majority of cases, are unsatisfactory from the standpoint of the formal theory. To make them less restrictive, the main approximation should be not the straight field, as was proposed in [93], but the toroidal field. Moreover, the calculations should be performed taking account of the fact that no expansion is needed to arrive at Eq. (1.1) in the asymptotic limit $\tilde{B}/B_0 \to 0$. This conception was realized in [131, 158].

All necessary calculations and proofs are described in [158] and [131] using the flux coordinates. Their introduction at the initial stage of calculations allows one to reduce the amount of calculations as a result of explicitly accounting for the conditions $\mathbf{B} \cdot \nabla p = \mathbf{j} \cdot \nabla p = 0$ following from Eq. (2.1a), but this may create inconveniences for the unprepared reader, since the expressions and operators acquire a specific form in the curvilinear flux coordinates. Here we describe another approach with similar emphasis on $\mathbf{B} \cdot \nabla p = \mathbf{j} \cdot \nabla p = 0$ from the very beginning of the calculations, but completely free from the technical difficulties related to the special technique of flux coordinates.

Actually the transition to flux coordinates was necessary in [131, 158] to adequately take into account the complex three-dimensional geometry of the magnetic surfaces of a stellarator. Formally this transition corresponds to some change of variables. When flux coordinates are used, such a change is always carried out simultaneously in all functions and operators. Contrarily, in the approach proposed here the change of variables is made *only* in the functions, not in the operators, and furthermore, not in all functions and not at the beginning of calculations, but only when it is absolutely necessary. Separating the problem of complex geometry from the technical nuances of the use of flux coordinates, it is possible to pass entirely from Eqs. (2.1a) and (2.1b) to the two-dimensional equation (1.2) without excessive complications, retaining the elegance and simplicity at each step of the transformations and not screening out the general relations by the details of the calculations. These qualities, in combination with the strictness of the approach, entirely justify this treatment (the next after [131]) of the analytical description of MHD plasma equilibrium in stellarators.

Let us start from the equation

$$\mathbf{B} \cdot \nabla x = y, \tag{2.4}$$

whose solution will show how the geometrical difficulties mentioned arise and how they can be overcome. A discussion of the main elements of the transformations leading from Eqs. (2.1) to the two-dimensional equation (1.2) is necessary to understand the basic ideas, but it is not the only motive. We are obliged to consider Eq. (2.4) because similar equations will be repeatedly encountered in the subsequent analysis.

Equations of the type of (2.4), which we inevitably have to treat in the theory of equilibrium of toroidal plasmas, are called magnetic differential equations (MDE) [21]. It is assumed that the unknown $x$ in an MDE is a single-valued (twice-periodic) function, and $y$ satisfies the natural conditions of solvability

$$\int y \, d\tau = 0, \quad \oint \frac{y}{B} \, dl = 0, \tag{2.5}$$

where the first integral is taken over the volume between any two magnetic surfaces, and the second along a closed field line (see [21]).

In the case of symmetry, the MDE becomes a rather simple ordinary differential equation, but in three-dimensional geometry it is already a partial differential equation whose solution requires integration along the field lines.

In conventional stellarators the lines of the magnetic field lie on toroidal surfaces whose asymmetry is not very large. This allows an easy reduction of the problem to two dimensions. The substitution

$$x = \bar{x} + \tilde{x} \tag{2.6}$$

allows Eq. (2.4) to be decomposed into two parts:

$$\bar{\mathbf{B}} \cdot \nabla \bar{x} + \langle \tilde{\mathbf{B}} \cdot \nabla \tilde{x} \rangle_\zeta = \bar{y}, \tag{2.7a}$$

$$\tilde{\mathbf{B}} \cdot \nabla \tilde{x} + \tilde{\mathbf{B}} \cdot \nabla \bar{x} = \tilde{y}. \tag{2.7b}$$

The "perturbation" $\tilde{\mathbf{B}}$ is considered to be small in Eq. (2.2), so that the quadratic term $\tilde{\mathbf{B}} \cdot \nabla \tilde{x}$ is omitted in the last equation. Here and in what follows the standard notation is used for the averaging over $\zeta$ and for rapidly oscillating quantities:

$$\bar{f} \equiv \langle f \rangle_\zeta = \frac{1}{2\pi} \int_0^{2\pi} f \, d\zeta, \quad \tilde{f} = f - \langle f \rangle_\zeta, \quad \hat{\tilde{f}} = \int \tilde{f} \, d\zeta, \tag{2.8}$$

and, additionally, the condition $\oint \hat{\tilde{f}} \, d\zeta = 0$ should be satisfied in the latter case.

In Eq. (2.7b), one elementary operation, the linearization, has already been done. The next step of stellarator expansion is the replacement of the operator $\bar{\mathbf{B}} \cdot \nabla$ by $B_t \mathbf{e}_\zeta \cdot \nabla$ in this equation, where $B_t$ is the toroidal component of the field $\bar{\mathbf{B}}$,

$$\bar{\mathbf{B}} = B_t \mathbf{e}_\zeta + \bar{\mathbf{B}}_p, \tag{2.9}$$

and the subscript $p$ designates the poloidal component. After this Eq. (2.7b) is simply integrated, and the explicit expression

for $\tilde{x}$ can be represented in the form

$$\tilde{x} = -\delta\mathbf{r} \cdot \nabla\bar{x} + \frac{r}{B_t}\hat{\tilde{y}}, \tag{2.10}$$

where

$$\delta\mathbf{r} = \frac{r}{B_t}\hat{\tilde{\mathbf{B}}}_p \cong \frac{r^2}{RB_0}\hat{\tilde{\mathbf{B}}}_p, \tag{2.11}$$

and $\hat{\tilde{\mathbf{B}}}_p$ is a vector with components $\hat{\tilde{B}}_r = \int \tilde{B}_r\, d\zeta$ and $\hat{\tilde{B}}_z$. The approximate equality in Eq. (2.11) corresponds to the replacement of $B_t$ by $B_0R/r$, where, let us recall, $R$ is the radius of the geometrical axis of a stellarator and $B_0$ is the toroidal field at this axis.

After substitution of the found function $\tilde{x}$ into Eq. (2.7a), this equation can be transformed to

$$\left(\bar{\mathbf{B}} + \mathbf{B}^*\right) \cdot \nabla\bar{x} = \bar{y} - \left\langle \tilde{\mathbf{B}} \cdot \nabla\left(\frac{r}{B_t}\hat{\tilde{y}}\right)\right\rangle_\zeta, \tag{2.12}$$

where

$$\mathbf{B}^* \equiv \frac{1}{2\pi}\left[\nabla\psi_V \times \nabla\zeta\right]. \tag{2.13}$$

The latter can be called an "effective poloidal field." Being induced by the helical field, it appears in equations when they are averaged over $\zeta$. The function $\psi_V$ is the poloidal flux of the helical field $\tilde{\mathbf{B}}$:

$$\psi_V = \frac{\pi r^2}{B_t}\left\langle\left[\tilde{\mathbf{B}} \times \hat{\tilde{\mathbf{B}}}\right] \cdot \frac{\nabla\zeta}{|\nabla\zeta|}\right\rangle_\zeta = \frac{2\pi r^2}{B_t}\langle\tilde{B}_z\hat{\tilde{B}}_r\rangle_\zeta. \tag{2.14}$$

Deriving Eq. (2.12) from Eqs. (2.7), we used the identity

$$\left\langle \tilde{\mathbf{B}} \cdot \nabla\left(\delta\mathbf{r} \cdot \nabla\bar{f}\right)\right\rangle_\zeta = -\mathbf{B}^* \cdot \nabla\bar{f}, \tag{2.15}$$

which can be elegantly but strictly proven. Let us do so.

Assume that $\mathbf{c}$ is some axially symmetric vector field:

$$\mathbf{c} = c_r(r,z)\mathbf{e}_r + c_z(r,z)\mathbf{e}_z. \tag{2.16}$$

The auxiliary relationship

$$2\tilde{B}_r\left(\hat{\tilde{\mathbf{B}}}\cdot\mathbf{c}\right)=\left[\tilde{\mathbf{B}}\times\hat{\tilde{\mathbf{B}}}\right]\cdot\left[\mathbf{e}_r\times\mathbf{c}\right]+\frac{\partial}{\partial\zeta}\left(\hat{\tilde{B}}_r\hat{\tilde{\mathbf{B}}}\cdot\mathbf{c}\right), \qquad (2.17)$$

whose validity can be easily verified, after the averaging over $\zeta$ gives

$$\left\langle\tilde{B}_r\left(\hat{\tilde{\mathbf{B}}}\cdot\mathbf{c}\right)\right\rangle_\zeta=\frac{\psi_V}{2\pi}\frac{B_t}{r}\left[\mathbf{e}_r\times\mathbf{c}\right]\cdot\nabla\zeta. \qquad (2.18)$$

Here we have used definition (2.14) of the function $\psi_V$. The latter two relationships remain in force when the pair $\tilde{B}_r$, $\mathbf{e}_r$ is replaced by $\tilde{B}_z$, $\mathbf{e}_z$. Hence,

$$\left\langle\tilde{\mathbf{B}}_p\left(\delta\mathbf{r}\cdot\mathbf{c}\right)\right\rangle_\zeta=\frac{\psi_V}{2\pi}\left[\mathbf{c}\times\nabla\zeta\right]. \qquad (2.19)$$

Hereafter this formula will be used many times. We shall call Eq. (2.19) the *main identity of the averaging method*, because all calculations with averaging over $\zeta$ are related in different ways to Eq. (2.19). This, probably, had not been noticed before in analytical calculations. Therefore, we especially emphasize that many complicated derivations can be substantially simplified if from the very beginning we have Eq. (2.19) at hand.

Here we need a consequence of Eq. (2.19):

$$\operatorname{div}\left\langle\tilde{\mathbf{B}}_p\cdot\left(\delta\mathbf{r}\cdot\nabla\bar{f}\right)\right\rangle_\zeta=-\mathbf{B}^*\cdot\nabla\bar{f}, \qquad (2.20)$$

which gives the necessary result (2.15) after reduction of the left-hand side of Eq. (2.20) to the necessary form by means of

$$\left\langle\operatorname{div}\gamma\tilde{\mathbf{B}}_p\right\rangle_\zeta=\left\langle\operatorname{div}\gamma\tilde{\mathbf{B}}\right\rangle_\zeta=\left\langle\tilde{\mathbf{B}}\cdot\nabla\gamma\right\rangle_\zeta. \qquad (2.21)$$

Let us note that this proof of Eq. (2.15) is much simpler than that described in [131], p. 313.

Finally, the solution of Eq. (2.4) can be written as

$$x=\bar{x}+\tilde{x}=\bar{x}-\delta\mathbf{r}\cdot\nabla\bar{x}+\frac{r}{B_t}\hat{\tilde{y}}, \qquad (2.22)$$

and $\bar{x}$ must be found from the two-dimensional equation (2.12). The oscillating part $x$ is found from the linearized equation (2.7b), hence we can say that (2.22) is the solution of Eq. (2.4) in the linear approximation in $|\tilde{\mathbf{B}}|/B_t$.

It should be kept in mind that $\tilde{x}$ in the form (2.10) is obtained from Eq. (2.7b) *if* the differentiation over $\zeta$ is left only in the operator $\mathbf{B} \cdot \nabla$. This can be done if the rotational transform over the period of a system is much smaller than unity. In this case, $|\mathbf{B}_p \cdot \nabla \tilde{x}| \ll |B_t \mathbf{e}_\zeta \cdot \nabla \tilde{x}|$, which allows us to neglect the first term. For completeness it is also useful to compare $|\tilde{y}|$ and $|\mathbf{B}_p \cdot \nabla \tilde{x}|$, using the first term from the right-hand side of Eq. (2.10) for the estimate of $\tilde{x}$. If $|\tilde{y}| \leq |\mathbf{B}_p \cdot \nabla \tilde{x}|$, $|\tilde{\mathbf{B}} \cdot \nabla \tilde{x}|$, then the term with $\tilde{y}$ in Eq. (2.10) can be neglected, and only $\bar{y}$ can be left on the right-hand side of Eq. (2.12). However, the presence of the term with $\tilde{y}$ in Eq. (2.12) does not change anything in the further procedure of the solution of this equation, since in the problems of interest $\tilde{y}$ is the known function. Keeping $\tilde{y}$ on the right-hand side of Eq. (2.12), we should check whether or not the related additive to $\bar{y}$ is small. If it is too small, there is no need to keep it.

In conventional stellarators it is always true that

$$\frac{\tilde{B}}{B_t} \ll 1, \quad \frac{\mu}{m} \ll 1, \tag{2.23}$$

where $\mu$ is the rotational transform and $m$ is the number of periods of a system. Therefore, the expansion in these parameters is quite justified for the solution of stellarator problems. In our case, such an expansion determines the accuracy of calculation of the function $\psi_V$.

In stellarator theory, the most interesting cases are those where the presence of $\mathbf{B}^* \cdot \nabla$ on the left-hand side of Eq. (2.12) greatly influences the result. The opposite case corresponds to the asymptotic transition to a tokamak. At such a transition, incidently, the condition $\mu/m \ll 1$ becomes unnecessary, since it was used only to find the field $\mathbf{B}^*$, which disappears at $\tilde{B} \to 0$.

The helical field $\tilde{\mathbf{B}}$ displays itself in Eq. (2.12) through $\mathbf{B}^*$, which can be considered as a field of given "stationary sources." The control field and the field of plasma currents give the additive contributions to the real field $\bar{\mathbf{B}}$. Larger $\beta$ and stronger control fields correspond to the "strengthening" of $\bar{\mathbf{B}} \cdot \nabla$ in Eq. (2.12). Our aim is to consider problems in which the contributions from $\mathbf{B}^* \cdot \nabla$ and $\bar{\mathbf{B}} \cdot \nabla$ are comparable.

## 2.2. Real and averaged magnetic surfaces

A particular example of MDE is the equation

$$\mathbf{B} \cdot \nabla \Psi = 0, \tag{2.24}$$

which should be solved, at least, because such is the longitudinal component of the equilibrium equation (2.1a): $\mathbf{B} \cdot \nabla p = 0$. Irrespective of (2.1a), Eq. (2.24) serves to find the magnetic surfaces $\Psi = \text{const}$. In this case, the function $\Psi$ is usually called a flux function.

In a stellarator the magnetic field is represented in the form (2.2), and the function $\Psi$ can be accordingly represented as

$$\Psi = \psi + \tilde{\psi}, \tag{2.25}$$

where $\psi = \psi(r, z)$ is the part of $\Psi$ independent of $\zeta$, and $\tilde{\psi}$ is the rapidly oscillating component of $\Psi$. According to Eq. (2.10)

$$\tilde{\psi} = -\delta\mathbf{r} \cdot \nabla\psi, \tag{2.26}$$

where $\delta\mathbf{r}$ is the vector (2.11). Thus, the complete solution of the equation $\mathbf{B} \cdot \nabla \Psi = 0$ is expressed through the "two-dimensional" function $\psi$:

$$\Psi = \psi + \tilde{\psi} = \psi - \delta\mathbf{r} \cdot \nabla\psi = \psi(\mathbf{r} - \delta\mathbf{r}). \tag{2.27}$$

The three-dimensionality of the configuration is taken into account here in the linear approximation in $|\tilde{\mathbf{B}}|/B_t$.

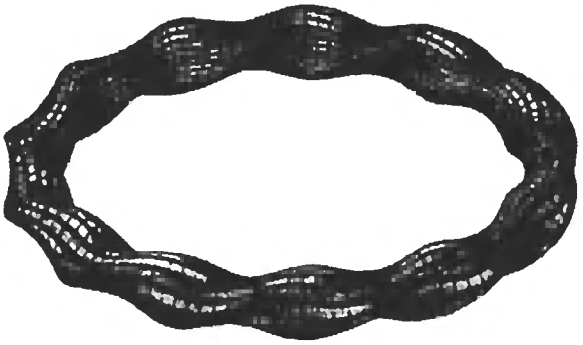

**Fig. 2.2.** Magnetic surface in an $\ell = 2$ stellarator.

Relationship (2.27) shows that after the change of variables (the subscript $s$ originates from the word "surface")

$$\mathbf{r}_s = \bar{\mathbf{r}}_s + \delta\mathbf{r} \tag{2.28}$$

the function $\Psi\left(\mathbf{r}_s\right)$ becomes a function of two variables in coordinates $\bar{\mathbf{r}}_s$. Geometrically, the vector transformation (2.28) corresponds to a deformation of space in two directions (in the transverse cross section, but the coordinate $\zeta$ is not touched), such that the magnetic surfaces are transformed from helically twisted (Fig. 2.2) into axially symmetric toroids. A field of "vectors of deformation" $\delta\mathbf{r}$ for an $\ell = 2$ stellarator is shown in Fig. 2.3.

It is easy to confirm that equality (2.28) gives the direct relation between the coordinates $\mathbf{r}_s$ of the real magnetic surface $\Psi = \text{const}$ and the coordinates $\bar{\mathbf{r}}_s$ of its averaged image $\psi = \text{const}$ (Fig. 2.4). Indeed, $\mathbf{r}_s$ and $\bar{\mathbf{r}}_s$ should satisfy the equation

$$\Psi(\mathbf{r}_s) = \psi(\bar{\mathbf{r}}_s) = \text{const}. \tag{2.29}$$

From this, with account of Eq. (2.27), we immediately obtain Eq. (2.28). Let us note that Eq. (2.28) is also useful in allowing us to find the geometrical parameters of averaged surfaces $\psi = \text{const}$ from the results of three-dimensional calculations, which are necessary for two-dimensional calculations.

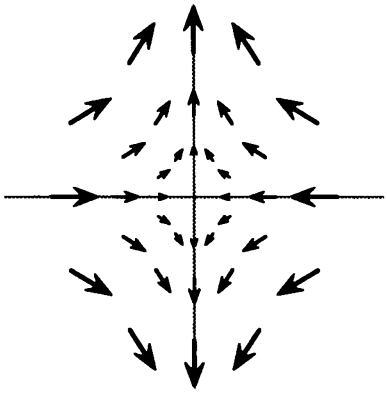

**Fig. 2.3.** Vector field $\delta\mathbf{r}$ in an $\ell = 2$ stellarator.

Relationships (2.27) and (2.28) clearly explain the meaning of the transition to a two-dimensional description of stellarators for any method of reduction of the equilibrium equations (2.1) to two-dimensional. It is possible to say that the construction of a two-dimensional model of a stellarator actually rests upon the change of variables (2.28). Usually the transition $3D \to 2D$ is explained by other arguments, but the geometrical interpretation seems to us the most simple and natural.

In many papers, in mentioning the averaging method the authors incidentally note that some part of the information is allegedly lost with its use. This is not correct, because working with two-dimensional images it is always possible to restore, if necessary, the true three-dimensional picture with the help of Eqs. (2.27) or (2.28), as was done, for example, in [159] or [281].

When relation (2.27) between $\Psi$ and $\psi$ is established, Eq. (2.24) is reduced to eq. (2.7a) with $\bar{y} = 0$. In the zero approximation it becomes the trivial identity $B_t\,\partial\psi/\partial\zeta = 0$, hence, the operator $\bar{\mathbf{B}}_p \cdot \nabla$ cannot be neglected. Substitution of $\tilde{\psi}$ in the form (2.26) into Eq. (2.7a) and averaging of $\tilde{\mathbf{B}} \cdot \nabla\tilde{\psi}$ over $\zeta$ with

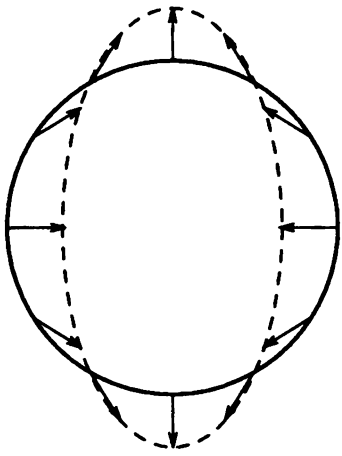

**Fig. 2.4.** Cross section of the averaged (solid line) and real (dashed line) magnetic surfaces. The arrows show the vectors $\delta\mathbf{r}$.

the help of Eq. (2.15) transforms this equation into

$$\left(\mathbf{B}_p + \frac{1}{2\pi}\left[\nabla\psi_V \times \nabla\zeta\right]\right) \cdot \nabla\psi = 0, \tag{2.30}$$

which, certainly, can be considered as a particular case of relation (2.12). In Eq. (2.30), $\mathbf{B}_p$ is the axially symmetric poloidal field which, by virtue of div $\mathbf{B}_p = 0$, can be represented as

$$\mathbf{B}_p = \text{rot}\,\mathbf{A}_t = \left[\nabla\left(rA_t\right) \times \nabla\zeta\right], \tag{2.31}$$

where $A_t$ is the toroidal component of the vector potential. Thus, we finally obtain for $\psi$

$$\left[\nabla\left(2\pi r A_t + \psi_V\right) \times \nabla\zeta\right] \cdot \nabla\psi = 0. \tag{2.32}$$

The equality $[\nabla f \times \nabla g] \cdot \nabla\zeta = 0$, where $f = f(r,z)$ and $g = g(r,z)$, means that $\nabla f$ and $\nabla g$ are parallel and, hence, $f = f(g)$. The conditions $f = \text{const}$ and $g = \text{const}$ are equivalent in this case. Therefore, if the surfaces $f = \text{const}$ are searched, it is possible to put $f = g$ without loss of generality.

From this it follows that the equality

$$\psi = 2\pi r A_t + \psi_V \tag{2.33}$$

not only satisfies Eq. (2.32) but also utterly completes [together with Eq. (2.27)] the search for the flux function $\Psi$ for a given magnetic field of a stellarator. Arising at the last stage, the freedom in the choice of the form of the solution is related to the fact that the initial Eq. (2.24) is satisfied for the whole family of functions $f(\Psi)$, where $\Psi$ is any particular solution to Eq. (2.24).

The choice of the solution of Eq. (2.32) in the form (2.33) gives a real physical meaning to the function $\psi$. It is easy to show that it is the external (with respect to a magnetic surface) poloidal magnetic flux.

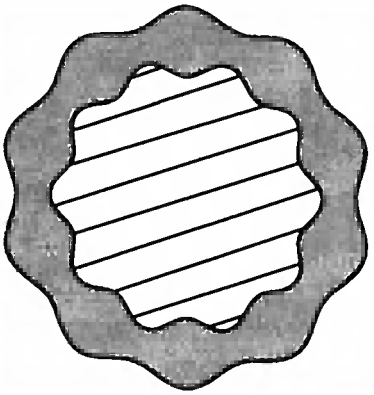

**Fig. 2.5.** Magnetic surface and the surface (hatched), the flux through which is called poloidal.

By definition, the poloidal flux $\psi_{\rm pol}$ is the flux "embraced" from the outside by a toroidal magnetic surface as by a ring (see Fig. 2.5). The conditions $\mathbf{B} \cdot \nabla\Psi = 0$ and $\operatorname{div} \mathbf{B} = 0$ allow a horizontal partition bounded by a "wavy" contour lying on a magnetic surface

$$r = \bar{r} + \delta r \tag{2.34}$$

to be taken for calculating $\psi_{\rm pol}$, where $\delta r = \mathbf{e}_r \cdot \delta\mathbf{r}$, and $\delta\mathbf{r}$ is

the vector (2.11). In this case,

$$\psi_{\text{pol}} = \int B_z \, dS = \int B_z \, r \, dr \, d\zeta = 2\pi \Big\langle \int_0^{\bar{r}+\delta r} r B_z \, dr \Big\rangle_\zeta . \qquad (2.35)$$

Integration of $\bar{B}_z$ on the right-hand side of Eq. (2.35) gives $2\pi r A_t$, and $tB_z$ gives rise to the function $\psi_V$. It is possible to confirm this with the help of the formula

$$\frac{1}{2\pi} \int \frac{f(\mathbf{r})}{r} \, dS = \Big\langle \int_0^{\bar{r}+\delta r} f(\mathbf{r}) \, dr \Big\rangle_\zeta = \int_0^{\bar{r}} \Big\langle f(\bar{\mathbf{r}}) + \frac{\partial}{\partial \bar{r}} (f \delta r) \Big\rangle_\zeta \, d\bar{r}, \qquad (2.36)$$

which corresponds to the change of variables (2.34) with account of the first-order small terms.

By direct calculation we have obtained $\psi_{\text{pol}} = \psi$. Thus, at the chosen normalization the equality (2.33) reflects the fact that the poloidal flux in a stellarator is the sum of two fluxes, of axially symmetric and helical fields.

An internal equilibrium problem is formally solved when the function $\psi$ is found. If $A_t = 0$ (only toroidal and helical fields are present), then $\psi = \psi_V$. This shows the basic difference between a stellarator and tokamak: the vacuum magnetic configuration of a stellarator has magnetic surfaces that are described by the Eq. $\psi_V = \text{const}$.

At a given $\psi_V$ the property of the vacuum configuration could be changed with the help of an external poloidal field, included in Eq. (2.33) through

$$A_t = A_{\text{ext}} + A_{\text{pl}}, \qquad (2.37)$$

where $A_{\text{ext}}$ is the part of $A_t$ created by an external field and $A_{\text{pl}}$ is the part created by the currents in the plasma. The problem of optimization of a stellarator is thus reduced to finding the best combination $\psi_V + 2\pi r A_{\text{ext}}$. But in problems of equilibrium control it is necessary, if possible, to answer a more subtle question: what could be the best combination $\psi_V + 2\pi r A_t$? The latter case

implies that it is necessary to vary $A_{\rm ext}$ during the discharge in order to minimize the deterioration of a configuration induced by $A_{\rm pl}$. For conventional stellarators even the first problem is not yet completely resolved. But the theory has already reached such a level of maturity that its predictions on plasma equilibrium control have become the subject of purposeful experimental study [104, 220, 240].

## 2.3. Integral quantities

One of the integral quantities already appeared in the previous section: it was the function $\Psi$. At each point it satisfies Eq. (2.24), but it can also be calculated as the integral (2.35). By definition, any quantity that does not vary on a magnetic surface is called a surface quantity. We shall use this terminology when it is necessary to point out functional dependences like $f(\Psi)$ or $f(\psi)$. The word "integral" will be used to specify a method of calculating quantities that are not necessarily surface quantities.

In many problems one has to know the values of quantities averaged over the volume of the layer between nearby magnetic surfaces:

$$\langle X \rangle \equiv \frac{d}{dV} \int_V X \, d\tau. \tag{2.38}$$

The equality (2.28) suggests that the integration over $V$ in volume integrals like (2.38) will be simplified after the change of variables (2.28), which transforms the region of integration $V$ into the axially symmetric toroidal tube $V_0$. For such a change of variables, the volume element $d\tau$ is transformed by the rule

$$d\tau = \left(1 + \operatorname{div} \delta\mathbf{r}\right) d\bar{\tau}, \tag{2.39}$$

so that we finally obtain

$$\int_V f(\mathbf{r}) \, d\tau = \int_{V_0} \left[ f(\bar{\mathbf{r}}) + \operatorname{div} (f \, \delta\mathbf{r}) \right] d\bar{\tau}. \tag{2.40}$$

The two last expressions are valid in the linear approximation in "perturbation" $\delta\mathbf{r}$. This accuracy is sufficient for conventional stellarators if equality (2.40) is applied for calculation of

the desired quantities in the lowest non-vanishing order (as, for example, the flux $\psi_V$ of a helical field $\tilde{\mathbf{B}}$) or small corrections to the terms of the main approximation. For appropriate grouping of terms the calculations are frequently reduced just to the second case. For example, large constants that determine the order of magnitude of $\mathbf{B}^2$ and $\mathbf{B} \cdot \nabla\zeta$ in toroidal systems with a strong longitudinal field are simply carried out of the integrals $\langle \mathbf{B}^2 \rangle$ and $\langle \mathbf{B} \cdot \nabla\zeta \rangle$, and only those values that describe the inhomogeneity of $\mathbf{B}^2$ and $\mathbf{B} \cdot \nabla\zeta$ on a magnetic surface should be integrated.

The transformation (2.39) preserves the toroidal volume. Therefore, $V = V_0$ (without taking account of the corrections quadratic in $\tilde{\mathbf{B}}/B_t$) and, according to Eq. (2.40),

$$\langle f \rangle = \langle f + \operatorname{div}(f\,\delta\mathbf{r}) \rangle_0, \tag{2.41}$$

where $\langle \ldots \rangle_0$ designates the "quasi-tokamak" averaging

$$\langle X \rangle_0 \equiv \frac{d}{dV_0} \int_{V_0} X\, d\bar{\tau}, \tag{2.42}$$

in which the integration over $\zeta$ corresponds to the averaging in $\zeta$ at fixed $r$ and $z$.

For the two types of functions that we have to deal with in stellarator analysis, we obtain from Eq. (2.41)

$$\langle f(r,z) \rangle = \langle f(r,z) \rangle_0, \tag{2.43}$$

$$\langle \tilde{f} \rangle = \langle \operatorname{div}(\tilde{f}\delta\mathbf{r}) \rangle_0 = -\left\langle \tilde{\mathbf{B}} \cdot \nabla \left( \frac{r}{B_t} \hat{\tilde{f}} \right) \right\rangle_0. \tag{2.44}$$

The last equality can be proved by substitution of the explicit expression (2.11) for $\delta\mathbf{r}$ with $\tilde{\mathbf{B}}_p = \tilde{\mathbf{B}} - \mathbf{e}_\zeta \tilde{B}_\zeta$ and by separation of the complete derivatives with respect to $\zeta$ in the integrand, which do not make a contribution to $\langle \ldots \rangle_0$.

Equality (2.44) helps to significantly simplify the calculation of many integral values for a conventional stellarator. For example, using the main identity of the averaging method (2.19),

we obtain from (2.44)

$$\langle \tilde{\mathbf{B}} \cdot \mathbf{c} \rangle = \left\langle \operatorname{div} \frac{\psi_V}{2\pi} \left[ \nabla\zeta \times \mathbf{c} \right] \right\rangle_0, \tag{2.45}$$

where $\mathbf{c}$ is the arbitrary poloidal vector whose components depend on $r$ and $z$ only. From here it follows, in particular, that

$$\langle \tilde{\mathbf{B}} \cdot \nabla \bar{f} \rangle = \langle \mathbf{B}^* \cdot \nabla \bar{f} \rangle_0, \tag{2.46}$$

where $\mathbf{B}^*$ is the "effective poloidal field" (2.13). These equalities will be required in further calculations.

Using Eq. (2.44), it is easy also to confirm that

$$\langle B_t \tilde{B}_\zeta + \tilde{\mathbf{B}}^2 \rangle = 0. \tag{2.47}$$

This non-trivial equality allows one to get rid of the term with $\tilde{B}_\zeta$ in $\langle \mathbf{B}^2 \rangle$ and thus to proceed to the integration of the type (2.42). Allocating a combination (2.47) in $\langle \mathbf{B}^2 \rangle$ and neglecting the small value $2\langle \mathbf{B}_p \cdot \tilde{\mathbf{B}} \rangle$, we obtain

$$\langle \mathbf{B}^2 \rangle = \langle B_t^2 + \mathbf{B}_p^2 - \tilde{\mathbf{B}}^2 \rangle. \tag{2.48}$$

In tokamaks, $rB_t$ is a constant on a magnetic surface. In [131], it was shown that with a high accuracy this is also correct for a stellarator even for finite pressure of the plasma (for a vacuum field $rB_t = RB_0 = \text{const}$ everywhere). With this property, Eq. (2.48) is reduced to the form

$$\langle \mathbf{B}^2 \rangle = \frac{r^2 B_t^2}{R^2} \left\{ 1 - \left\langle \Omega - \frac{\mathbf{B}_p^2}{B_t^2} \frac{R^2}{r^2} \right\rangle \right\}, \tag{2.49}$$

where $R = \text{const}$ is the major radius and

$$\Omega \equiv 1 - \frac{R^2}{r^2} + \frac{\langle \tilde{\mathbf{B}}^2 \rangle_\zeta}{B_0^2}. \tag{2.50}$$

In the last term we have replaced $rB_t/R$ by $B_0$, which is the vacuum longitudinal field on the axis of a stellarator ($r = R$).

In a similar manner, we can prove with the help of Eq. (2.47) that

$$\langle \mathbf{B} \cdot \nabla\zeta \rangle = \frac{rB_t}{R^2} \left(1 - \langle \Omega \rangle\right). \tag{2.51}$$

The unity in Eqs. (2.49) and (2.51) corresponds to the explicit separation of the large constant, which was mentioned above. The remaining averaged quantities play the role of small corrections and should, therefore, be calculated in the lowest approximation by rule (2.43). In the limit $|\widetilde{\mathbf{B}}| \to 0$, the equalities (2.48), (2.49), and (2.51) precisely turn into the tokamak expressions, as should be expected from the strict approach when only those approximations that are objectively dictated by the character of the problem are made.

Thus, for conventional stellarators the calculations of $\langle \mathbf{B}^2 \rangle$ and $\langle \mathbf{B} \cdot \nabla\zeta \rangle$ can be reduced to the "tokamak" calculations, with integration over the axially symmetric volume. The only difference between a stellarator and a tokamak is the presence of the quantity

$$\Omega^0 \equiv \frac{\langle \widetilde{\mathbf{B}}^2 \rangle_\zeta}{B_0^2} \tag{2.52}$$

in Eqs. (2.49) and (2.51), which gives the "cylindrical" asymptotic ($R/r \to 1$) of the function (2.50).

The expressions obtained for the integral quantities $\langle \mathbf{B}^2 \rangle$ and $\langle \mathbf{B} \cdot \nabla\zeta \rangle$ will be of use when working with the equilibrium equations (2.1). It is essential that the behavior of $\langle \mathbf{B}^2 \rangle$ and $\langle \mathbf{B} \cdot \nabla\zeta \rangle$ is determined by two functions: $rB_t$ and $\langle \Omega \rangle$ (the quantity $\mathbf{B}_p^2/B_t^2$ in Eq. (2.49) can be neglected). The first differs from the vacuum value $RB_0$ only to the degree of the diamagnetic effect. In other words, it is almost constant over the whole cross section of a plasma column. The second quantity, $\langle \Omega \rangle$, is always small compared with unity. Therefore, when, for example, we extract the oscillating components from $\mathbf{B}^2/\langle \mathbf{B}^2 \rangle$ and $\mathbf{B} \cdot \nabla\zeta / \langle \mathbf{B} \cdot \nabla\zeta \rangle$, we can disregard the distinctions between $\langle \mathbf{B}^2 \rangle$ and $\langle \mathbf{B}^2 \rangle_0$, and $\langle \mathbf{B} \cdot \nabla\zeta \rangle$ and $\langle \mathbf{B} \cdot \nabla\zeta \rangle_0$.

One of the advantages of the proposed method consists of the fact that the results of the volume averaging are expressed

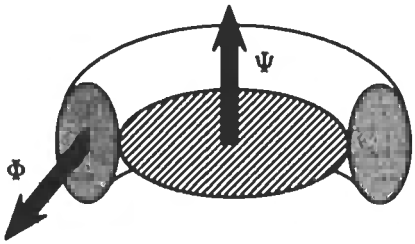


**Fig. 2.6.** Toroidal magnetic surface and related magnetic fluxes: poloidal, $\Psi$, and toroidal, $\Phi$.

through the magnetic field [see Eqs. (2.44)–(2.51)]. This is very convenient for estimates and comparisons. But when surface (or flux) quantities are mentioned, absolutely different expressions are meant. For example,

$$\langle \mathbf{B} \cdot \nabla\zeta \rangle V' = 2\pi\Phi', \tag{2.53}$$

$$\langle \mathbf{B}^2 \rangle V' = F\Phi' - J\Psi', \tag{2.54}$$

where $\Phi$ and $\Psi$ are the toroidal and poloidal magnetic fluxes,

$$\Phi = \int \mathbf{B} \cdot d\mathbf{S}_t, \quad \Psi = \int \mathbf{B} \cdot d\mathbf{S}_p \tag{2.55}$$

(see Fig. 2.6), and $J$ and $F$ are similar currents,

$$J = \int \mathbf{j} \cdot d\mathbf{S}_t, \quad F = \int \mathbf{j} \cdot d\mathbf{S}_p, \tag{2.56}$$

the prime designates differentiation with respect to the arbitrary flux function $a = a\big(\Psi\big)$.

The validity of equality (2.53) can be checked rather easily:

$$\Phi = \int \mathbf{B} \cdot d\mathbf{S}_t = \frac{1}{2\pi} \int_V \operatorname{div} \zeta\mathbf{B}\, d\tau = \frac{1}{2\pi} \int_V \mathbf{B} \cdot \nabla\zeta\, d\tau, \tag{2.57}$$

and here we need only definition (2.38).

Relationship (2.54), the similar equality

$$\langle \mathbf{j} \cdot \mathbf{B} \rangle V' = FJ' - JF', \tag{2.58}$$

and also the Kruskal–Kulsrud equation

$$p'V' = J'\Psi' - F'\Phi', \tag{2.59}$$

which is the integral consequence of the equilibrium Eq. (2.1a), are valid for any toroidal configuration. They are well known, and we give them here without derivation. If necessary, it can be found, for example, in [131].

In the following, Eqs. (2.53)–(2.59) will be necessary, at least, to transform the equilibrium equation to a form containing the longitudinal current $J$ explicitly.

## 2.4. Currents in equilibrium configurations

As was explained in Section 2.2, the longitudinal projection of the equilibrium Eq. (2.1a) for a conventional stellarator is finally reduced to Eq. (2.30). To use Eq. (2.1a) completely, we also have to take into account that its transverse component is transformed into

$$\mathbf{j} = \alpha\mathbf{B} + \frac{[\mathbf{B} \times \nabla p]}{\mathbf{B}^2}, \tag{2.60}$$

where $\alpha$ is an unknown function.

For all further transformations there are only Maxwell's equations (2.1b) at our disposal. It is well known that the consequence of the second equation, $\operatorname{div}\mathbf{j} = 0$, together with $\operatorname{div}\mathbf{B} = 0$, gives an equation for $\alpha$:

$$\mathbf{B} \cdot \nabla\alpha = -\left[\mathbf{B} \times \nabla p\right] \cdot \nabla\frac{1}{\mathbf{B}^2}. \tag{2.61}$$

This is already the second, now non-uniform magnetic differential equation, which should be solved in the course of simplification of the initial system (2.1). The right-hand side of Eq. (2.61) is the product of three quantities. Therefore, transforming it into the form $\bar{y} + \tilde{y}$, we shall obtain a chain of seven terms. The procedure for solving Eq. (2.61) by the scheme described in Section 2.2 thus becomes extremely cumbersome. It is possible to assert that this stage of calculations was the most

difficult and cumbersome of all known attempts at a general solution of the problem of plasma equilibrium in conventional stellarators. Even the use of the redundant simplifying assumptions [93, 119–121, 140, 155] or flux coordinates [139, 145, 131, 278, 279] could not provide the necessary facilitation of the calculations.

But the final result always appeared compact because of the cancellation of a number of terms after lengthy calculations. This brings us to the idea that there should be another, much better way of solving Eq. (2.61). A helpful hint can be found in [131] in the section devoted to systems of flux coordinates. It is shown there, in particular, that the most simple expression for the product $\mathbf{j} \cdot \mathbf{B}$ is obtained in the Hamada coordinates:

$$\mathbf{j} \cdot \mathbf{B} = \langle \mathbf{j} \cdot \mathbf{B} \rangle + \mathbf{j} \cdot \nabla f_H, \tag{2.62}$$

where $f_H$ is some periodic function describing the Hamada coordinates, which is subject to the condition

$$\mathbf{B} \cdot \nabla f_H = \mathbf{B}^2 - \langle \mathbf{B}^2 \rangle. \tag{2.63}$$

The equality (2.62) allows $\alpha$ to be expressed in the form

$$\alpha \equiv \frac{\mathbf{j} \cdot \mathbf{B}}{\mathbf{B}^2} = \frac{\langle \mathbf{j} \cdot \mathbf{B} \rangle}{\langle \mathbf{B}^2 \rangle} + \frac{1}{\langle \mathbf{B}^2 \rangle} \frac{\left[ \mathbf{B} \times \nabla p \right]}{\mathbf{B}^2} \cdot \nabla f_H, \tag{2.64}$$

and to complete the calculations, we have to solve the remaining equation (2.63), which is much simpler than initial equation (2.61).

Before moving on further, we note that relationships (2.60)–(2.64) are valid for any toroidal configuration. Moreover, it is necessary to note that there are no attributes of flux coordinates in Eqs. (2.62)–(2.64). This means that it should also be possible to obtain expression (2.64) without using the flux coordinates.

Indeed, for this purpose it is enough to use only the equality (2.63), which can be considered as a definition of $f_H$ or a

convenient representation of $\mathbf{B}^2$. The corresponding substitution

$$\frac{1}{\mathbf{B}^2} = \frac{1}{\langle \mathbf{B}^2 \rangle} \left( 1 - \frac{\mathbf{B} \cdot \nabla f_H}{\mathbf{B}^2} \right) \tag{2.65}$$

immediately allows Eq. (2.61) to be integrated by commutation of operators by the general rule

$$\begin{aligned} \mathbf{a} \cdot \nabla \big( \mathbf{b} \cdot \nabla f \big) &= \mathbf{b} \cdot \nabla \big( \mathbf{a} \cdot \nabla f \big) \\ &+ \big( \mathbf{a}\, \mathrm{div}\, \mathbf{b} - \mathbf{b}\, \mathrm{div}\, \mathbf{a} - \mathrm{rot}\, [\mathbf{a} \times \mathbf{b}] \big) \cdot \nabla f. \end{aligned} \tag{2.66}$$

As a result we obtain

$$\mathbf{j} = \frac{\langle \mathbf{j} \cdot \mathbf{B} \rangle}{\langle \mathbf{B}^2 \rangle} \mathbf{B} + \frac{\big[ (\mathbf{B} - \nabla f_H) \times \nabla p \big]}{\langle \mathbf{B}^2 \rangle}, \tag{2.67}$$

and Eq. (2.62) appears as simply a particular consequence of this equality (the projection to $\mathbf{B} - \nabla f_H$).

The compact expression (2.67) deserves special attention. It is obtained as a result of the solution of equations $\nabla p = [\mathbf{j} \times \mathbf{B}]$ and $\mathrm{div}\, \mathbf{j} = 0$ and satisfies them identically. Moreover, both terms in Eq. (2.67) are solenoidal and are simpler than the constituents of the customary equality (2.60). At last, with Eq. (2.67) we can reformulate the problem of equilibrium.

If we supplement Eq. (2.67) by

$$\mathbf{B} \cdot \nabla p = 0, \tag{2.68}$$

then the equation $\nabla p = [\mathbf{j} \times \mathbf{B}]$ can be forgotten as having been already completely used. The problem then becomes magnetostatic: all that remains is to solve Maxwell's equations (2.1b) for a given distribution (2.67) of the current density $\mathbf{j}$. The specific feature of this problem is that $\mathbf{j}$ depends on the unknown solution in a whimsical way and, moreover, there are two additional conditions, (2.63) and (2.68). But in spite of all its non-triviality, the problem, nevertheless, consists of calculation of the magnetic field by Maxwell's equations.

Maxwell's equations are linear. Therefore, it is possible to decompose them into two pairs, for the helical,

$$\operatorname{div} \tilde{\mathbf{B}} = 0, \quad \tilde{\mathbf{j}} = \operatorname{rot} \tilde{\mathbf{B}}, \tag{2.69a}$$

and for the axially symmetric components of $\mathbf{B}$ and $\mathbf{j}$:

$$\operatorname{div} \bar{\mathbf{B}} = 0, \quad \bar{\mathbf{j}} = \operatorname{rot} \bar{\mathbf{B}}. \tag{2.69b}$$

It would be possible to treat them separately if $\bar{\mathbf{j}}$ and $\tilde{\mathbf{j}}$ were independent. But, on the contrary, they are coupled in the equilibrium problem. Their relation is given implicitly by the equality (2.67). The complex character of the distribution $\mathbf{j}(\mathbf{r})$, dictated by Eq. (2.67), does not hinder further simplification of the equations, if the equilibrium configuration is symmetrical. The stellarators are not symmetrical, but the asymmetry of conventional stellarators, as was already mentioned, can be considered as a result of perturbation. Let us try to clarify how the current density $\mathbf{j}$ is decomposed into $\bar{\mathbf{j}}$ and $\tilde{\mathbf{j}}$ under such perturbation.

In Section 2.3, we already noted that $\langle \mathbf{B}^2 \rangle$ hardly differs from $\langle \mathbf{B}^2 \rangle_0$. Therefore, in finding $\bar{\mathbf{j}}$ and $\tilde{\mathbf{j}}$ from Eq. (2.67) the quantity $\langle \mathbf{B}^2 \rangle$ can be treated as a constant. A "good" denominator of Eq. (2.67) is the essential advantage, since all other operations with Eq. (2.67) appear rather simple.

To decompose $\mathbf{j}$ into $\bar{\mathbf{j}}$ and $\tilde{\mathbf{j}}$ in Eq. (2.67), we should first calculate the quantity $\langle \alpha_0 \mathbf{B} \rangle_\zeta$, where

$$\alpha_0 \equiv \frac{\langle \mathbf{j} \cdot \mathbf{B} \rangle}{\langle \mathbf{B}^2 \rangle}. \tag{2.70}$$

In a stellarator the helical field $\tilde{\mathbf{B}}$ can be stronger than the poloidal field $\mathbf{B}_p$; therefore, both terms should be taken into account in the poloidal component of $\langle \alpha_0 \mathbf{B} \rangle_\zeta$:

$$\left\langle \alpha_0 (\mathbf{B}_p + \tilde{\mathbf{B}}_p) \right\rangle_\zeta = \bar{\alpha}_0 \mathbf{B}_p + \left\langle \tilde{\alpha}_0 \tilde{\mathbf{B}}_p \right\rangle_\zeta. \tag{2.71}$$

According to Eq. (2.27), any surface function $S(\Psi)$ can be represented in the form

$$S = \bar{S} - \delta \mathbf{r} \cdot \nabla \bar{S}. \tag{2.72}$$

Therefore, we should substitute $\tilde{\alpha}_0 = -\delta\mathbf{r}\cdot\nabla\bar{\alpha}_0$ into Eq. (2.71), where $\delta\mathbf{r}$ is the vector (2.11). This leads to an expression looking like (2.19), so that in the final account we obtain

$$\langle\alpha_0\mathbf{B}\rangle_\zeta \doteq \bar{\alpha}_0\mathbf{B}_p - \frac{\psi_V}{2\pi}\left[\nabla\bar{\alpha}_0\times\nabla\zeta\right] + \bar{\alpha}_0 B_t\mathbf{e}_\zeta. \tag{2.73}$$

The simple form of the toroidal component is a consequence of the fact that the helical field is much weaker than the toroidal field.

Slightly more difficult would be the averaging of the second term in Eq. (2.67) over $\zeta$ if it were carried out in a "direct" manner. But in this case it is also possible to offer an elegant move that helps to surmount all difficulties. The identity

$$\left[(\mathbf{B}-\nabla f_H)\times\nabla p\right] = p\,\mathbf{j} - \operatorname{rot} p(\mathbf{B}-\nabla f_H) \tag{2.74}$$

allows Eq. (2.67) to be rewritten in the form

$$\mathbf{j}\left(1-\frac{p}{\langle\mathbf{B}^2\rangle}\right) = \alpha_0\mathbf{B} - \frac{1}{\langle\mathbf{B}^2\rangle}\operatorname{rot} p(\mathbf{B}-\nabla f_H). \tag{2.75}$$

It is much easier to work with this expression: the value $p\mathbf{B}$ is combined exactly as $\alpha_0\mathbf{B}$, and it remains to treat the combination $p\nabla f_H$. The explicitly detached small (or more precisely, very small) parameter on the left-hand side does not create any problem.

It follows from Eq. (2.63) that

$$\tilde{\mathbf{B}} - \nabla\tilde{f}_H = -\tilde{\mathbf{B}} + \nabla(\delta\mathbf{r}\cdot\nabla\bar{f}_H); \tag{2.76}$$

therefore

$$\begin{aligned}\langle p(\mathbf{B}-\nabla f_H)\rangle_\zeta &= \bar{p}\,(\bar{\mathbf{B}}-\nabla\bar{f}_H)\\ &\quad - \left\langle\tilde{p}\left(\tilde{\mathbf{B}}-\nabla(\delta\mathbf{r}\cdot\nabla\bar{f}_H)\right)\right\rangle_\zeta.\end{aligned} \tag{2.77}$$

The toroidal component of this vector is determined by the strong toroidal field. The terms quadratic in $\tilde{\mathbf{B}}$, which are obtained here at the averaging over $\zeta$, should be kept only in the

poloidal component. It is clear that the quantity $\langle \tilde{p}\nabla(\delta\mathbf{r}\cdot\nabla\bar{f}_H)\rangle_\zeta$ can be disregarded, since it is much smaller than $\bar{p}\nabla\bar{f}_H$. The other value can be transformed with the help of the main identity (2.19) of the averaging method:

$$\langle \tilde{p}\tilde{\mathbf{B}}_p \rangle_\zeta = -\langle \tilde{\mathbf{B}}_p(\delta\mathbf{r}\cdot\nabla\bar{p})\rangle_\zeta = -\frac{\psi_V}{2\pi}\left[\nabla\bar{p}\times\nabla\zeta\right]. \qquad (2.78)$$

As a result we obtain

$$\langle p(\mathbf{B}-\nabla f_H)\rangle_\zeta = \bar{p}B_t\mathbf{e}_\zeta + \bar{p}(\bar{\mathbf{B}}-\nabla\bar{f}_H) + \frac{\psi_V}{2\pi}\left[\nabla\bar{p}\times\nabla\zeta\right]. \qquad (2.79)$$

All other transformations are already disassociated with the averaging. Passing through a simple algebra, we finally obtain for the components of $\bar{\mathbf{j}}$

$$\bar{\mathbf{j}}_p = \bar{\alpha}_0\mathbf{B}_p + \frac{\psi_V}{2\pi}\left[\nabla\zeta\times\nabla\bar{\alpha}_0\right] + \frac{rB_t}{\langle\mathbf{B}^2\rangle}\left[\nabla\zeta\times\nabla\bar{p}\right] \qquad (2.80)$$

and

$$\bar{j}_\zeta = \bar{\alpha}_0 B_t + \frac{r}{\langle\mathbf{B}^2\rangle}\left\{\left[\nabla\bar{p}\times\nabla\zeta\right]\cdot(\mathbf{B}_p-\nabla\bar{f}_H) + \mathrm{div}\,\frac{\psi_V}{2\pi r^2}\nabla\bar{p}\right\}. \qquad (2.81)$$

These expressions differ from those for a tokamak only by the presence of the function $\psi_V$. We have shown and explained in detail how the terms with $\psi_V$ appear in calculations. In addition to the presented derivation, it is useful to discuss the general properties of the initial and final expressions.

We begin from the fact that div and $\langle\ldots\rangle_\zeta$ are commuting operations. Then from $\mathrm{div}\,\alpha_0\mathbf{B} = 0$, it follows that

$$\langle\,\mathrm{div}\,\alpha_0\mathbf{B}\,\rangle_\zeta = \mathrm{div}\,\langle\,\alpha_0\mathbf{B}\,\rangle_\zeta = 0. \qquad (2.82)$$

With account of Eq. (2.73) this leads to

$$\left(\bar{\mathbf{B}}+\mathbf{B}^*\right)\cdot\nabla\bar{\alpha}_0 = 0, \qquad (2.83)$$

where $\mathbf{B}^*$ is the vector (2.13). This equality is satisfied identically, since, by definition, $\bar{\alpha}_0 = \alpha_0(\psi)$, and

$$\mathbf{B}_p + \mathbf{B}^* = \frac{1}{2\pi}\left[\nabla\psi \times \nabla\zeta\right], \tag{2.84}$$

which is the consequence of Eqs. (2.31) and (2.33). Exactly the same cancellation of two terms with $\bar{\alpha}_0$ happens when $\bar{\mathbf{j}}_p$ in the form (2.80) is substituted into $\operatorname{div}\bar{\mathbf{j}} = 0$.

These simple operations allow us to confirm that the term with $\psi_V$ is "legally" present in Eq. (2.80), and we have not made a mistake in its calculation. It describes an interesting effect, the appearance of an additional (in comparison with a tokamak) poloidal current at $\alpha_0 \neq 0$. It deserves mentioning that this effect was observed experimentally [282] when nothing was known about it in theory. Later, an expression similar to (2.80) was calculated for the case of circular magnetic surfaces [131]. The present analysis is free from such restrictions.

In the Eq. $\operatorname{div}\bar{\mathbf{j}} = \operatorname{div}\bar{\mathbf{j}}_p = 0$, only the terms with $\bar{\alpha}_0$ from Eq. (2.80) are identically canceled, and the remaining part is

$$\left[\nabla\zeta \times \nabla\bar{p}\right] \cdot \nabla(rB_t) = 0. \tag{2.85}$$

From here it follows that

$$rB_t = \frac{F(\psi)}{2\pi}. \tag{2.86}$$

It is easy to confirm that here $F$ is the external poloidal current determined by the equality (2.56). The current $F$ is present in the Grad–Shafranov Eq. (1.1), and relation (2.86) of $rB_t$ with $F$ will be used for the reduction of the analogous equation for a stellarator to a similar form. Note that property (2.86) has already been used for the reduction of equality (2.48) to the form (2.49).

To complete the discussion of expression (2.80) for $\bar{\mathbf{j}}_p$, we note that $\bar{\mathbf{j}}_p$ is required only for the equation

$$\bar{\mathbf{j}}_p = \operatorname{rot} B_t \mathbf{e}_\zeta, \tag{2.87}$$

which serves for calculation of the diamagnetic effect. It is necessary to treat this equation with care, since at large $\alpha_0$ the accuracy of Eq. (2.80) can appear insufficient. Indeed, the substitution of the obtained expression for $\bar{\mathbf{j}}_p$ into Eq. (2.87) results in

$$\nabla\left(2\pi r B_t + \bar{\alpha}_0\psi_V\right) = \bar{\alpha}_0\nabla\psi - \frac{2\pi r B_t}{\langle \mathbf{B}^2\rangle}\nabla\bar{p}. \tag{2.88}$$

But, strictly speaking, it does not agree with Eq. (2.86). If we trust Eq. (2.88), then the replacement

$$rB_t \longrightarrow rB_t + \frac{\bar{\alpha}_0}{2\pi}\psi_V \tag{2.89}$$

should be made on the left-hand side of Eq. (2.86). Otherwise, the opposite replacement should be made on the left-hand side of Eq. (2.88).

Actually, there is no big difference in these two cases because

$$\frac{|\bar{\alpha}_0\psi_V|}{2\pi r B_t} \sim \frac{|B_J B^*|}{B_t^2} \ll 1, \tag{2.90}$$

where $B_J$ is the field of the longitudinal current. Nevertheless, it should be admitted that the proposal (2.89) is more correct. The term with $\psi_V$ in $\bar{\mathbf{j}}_p$ represents the main order of magnitude of the quantity arising at the averaging of $\alpha_0\mathbf{B}$. Therefore, we have no right to reject it in Eq. (2.80). At the same time, the replacement (2.89) in Eq. (2.80) would remove at once the contradictions between $\operatorname{div}\mathbf{j}_p = 0$ and $\bar{\mathbf{j}}_p = \operatorname{rot} B_t\mathbf{e}_\zeta$. This can be regarded as an indication of the result that should be expected in calculation of the corrections quadratic in $\tilde{B}/B_t$ in the term with a pressure $p$ in $\bar{\mathbf{j}}_p$. These small corrections were not taken into account in Eq. (2.80), which has resulted in an unexpected, though inessential contradiction.

The smallness of quantities (2.90) allows us to forget this, to neglect the small value with $\psi_V$ in Eq. (2.88) and to use Eq. (2.86). But it is necessary to remember that with a formal approach to the results obtained by the expansion method it is sometimes possible to run into similar situations. Our goal is a

reliable self-consistent description without latent dangers. The example considered shows that in this respect the discussion of the results and their cross-checking is not less (but, maybe, even more) useful than a purely technical increase in the accuracy of calculations.

Actually, we have touched upon a problem of the accuracy limits. Any model is good when it describes an effect far from the threshold of its appearance. For large plasma pressure and small current, for example, it follows from (2.88) that

$$\frac{F'(\psi)}{F} = -\frac{p'(\psi)}{\langle \mathbf{B}^2 \rangle}. \tag{2.91}$$

This literally coincides with the exact consequence of Eqs. (2.54) and (2.59) for a current-free plasma. Thus, in this limiting case, which is the most interesting for stellarators, no problem remains with the approximate expression (2.80) for $\bar{\mathbf{j}}_p$.

## 2.5. Longitudinal current in a stellarator

The component $\bar{j}_\zeta$ drops out of the equation $\operatorname{div} \bar{\mathbf{j}} = 0$; therefore, it is necessary to search for another way of independent verification of Eq. (2.81).

The known and easily derived property of the averaging (2.38) over the layer between nearby magnetic surfaces

$$\langle \operatorname{div} \mathbf{q} \rangle = \frac{d}{dV} \langle \mathbf{q} \cdot \nabla V \rangle \tag{2.92}$$

gives for any periodic function $\varphi$

$$\left\langle \left[ \nabla\zeta \times \nabla V \right] \cdot \nabla\varphi \right\rangle = \left\langle \operatorname{div} \varphi \left[ \nabla\zeta \times \nabla V \right] \right\rangle = 0. \tag{2.93}$$

Therefore, if the helical field $\tilde{\mathbf{B}}$ is considered as a vacuum field ($\tilde{\mathbf{B}} = \nabla\varphi$), we should obtain

$$\left\langle \operatorname{div} p \left[ \tilde{\mathbf{B}} \times \nabla\zeta \right] \right\rangle = \left\langle \tilde{\mathbf{B}} \cdot \left[ \nabla\zeta \times \nabla p \right] \right\rangle = 0. \tag{2.94}$$

This reduces to

$$\left\langle \operatorname{div}\left[\tilde{p}\,\tilde{\mathbf{B}} \times \nabla\zeta\right]\right\rangle = -\left\langle \tilde{\mathbf{B}} \cdot \left[\nabla\zeta \times \nabla\tilde{p}\right]\right\rangle. \tag{2.95}$$

The value $\langle \tilde{p}\,\tilde{\mathbf{B}}_p \rangle_\zeta$ on the left-hand side of this equality has been already calculated [see Eq. (2.78)]. This very quantity gives rise to the term with $\psi_V$ in $\bar{j}_\zeta$. The right-hand side of Eq. (2.95) exactly corresponds to expression (2.45), with the aid of which Eq. (2.95), as should be expected, is transformed into an identity.

To clarify how these formal operations are related to the expression obtained for $\bar{j}_\zeta$, let us turn to the equality

$$\langle \mathbf{j} \cdot \nabla\zeta \rangle = 2\pi \frac{dJ}{dV}, \tag{2.96}$$

where $J$ is the longitudinal current flowing through the magnetic surface and $V$ is the volume inside. This equality follows from definitions (2.56) and (2.38) and can be proved in one line, in the same way as Eq. (2.53) by means of Eq. (2.57). On the left-hand side, the quantity $\mathbf{j} \cdot \nabla\zeta$ can be replaced by $\operatorname{div}[\mathbf{B} \times \nabla\zeta]$, since $\mathbf{j} = \operatorname{rot}\mathbf{B}$. After that, with the help of Eq. (2.92) we obtain

$$J = \frac{1}{2\pi}\left\langle \left[\nabla V \times \mathbf{B}\right] \cdot \nabla\zeta \right\rangle. \tag{2.97}$$

According to Eq. (2.93), the vacuum magnetic field drops out from here. This is also true for the helical field alone.

Now it easy to explain the meaning of the example with Eq. (2.94): it actually shows how the term with $\psi_V$ is canceled out if the net current $J$ is calculated "directly" through calculation of both terms in

$$\langle \mathbf{j} \cdot \nabla\zeta \rangle = \langle \bar{\mathbf{j}} \cdot \nabla\zeta \rangle + \langle \tilde{\mathbf{j}} \cdot \nabla\zeta \rangle \tag{2.98}$$

with $\bar{j}_\zeta$ given by Eq. (2.81).

Above we discussed only the calculations and checking of the final expressions. Now it is time to look at the formally derived result from the standpoint of its practical application.

The main difference between stellarators and tokamaks and the main advantage of stellarators is that they do not need a longitudinal current for plasma equilibrium. The purpose of all experimental programs on stellarators is the study of the current-free plasma, $J = 0$. Therefore, it is desirable to make possible an easy transition to this limiting case in the equations. For this purpose, we transform the expression for $\mathbf{j}$ to a form containing the current $J$ explicitly.

The general relationships (2.53), (2.54), (2.58), and (2.59) allow the presentation of $\alpha_0$ in the form

$$\alpha_0 \equiv \frac{\langle \mathbf{j} \cdot \mathbf{B} \rangle}{\langle \mathbf{B}^2 \rangle} = \frac{2\pi}{\langle \mathbf{B} \cdot \nabla\zeta \rangle} \left\{ \frac{dJ}{dV} + \frac{J}{\langle \mathbf{B}^2 \rangle} \frac{dp}{dV} \right\}. \tag{2.99}$$

After the transformation of the second term with the aid of Eq. (2.97) and the substitution of $\alpha_0$ into Eq. (2.67), we obtain

$$\mathbf{j} = \frac{2\pi}{\langle \mathbf{B} \cdot \nabla\zeta \rangle} \frac{dJ}{dV} \mathbf{B} + \mathbf{j}_1 - \frac{\langle \mathbf{j}_1 \cdot \nabla\zeta \rangle}{\langle \mathbf{B} \cdot \nabla\zeta \rangle} \mathbf{B}, \tag{2.100}$$

where

$$\mathbf{j}_1 \equiv \frac{\left[ (\mathbf{B} - \nabla f_H) \times \nabla p \right]}{\langle \mathbf{B}^2 \rangle}. \tag{2.101}$$

Note that $f_H$ drops out from $\langle \mathbf{j}_1 \cdot \nabla\zeta \rangle$ by virtue of Eq. (2.93).

The convenience of such a representation is obvious: only the first term in Eq. (2.100) gives a contribution to $\langle \mathbf{j} \cdot \nabla\zeta \rangle$, and it vanishes at $J = 0$. Our purpose would be achieved if we could retain a similar structure for $\bar{j}_\zeta$ after averaging over $\zeta$.

The quantity $\bar{j}_\zeta$ is already calculated, and now we have to reduce it to another form similar to that expressed by Eq. (2.100).

As a starting point the general equality (2.97) can be used. As has been mentioned, the helical field drops out of Eq. (2.97) (in the vacuum approximation, strictly speaking). Therefore, in a conventional stellarator

$$J = \frac{1}{2\pi} \left\langle \left[ \nabla V \times \bar{\mathbf{B}} \right] \cdot \nabla\zeta \right\rangle_0 = -\frac{dV}{d\psi} \left\langle \mathbf{B}_p \cdot (\mathbf{B}_p + \mathbf{B}^*) \right\rangle_0, \tag{2.102}$$

and Eq. (2.81) is reduced to

$$\bar{j}_\zeta = \bar{\alpha}_0 B_t - \frac{2\pi r}{\langle \mathbf{B}^2 \rangle} J \frac{dp}{dV_0} + \frac{2\pi r}{\langle \mathbf{B}^2 \rangle} \frac{dp}{d\psi} \left( \lambda - \langle \lambda \rangle_0 \right), \qquad (2.103)$$

where

$$\lambda \equiv (\mathbf{B}_p + \mathbf{B}^*) \cdot (\mathbf{B}_p - \nabla \bar{f}_H), \qquad (2.104)$$

and $\mathbf{B}^*$ is the "effective field" (2.13). Just such a structure of $\bar{j}_\zeta$ is optimal for the transition to the case of a current-free plasma: at $J = 0$ the first two terms in Eq. (2.103) disappear, and the remaining term does not give a contribution to the integral current.

In converting Eq. (2.81) into Eq. (2.103), we used the fact that $\bar{p} = p(\psi)$ and

$$\left[ \nabla \bar{p} \times \nabla \zeta \right] = 2\pi \frac{dp}{d\psi} \left( \mathbf{B}_p + \mathbf{B}^* \right). \qquad (2.105)$$

Moreover, we disregarded the term with $\psi_V$, which is small at $\beta \ll 1$ typical for stellarators. Then the term with $\tilde{\mathbf{j}}$ in Eq. (2.98) should be also rejected. In other words, using expression (2.103) for $\bar{j}_\zeta$, one should perform the averaging $\langle \mathbf{j} \cdot \nabla \zeta \rangle$ "in a tokamak way":

$$\langle \mathbf{j} \cdot \nabla \zeta \rangle = \langle \bar{\mathbf{j}} \cdot \nabla \zeta \rangle_0. \qquad (2.106)$$

So far the function $f_H$ contained in Eq. (2.104) has remained unknown. It is defined by condition (2.63). Therefore, in conformity with Eqs. (2.12) and (2.48), its axially symmetric component $\bar{f}_H$ should satisfy the equation

$$(\mathbf{B}_p + \mathbf{B}^*) \cdot \nabla \bar{f}_H = \langle \bar{\mathbf{B}}^2 - \tilde{\mathbf{B}}^2 \rangle_\zeta - \langle \bar{\mathbf{B}}^2 - \tilde{\mathbf{B}}^2 \rangle_0. \qquad (2.107)$$

Here we took into account that

$$\left\langle \tilde{\mathbf{B}} \cdot \nabla \left( \frac{r}{B_t} \bar{\mathbf{B}} \cdot \hat{\tilde{\mathbf{B}}} \right) \right\rangle_\zeta = \langle \tilde{\mathbf{B}}^2 \rangle_\zeta. \qquad (2.108)$$

It turns out that there is no need to solve the equation for $\bar{f}_H$ because exactly the combination (2.107) is necessary for Eq. (2.103). Finally, with the aid of Eq. (2.107) we obtain

$$\lambda - \langle\lambda\rangle_0 = \langle B_t^2 - \mathbf{B}_p \cdot \mathbf{B}^* - \tilde{\mathbf{B}}^2\rangle_0 - \langle B_t^2 - \mathbf{B}_p \cdot \mathbf{B}^* - \tilde{\mathbf{B}}^2\rangle_\zeta. \quad (2.109)$$

Of course, the averaging over $\zeta$ is applied here to $\tilde{\mathbf{B}}^2$ only.

The quantity $\mathbf{B}_p^2$ was canceled out in Eq. (2.109), and $\mathbf{B}_p \cdot \mathbf{B}^*$ can be omitted since it is substantially (as a minimum, by factor of $\mu/m$) smaller than $\tilde{\mathbf{B}}^2$. In stellarators $\beta \ll 1$; therefore, the remaining $B_t^2$ and $\tilde{\mathbf{B}}^2$ in Eq. (2.109) can be replaced by their vacuum values. The same can also be done with $\langle\mathbf{B}^2\rangle$. After that, expression (2.103) will be ready for practical applications: at a given pressure and current (for example, $J = 0$), the dependence on the unknown solution $\psi(r, z)$ will remain there, as in case of axial symmetry, but for further progress it will already be possible to apply the methods of the tokamak theory.

In the Grad–Shafranov Eq. (1.1), the right-hand side is expressed through the pressure $p$ and external poloidal current $F$. Therefore, for convenience of comparison of the stellarator and tokamak equations, we should represent the quantity $\bar{j}_\zeta$ as a function of $p$ and $F$.

Besides Eq. (2.99), in the general case the following equality is valid for $\alpha_0$:

$$\alpha_0 = \frac{dF}{d\Psi} + \frac{F}{\langle\mathbf{B}^2\rangle}\frac{dp}{d\Psi}, \quad (2.110)$$

so that the initial expression (2.67) for the current density $\mathbf{j}$ can be rewritten in the form

$$\mathbf{j} = \frac{dF}{d\Psi}\mathbf{B} + \frac{1}{\langle\mathbf{B}^2\rangle}\frac{dp}{d\Psi}\left\{F\mathbf{B} - \left[\nabla\Psi \times (\mathbf{B} - \nabla f_H)\right]\right\}. \quad (2.111)$$

A similar form can also be given to $\bar{j}_\zeta$:

$$\bar{j}_\zeta = \frac{dF}{d\psi}B_t + \frac{2\pi r}{\langle\mathbf{B}^2\rangle}\frac{dp}{d\psi}\left(\lambda + B_t^2\right). \quad (2.112)$$

With account for Eqs. (2.104), (2.107), and (2.48), the multiplier on the right-hand side can be expressed through the magnetic field:

$$\lambda + B_t^2 = \mathbf{B}_p \cdot \mathbf{B}^* + \langle \tilde{\mathbf{B}}^2 \rangle_\zeta + \langle \mathbf{B}^2 \rangle. \tag{2.113}$$

Finally, we obtain

$$\bar{j}_\zeta = \frac{FF'(\psi)}{2\pi r} + 2\pi r \frac{dp}{d\psi} \left( 1 + \frac{\langle \tilde{\mathbf{B}}^2 \rangle_\zeta + \mathbf{B}_p \cdot \mathbf{B}^*}{\langle \mathbf{B}^2 \rangle} \right). \tag{2.114}$$

Certainly, here the quantity $\mathbf{B}_p \cdot \mathbf{B}^*$ can also be neglected.

Thus, for a conventional stellarator the general expression (2.67) for the equilibrium current $\mathbf{j}$ can be decomposed into two components:

$$\mathbf{j} = \bar{\mathbf{j}} + \tilde{\mathbf{j}}, \tag{2.115}$$

and $\bar{\mathbf{j}}$ appears to be practically independent of $\tilde{\mathbf{j}}$. The helical field $\tilde{\mathbf{B}}$ depends on $\tilde{\mathbf{j}}$, but at $\beta \ll 1$ it hardly differs from the vacuum field. This fact is always used in the theory of stellarators; therefore, we shall take it without formal proof, although it could be easily proved on the basis of the same formula (2.67) for $\mathbf{j}$. The possibility of replacement of $\tilde{\mathbf{B}}$ by the vacuum field in the expressions obtained for $\bar{\mathbf{j}}$, $\psi_V$, $\mathbf{B}^*$, etc. means that it is possible to manage the equilibrium problem without the solution of the pair of equations (2.69a) for $\tilde{\mathbf{j}}$ and $\tilde{\mathbf{B}}$. Thus, the two-dimensional model of a conventional stellarator appears to be closed if the vacuum helical magnetic field is known.

## 2.6. Two-dimensional equation of plasma equilibrium in stellarators

After deriving the expression for $\bar{j}_\zeta$, we have closely approached our final purpose, the derivation of the scalar two-dimensional equilibrium equation for stellarators, similar to the Grad–Shafranov Eq. (1.1).

Equality (2.33) allows us to rewrite Eq. (2.31) in the form

$$\mathbf{B}_p = \frac{1}{2\pi} \left[ \nabla(\psi - \psi_V) \times \nabla\zeta \right]. \tag{2.116}$$

From Maxwell's equation $\mathbf{j} = \operatorname{rot} \mathbf{B}$ it follows that

$$\operatorname{rot} \mathbf{B}_p = \bar{j}_\zeta \mathbf{e}_\zeta, \tag{2.117}$$

which, with account of Eq. (2.116), is transformed into

$$\operatorname{div} \frac{\nabla(\psi - \psi_V)}{r^2} = -\frac{2\pi \bar{j}_\zeta}{r}. \tag{2.118}$$

This is already almost Eq. (1.2). It only remains to substitute here the function $\bar{j}_\zeta$, which was calculated above.

Equation (2.118) is absolutely exact physically and mathematically, because it is the direct consequence of Maxwell's equations, obtained without any assumption. The loss of accuracy (in the direct mathematical sense) can happen only at the stage where $\psi_V$ and $\bar{j}_\zeta$ are substituted into Eq. (2.118), for example, $\psi_V$, calculated using formula (2.14). But this is the inevitable expense of physical modeling, which is better when the initial theoretical model is more precise, when fewer restrictions are introduced, and when they are introduced as late as possible.

We especially emphasize here that Eq. (2.118) is absolutely exact, since in the analytical theory of stellarators (not of hypothetically straight, but of real stellarators) an approximate description is a norm. But in the "old" theory the model constructions always began much earlier than was actually necessary. The initial distortion of the main equations resulted in an unjustified loss of accuracy and greatly complicated the application of standard methods of mathematical physics for their solution. Also, the analogies that could prompt the transfer of methods and ideas already developed from one area into another remained unnoticed.

For example, it is enough to recall the Greene–Johnson equation [93, 137], known since 1961, which in our notation has the form

$$\nabla^2 A_t = -\bar{j}_\zeta. \tag{2.119}$$

This is the analogue of Eq. (2.118), which corresponds to the

replacement of the operator $r^2\mathrm{div}\,\nabla/r^2$ by $\nabla^2$ on its left-hand side. At large aspect ratios the difference of the solutions to Eqs. (2.118) and (2.119) inside the plasma is insignificant. But the external boundary problems with different operators have different Green's functions, which makes it dangerous to use Eq. (2.119) outside the plasma. The "cylindrical" form of Eq. (2.119) has provoked even the authors of [93] to make a mistake, which was then repeated more than 20 years later in [222]: a "cylindrical" Green's function was offered to Eq. (2.119). However, in the problems of calculation of the external confining field, which are discussed below in detail, the account of toroidicity is of principal importance. The use of the Green's function from [93, 222] would lead (this will be clear from the subsequent discussion in Section 3) to a result physically incorrect in the tokamak limit. In this case, the aspiration to a more exact description of a stellarator, besides the theoretical, also acquires quite a practical importance.

The problem of the accuracy of Eq. (2.119) also arises naturally in the simulation of stellarators with moderate aspect ratios like the ATF ($A = 7$) or CHS ($A = 5$).

Finally, since the Greene–Johnson equation was written exactly in the form (2.119) (other units were used in the original and, consequently, there was also the multiplier $4\pi$ on the right-hand side), unnoticed and unused was the analogy between Eq. (2.119) and the Grad–Shafranov equation (1.1), which greatly delayed the development of the theory of plasma equilibrium and stability in stellarators next to the incomparably more successful development of the tokamak theory. Even in the early 1980s during a new burst of activity in stellarator research, as mentioned in the first section, there was still no understanding that Eq. (2.119) in combination with other known methods of the equilibrium theory could be rather effective.

As for Eq. (2.118), the transition to a tokamak is trivial ($\psi_V = 0$), mathematically precise, and its left-hand side is already cast in the same form as that in Eq. (1.1). To convert Eq. (2.118) into the exact analogue of Eq. (1.1), on the right-hand

side we should substitute $\bar{j}_\zeta$ in the form (2.114). Then we obtain

$$\operatorname{div} \frac{\nabla(\psi - \psi_V)}{r^2} = -4\pi^2 p'(\psi) \left(1 + \frac{\langle \tilde{\mathbf{B}}^2 \rangle_\zeta}{\langle \mathbf{B}^2 \rangle}\right) - \frac{FF'(\psi)}{r^2}. \quad (2.120)$$

This is the final result, the last and the main equation that completes the reduction of the initial equilibrium equations (2.1) to the two-dimensional equation for a conventional stellarator with a plane circular axis.

The obvious similarity of Eqs. (2.120) and (1.1) automatically removes the problem of the limiting transition to a tokamak, and, moreover, the procedure of derivation of Eq. (2.120) guarantees that restrictions similar to (2.3) are not required for such a transition.

Another extreme (and the most interesting) case is the current-free stellarator. At $J = 0$, the quantity $FF'(\psi)$ is related to $p'(\psi)$ by relationship (2.91), so that $4\pi^2 R^2 p'(\psi) + FF'(\psi) \cong 0$. Because of this cancellation of the main terms it is necessary to keep a small quantity with $\langle \tilde{\mathbf{B}}^2 \rangle_\zeta$ on the right-hand side of Eq. (2.120). If $J = 0$, then, according to Eqs. (2.103) and (2.109),

$$\bar{j}_\zeta = \frac{2\pi r}{\langle \mathbf{B}^2 \rangle} \frac{dp}{d\psi} \left( \langle B_t^2 - \tilde{\mathbf{B}}^2 \rangle_0 - \langle B_t^2 - \tilde{\mathbf{B}}^2 \rangle_\zeta \right). \quad (2.121)$$

The other forms of $\bar{j}_\zeta$ obtained from the general equality (2.103) for the cases where it could be necessary to take into account a longitudinal current are shown in the previous subsection.

The current (2.121) is called a longitudinal equilibrium current, or a dipole or Pfirsch–Schlüter current. The difference $\langle B_t^2 \rangle - B_t^2$ is always nonzero, because $B_t \sim 1/r$ is stronger on the inner side of the torus and weaker on the outer side. Therefore, at nonzero pressure gradient we have $\bar{j}_\zeta \not\equiv 0$. With growing pressure $|\bar{j}_\zeta|$ also grows, and the deviation of $\psi$ from the vacuum value of $\psi_V + 2\pi r A_{\text{ext}}$ becomes larger and larger [see Eq. (2.118)]. The distortions of surfaces $\psi = \text{const}$ are allowable only to some degree. The pressure at which the admissible

threshold is reached is called an equilibrium limit. Accordingly, $\beta$ (the ratio of plasma pressure to magnetic pressure) cannot be greater than $\beta_{\rm eq}$.

In conventional stellarators the theoretical limit $\beta_{\rm eq}$ is not too high. As can be seen from Eq. (2.118), it could be possible to increase it, if at the given $\beta$ the value of $\bar{j}_\zeta$ could be reduced. It is easier to evaluate $\bar{j}_\zeta$ than to solve an equilibrium problem. Moreover, in an experiment it is possible to measure the magnetic field created by this current. Thus, besides the formal solution of equilibrium problems we shall also discuss the problem of suppression of the Pfirsch–Schlüter current.

Equation (1.2) or (2.120) will be the basis of the statement of particular problems below. As was shown, it is a consequence of the *exact* equation (2.118), where $\psi_V$ and $\bar{j}_\zeta$ should be substituted. When these quantities are calculated by the expansion method, which only determines the level of the error introduced, the traditional restrictions (2.3) can be eased. Therefore, it is possible *a priori* to guarantee a high accuracy for Eq. (1.2). The numerical calculations [39, 42, 51, 59, 283] have confirmed this.

It is interesting to note that the accuracy of the results obtained with the help of a code based on the analogue of Eq. (1.2) surprised the authors of [53] and [283]: in the introduction to [53] and in the conclusion of [283], it was directly said that the results of the calculations appeared much more accurate than one had any reason to expect. This evidence of uncertainty and doubts in the reliability of the two-dimensional model deserves special attention because one of the authors of these publications is J. Johnson himself, whose name was repeatedly and respectfully mentioned above in connection with Eq. (2.119) and the idea of stellarator approximation. It indicated that the theory overloaded by small parameters and by expansions was far from complete and clear. Therefore, revision and improvement of the theory were objectively necessary. The substantiation of the two-dimensional approach offered above removes this problem. It allows a precise separation of the exact from the approximate and a minimization of the "losses."

Equation (1.2) or (2.120), on the one hand, generalizes the Grad–Shafranov equation on stellarators and, on the other, comprises all known two-dimensional equations for a conventional stellarator as particular cases. This was explained in [131, 158], and here the "direct" derivation of Eq. (2.120) eliminates the need for an additional proof. It is clear that in any reliable approach the differences could be only in the form of the final equations, in the notation, and in the accuracy of calculation of $\psi_V$ and $\bar{j}_\zeta$.

We have already said a lot about the Greene–Johnson equation [93]. It is contained in Eqs. (1.2) and (2.120) as a particular case corresponding to small toroidicity ($A = R/b \gg 1$). The transfer to this equation is performed when the toroidal corrections are neglected on the left-hand side of Eq. (1.2), but are taken into account on the right-hand side in the lowest approximation. Then Eq. (1.2) is transformed into

$$\nabla^2(\psi - \psi_V) = -4\pi^2 R^2 \left\{ p'(\psi) \left[\Omega - \langle\Omega\rangle\right] + J'(V) \right\}, \qquad (2.122)$$

where $\Omega$ is the quantity (2.50). The longitudinal current $J$ is explicitly allocated here for the convenience of description of a current-free plasma.

The similarity of the Grad–Shafranov equation (1.1) and the two-dimensional equilibrium equation (1.2) for a plasma in conventional stellarators makes it possible to use the standard technique and methods of the tokamak theory for their solution. They are described in detail in a number of review articles (see [130, 205, 207, 237]), so only the characteristic features of stellarator equilibrium problems will be discussed below, when needed.

In the solution of the Eqs. (1.1), (1.2), or (2.120) it is necessary to specify either $p(\psi)$ and $F(\psi)$ contained explicitly on the right-hand side, or other surface quantities that allow $p$ and $F$ to be expressed through them. For example, instead of $F$ it is possible to prescribe the longitudinal current $J(\psi)$ or the rotational transform $\mu(\psi)$. In addition, for stellarators both $\psi_V$ and

$\Omega^0$ must be given. Finally, in the simplest case, the shape and position of the plasma boundary should be prescribed. In such a formulation the problem and its solution are called a "fixed-boundary equilibrium." If the plasma boundary is not known, then we talk about the "free-boundary plasma equilibrium." In any case, for the complete solution of the problem it is necessary to take care of matching the magnetic field in the plasma with the external magnetic field. This problem will be discussed below in Section 4. But the next section is devoted to the main equation (2.120) and its properties and to models necessary for the solution of particular problems.

# 3. Analytical models

## 3.1. Two-dimensional model of a stellarator

We have repeatedly emphasized the similarity of Eqs. (1.2) and (2.120) with the Grad–Shafranov equation (1.1). Let us now discuss their differences and the specific features of formulation of equilibrium problems on the basis of the two-dimensional scalar equation (1.2).

Equation (1.2) differs from the Grad–Shafranov equation (1.1) in that it contains two additional functions $\psi_V$ and $\Omega^0$, which are determined by relationships (2.14) and (2.52). To calculate them we need to know the helical field $\widetilde{\mathbf{B}}$. At small $\beta$ this field practically does not differ from the vacuum field $\nabla\varphi_h$, so that $\widetilde{\mathbf{B}} = \nabla\varphi_h$ is always substituted into Eqs. (2.14) and (2.52).

For real installations the vacuum helical field $\widetilde{\mathbf{B}}$ is usually calculated directly from the given currents in the helical windings. Modern computers allow this to be done to any desired accuracy. For a particular installation it is enough to make such a calculation only once or to calculate several variants for different regimes of operation. After that, for numerical simulation of equilibrium on the basis of Eq. (1.2), the obtained data should be transformed into $\psi_V$ and $\Omega^0$. The problem can be further

solved in the same way as for tokamaks on the basis of Eq. (1.1).

Despite the abundance of numerical calculations the need for analytical modeling does not disappear. Just the opposite, the correct qualitative description of an effect, always being the basis of physical understanding of the phenomena, also becomes necessary both for evaluation and for generalization of separated, though mathematically exact numerical results.

In the analytical description, the potential $\varphi_h$ of the vacuum helical field in stellarators can be represented in the most general form as a set of harmonics:

$$\varphi_h = \sum_{m>0,\ell} \varphi_{\ell m}(\rho)\, \sin\bigl(\ell u - m\zeta + \alpha_{\ell m}\bigr). \tag{3.1}$$

Here $\rho$, $u$, $\zeta$ are the quasi-cylindrical coordinates attached to the geometrical axis of the installation $r = R$ (Fig. 2.1), and $\alpha_{\ell m}$ are the constants. One harmonic usually dominates in the decomposition (3.1). Its multipolarity $\ell$ and number of periods $m$ along the major circumference are always mentioned among the main characteristics of a stellarator. Usually $\ell = 2$; sometimes $\ell = 3$. Accordingly, they are distinguished as two- and three-turn stellarators.

After the substitution of Eq. (3.1) into Eq. (2.14) we obtain for $\psi_V$:

$$\psi_V = -\frac{\pi r^2}{\rho B_t} \sum_{\substack{m>0 \\ \ell,n}} \frac{d\varphi_{\ell m}}{d\rho}\, \varphi_{nm}(\rho) \frac{n}{m} \times \cos\Bigl[(\ell - n)u + \alpha_{\ell m} - \alpha_{nm}\Bigr]. \tag{3.2}$$

The function $\psi_V$ describes the averaged vacuum magnetic surfaces of a stellarator. In the elementary case, when the external axially symmetric (control) field is absent, the equation for the surfaces, as clear from Eq. (1.2), is $\psi_V = \text{const}$. The helical field of a stellarator should be chosen in such a way that these surfaces in the operating volume are enclosed toroids. The presence of large terms proportional to $\cos(\ell - n)u$ in Eq. (3.2) is, generally speaking, undesirable. They are associated with deformations

and even the splitting of magnetic surfaces with the formation of multi-axial configurations with a complex petal structure [93]. Such terms appear in Eq. (3.2) only when there are at least two harmonics with the same period in $\zeta$ in Eq. (3.1). They are sometimes called "interacting" or satellite harmonics.

The function $\psi_V$ is determined basically by the main harmonic of the helical field: $\ell = 2$ in two-turn and $\ell = 3$ in three-turn stellarators. If the amplitudes of satellites are small, then to an accuracy within the toroidal corrections $\psi_V = \psi_V(\rho)$. The independence of $\psi_V$ from $u$ means that the averaged vacuum magnetic surfaces are nested toroids of circular cross section. The creation of a similar geometry is the desired goal when the parameters of the magnetic system of a stellarator are chosen. We shall therefore restrict ourselves to this case of practical interest when particular examples are considered.

Stellarators are traditionally systems with a large aspect ratio $A = R/b$ ($b$ is the average minor radius of the plasma). By some stretch, even the ATF ($A = 7$) and the CHS with $A = 5$, which is the most compact helical system among the operating devices, can be attributed to this family. In stellarators with a large aspect ratio it is possible to use a cylindrical representation for the potential $\varphi_h$:

$$\varphi_h = \sum_{m>0,\ell} B_0 R \frac{\ell}{m} \varepsilon_{\ell m} I_\ell(m\rho/R) \sin\left(\ell u - m\zeta + \alpha_{\ell m}\right), \quad (3.3)$$

where $B_0$ is the strength of the longitudinal field at the axis, $I_\ell$ is the modified Bessel function, and $\varepsilon_{\ell m}$ are dimensionless coefficients. At $A \gg 1$, it is also possible to replace $r$ by $R$ (the radius of the geometrical axis) in Eq. (3.2). For a single harmonic of the helical field we then obtain

$$\psi_V = \psi_V^\ell(\rho) = -\pi R^4 B_0 \varepsilon_{\ell m}^2 \frac{\ell^3}{m^3} \frac{dI_\ell^2}{d\rho^2}. \quad (3.4)$$

If $\varphi_h$ is the sum of non-interacting harmonics, then it is necessary to carry out a summation over $\ell$ in Eq. (3.4).

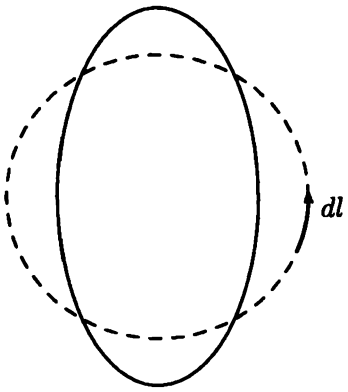


**Fig. 3.1.** Boundary of the transverse cross section of the real magnetic surface and of its averaged image $\psi = \text{const}$ (dashed line).

If $\psi_V = \psi_V(\rho)$, then in addition to Eq. (3.4) another simple expression for this function may be given. In the tokamak theory there is a well-known formula for the rotational transform $\mu$:

$$\frac{1}{\mu} = \oint \frac{B_t dl}{|\nabla \psi|}, \tag{3.5}$$

where $dl$ is the element of length of the contour $\psi = \text{const}$ in the cross section $\zeta = \text{const}$. It is easy to show that this relation is also valid for conventional stellarators ($\mu = -d\psi/d\Phi$; $d\Phi \cong \int B_t \, dS_\perp$ is the longitudinal magnetic flux between the adjacent magnetic surfaces, $dS_\perp \cong -dl \, d\psi/|\nabla\psi|$). In this case, the integral in Eq. (3.5) should be calculated along the "average" boundary (Fig. 3.1). For a stellarator with circular vacuum averaged magnetic surfaces, it follows from Eq. (3.5) that

$$\mu_h = -\frac{\psi_V'(\rho)}{2\pi\rho B_0}. \tag{3.6}$$

Here $\mu_h$ is the vacuum rotational transform. This relationship allows the transformation of the term with $\psi_V$, which plays the

role of a source in Eq. (1.2), into the convenient form

$$\operatorname{div} \frac{\nabla \psi_V}{r^2} \cong -\frac{2\pi B_0}{R^2} \frac{1}{\rho} \frac{\partial}{\partial \rho} \left( \rho^2 \mu_h \right). \tag{3.7}$$

Here $\psi_V = \psi_V(\rho)$, and toroidal corrections are neglected.

The function $\mu_h$ is one of the main characteristics of a stellarator and is known for each installation. It is not only already calculated at the research and design stage [29, 38–46, 48–59], but is also measured experimentally [27–29, 32, 33]. For known $\mu_h$ it is natural to use expression (3.6) in order to find $\psi_V$. First, this eliminates the need for calculation of $\psi_V$ from vacuum fields, which should be calculated themselves in advance. Second, the transition from $\psi_V$ to $\mu_h$ makes the formulation of the equilibrium problem more physical and facilitates interpretation of the results. Finally, it allows the construction of a simple theoretical model of a stellarator, since it is always possible to approximate $\mu_h$ by a simple dependence, for example, by

$$\mu_h = \mu_0 + (\mu_b - \mu_0)\rho^2/b^2, \tag{3.8}$$

where $\rho$, let us recall, is the radius measured in the transverse cross section from the geometrical axis (Fig. 2.1), $b$ is the characteristic transverse dimension, $\mu_0 = \mu_h(0)$, $\mu_b = \mu_h(b)$. Sometimes for a more accurate description of a stellarator it is necessary, as follows from Eqs. (3.4) and (3.6), to add a term proportional to $\rho^4$ into Eq. (3.8), but this is a minor technical detail.

In the MHD theory of plasma equilibrium and stability, the model of a stellarator with a parabolic profile $\mu_h$ appeared to be extremely useful. Because Eq. (3.8) includes the shear, which is one of the major characteristics of a stellarator, this model allows the description of both classes of systems that are interesting in practice: the $\ell = 2$ and $\ell = 3$ stellarators.

By definition, $\mu_h$ is an integral characteristic of a vacuum magnetic configuration [see Eq. (3.5)], and $\psi_V$ can be expressed through $\mu_h$ only at $\psi_V = \psi_V(\rho)$. The last condition is an idealization which, however, is justified in the majority of cases. Physically it means that the cross sections of the averaged magnetic

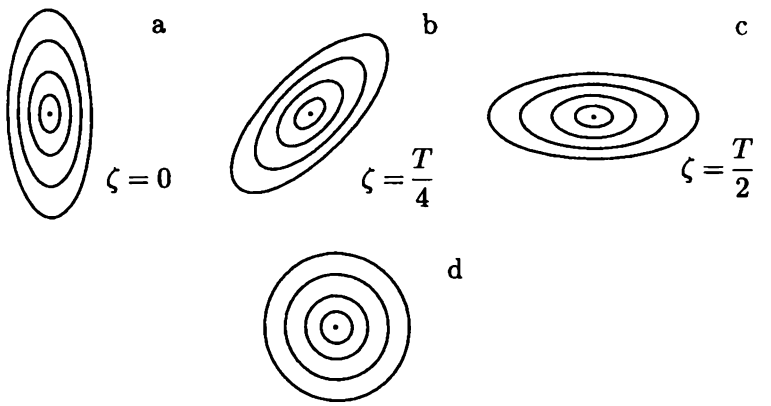


**Fig. 3.2.** Cross sections of the real (a–c) and averaged (d) magnetic surfaces in a configuration with $\psi_V = \psi_V(\rho)$; $T$ is the period of the helical field.

surfaces are circular, and their centers coincide. The real three-dimensional surfaces thus should have a common axis $r = R$, and the form of their cross sections should be the same at different toroidal angles $\zeta$ (Fig. 3.2). In other words, the different cross sections should differ only in orientation. From the series of configurations that can be obtained in a stellarator, it is always possible to find one that corresponds to these criteria. Its parameters should be used as the basis for determining $\psi_V$. The radius $R$ thus may differ from the radius of the vacuum chamber. This should be taken into account in the formulation of the problem and analysis of the results.

Finally, besides $\psi_V$ it is also necessary to know the function $\Omega^0$. Calculating it using Eq. (2.52), for a stellarator with non-interacting harmonics we obtain

$$\Omega^0 = -\frac{1}{2\pi R^2 B_0} \sum_{\ell} \frac{m}{\ell} \left[ 2\psi_V^{\ell} + \rho \frac{d\psi_V^{\ell}}{d\rho} \right], \tag{3.9}$$

where $\psi_V^{\ell}$ is function (3.4). In the elementary case, when there is only one harmonic of the helical field, $\Omega^0$ is expressed directly

through $\mu_h$:

$$\Omega^0 \equiv \frac{\langle \tilde{\mathbf{B}}^2 \rangle_\zeta}{B_0^2} = \frac{m}{\ell} \frac{1}{R^2} \int_0^\rho \frac{\left[\mu_h(x) x^4\right]'}{x^2} dx. \tag{3.10}$$

Here the relation (3.6) of $\psi_V$ with $\mu_h$ is taken into account.

The value $\Omega^0$ is usually small and does not significantly influence the plasma equilibrium. An exception is the Heliotron E, for which it is impossible to neglect the quantity $\Omega^0$ on the right-hand side of the equilibrium equation.

Let us note that $\Omega^0$ is an increasing function of the radius $\rho$. Because of this a straight stellarator has a so-called "magnetic hill":

$$\frac{d^2 V_0}{d\Phi^2} = \frac{R}{\rho B_0^2} \frac{d\Omega^0}{d\rho} > 0. \tag{3.11}$$

Here $V$ is the volume inside the magnetic surface, and $\Phi$ is the longitudinal (toroidal) magnetic flux. The subscript "0" at $V$ indicates that the derivative is taken at $\beta = 0$. Function (3.11) is a component of the "magnetic well" (hill) and plays a significant role in stability criteria.

The reason why $\Omega^0$ appears in equilibrium equations is the inhomogeneity of $\mathbf{B}^2$ associated with the helical field. This affects the quantity $\bar{j}_\zeta$. The function $\Omega^0$ enters $\bar{j}_\zeta$ in the combination $\Omega^0 - R^2/r^2$ [see Eq. (2.121)]. By the selection of harmonics of the helical field it is possible to ensure that $\Omega^0$ will have a cosine component $C_1(\rho)\cos u$ with $C_1 > 0$. It was expected that, owing to this, it could be possible to significantly reduce the value of the Pfirsch–Schlüter current (2.121) and, as a consequence, increase $\beta_{\text{eq}}$ even at small amplitudes of the satellite harmonics [284]. This would also mean that the solution of plasma equilibrium problems might be sensitive to the choice of approximations for the functions $\psi_V$ and $\Omega^0$, and instead of the model of circular co-axial surfaces $\psi_V = \psi_V(\rho) = \text{const}$ it would be necessary to use a much more complicated model accounting for small details of the real geometry of magnetic surfaces. But the forecast of [284] appears incorrect [285], so there should be

no serious doubts concerning the model with $\psi_V = \psi_V(\rho)$ and $\Omega^0 = \Omega^0(\rho)$, and excessive complications in the majority of cases are not necessary. The arguments substantiating this standpoint are described in Section 3.4.

## 3.2. Minimal set of parameters

When the general theoretical model is simplified for practical applications, the natural question arises of what is the minimal set of numerical parameters and functions needed for an adequate description of the equilibrium configuration. To determine the main combinations of parameters, let us make a transition to dimensionless variables in Eq. (2.122), where we shall put $J = 0$.

We should start from the function $\psi_V$, because in Eq. (1.2) the term with $\psi_V$ plays the role of a source that is not associated with the plasma but is defined by the given vacuum magnetic field. In stellarators with "on average" circular vacuum magnetic surfaces the function $\psi_V$ is expressed through the vacuum rotational transform $\mu_h$:

$$\psi_V = -2\pi B_0 \int \rho\, \mu_h(\rho)\, d\rho = \psi_V^0 \int^{\xi} 2x \frac{\mu_h}{\mu_b}\, dx, \tag{3.12}$$

where $\psi_V^0$ is the constant given by

$$\psi_V^0 \equiv -\pi B_0 \mu_b b^2, \tag{3.13}$$

and $\xi \equiv \rho/b$ is the dimensionless radius in the transverse cross section.

Taking account of Eq. (3.12), we transform the equilibrium equation (2.122) to the form

$$b^2 \nabla^2 \frac{S}{2} = \frac{d}{dS}\left(\frac{\beta(S)}{\beta_{\text{eq}}^0}\right)\left(\left\langle \frac{R}{b}\Omega \right\rangle - \frac{R}{b}\Omega\right) + \frac{1}{\xi}\frac{d}{d\xi}\left(\xi^2 \frac{\mu_h}{\mu_b}\right), \tag{3.14}$$

where $S \equiv \psi/\psi_V^0$, $\Omega$ is function (2.50), and $\beta_{\text{eq}}^0$ is the value frequently used as a rough estimate of $\beta_{\text{eq}}$:

$$\beta_{\text{eq}}^0 \equiv \mu_b^2 \frac{b}{R}, \tag{3.15}$$

with $b$ and $R$ being, respectively, the minor and major radii of the plasma column, $\mu_b$ is the rotational transform at the edge of the column, and

$$\beta(S) \equiv \frac{2p(S)}{B_0^2}. \tag{3.16}$$

The right-hand side of Eq. (3.14) is completely determined by three functions:

$$\frac{\beta(S)}{\beta_{\rm eq}^0}, \quad \frac{\mu_h}{\mu_b}, \quad \frac{R}{b}\Omega. \tag{3.17}$$

The first characterizes the value of the plasma pressure and its profile; the other two characterize the magnetic configuration of the stellarator, the profile of the vacuum rotational transform, and the inhomogeneity of the vacuum magnetic field. The equilibrium equations for the configurations, having an identical set of parameters (3.17), identically coincide.

For stellarators with $\psi_V = \psi_V(\rho)$, one can use relationship (3.10); therefore, the last of the functions (3.17) can be represented in the form

$$\frac{R}{b}\Omega = \frac{R}{b}\frac{\langle\tilde{\mathbf{B}}^2\rangle_\zeta}{B_0^2} - 2\xi\cos u = \frac{\omega^0}{\ell}\int\limits_0^\xi \left(\frac{\mu_h}{\mu_b}x^4\right)'\frac{dx}{x^2} - 2\xi\cos u, \tag{3.18}$$

where

$$\omega^0 \equiv \mu_b\frac{mb}{R}. \tag{3.19}$$

Accordingly, it is possible to replace the function $R\Omega/b$ in Eq. (3.17) by the constant $\omega^0/\ell$. The above is now reduced to the statement that stellarators with identical

$$\frac{\mu_h}{\mu_b}, \quad \frac{\omega^0}{\ell} \tag{3.20}$$

are indiscernible from the standpoint of the equilibrium equation (2.122) or (3.14) [286]. At identical $\beta(S)/\beta_{\rm eq}^0$ and boundary conditions, the equilibrium configurations in such stellarators will be

physically similar. Let us recall that here $\ell$ is the multipolarity of the helical field, and $m$ is the number of periods of this field along the major circumference of the device.

If $\mu_h$ is parabola (3.8), then instead of $\mu_h/\mu_b$ in Eq. (3.20) it is enough to simply specify the ratio $\mu_0/\mu_b$. Therefore, conventional stellarators with on average circular vacuum magnetic surfaces and with a parabolic profile of $\mu_h$ and a large aspect ratio (a quite realistic model) can be represented as a two-parametrical family, the "points" on a plane $\mu_0/\mu_b$, $\omega^0/\ell$. Stellarators with identical pairs of these quantities can be called equivalent. The solution $S(\mathbf{r})$ of Eq. (3.14) for one of them will also be valid for all other stellarators with the same $\mu_0/\mu_b$, $\omega^0/\ell$. In dimensionless variables, the equilibrium configurations with identical $\beta(S)/\beta^0_{\text{eq}}$ for identical shape and position of the plasma boundary should be completely equivalent in such stellarators. At present, the majority of problems of MHD plasma equilibrium are solved numerically and for particular parameters of a system. The principle of equivalence (actually, simple scalings) allows the transfer of the results of such calculations to uninvestigated areas.

The main characteristic of a stellarator, which determines its capabilities and the properties of the equilibrium configuration to a greater degree than other parameters, is the rotational transform $\mu_h$. As was shown above, in a problem of equilibrium, it is not the absolute values of $\mu_h$ that is important, but the radial dependence of this function, the "normalized" profile, $\mu_h/\mu_b$. In terms of $\mu_h/\mu_b$, all stellarators with $\psi_V = \psi_V(\rho)$, from shearless ($\mu_0 = \mu_b$) to $\ell = 3$ stellarators ($\mu_0 = 0$), are described by the single parameter $\mu_0/\mu_b$, which can vary from zero to unity (Fig. 3.3). Here, as usual, $\mu_0$ and $\mu_b$ are the values of $\mu_h$ at the geometrical axis of the stellarator and at the distance $b$ from this axis.

The value $\omega^0$ is associated with the existence of a specific limit on the plasma pressure, at which the equilibrium of the plasma becomes unstable with respect to displacements of the column as a whole [137]. Mikhailov has shown [139] that

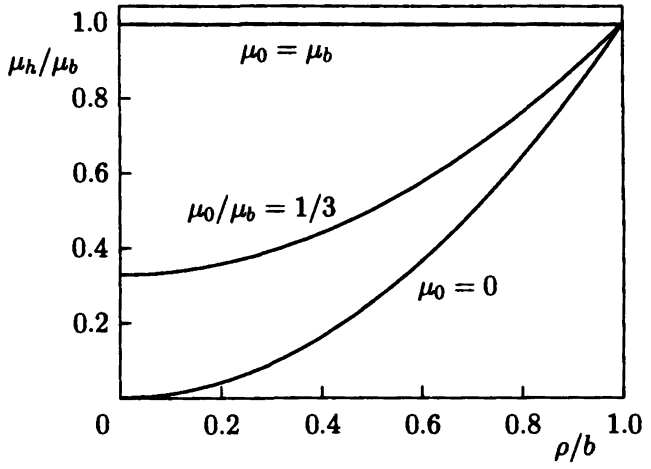


**Fig. 3.3.** Normalized profiles of the vacuum rotational transform in the model (3.8).

this limit is well beyond the usual equilibrium limit $\beta_{\rm eq}$. Nevertheless, the term $\langle\tilde{\mathbf{B}}^2\rangle_\zeta/B_0^2$ must sometimes be retained in the equilibrium equation: in stellarators like the Heliotron E, with a large magnetic hill, it results in an appreciable decrease of $\beta_{\rm eq}$. After looking at Eq. (3.18), one can conclude that this can be expected only at $\omega^0$ comparable to one or two, since

$$\frac{1}{\ell}\int_0^\xi \left(\frac{\mu_h}{\mu_b}x^4\right)'\frac{dx}{x^2} = \frac{2}{\ell}\left[\frac{\mu_h}{\mu_b}\xi^2 - \frac{1}{2}\int_0^\xi \frac{\mu_h'}{\mu_b}x^2\,dx\right] \le 1, \qquad (3.21)$$

and only $\omega^0$ determines the order of magnitude of the first term in Eq. (3.18). At $\omega^0 \ll 1$, it is small in comparison with the second term $(-2\xi\cos u)$ and has a negligible effect on the plasma equilibrium. In this case, the absolute identity of values $\omega^0$ is not needed to consider stellarators as equivalent. It is sufficient if the $\mu_0/\mu_b$ are the same.

A concrete example of such systems is the family of shearless stellarators of the W VII-A type (see Ref. [70]). Indeed, in

stellarators with a single harmonic in the helical field

$$\mu_h = \frac{m\varepsilon^2}{4}\left[1 + \frac{1}{2}\left(\frac{m\rho}{R}\right)^2 + \frac{7}{96}\left(\frac{m\rho}{R}\right)^4 + \cdots\right]. \tag{3.22}$$

This formula can be easily obtained using Eq. (3.6) and keeping the first three terms of the expansion of the Bessel function $I_2$ in Eq. (3.4). The shear is small if $mb/R \ll 1$. Accordingly, $\omega^0 \ll 1$ at $\mu_b \leq 1$. In W VII-A, for example, $\omega^0 = 0.06$. The equilibrium equations of a current-free plasma in shearless stellarators can differ only because of the difference in $\beta(S)/\beta^0_{\text{eq}}$. But the distinctions in parameters of these systems are not important in equilibrium problems. Therefore, to analyze them, it could be quite sufficient to consider one particular variant only with necessary profiles $\beta(S)/\beta^0_{\text{eq}}$ and shapes of the plasma.

In shearless stellarators $\mu_0/\mu_b = 1$. The $\ell = 3$ stellarators also have one common characteristic: $\mu_h/\mu_b = \xi^2$. Though $\omega^0$ can be of the order of unity in these systems (in the Uragan-3, $\omega^0 \simeq 0.7$), it is necessary to remember that in this case

$$\frac{R}{b}\Omega = \frac{\omega^0}{2}\xi^4 - 2\xi\cos u. \tag{3.23}$$

The first term can give an appreciable contribution to $R\Omega/b$ at the periphery only, and sometimes not at all. Therefore, a lot of $\ell = 3$ stellarators can be almost "similar."

In practice, we need to compare stellarators that are not equivalent in the strict sense of the word (see Table 3.1). For such a comparison, priority should be given to comparing the values of $\mu_0/\mu_b$ as the most significant parameters. The proximity of $\mu_0/\mu_b$ in different devices means that irrespective of the relations between other parameters the equilibrium configurations in these installations should be similar. Section 4.4, devoted to the Pfirsch–Schlüter current, can serve as another more detailed proof of this statement. In particular, it is shown there that the influence of the term with $\omega^0$ in Eq. (3.18) on equilibrium is weak even for $\omega^0$ of the order of 1 or 2.

**Table 3.1.** Parameters of some conventional stellarators ($\omega^0 = \mu_b mb/R$, $\beta^0_{eq} = \mu_b^2 b/R$).

| Installation | $m$ | $b$, cm | $R$, cm | $\mu_b$ | $\omega^0$ | $\beta^0_{eq}$ | $\mu_0$ | $\frac{\mu_0}{\mu_b}$ |
|---|---|---|---|---|---|---|---|---|
| Uragan-3 | 9 | 13.5 | 100 | 0.6 | 0.729 | 4.86 | 0 | 0 |
| Heliotron E | 19 | 20 | 220 | 2.5 | 4.3 | 56.8 | 0.5 | 0.2 |
| Liven'-2 | 14 | 11.5 | 100 | 0.78 | 1.26 | 7 | 0.22 | 0.28 |
| Liven'-2M | 8 | 19.4 | 112 | 0.8 | 1.11 | 11.1 | 0.25 | 0.31 |
| CHS | 8 | 20 | 100 | 1 | 1.6 | 20 | 0.3 | 0.33 |
| ATF | 12 | 30 | 210 | 0.95 | 1.63 | 12.9 | 0.35 | 0.37 |
| LHD | 10 | 60 | 390 | 1 | 1.54 | 15.4 | 0.5 | 0.5 |
| Uragan-2M | 4 | 15 | 157 | 0.6 | 0.23 | 3.4 | 0.4 | 0.67 |

Thus, the minimal set of parameters necessary to describe the magnetic configuration of conventional stellarators in equilibrium problems consists of three constants: $\mu_0/\mu_b$, $\beta^0_{eq}$, and $\omega^0$. These dimensionless parameters are the best basis for comparison of different installations and for the generalization of particular results.

## 3.3. Description of the inner part of the plasma

Thus far we have discussed the general properties of equilibrium equations, the reduction of the system of equations (2.1) to the scalar two-dimensional equilibrium equation (2.120) for a conventional stellarator, and the functions that appear in this equation. It is known that the exact analytical solution of such equations is possible only in separate particular cases [130, 287–291] under restrictions that could not be called natural. Therefore, in an analytical treatment of real situations, for the sake of solvability of a problem one has to sacrifice the accuracy of the results by simplifying the initial models.

For the entire variety of analytical methods of solving the equilibrium equations, the main feature is the reduction of two-

dimensional equations to one-dimensional. For this purpose, the shape of the surfaces $\psi = \text{const}$ is prescribed explicitly with the help of one or two, and only in rare exceptional cases [292, 293] by more, parameters. Most frequently used is the model of circular shifted surfaces [130, 131, 237, 252, 253], which takes into account the main effect of the finite pressure of a plasma in toroidal systems — the displacement of magnetic surfaces outward from the center of the axis curvature (known as the Shafranov shift).

It is known that the non-circular plasma shape in a tokamak is preferable to the circular one in many respects [7, 167, 203–207]. Therefore, many modern and even more so future tokamaks are designed for operation with a non-circular plasma. Probably, trend will finally predominate in stellarator research also. As already mentioned, configurations with on average non-circular magnetic surfaces were studied for the first time when the ATF was designed [36, 45].

To have the possibility of analyzing such configurations, in addition to the shift of the surfaces it is necessary to take account, at least, of their elongation also. Having assumed, for example, that the averaged magnetic surfaces are shifted ellipses:

$$\begin{aligned} r &= R - \rho\cos u = R + \Delta - a\cos\theta, \\ z &= \rho\sin u = Ka\sin\theta. \end{aligned} \tag{3.24}$$

Here $R$ is the radius of the geometrical axis, $\Delta$ is the shift of the centers of magnetic surfaces $a = \text{const}$ with respect to this axis, and $K$ is their elongation (see Fig. 3.4). In numerical calculations for the explicit parametrical description of the shape of magnetic surfaces, several dozen or sometimes even more than a hundred harmonics are required (see Refs. [44, 180, 242, 243]). It is clear that in this respect model (3.24) is limited. However, for a qualitative description of many effects it appears to be useful.

The radial dependence of $\Delta(a)$ and $K(a)$ should be found from the equilibrium equation (2.120). The derivation of equations for $\Delta$ and $K$ (but with the restriction $|K-1| \ll 1$) is described in detail and with proper references in [130, 131] and

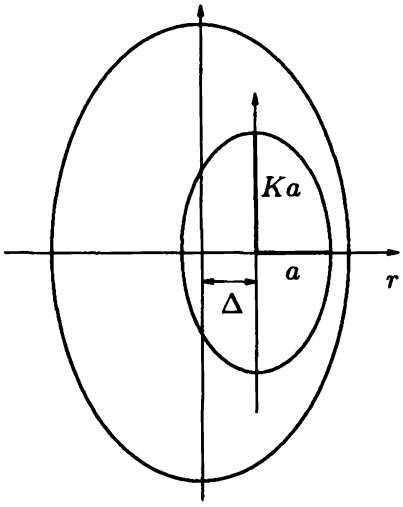


**Fig. 3.4.** Elliptical shifted magnetic surfaces.

will not be discussed here. We shall only note that this derivation is usually carried out in curvilinear flux coordinates, which entails cumbersome calculations of the metric tensor of these coordinates (see [145]). However, the necessary equations could also be derived without the transition to flux coordinates.

For this purpose, one should multiply Eq. (2.118) by a suitable function $f$ and then average the equation over the layer between nearby surfaces $\psi = \text{const}$ [see Eq. (2.42)]. In the resulting equation, the left-hand side contains the combination

$$\left\langle f \operatorname{div} \frac{\nabla\psi}{r^2} \right\rangle = \frac{d}{dV}\left\langle f \frac{\nabla\psi \cdot \nabla V}{r^2} \right\rangle - \left\langle \frac{\nabla\psi \cdot \nabla f}{r^2} \right\rangle, \tag{3.25}$$

where the second term can be eliminated by the proper choice of $f$. As a result we obtain

$$\frac{d}{dV}\left\langle f \frac{\nabla\psi \cdot \nabla V}{r^2} \right\rangle = \left\langle f\left(\operatorname{div} \frac{\nabla\psi_V}{r^2} - \frac{2\pi}{r}\bar{j}_\zeta\right)\right\rangle. \tag{3.26}$$

These equations are the typical moment equations. The first, with $f = 1$, is the differential analogue of the equality

(2.102). Other $f$ give the equations for the dipole, quadrupole, and other components of $\psi$. The subscript "0" is dropped here, but actually the integration is performed over the axially symmetric toroidal tubes $\psi(r,z) = \text{const}$.

Equality (3.25) is obtained with the help of Eq. (2.92). Using Eq. (2.92) once again, we obtain

$$\left\langle \frac{\nabla\psi \cdot \nabla f}{r^2} \right\rangle = \frac{d\psi}{dV} \int \left\langle \operatorname{div} \frac{\nabla f}{r^2} \right\rangle dV. \tag{3.27}$$

This value is zero if $f$ is chosen from the condition

$$\operatorname{div} \frac{\nabla f}{r^2} = 0. \tag{3.28}$$

The substitution

$$\nabla f = r^2 \left[ \nabla g \times \nabla \zeta \right] \tag{3.29}$$

turns Eq. (3.28) into the Laplace equation

$$\nabla^2 g = 0, \tag{3.30}$$

so it is not difficult to find the functions $f$. Solutions of Eq. (3.28) in different forms were discussed in detail by Braams [294]. Some of them were mentioned by Zakharov and Shafranov [130]. For completeness, let us show here the most simple solutions:

$$f = 1, \quad z, \quad r^2, \quad r^2 z, \quad r^4 - 4r^2 z^2. \tag{3.31}$$

Assume that the form of surfaces $\psi = \text{const}$ is explicitly given by relationships (3.24). Then

$$\nabla a = \frac{Ka}{D} \left( \mathbf{e}_z \frac{\sin\theta}{K} - \mathbf{e}_r \cos\theta \right), \tag{3.32}$$

$$\nabla\theta = \frac{1}{D} \left( \mathbf{e}_z (\cos\theta - \Delta') + \mathbf{e}_r K (1 + 2d) \sin\theta \right), \tag{3.33}$$

where $d \equiv aK'/(2K)$,

$$\begin{aligned} D &\equiv \left( \left[ \nabla a \times \nabla\theta \right] \cdot \mathbf{e}_\zeta \right)^{-1} \\ &= Ka \left( 1 - \Delta' \cos\theta + 2d \sin^2\theta \right), \end{aligned} \tag{3.34}$$

and all calculations in Eq. (3.26) are reduced to the integration

$$\langle f(a,\theta)\rangle V' = 2\pi \int_0^{2\pi} f r D \, d\theta. \tag{3.35}$$

In the elementary case $K = 1$ one can obtain from Eq. (3.26)

$$\left((\mu_h \Delta)' a^3\right)' + \frac{1}{\mu_J}\left(\mu_J^2 a^3 \Delta'\right)' = \frac{2p'(a)a^2 R}{(\mu_h + \mu_J)B_0^2} \times \left(1 + B_0^2 V_0''(\Phi)\frac{\Delta}{2}\right), \tag{3.36}$$

where $V_0''(\Phi)$ is the quantity given by Eq. (3.11), and $\mu_J = RJ/(a\Phi')$ is the rotational transform due to the toroidal current.

For the first time the equation for $\Delta$ for the case of circular surfaces ($K = 1$) in a stellarator was derived by Greene et al. [137]. Later it was derived by other methods and refined and analyzed by other authors [131, 139, 140, 145, 147, 152, 153, 161]. In some cases, instead of (3.24), the transformation $\rho = a + \Delta\cos\theta$ and the expansion in $\Delta/a$ were used, which, strictly speaking, could be applied for the description of only the peripheral part of a plasma column, far from the magnetic axis. Form (3.36) of the equation was proposed in [145].

At $\mu_h = 0$, $V_0''(\Phi) = 0$, Eq. (3.36) describes a tokamak. This case was explained in detail by Zakharov and Shafranov [130]. As can be seen from Eq. (3.36), stellarators have a number of essential distinctions from tokamaks. First, Eq. (3.36) has a "good" solution at $\mu_J = 0$. This is a consequence of the fact that the vacuum field of a stellarator has a rotational transform, and a longitudinal current is not necessary for plasma equilibrium. Second, Eq. (3.36) for a tokamak contains only derivatives of the shift $\Delta$, whereas for stellarators with shear the left-hand side of Eq. (3.36) also contains the shift $\Delta$ itself. The geometrical axis in such stellarators is the distinguished center, and the vacuum magnetic field counteracts the plasma shift with respect to this axis. Finally, there is a term with a "magnetic hill" $V_0''(\Phi)$ and

shift $\Delta$ on the right-hand side of Eq. (3.36). Usually their product is small (see Table 3.1). The only exception is Heliotron E with large $V_0''(\Phi)$ which, in addition, allows operation with a large shift of the plasma column [240].

For stellarators, the most interesting is the case of current-free plasma. At $\mu_J = 0$, the result of integrating (3.36) is the quantity $(\mu_h\Delta)'$, so that

$$\frac{(\mu_h\Delta)'}{\mu_b}\Big|_{\Gamma_p} = \frac{\beta_0}{\beta_{\rm eq}^0}\int_0^b \frac{p'(a)}{p_0}\frac{\mu_b}{\mu}\frac{a^2}{b^2}\left[1 + B_0^2 V_0''(\Phi)\frac{\Delta}{2}\right]da, \qquad (3.37)$$

where $\beta_{\rm eq}^0 = \mu_b^2 b/R$ is defined by Eq. (3.15), $\beta_0 = 2p_0/B_0^2$, $p_0 = p(0)$ is the value of $p$ at the axis, and $\Gamma_p$ shows that the function is evaluated at the plasma boundary $a = b$.

Equation (3.36) is imperfect. It is quite suitable for the description of shearless stellarators. But the larger the shear, the worse it describes the near-axis region. Attempts to improve Eq. (3.36) result in such complications that it becomes useless: it is virtually impossible to use it (see Refs. [131, 147, 150]). Therefore, we shall not discuss here the more complicated versions of Eq. (3.36) accounting for the nonlinear terms.

In problems of plasma-equilibrium control, finally we have to consider the integral effects. Inaccuracy in the description of the central region may be inessential if this region does not give a large contribution to the integral force balance. In such cases, Eq. (3.36) is quite acceptable for applications. Below we shall use its consequence (3.37).

Let us note that in the two extreme cases expression (3.37) is easily integrated for any $p(a)$. For shearless stellarators ($\mu_h = \mu_b = \text{const}$), Eq. (3.37) reduces to

$$\Delta'(b) = -\beta/\beta_{\rm eq}^0, \qquad (3.38)$$

where $\beta = 2\bar{p}/B_0^2$, and $\bar{p}$ is the average over the whole cross

section of the plasma:

$$\bar{p} \equiv \frac{2}{b^2} \int_0^b p(a) a \, da. \tag{3.39}$$

For an $\ell = 3$ stellarator ($\mu_h = \mu_b a^2/b^2$), we obtain from Eq. (3.37)

$$\frac{(\mu_h \Delta)'}{\mu_b}\Big|_{\Gamma_p} = -\frac{\beta_0}{\beta_{\rm eq}^0}. \tag{3.40}$$

In both cases we have disregarded the term with $V_0''(\Phi)$ in Eq. (3.37).

### 3.4. Effect of satellite harmonics on the stellarator configuration

Formally, this section can be considered as a continuation of Section 3.1, but with respect to the main theme of the review it appears to be auxiliary, thus it is placed at the end of Section 3.

The auxiliary character of the results submitted below is not at all obvious beforehand. Just the opposite, because the helical field in a real stellarator always contains several satellite harmonics [77, 295, 296] besides the main one, and even if the satellite amplitudes are small, in numerical calculations sometimes up to several dozen such satellites are taken into account [180, 242, 243, 297–300]. Furthermore, it is sometimes affirmed that the results of the calculations are sensitive to the choice of model for the magnetic field. To what degree does it concern the plasma equilibrium? Can small satellites strongly affect the equilibrium? We must answer these questions at least for substantiation of the model of a stellarator with $\psi_V = \psi_V(\rho)$ described above.

The presence of the satellites manifests itself, first of all, in the quantity $\mathbf{B}^2$, whose behavior on magnetic surfaces largely

determines the physics of plasma confinement in toroidal magnetic systems. It is enough to recall that $\mathbf{B}^2$ is explicitly contained in the equations for the Pfirsch–Schlüter current, the stability criteria (for example, in the expression for the magnetic well [87]), in the drift Hamiltonian for the charged particles in the magnetic field [301–304], and in the equations for the bootstrap current [305–307]. The addition of satellites to the main harmonic of the helical field [102, 144, 284, 308–318] is actually proposed to make the desired change of $\mathbf{B}^2$.

The appearance of additional harmonics in the magnetic field $\mathbf{B}$ should inevitably change the geometry of the magnetic surfaces. Consequently, in calculations of $\mathbf{B}^2$ as a function of coordinates on a magnetic surface it is not correct, generally speaking, to take into account the additional contribution to $\mathbf{B}$ only, but it is also necessary to take into account the accompanying deformations of the "coordinate system." This nontrivial circumstance was discussed in detail in [285].

The MHD theory of plasma equilibrium must give a self-consistent description of a configuration, with a one-to-one correspondence between the geometry of the magnetic surfaces and the magnetic field. This is one of the key problems in the theory of toroidal systems with magnetic confinement of a plasma; therefore, this problem has been fairly well studied. There are brilliant reviews [20, 21] devoted to it and to clarification of its general principles. A lot of work has been done to carry out direct numerical calculations of the magnetic configurations produced by given external currents and with account of finite plasma pressure (see, for example, [45, 58, 64, 77, 242, 243, 296–298, 316]). Finally, for a conventional stellarator there is an elegant solution [93, 222] (see also [20]) expressed by the simple equality (2.33), obtained using the averaging method [275].

To calculate $\psi$ using Eq. (2.33), one needs to know the magnetic field. The field of the plasma currents (the additive contribution to $A_t$) is determined after the solution of the equilibrium problem. But for the vacuum configuration of a stellarator the relation of $\psi$ to the field $\mathbf{B}$ is given directly by Eq. (2.33).

The influence of the helical field on the geometry of the magnetic surfaces $\psi = \text{const}$ is described by the function $\psi_V$ [see Eq. (2.14)]. In the vacuum approximation, $\psi_V$ is given by formula (3.2), which can be rewritten in the symmetric form

$$\psi_V = -\pi R^2 B_0 \sum_{\substack{m>0 \\ k,n}} \frac{\psi_{kn}(\rho)}{m} \cos\left[(k-n)u + \alpha_{km} - \alpha_{nm}\right]. \quad (3.41)$$

Here

$$\psi_{kn} \equiv \frac{1}{2\rho B_0^2}\left[k\varphi_{km}\frac{d\varphi_{nm}}{d\rho} + n\varphi_{nm}\frac{d\varphi_{km}}{d\rho}\right], \quad (3.42)$$

and $\varphi_{im}$ are the coefficients of expansion (3.1) of the potential $\varphi_h$; the toroidal corrections are disregarded.

By definition, $\psi_{kn} = \psi_{nk}$. Note that the right-hand side of Eq. (3.42) contains the harmonics $\varphi_h$ with an identical period in the toroidal angle $\zeta$. Only at identical $m$ can the harmonics with different multipolarity ($k \neq n$) make a "non-diagonal" contribution to $\psi_V$. Perhaps this is the reason why they are called sometimes "interacting." In the absence of such harmonics $\psi_V = \psi_V(\rho)$, and the contribution of harmonics with different $m$ to this function is additive.

There are satellites with the same $m$ as that of the main harmonic in, for example, the ATF [243, 319], Heliotron E [243], Uragan-2M [318]; according to calculations they should also be in the LHD [298] and Liven'-2/4 [102, 317]. When satellites are proposed as a means of optimization of a magnetic configuration [102, 144, 284, 308–318], the harmonics with the same $m$ are always implied. Then inevitably $\psi_V = \psi_V(\rho, u)$.

Indeed, let the helical field be a composition of the main harmonic $(m, \ell)$ and two satellites $(m, \ell \pm 1)$:

$$\varphi_h = \sum_{\ell-1}^{\ell+1} \varphi_k(\rho)\, \sin(ku - m\zeta). \quad (3.43)$$

Then we obtain from the general expression (3.41)

$$\psi_V = -\frac{\pi R^2 B_0}{m}\left(\psi_0(\rho) + \psi_1(\rho)\cos u + \psi_2(\rho)\cos 2u\right), \quad (3.44)$$

where

$$\psi_0 = \psi_{\ell\ell} + \psi_{\ell-1,\ell-1} + \psi_{\ell+1,\ell+1}, \quad (3.45)$$

$$\psi_1 = 2\left(\psi_{\ell,\ell-1} + \psi_{\ell,\ell+1}\right), \quad (3.46)$$

$$\psi_2 = 2\psi_{\ell-1,\ell+1}, \quad (3.47)$$

To calculate these functions in the large-aspect-ratio approximation, one can use for $\varphi_k$ the substitution

$$\varphi_k = B_0\gamma_k\frac{R}{m}I_k(x), \quad (3.48)$$

where $x \equiv m\rho/R$, $\gamma_k$ are constants describing the amplitudes of the harmonics, and $I_k$ are modified Bessel functions.

In expression (3.43), we restrict ourselves to the two nearest satellites, $\ell \pm 1$, as the most important in all the cases mentioned above [102, 144, 284, 298, 308–319]. These satellites are responsible for the appearance of the term $\psi_1 \cos u$ in the expression for $\psi_V$, which corresponds to the shifting of magnetic surfaces $\psi_V = \text{const}$. The terms proportional to $\cos 2u$ describe the elongation of the surfaces, which is an effect similar to the action of a quadrupole field [256]. The satellite amplitudes are usually smaller than the amplitude of the fundamental harmonic, and sometimes one of them may be even much smaller. In such a situation, the function $\psi_2$ quadratic in $\varphi_{\ell\pm1}$ is small, and the main effect of the satellites is described in Eq. (3.44) by the function $\psi_1$.

The general relationships given above allow us to explicitly write the following for an $\ell = 2$ stellarator with two "interacting" satellites $\ell = 1$ and $\ell = 3$:

$$\psi_0 = \frac{x^2}{16}\left[\gamma_2^2\left(1+\frac{x^2}{4}\right) + \gamma_1^2\left(2+\frac{5}{16}x^2\right) + \gamma_3^2\frac{x^2}{16}\right] + \frac{\gamma_1^2}{4}, \quad (3.49)$$

$$\psi_1 = \gamma_2\left[\gamma_1\frac{x}{4}\left(1+\frac{3}{8}x^2\right) + \gamma_3\frac{x^3}{32}\right]. \quad (3.50)$$

These expressions are obtained by expansion in powers of $x$ up to $x^4$ inclusive. As can be seen from Eq. (3.50), the shift of surfaces $\psi_V = \text{const}$ arises mainly due to the lowest satellite, $\ell = 1$. For small amplitudes of satellites one can use the simple formula

$$\Delta = \frac{R}{m}\left(2\frac{\gamma_1}{\gamma_2} + \frac{\gamma_3 - \gamma_1}{\gamma_2}\frac{x^2}{4}\right) \tag{3.51}$$

for an estimate of this shift.

For the description of the stellarator magnetic configuration it is necessary, besides $\psi_V$, also to know $\Omega^0$. Using expansion (3.1), it is easy to confirm that in the general case

$$\Omega^0 \equiv \frac{\langle\tilde{\mathbf{B}}^2\rangle_\zeta}{B_0^2} = \sum_{\substack{m>0\\k,n}} \frac{1}{k+n}\frac{1}{\rho}\frac{d}{d\rho}\left(\rho^2\psi_{kn}\right) \times \cos\left[(k-n)u + \alpha_{km} - \alpha_{nm}\right], \tag{3.52}$$

where $\psi_{kn}$ are the functions (3.42).

If all harmonics, the main one and the satellites, have an identical period in $\zeta$ and, in addition, $m\rho/R \ll 1$, then, approximately,

$$\Omega^0 = -\frac{m}{\pi R^2 B_0}\psi_V. \tag{3.53}$$

Indeed, near the axis $\varphi_k \sim \rho^k$, so that the expansion in $\rho$ of the functions $\psi_{kn}$ starts from the term proportional to $\rho^{k+n-2}$. If we restrict ourselves to this term only, the whole block before the cosine in Eq. (3.52) will be transformed into $\psi_{kn}$, and expressions (3.52) and (3.41) will become similar, which is shown by formula (3.53).

Relationship (3.53) means that in the vacuum approximation, when no distinction is made between $\psi$ and $\psi_V$, $\tilde{\mathbf{B}}^2$ drops out from Eq. (2.121) and, therefore, the helical field does not render any influence on the Pfirsch–Schlüter current. Thus, in the presence of "interacting" satellites the Pfirsch–Schlüter current remains the same as in their absence.

This conclusion deserves special attention, since quite the opposite opinion exists in theory. Despite the scarce proofs given to support it, this opinion is widely known because of the attractiveness of the idea.

The possibility of reducing the Pfirsch–Schlüter current by a proper choice of satellite harmonics in conventional stellarators was discussed by Kovrizhnykh [313]. Later this idea was developed in more detail by Shishkin [284], but without references to [313] and without comparison of the presented result with previous predictions [313]. Quantitatively and in some aspects even qualitatively the results in [313] and [284] do not agree, but both authors unequivocally defend the statement about the strong dependence of $\bar{j}_\zeta$ on the amplitudes of "interacting" satellites.

In both cases, this incorrect (for the conditions specified in [313] and [284]) conclusion is a consequence of the fact that the dependence of $\psi_V$ on satellites was completely ignored in both [313] and [284]. A detailed explanation of this circumstance and a proof of the necessity of self-consistent calculation of both $\psi_V$ and $\Omega^0$ can be found in [285]. Actually, it was shown in [285] that in the model used in [284] relation (3.53) of $\psi_V$ with $\Omega^0(\rho, u)$ was violated at the very beginning of the calculations by the assumption $\psi_V = \psi_V(\rho)$, which is inadmissible in the context of the problem.

Conversely, the analytical model used by Kovrizhnykh [313] is faultless up to the last formula. But its application requires knowledge of the geometry of the magnetic surfaces. The implicit assumption $\psi_V = \psi_V(\rho)$ at the transition to calculations with $\Omega^0 = \Omega^0(\rho, u)$ is the reason for the incorrect final conclusion.

When applied to [313], our disproof based on Eq. (3.53) may seem insufficient, since more terms were taken into account in the expansion of $\Omega^0$ in $m\rho/R$ in [313] than in Eq. (3.53). However, such details do not change the main point. Let us show this within the framework of model (3.43) at $\ell = 2$, which corresponds to the initial assumptions in [313].

For $\varphi_h$ consisting of three harmonics, the function $\Omega^0$ looks like that in Eq. (3.44):

$$\Omega^0 = \Omega_0^0(\rho) + \Omega_1^0(\rho)\cos u + \Omega_2^0(\rho)\cos 2u. \qquad (3.54)$$

The functions $\Omega_i^0$ contained here are calculated from formulas (3.52) and (3.42) (see also [285]). Substitution of $\varphi_k$ in the form (3.48) into Eq. (3.42) yields for the case $\ell = 2$ with two nearest satellites:

$$\Omega_1^0 = \gamma_2 \left[ \gamma_1 \frac{x}{4} \left( 1 + \frac{5}{8} x^2 \right) + \gamma_3 \frac{x^3}{32} \right], \qquad (3.55)$$

where $x = m\rho/R$. The terms of higher order in $x$ are rejected here. The value of the Pfirsch–Schlüter current (2.121) is determined by the combination

$$B_t^2 - \langle \tilde{\mathbf{B}}^2 \rangle_\zeta \cong B_0^2 \left[ 1 - \Omega_0^0(x) + \left( 2\frac{x}{m} - \Omega_1^0 \right) \cos u \right]. \qquad (3.56)$$

In tokamaks and stellarators this current originates from the toroidicity, which gives the term $2(x/m)\cos u$ in Eq. (3.56). The satellites give rise to a similar term, but with another dependence on $x$. The toroidal inhomogeneity in Eq. (3.56) could be compensated for under the condition

$$2\frac{x}{m} - \Omega_1^0 = 0, \qquad (3.57)$$

which can be satisfied by a suitable choice of $\gamma_1$ and $\gamma_3$ in Eq. (3.55):

$$\gamma_1\gamma_2 = \frac{8}{m}, \quad 5\gamma_1 = -\gamma_3. \qquad (3.58)$$

This exactly reproduces the logic and the resulting expressions of [313]. It was asserted then [313] that Eq. (3.58) corresponds to the absence of the Pfirsch–Schlüter current. But this conclusion is wrong. Under condition (3.57), we obtain for $\bar{j}_\zeta$ from Eq. (2.121):

$$\bar{j}_\zeta = 2\pi R p'(\psi) \left[ \Omega_0^0(x) - \langle \Omega_0^0(x) \rangle \right]. \qquad (3.59)$$

Usually $|\Omega_0^0 - \langle \Omega_0^0 \rangle| \ll 2\rho/R$, or even identically zero when the magnetic surfaces are described by $\rho = \text{const}$. Hence, the conclusion [313] on the suppression of the Pfirsch–Schlüter current by choice (3.58) appears "natural." But (3.58) is an extremely

unusual choice, for which the customary relations between parameters are violated. In particular, the difference $\Omega_0^0 - \langle\Omega_0^0\rangle$ unexpectedly becomes very large because of the large satellite-induced shifting of the magnetic surfaces. When, for example, Eq. (3.51) is used for estimates, the same expression for $\bar{j}_\zeta$ is obtained from Eq. (3.59) as for the case without satellites.

The Pfirsch–Schlüter current is an important characteristic of an equilibrium configuration. Precisely $\bar{j}_\zeta$ determines how far the equilibrium solution $\psi(\mathbf{r})$ differs from the vacuum one [see Eq. (2.118)]. Our consideration allows us to conclude that we should trust in the expressions for $\bar{j}_\zeta$ obtained in the model without satellites.

# 4. Control of plasma equilibrium using a vertical magnetic field

## 4.1. Boundary conditions in equilibrium problems

External control magnetic fields influence the solution of the equilibrium problem through the boundary conditions.

In toroidal fusion devices, the plasma usually has a sharp boundary that naturally divides the space into internal and external regions. This boundary is flexible and should adjust itself to any variation of the magnetic field $\mathbf{B}$ so that $\mathbf{B}$ has no normal component to this surface. This very condition brings a specific character to plasma equilibrium problems. In all other respects, the plasma boundary can be considered as a usual surface between a conducting medium and vacuum, and one can use the known results of electromagnetic theory.

Following the general ideology of the reduction of the three-dimensional equilibrium problem to two-dimensions, it is necessary to aspire to independent formulations of the boundary conditions for $\bar{\mathbf{B}}$ and $\tilde{\mathbf{B}}$. In conventional stellarators, the helical field is not appreciably distorted even at high $\beta$, hence, first of all, the boundary conditions are necessary for an axially symmetric field $\bar{\mathbf{B}}$.

Two conditions on the boundary, the absence of the normal component (from both sides) and the usual relation between the tangential components, are valid for the total field $\mathbf{B} = \bar{\mathbf{B}} + \tilde{\mathbf{B}}$. By expansion and averaging over $\zeta$ these conditions can be reduced to equations where the unknowns will be $\bar{\mathbf{B}}$ and the "averaged boundary" $\psi = \psi_b = \text{const}$. This is the direct way, but it is possible to act in a different manner. To simplify the problem to the maximal degree and simultaneously secure the result against simplifying assumptions, one should start from the Maxwell equations.

The field $\bar{\mathbf{B}}$ is related to the current $\bar{\mathbf{j}}$ by the equation $\bar{\mathbf{j}} = \text{rot}\,\bar{\mathbf{B}}$, which does not contain the helical field. We need the consequence of this equation

$$\mathcal{L}(rA_t) \equiv -r\text{div}\,\frac{\nabla(rA_t)}{r^2} = \bar{j}_\zeta, \tag{4.1}$$

where $A_t$ is the toroidal component of the vector potential of the axially symmetric poloidal magnetic field $\mathbf{B}_p$. It was explained above that substitution of $\bar{j}_\zeta$ turns Eq. (4.1) into Eqs. (1.1) or (1.2). In our case, an explicit expression for $\bar{j}_\zeta$ is not needed. It is important only that the current $\bar{j}_\zeta$ flows in a limited volume inside some torus. Therefore, Eq. (4.1) must be solved under conditions

$$rA_t \to 0 \quad \text{at} \quad r^2 + z^2 \to \infty \quad \text{and at} \quad r \to 0. \tag{4.2}$$

For a ring unit current $j_0 = \delta(r - r')\,\delta(z - z')$ lying in the plane $z = z'$ the solution of Eq. (4.1) is known (see, for example, [320]):

$$rA_0 = G = \frac{\sqrt{rr'}}{\pi t}\left[\left(1 - \frac{t^2}{2}\right)K(t) - E(t)\right]. \tag{4.3}$$

Here $r'$ is the radius of this ring whose center lies on the axis $z$; $K$ and $E$ are complete elliptical integrals of the first and second kind, and

$$t^2 \equiv \frac{4rr'}{(r + r')^2 + (z - z')^2}. \tag{4.4}$$

With the help of the function $G$, which is the Green's function of problem (4.1) with conditions (4.2), the vector potential $\mathbf{A_S} = A_S \mathbf{e}_\zeta$ of the field of currents $\bar{j}_\zeta$ flowing inside the axially symmetric torus with cross section $S$ (a particular solution to Eq. (4.1)) is represented in the integral form:

$$rA_s = \int\limits_S G(r, z; r', z')\, \bar{j}_\zeta(r', z')\, dr'\, dz'. \tag{4.5}$$

Together with the second Green's formula, which for the functions independent of $\zeta$ is reduced to the equality

$$\int\limits_S (v\mathcal{L}u - u\mathcal{L}v)\, dr\, dz = \oint\limits_\Gamma \frac{1}{r}\left(u\frac{\partial v}{\partial n} - v\frac{\partial u}{\partial n}\right) dl, \tag{4.6}$$

relationship (4.5) leads to

$$rA_S - \eta r A_t = \oint\limits_\Gamma \left[A_t(r', z')\frac{\partial G}{\partial n'} - \frac{G}{r'}\frac{\partial}{\partial n'}(r'A_t)\right] dl', \tag{4.7}$$

where $\Gamma$ is the boundary of $S$ in the cross section $\zeta = \text{const}$, $A_t = A_S + A_{\text{ext}}$, and $A_{\text{ext}}$ is the part of $A_t$ that is created by toroidal currents external to $\Gamma$ (by all currents flowing outside $S$), $\partial/\partial n \equiv \mathbf{n}\cdot\nabla$, $\mathbf{n}$ is the normal to $\Gamma$ in the plane $\zeta = \text{const}$, and

$$\eta \equiv -\oint\limits_\Gamma \frac{1}{r'}\frac{\partial G}{\partial n'}\, dl' = \begin{cases} 1, & (r, z) \in S, \\ 1/2, & (r, z) \in \Gamma, \\ 0, & (r, z) \notin S \cup \Gamma. \end{cases} \tag{4.8}$$

According to Eq. (2.33), the value $A_t$ can be represented in the form

$$A_t = \frac{\psi - \psi_V}{2\pi r}. \tag{4.9}$$

Substituting this into the right-hand side of Eq. (4.7), we obtain for a contour $\Gamma_p$ lying on the "averaged" boundary of the plasma column

$$rA_{\text{pl}} - \eta r(A_{\text{pl}} + A_{\text{ext}}) = \oint\limits_{\Gamma_p} G\,\bar{\mathbf{B}}\cdot d\mathbf{l} - \frac{1}{2\pi}\oint\limits_{\Gamma_p} \frac{\psi_V}{r'}\frac{\partial G}{\partial n'}\, dl' - \eta\frac{\psi_b}{2\pi}. \tag{4.10}$$

Here $A_{\rm pl}$ is the plasma-produced part of $A_t$, which describes the self-field of the plasma currents, $d\mathbf{l} \equiv [\mathbf{e}_\zeta \times \mathbf{n}']\, dl'$ (see Fig. 3.1), and $\psi_b = \psi|_{\Gamma_p}$ is the value of $\psi$ on the plasma boundary. At the transition from Eq. (4.7) to Eq. (4.10) we took account of the fact that, by definition, $\psi|_{\Gamma_p} = \text{const}$.

Formula (4.10) is equally applicable to both tokamaks and stellarators. The stellarator differs from a tokamak in that the magnetic surfaces $rA_{\rm ext} = \text{const}$ of the axially symmetric field $\bar{\mathbf{B}}$ do not coincide with the averaged magnetic surfaces $\psi = \text{const}$ of the total field $\bar{\mathbf{B}} + \tilde{\mathbf{B}}$. Because of this circumstance, a non-trivial contribution [the term with $\psi_V$ in Eq. (4.10)] comes from the first term on the right-hand side of Eq. (4.7). In a tokamak we would have $\psi_V = 0$. In this case, Eq. (4.10) is the mathematical formulation of the virtual casing principle [230].

The method called the virtual casing principle is based on a simple physical analogy. It is known that the calculation of the external confining field and self-fields of the plasma currents can be reduced to the calculation of the field produced by the current $\mathbf{i} = [\mathbf{n} \times \mathbf{B}]$ "flowing" along the plasma surface (see, for example, [20, 130, 230, 237]). Here $\mathbf{B}$ and $\mathbf{n}$ are, respectively, the real magnetic field on the plasma boundary and the normal to the boundary. For a tokamak the calculation of the field of this current using Eq. (4.5) leads directly to Eq. (4.10). In a stellarator the plasma boundary is asymmetrical, and in this case the magnetic field of the surface current $\mathbf{i}$ should be calculated with the Green's function of the three-dimensional Laplace equation. Such a direct numerical calculation of the plasma fields in a stellarator was used in [243].

The presence of small parameters allows stellarator problems to be solved by the expansion method. As was discussed in the first section, attempts to reduce the virtual casing principle to two-dimensions were made in [119–121]. But in these works the plasma was described by the method of expansion in powers of $\rho$, which is completely incompatible with a strict account of conditions (4.2). The problem was resolved later [232]

when the virtual casing principle was joined to the more universal classical stellarator approximation [93, 135–138]. The general formulation of the reduced two-dimensional virtual casing principle for a stellarator [232] is, actually, another way of deriving Eq. (4.10).

The way to Eq. (4.10) shown above is mathematically strict and irreproachable and does not require explanatory comments. Nevertheless, in addition to this formal derivation of Eq. (4.10) we shall adduce, following [232], another one, expressed in quite another language. Its advantage is that, being a direct generalization of the virtual casing principle for tokamaks [230] to stellarators, it is clear and, moreover, it visually demonstrates both the similarity and difference between tokamaks and stellarators. We have repeatedly emphasized the usefulness of analogies, but direct analogies are dangerous. The "physical" derivation of Eq. (4.10) presented below shows that for the "tokamak" geometry of the two-dimensional image of a stellarator the result appears quite different from that for a tokamak only because the "average" poloidal field $\mathbf{B}_p$ has a nonzero normal component on the "average" boundary $\psi = \psi_b$. In the following, we call this axially symmetric surface simply a boundary or plasma surface, without mentioning the averaging.

The axially symmetric component of the poloidal field in a stellarator can be represented in the form (2.116). In tokamaks, $\psi_V = 0$ and, accordingly, $\mathbf{B}_p \cdot \nabla\psi = 0$. In stellarators, $\psi_V \neq 0$, so that on the surfaces $\psi = \text{const}$, coinciding with "average" isobars, $\mathbf{B}_p \cdot \nabla\psi \neq 0$. For this very reason, it is impossible to use the known result [230] for a tokamak directly here.

But it is possible to try to reduce the problem to that already resolved in [230]. For this purpose let us introduce an auxiliary vector field

$$\mathbf{b} = \mathbf{B}_p + \mathbf{b}^*, \tag{4.11}$$

where $\mathbf{b}^*$ is the poloidal field which we determine in the internal area (inside the plasma) as coinciding with the "effective" field

$\mathbf{B}^*$ introduced earlier:

$$\mathbf{b}^* = \frac{1}{2\pi}\left[\nabla\psi_V \times \nabla\zeta\right]. \tag{4.12}$$

We continue it into the external area so that it would look like a real vacuum magnetic field there. This means that outside the plasma we require fulfillment of the conditions $\operatorname{div}\mathbf{b}^* = 0$ and $\operatorname{rot}\mathbf{b}^* = 0$. Also, $\mathbf{b}^*$ must be finite at $r = 0$ and vanish at infinity.

For the field $\mathbf{b}$ in Eq. (4.11), the problem of finding its components $\mathbf{b}_{\text{ext}}$ created by the external sources could be stated and resolved in the same way as for a tokamak in [230]. It is only necessary to remember that some "currents" and "fields" in this case are not real and return to real quantities after finishing the calculations.

We assume, as in [230], that the plasma surface coincides with an ideally conducting casing carrying a surface current

$$\mathbf{i}_c = \left[\mathbf{b} \times \mathbf{n}\right]. \tag{4.13}$$

For a plasma this current is the only source of the external field, and outside the plasma the fields of the two "currents" $\operatorname{rot}\mathbf{b}$ and $\mathbf{i}_c$ completely cancel each other. In other words,

$$\mathbf{b}_c = \begin{cases} \mathbf{b}_{\text{ext}} = \mathbf{B}_{\text{ext}} + \mathbf{b}^*_{\text{ext}}, & \text{in plasma,} \\ -\mathbf{b}_{\text{pl}} = -(\mathbf{B}_{\text{pl}} + \mathbf{b}^*_{\text{pl}}), & \text{in vacuum,} \end{cases} \tag{4.14}$$

where $\mathbf{b}_c$ is the field of the surface current $\mathbf{i}_c$. Introducing the vector potential $\mathbf{A} = A_t\mathbf{e}_\zeta$ for each component of the field, we obtain

$$rA_c = \begin{cases} rA_{\text{ext}} + \psi_V/(2\pi) - rA_{j^*}, & \text{in plasma,} \\ -rA_{\text{pl}} - rA_{j^*}, & \text{in vacuum.} \end{cases} \tag{4.15}$$

Here we have used the fact that, by definition, $\mathbf{b}^*_{\text{pl}} = \mathbf{b}_{j^*}$ is the field of the "current" $\mathbf{j}^* = \operatorname{rot}\mathbf{b}^*$ flowing through the plasma, and $\mathbf{b}^*_{\text{ext}} = \mathbf{b}^* - \mathbf{b}_{j^*}$.

The field $\left[\nabla(rA_t) \times \nabla\zeta\right]$ of the current $\bar{j}_\zeta$ is calculated using formula (4.5) with a source function given by Eq. (4.3). For the surface current (4.13) on the plasma boundary, the expression $\bar{j}_\zeta dS = \bar{j}_\zeta dr\, dz$ in the integral should be replaced by $(\mathbf{i}_c \cdot \mathbf{e}_\zeta)dl$:

$$rA_c = \oint G(\mathbf{B}_p + \mathbf{b}^*) \cdot d\mathbf{l}. \tag{4.16}$$

With the help of the second Green's formula the integral of the type (4.5) for $rA_{j^*}$ is reduced to

$$rA_{j^*} = \oint G\,\mathbf{b}^* \cdot d\mathbf{l} + \frac{1}{2\pi}\oint \frac{\psi_V}{r'}\frac{\partial G}{\partial n'}\,dl' + \eta\frac{\psi_V}{2\pi}. \tag{4.17}$$

Substituting both these expressions into Eq. (4.15), we obtain

$$\begin{aligned}\oint_{\Gamma_p} G\,\mathbf{B}_p \cdot d\mathbf{l} - \frac{1}{2\pi}\oint_{\Gamma_p} \frac{\psi_V}{r'}\frac{\partial G}{\partial n'}\,dl' \\ = \begin{cases} rA_{\mathrm{pl}}, & \text{in vacuum,} \\ -rA_{\mathrm{ext}} + \mathrm{const}, & \text{in plasma,}\end{cases}\end{aligned} \tag{4.18}$$

where the values $rA_{\mathrm{pl}}$ and $rA_{\mathrm{ext}}$, which we have to calculate in problems of plasma-equilibrium control and magnetic diagnostics, are already expressed through real quantities.

It is easy to confirm that Eq. (4.18) is exactly the same as Eq. (4.10). At $\psi_V = 0$, Eq. (4.18) coincides with the known result for a tokamak [230]. The application of (4.18) for tokamaks is described in [130, 205, 207].

Thus, if the poloidal field $\mathbf{B}_p$ on the plasma boundary $\Gamma_p$ is known, the self-field of the plasma outside the plasma column and the external confining field are calculated with the help of Eq. (4.18). We shall use this equation as the basis of further analysis.

If the external magnetic field is known, Eq. (4.18) serves to find the plasma boundary $\Gamma_p$. Then any property of $\Gamma_p$, distinguishing it from other magnetic surfaces, should be specified in addition. For example, it is possible to require that the

plasma boundary touches the limiter or is limited by a separatrix. Other conditions are also possible (see [130, 205, 207, 237]). Frequently in MHD calculations, on the contrary, the shape and position of the plasma boundary are given. In this case Eq. (4.18) allows the determination of the external field necessary to force the plasma column to acquire the desired shape and position. Such problems arise when the optimal configurations are found after studying the plasma equilibrium and stability and it is necessary to understand what is really required to create them.

Equation (4.18), as well as Eq. (2.118), is mathematically exact. To find $rA_{\rm pl}$ and $rA_{\rm ext}$ with its help, it is necessary somehow to prescribe the plasma boundary $\Gamma_p$, the field $\mathbf{B}_p$ on this boundary, and the function $\psi_V$. This is already a physical modeling, to which we now proceed.

## 4.2. Reduction of the boundary conditions

In analytical calculations for stellarators, the large-aspect-ratio approximation, $A \gg 1$, is always used. The reliability and accuracy of a result then depend on how consistently the expansion in $A^{-1}$ is carried out. The necessity of advancing to one order or another of the expansion in $A^{-1}$ is determined by the problem to be solved. In calculations of the diamagnetic signal, for example, the terms of the order of $A^{-1}$ already play the role of small corrections [321, 322]. But in calculations using formula (4.18) it is absolutely necessary, in addition to the main term, to take account of the following term of expansion of the Green's function $G$ (4.3) in powers of $A^{-1}$.

The approximate expression for $G$, which comprises the first two terms of the expansion of $G$ in the small parameters $x/R$ and $z/R$ ($t^2 \cong 1$), can be written in the form [233]

$$G_1(\mathbf{r},\mathbf{r}') = G_0 - \frac{x+x'}{2R}\left[G_0 + \frac{R}{2\pi}\right]. \qquad (4.19)$$

Here $G_0$ corresponds to the "cylindrical" approximation,

$$G_0 = \frac{R}{2\pi}\left[\ln\frac{8R}{\sqrt{(x-x')^2+(z-z')^2}} - 2\right], \tag{4.20}$$

$x = R - r$, and $R$ is the radius of the circular axis, near to which we need to know the behavior of $G(\mathbf{r}, \mathbf{r}')$. As will be clear from the following, the simplified expressions for $G$, equivalent to $G_0$, which were given in the well-known works [93, 222], are, generally speaking, unacceptable for calculation of $rA_{\text{pl}}$ and $rA_{\text{ext}}$.

The large-aspect-ratio approximation is the first step in the simplification of the problem. The second will be the assumption that the cross section of the plasma is circular "on average." Its boundary $\Gamma_p$ can then be described by the equation

$$b^2 = \rho^2 + \Delta_b^2 + 2\rho\Delta_b \cos u, \tag{4.21}$$

where $b$ is the radius of the plasma cross section and $\Delta_b$ is the shift of its center relative to the geometrical axis of the stellarator (Fig. 4.1).

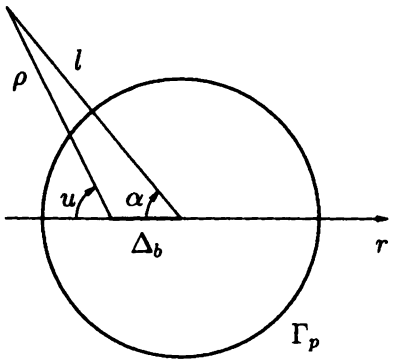


**Fig. 4.1.** Transverse cross section of the plasma column shifted to a distance $\Delta_b$ relative to the geometrical axis $\rho = 0$; $l, \alpha$ are the quasi-cylindrical coordinates associated with the center of the plasma column.

If the plasma boundary $\Gamma_p$ is circular, it is natural to calculate the integrals in the main equation (4.18) in polar coordinates $(l, \alpha)$ with origin at the center of $\Gamma_p$ (Fig. 4.1). Expansion (4.19) for the function $G$ is valid in the vicinity of *any* circular axis. We assume that in this case it passes through the center of $\Gamma_p$, $R = R_0 + \Delta_b$. Introducing

$$x = l\cos\alpha, \quad z = l\sin\alpha, \tag{4.22}$$

we make a transition to new coordinates in $G_0$ with the help of the identity [323]

$$\ln\frac{1}{\sqrt{1-2\xi\cos\omega+\xi^2}} = \sum\frac{\xi^n\cos n\omega}{n}, \tag{4.23}$$

where $|\xi| \le 1$. As a final result, we obtain the following form of $G_1$, which is convenient for our calculations:

$$G_1 = \frac{R}{2\pi}\left\{\ln\frac{8R}{l_{\max}} - 2 - \frac{x+x'}{2R}\left(\ln\frac{8R}{l_{\max}} - 1\right)\right.$$
$$\left. + \left(1 - \frac{x+x'}{2R}\right)\sum_{n=1}^{\infty}\xi^n\frac{\cos n(\alpha-\alpha')}{n}\right\}. \tag{4.24}$$

Here $\xi \equiv l_{\min}/l_{\max}$, $l_{\min} = \min\{b, l\}$ is the smaller of the two quantities $b$ (minor plasma radius) and $l$ (current minor radius), and $l_{\max} = \max\{b, l\}$ is the larger. The calculation of $rA_{\text{ext}}$ using Eq. (4.18) should be done in the internal area, where $l_{\min} = l$ and $l_{\max} = b$, so that $\xi$ still means the dimensionless minor radius: $\xi = l/b$.

Using expression (4.24), for the circular boundary $\Gamma_p$ we obtain

$$\oint_{\Gamma_p} G_1\mathbf{B}_p\cdot d\mathbf{l} = bR\left\{\sum_{n=1}^{\infty} H_n\xi^n\frac{\cos n\alpha}{2n}\right.$$
$$\left. + B_J\left[\ln\frac{8R}{l_{\max}} - 2 - \frac{l\cos\alpha}{2R}\left(\ln\frac{8R}{l_{\max}} - 1 + \frac{b}{l}\frac{\xi}{2}\right)\right]\right\}, \tag{4.25}$$

where $H_n$ are the coefficients of the Fourier expansion of the tangential component of $\mathbf{B}_p$ at the plasma edge:

$$\mathbf{B}_p \cdot \mathbf{e}_\alpha\Big|_{\Gamma_p} = B_J + \sum_{n=1}^{\infty} H_n \cos n\alpha. \tag{4.26}$$

Here we use a special designation $B_J$ to show that this value is determined only by the total longitudinal current $J$ in the plasma:

$$B_J = \frac{J}{2\pi b}. \tag{4.27}$$

In problems of plasma-position control, only the "zero" and first harmonics of (4.25) will be required. Therefore, in terms with $n \geq 2$ the toroidal corrections are omitted, although, if it were necessary, they could easily be incorporated.

For a circular plasma boundary $\Gamma_p$, the second integral in Eq. (4.18) takes the form

$$\oint_{\Gamma_p} \frac{\psi_V}{r'} \frac{\partial G}{\partial n'}\, dl' = b \sum_{n=1}^{\infty} \psi_n \int_0^{2\pi} \frac{\cos n\alpha'}{r'} \frac{\partial G}{\partial b}\, d\alpha' - \eta\psi_0, \tag{4.28}$$

where $\eta$ is the constant (4.8), $r' = R_0 + \Delta_b - b\cos\alpha'$, and $\psi_n$ are the amplitudes of the Fourier harmonics $\psi_V$ at $\Gamma_p$:

$$\psi_V\Big|_{\Gamma_p} = \sum_{n=0}^{\infty} \psi_n \cos n\alpha. \tag{4.29}$$

Taking into account Eq. (4.24) and retaining only the leading-order terms of the expansion, we obtain

$$\oint_{\Gamma_p} \frac{\psi_V}{r'} \frac{\partial G}{\partial n'}\, dl' = b \sum_{n=1}^{\infty} \psi_n \frac{\partial \xi^n}{\partial b} \frac{\cos n\alpha}{2n} - \eta\psi_0. \tag{4.30}$$

Substitution of the calculated integrals into the main equation (4.18) enables us to rewrite it in the form:

$$f_0 + f_1 \cos\alpha + \sum_{n=2}^{\infty} f_n \cos n\alpha = \begin{cases} rA_{\text{pl}}, & \text{in vacuum,} \\ -rA_{\text{ext}}, & \text{in plasma,} \end{cases} \tag{4.31}$$

where $f_n$ are the functions expressed through $H_n$ and $\psi_n$:

$$f_0 = bRB_J\left(\ln\frac{8R}{l_{\max}} - 2\right) + \frac{\eta\psi_0}{2\pi}, \tag{4.32}$$

$$f_1 = bRH_1\frac{\xi}{2} - \psi_1\frac{b}{4\pi}\frac{\partial\xi}{\partial b} - \frac{b}{2}lB_J\left(\ln\frac{8R}{l_{\max}} - 1 + \frac{b}{l}\frac{\xi}{2}\right), \tag{4.33}$$

$$f_n = bRH_n\frac{\xi^n}{2n} - \psi_n\frac{b}{4\pi n}\frac{\partial\xi^n}{\partial b}, \quad n \geq 2. \tag{4.34}$$

Now, to move further, it is necessary to prescribe the function $\psi_V$. It appears in Eq. (4.18) explicitly and, moreover, it enters $\mathbf{B}_p$ [see (2.116)]. We further assume that $\psi_V = \psi_V(\rho)$ and to find it use relationship (3.13) with parabolic $\mu_h(\rho)$ (3.8). In this case

$$\psi_V = -\pi B_0\rho^2\left[\mu_0 + (\mu_b - \mu_0)\frac{\rho^2}{2b^2}\right]. \tag{4.35}$$

The transition from "laboratory" coordinates to coordinates associated with the center of the plasma column (Fig. 4.1), is described by the equality

$$\rho\mathbf{e}_\rho = l\mathbf{e}_l + \Delta_b\mathbf{e}_r. \tag{4.36}$$

Accordingly, at the plasma edge ($l = b$)

$$\rho^2 = b^2 + \Delta_b^2 - 2b\Delta_b\cos\alpha, \tag{4.37}$$

so that

$$\psi_1 = 2\pi b\Delta_b B_0\left[\mu_0 + (\mu_b - \mu_0)\frac{b^2 + \Delta_b^2}{b^2}\right]. \tag{4.38}$$

The other coefficients of expansion (4.29) will not be needed.

So far we have made three simplifying assumptions: the aspect ratio of the installation is large, $\psi_V = \psi_V(\rho)$, and the $\mu_h$ profile is parabolic. Moreover, we assume that the plasma column is circular "on average" and is shifted in the direction $\mathbf{e}_r$ to a distance $\Delta_b$ relative to the geometrical axis $r = R_0$ (Fig. 4.1).

This is sufficient for calculation of all the values in Eq. (4.18) in a general form. But if we want to express $H_i$ in Eq. (4.26) through parameters describing the plasma configuration, then besides the plasma boundary we also have to prescribe explicitly the shape of the adjoining magnetic surfaces because expression (2.116) for $\mathbf{B}_p$ contains $\nabla\psi$.

Actually, we only have to know the value of $\mathbf{n}\cdot\nabla\psi$ on the plasma boundary. It is completely determined by the geometry of the surfaces $\psi = \text{const}$ near $\Gamma_p$, but knowledge of their shape inside the plasma is not needed for calculating $\mathbf{n}\cdot\nabla\psi$.

With the help of Eqs. (2.116), (3.32), and (4.36) it is easy to confirm that at a circular plasma boundary ($K = 1$)

$$\mathbf{B}_p\cdot\mathbf{e}_\alpha\Big|_{\Gamma_p} = B_0\frac{b}{r}\left[\mu\frac{1}{1-\Delta'(b)\cos\alpha} - \mu_h\left(1-\frac{\Delta_b}{b}\cos\alpha\right)\right]\Bigg|_{\Gamma_p}. \tag{4.39}$$

From here it is easy to find $H_i$. It is sufficient to use the simple identity

$$\frac{1}{1-\Delta'\cos\alpha} = \frac{1}{\sqrt{1-\Delta'^2}}\left\{1+2\sum_{n=1}^{\infty}\frac{\Delta'^n\cos na}{(1+\sqrt{1-\Delta'^2})^n}\right\}. \tag{4.40}$$

Calculating (4.39), we have taken into account that on the plasma boundary $\theta = \alpha$, $a = b$, and $\psi_V$ is expressed through $\mu_h$ by relationship (3.6). One should also keep in mind that on the right-hand side of Eq. (4.39) $\mu_h = \mu_h(\rho)$, and $\rho^2$ on the plasma boundary is determined by equality (4.37).

Now coming back to the main equation (4.31), it is possible to ascertain that the values $\psi_i$ and $H_i$ are expressed, if the plasma boundary $\Gamma_p$ is circular, in terms of two parameters: $\Delta_b$ and $\Delta'$. This is clear from the general relationships (4.35) and (4.39), where we must substitute expression (4.37). The value $\Delta_b$ has a clear geometrical meaning — it is the displacement of the center of the plasma column relative to the geometrical axis $\rho = 0$. This shift is a meaningful parameter in itself, which can be observed and measured by different methods. This and

the control of the value of $\Delta_b$ will be discussed in detail in the following two subsections. But $\Delta'$ is a more subtle characteristic. To express $\Delta'(b)$ through other values of practical interest, one has to solve the equilibrium equation (1.2). We already have a model result (3.37) at our disposal, enabling us to get rid of $\Delta'$.

Now that the left-hand side of Eq. (4.31) is calculated, we can proceed from calculations to physics.

### 4.3. Effect of a vertical field on the plasma-column position in stellarators

Analyzing the behavior of finite-pressure plasma in external fields, it is natural, first of all, to bring up the question of the plasma reaction to an external transverse field $B_\perp$ as one of the strongest means of influencing the equilibrium configurations.

The related physics was discussed in detail in a nicely written article by Friedberg et al. [185]. There, in particular, an apparent paradox was explained: in a stellarator the vertical field $B_\perp$ is capable of displacing the magnetic surfaces, but it does not produce a net inward/outward radial force on a current-free plasma. Why then it is possible to displace the plasma column along the major radius? The answer of the authors of [185] is that due to the variation of $B_\perp$ a current appears in the current-free plasma, and the interaction of this current with the vertical field gives a net body force shifting the plasma column. After the transition to a new equilibrium state this current dissipates, the radial force disappears, but the desired result, the plasma-column shift, has already been obtained.

The external field is related to the total equilibrium field **B** (more precisely, to its axially symmetric component) on an "averaged" plasma boundary $\Gamma_p$ by relationship (4.18), and for a "circular" plasma — by Eq. (4.31). In the latter case the main component of the external field is the uniform transverse field

$$B_\perp = B_z^{\rm ext}\Big|_{\rho=0} = \frac{1}{R}\frac{\partial}{\partial r}\left(rA_{\rm ext}\right)\Big|_{\rho=0}, \qquad (4.41)$$

which is also called vertical. From Eq. (4.31) we obtain for this field

$$B_\perp = -\frac{b}{2R}\left\{B_J\left(\ln\frac{8R}{b}-\frac{1}{2}\right)-\left(\frac{R}{b}H_1+\frac{\psi_1}{2\pi b^2}\right)\right\}. \qquad (4.42)$$

And after the substitution of Eq. (4.38) and of the consequence of Eq. (4.39)

$$H_1 = \frac{b}{R}B_J + \frac{b}{R}B_0\left\{\mu\Delta' + \left[\mu_0+\mu_2\left(3b^2+\Delta_b^2\right)\right]\frac{\Delta_b}{b}\right\} \qquad (4.43)$$

we finally obtain [233]

$$B_\perp = -\frac{b}{2R}\left\{B_J\left[\ln\frac{8R}{b}-\frac{3}{2}\right]-B_0\left[\mu\Delta'+\Delta_b\frac{(a^2\mu_h)'}{b^2}\right]\right\}\Big|_\Gamma. \qquad (4.44)$$

Here only terms linear in $\Delta'(b)$ and $\Delta_b/b$ are retained.

Expression (4.44) applies equally well to tokamaks and to stellarators for a "circular" plasma column. In tokamaks $\mu_h = 0$ and $B_0\mu(b) = B_J R/b$. In this case Eq. (4.44) literally coincides with the result of Greene et al. [236], and after substitution of the explicit expression for $\Delta'$ it is finally reduced to the relation well known in tokamak theory [130, 237]

$$B_\perp^t = -B_J\frac{b}{2R}\left[\ln\frac{8R}{b}+\beta_J+\frac{l_i}{2}-\frac{3}{2}\right], \qquad (4.45)$$

where

$$l_i = 2\int_0^b \frac{B_J^2(a)}{B_J^2(b)}\frac{a}{b^2}\,da \qquad (4.46)$$

is the specific internal inductance of the plasma column, dependent on the distribution of the longitudinal current, and $\beta_J = \beta B_0^2/B_J^2$. We note that using the cylindrical approximation (4.20) for the Green's function would lead to the disappearance of the term with $B_J$ in Eq. (4.42), which would make the transition to Eq. (4.45) impossible.

We mention a tokamak for two reasons. First, Eq. (4.44) is obtained from Eq. (4.18) using the models and methods of tokamak theory [130], which in many respects can serve as an example for stellarators. Then it is also natural to aspire to accuracy at least not less than is necessary for tokamaks and to require that the result would include, as a particular case, the proper tokamak relations. Our result (4.44) satisfies these conditions. Second, the comparison of stellarators, where the rotational transform is created by external fields, with tokamaks, where it is created by a longitudinal current flowing in the plasma, allows us better to understand the physics of these systems, to see their common features and basic distinctions. It is known that in tokamaks plasma equilibrium is impossible without an external vertical field. This can be easily seen from Eq. (4.44) or Eq. (4.45): $\ln 8 > 1.5$, and $\Delta' < 0$, so that the expressions in the brackets on the right-hand sides are positive. Moreover, at given $R$, $b$, and current and pressure profiles, no freedom remains in the choice of $B_\perp$. But for stellarators condition (4.44) appears less restrictive, actually because it contains an additional free parameter, the shift of the plasma column as a whole, $\Delta_b$. The parameter $B_J$ also becomes "free." For stellarators it is possible to put $B_J = 0$ and $B_\perp = 0$ simultaneously into Eq. (4.44). This corresponds to the equilibrium of a current-free plasma in a conventional stellarator field (free-boundary equilibrium without an external field). In this case, Eq. (4.44) gives the shift of the plasma column $\Delta_b$ due to the finite pressure of the plasma.

For an exact determination of $\Delta_b$ from Eq. (4.44) it is necessary to know $\Delta'$. The calculation of this value, dependent on pressure and current profiles, requires the solution of the equilibrium equation (1.2), which in the simplest case is reduced to the equation for the shift of magnetic surfaces (3.36). This was discussed in Section 3.3. Some important consequences of Eq. (4.44) can be seen, however, even without its solution: in the absence of a vertical field the plasma column should be appreciably displaced outwards at $\beta \to \beta_{eq}$.

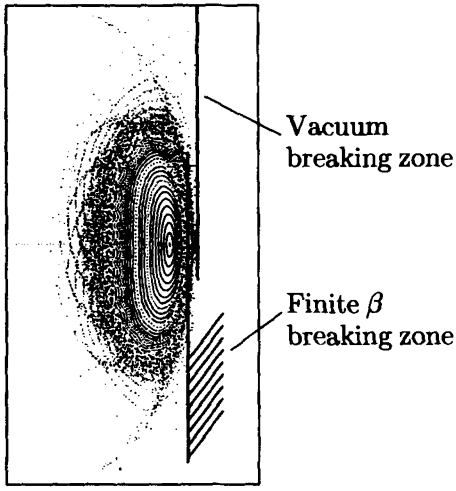


**Fig. 4.2.** Magnetic surfaces and breaking zones in vacuum and finite-pressure configurations in the $\ell = 2,\ m = 10$ Heliotron [64].

Indeed, according to Eq. (4.44) at $B_J = B_\perp = 0$ the relative magnitude of the plasma shift, $\Delta_b/b$, should be of the order of $\Delta'/2 - \Delta'/4$. But at $\beta$ close to the equilibrium limit, we have $\Delta'(b) \to -1$, so that $\Delta_b/b \leq 0.5 - 0.25$. These are very large displacements, which for many reasons are absolutely inadmissible in a large-scale experiment. Even if the gap between the plasma and the vacuum chamber wall were rather large, there would be a danger of the destruction of the external magnetic surfaces when the plasma moves outwards (Fig. 4.2). In stellarators, eventually it will be necessary to produce and maintain a plasma with fusion parameters. Then other accompanying factors would become critical. For example, only the asymmetry of thermal fluxes on the wall related to the plasma shift could become catastrophic for a stellarator-reactor, since even without this the key elements of an ITER-scale stellarator would necessarily operate in a strained regime. It is clear that the requirements of maintaining equilibrium in this case should be the same as for a tokamak. For example, the acceptable plasma shift in a stellarator has been evaluated as $\Delta_b/b \leq 10^{-2}$ [184].

Returning to less remote prospects, it is enough to mention the Large Helical Device [58, 274], which began operation in March 1998. It was optimized numerically for experiments with a plasma whose position was assumed to be fixed. Further, the plasma-wall gap in the LHD is not large, and the presence of a divertor presents, irrespective of other reasons, additional requirements on the accuracy of maintaining the plasma in a given position.

Thus, if special measures were not taken, the shift of the plasma as a whole, induced by its finite pressure, could appear at large $\beta$ an order of magnitude above the admissible level. This follows from Eq. (4.44). But from Eq. (4.44) it is also clear how this might be counteracted. A plasma column can be kept in its initial position with the help of a vertical field. Its value can be estimated as $|B_\perp| \le B^*/2$, where

$$B^* = B_0 \mu_h(b) \frac{b}{R} \tag{4.47}$$

is the "effective poloidal field" on the plasma boundary, which would produce the rotational transform $\mu_h(b)$. Indeed, if we required $\Delta_b = 0$, then at $\Delta' = -1$ corresponding to $\beta \to \beta_{\rm eq}$ we should obtain $B_\perp = -B^*/2$ from Eq. (4.44).

An illustration of this is the simple formula for a current-free plasma in a shearless stellarator:

$$\frac{\Delta_b}{b} = \frac{B_\perp}{B^*} - \frac{\Delta'}{2} = \frac{B_\perp}{B^*} + \frac{\beta}{2\beta^0_{\rm eq}}, \tag{4.48}$$

which is obtained from Eq. (4.44) taking account of expression (3.38) for $\Delta'$. In the presence of shear the corresponding relation is

$$\frac{\Delta_b}{b} = \frac{1}{2 - \mu_0/\mu_b} \left( \frac{B_\perp}{B^*} - \frac{\Delta'}{2} \right). \tag{4.49}$$

This shows that in stellarators with a large shear, at $\beta \to \beta_{\rm eq}$ the plasma column is shifted outward more weakly. This can be explained by the fact that at larger shear the dependence of the

magnetic-axis shift on $\beta$ becomes stronger. Therefore, at the same value of $B^*$, but at smaller $\mu_0$, the equilibrium limit $\beta_{eq}$ appears lower. However, the shift of the plasma as a whole is an integral effect. At identical $B^*$, but at smaller $\beta$, it appears to be weaker. These consequences of Eq. (4.49) are confirmed by the results of numerical calculation [243] (Fig. 4.3).

Expressions (4.44) and (4.49) are valid if the boundary plasma and adjoining magnetic surfaces are circular on average. It is quite unimportant what the surfaces are like inside the plasma, but we can say that at small $\beta$ they are still circular there. In this case, it is possible to use relationship (3.37) for exclusion of $\Delta'$. Then Eq. (4.44) is reduced to [233]

$$B_\perp = -\frac{b}{2R}\left\{B_J\left[\ln\frac{8R}{b}-\frac{3}{2}\right] - B_0\left[2\mu_h\frac{\Delta}{b}+\frac{2}{B_0^2}\frac{R}{b}\int_0^b \frac{a^2}{b^2}\frac{p'(a)}{\mu(a)}\,da\right]\right\}\Big|_\Gamma . \tag{4.50}$$

Here, however, two sources of the rotational transform, the longitudinal current and the helical field, can be incorporated simultaneously only at $\mu - \mu_h = \text{const}$. At a given $B_J$ and $\Delta_b$ (for example, at $\Delta_b = 0$), Eq. (4.50) gives the value of the field $B_\perp$ necessary for keeping the plasma in the given position. If, as happens in many experiments, $B_\perp$ and $B_J$ are given, then the plasma-column shift $\Delta_b$ can be found from here. In this case it is better to rewrite Eq. (4.50) in the form

$$\frac{\Delta_b}{b} = \frac{1}{B^*}\left\{B_\perp + \frac{b}{2R}B_J\left[\ln\frac{8R}{b}-\frac{3}{2}\right] - \frac{1}{B_0}\int_0^b \frac{a^2}{b^2}\frac{p'(a)}{\mu(a)}\,da\right\}. \tag{4.51}$$

Stellarators are designed for operation with a current-free plasma. In the absence of a longitudinal current, equality (4.51) becomes even simpler:

$$\Delta_b = \Delta_\perp + \Delta_\beta. \tag{4.52}$$

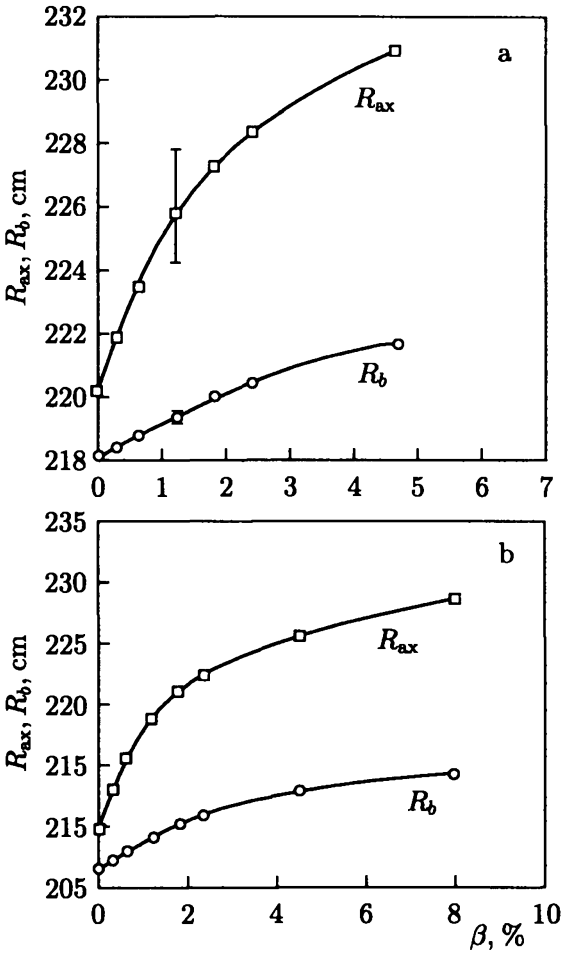


**Fig. 4.3.** Position of the magnetic axis $R_{ax} = R+\Delta_{ax}$ and of the center of the boundary magnetic surface $R_b = R + \Delta_b$ in the helical devices: (a) Heliotron E ($b = 21$ cm) and (b) ATF ($b = 27$ cm). The vertical bars show the variations of $R_{ax}$ and $R_b$ for variations of the profile $p(\psi)$ from the broad (smaller shifts) to the peaked one [243].

Here $\Delta_\perp$ is the displacement of the plasma column due to the external vertical magnetic field, and $\Delta_\beta$ is the shift due to the

finite pressure of the plasma:

$$\frac{\Delta_\perp}{b} = \frac{B_\perp}{B^*}, \quad \frac{\Delta_\beta}{b} = -\frac{\beta_0}{2\beta_{eq}^0} \int_0^b \frac{p'(a)}{p_0} \frac{\mu_b}{\mu(a)} \frac{a^2}{b^2}\, da. \tag{4.53}$$

Note that in the other simple expression, (4.49), the value of $\Delta'$ is determined by the combined effect of the vertical field and finite pressure. The transition from Eq. (4.49) to Eq. (4.53) corresponds to the separation of two effects with the help of Eq. (3.37).

The value $\Delta_\beta$ depends on profiles of the plasma pressure $p(a)$ and the rotational transform $\mu(a)$. For a parabolic profile of $\mu(a)$ [see Eq. (3.8)], in the two limiting cases expression (4.53) can be easily integrated. This allows a simple estimate for $\Delta_\beta$ to be made [235]:

$$\frac{\beta}{2\beta_{eq}^0} \leq \frac{\Delta_\beta}{b} \leq \frac{\beta_0}{2\beta_{eq}^0}. \tag{4.54}$$

Here $\beta_0 = 2p(0)/B_0^2$ is the local value, and $\beta = 2\bar{p}/B_0^2$ is the average over the cross section [see (3.39)]. The lower limit in Eq. (4.54) is reached at $\mu_0 = \mu_b$, i.e., in shearless stellarators; the upper limit — in three-turn stellarators with $\mu = \mu_b a^2/b^2$.

Summing up, we can say that the "margin of safety" of the vacuum magnetic configuration is not sufficient for maintaining the plasma at large $\beta$ in a stellarator: with increasing $\beta$ the plasma column can shift strongly outward. The effect is stronger at higher $\beta$. Thus, at large $\beta$ it becomes necessary to control the plasma position in a stellarator by means of an external vertical field reacting to variations of the plasma parameters. In tokamaks such control is carried out with the help of equilibrium control systems [122–128, 208–210, 324–328]. Stellarators designed for operation with a high-pressure plasma should also be equipped with a similar system.

These conclusions [232, 233, 235] are now confirmed by reliable numerical calculations [103, 243, 244, 281] and by the results of experiments in the CHS [103, 104] and Heliotron E [239–241].

In [103], a complete three-dimensional problem of plasma equilibrium in the CHS torsatron was solved numerically. It was shown that the plasma boundary should be shifted by 1 cm for $\beta$ of the order of 2%, which well agreed with Eq. (4.54). Naturally, it was then not difficult to detect experimentally [103] such a large displacement of the plasma column.

The results described in [243] have already been described above: they confirm the existence of the effect and the conclusions following from Eq. (4.49).

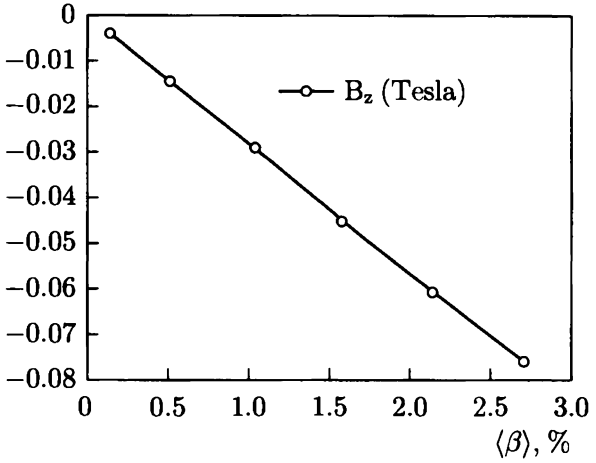


**Fig. 4.4.** Calculated values of the transverse magnetic field needed to keep the plasma column in the fixed position in LHD [244].

In [244], the free-boundary plasma equilibrium in the LHD was numerically studied with the help of the well-known code VMEQ. One problem was determining the conditions for which the plasma column in the LHD should not move when $\beta$ increases. In our notation, it corresponds to the requirement $\Delta_b = 0$. The result obtained [244] is shown in Fig. 4.4. This is the dependence of the confining field $B_\perp$ on $\beta$. It can be seen from Fig. 4.4 that this dependence remains linear at $\beta$ up to 3%. The agreement with Eq. (4.50) may seem surprising: we used an an-

alytical model that is much simpler than the simulation model [244]. However, this agreement, both qualitative and quantitative, is quite natural. The reasons for it have already been mentioned: the analytical model is based on the *exact* equations and, moreover, finally the integral effect is calculated. Therefore, absolute accuracy in the description of the plasma central region, where simple analytical models may be inadequate, is not required.

In [281], the two-dimensional problem of plasma equilibrium in the two-turn torsatron Uragan-2M (U-2M) was solved numerically. In the U-2M there is a limiter that "scrapes" the plasma column when it moves outward with increasing $\beta$. The words "plasma shift" were not used for the explanation of results in [281]. Instead it was stated that in the U-2M the area of the cross section of the last magnetic surface decreases by a factor of two for $\beta$ of the order of 1.5%. Clearly, the reason was precisely the plasma shift, which can be seen in an appropriate figure in [281]. For a particular example of U-2M, these results [281] confirm the general conclusions [233, 235] about the potential danger of the plasma-column shift as a whole at finite $\beta$.

Dynamic control of the plasma-column position [233, 235] in stellarator experiments with a high-pressure plasma was successfully carried out for the first time in the CHS torsatron [104]. Owing to the suppression of the plasma-column shift, it became possible to further improve the quality of the discharge.

Unique experiments on the measurement of the plasma-column shift as a whole have been carried out in the Heliotron E helical device [239–241]. The results obtained are shown schematically in Fig. 4.5. The shift $\Delta_\beta$ caused by the finite pressure of the plasma is always small in conditions of the Heliotron E [see estimates (4.54)]. In such a situation, the only means of making reliable measurements of $\Delta_\beta$ is magnetic diagnostics. The method of measurements [234] tested in the Heliotron E is based on Maxwell's equations and does not require any information on the profiles of the current or plasma pressure. The reliability of the results of [239–241] is therefore beyond doubt. As expected,

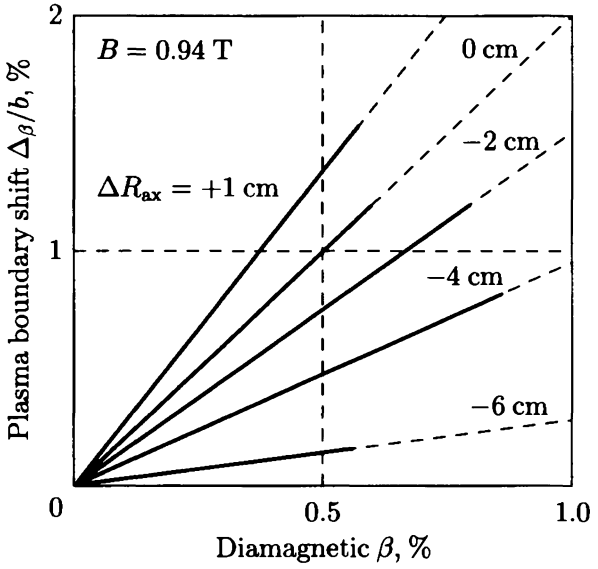


**Fig. 4.5.** Schematic view of the measured, pressure-induced plasma-column shift in Heliotron E configurations with different initial conditions [289]. The solid lines show the range of $\beta$ achieved in experiments; $\Delta R_{ax}$ is the initial shift of the vacuum magnetic axis relative to the geometrical axis $R = 220$ cm.

the measurements show a linear dependence of $\Delta_\beta$ on $\beta$. But it was unexpected that the coefficient of proportionality should be significantly different for different modes of operations.

For a strong initial inward displacement of the magnetic axis, the measured shift $\Delta_\beta$ was smaller than in the standard mode. It was clear that this was the consequence of the reduction of the Pfirsch–Schlüter current related to the magnetic hill and the inward plasma shift [137, 144]. But it was surprising that the effect was very strong. In the final account, the results of [239–241] appeared to be in good agreement with the predictions of the MHD theory. This agreement was achieved on the basis of the analysis submitted in the following two subsections.

## 4.4. Suppression of the Pfirsch–Schlüter current in conventional stellarators

The shift of the plasma as a whole and the change of shape of the magnetic surfaces are produced by the equilibrium toroidal current flowing through the plasma, which is also called the Pfirsch–Schlüter current. The influence of this current on the magnetic configuration is described by Eq. (2.118), and $\bar{j}_\zeta$ itself is given explicitly by expression (2.121). In the large-aspect-ratio approximation

$$\bar{j}_\zeta = 2\pi R p'(\psi) \left\{ \Omega - \langle \Omega \rangle_0 \right\}, \tag{4.55}$$

where $\Omega$ is the function (2.50), which can be approximated at $\rho/R \ll 1$ by

$$\Omega \equiv \Omega^0 + 1 - \frac{R^2}{r^2} \cong \Omega^0 - 2\frac{\rho}{R}\cos u, \tag{4.56}$$

and $\Omega^0$ is determined by equality (2.52).

As can be seen from Eq. (2.118), a large current results in large deformations of the magnetic surfaces (see Fig. 4.6). To make a configuration insensitive to the pressure, it is necessary to reduce $\bar{j}_\zeta$ at a given $p$. This might be possible if we could decrease the difference $\Omega - \langle \Omega \rangle_0$.

An ideal complete suppression of the Pfirsch–Schlüter current could be achieved if $\Omega$ could be made constant on a magnetic surface. However, in the normal situation $\Omega - \langle \Omega \rangle_0 \neq 0$ because of toroidicity. The typical behavior of the two components of $\Omega$ is shown in Fig. 4.7. The value $\Omega$ is equal to the distance between the solid and dashed curves accounting for their relative positions, which is shown by arrows. The picture is obviously asymmetrical: $\Omega$ has opposite signs on the left and right sides of the axis $r = R$.

As a measure of the deviation of $\Omega$ from its average value $\langle \Omega \rangle_0$ on a magnetic surface, we can use the difference

$$\delta\Omega = \Omega|_{\text{in}} - \Omega|_{\text{out}}, \tag{4.57}$$

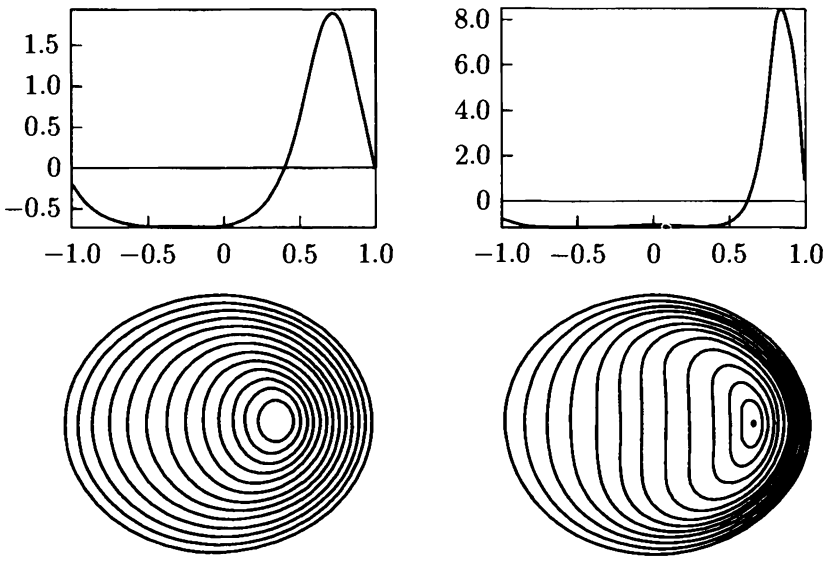


**Fig. 4.6.** Equilibrium current $\bar{j}_\zeta$ and averaged magnetic surfaces in an $\ell = 2$ stellarator at finite plasma pressure [155]. On the left side $\beta_0 = 0.32\beta^0_{\rm eq}$, and on the right side $\beta_0 = 1.28\beta^0_{\rm eq}$, where $\beta_0 = 2p(0)/B_0^2$, $\beta^0_{\rm eq} = \mu_b^2 b/R$.

where the subscripts "in" and "out" specify the inward and outward sides. Let $\rho_{\rm in}$ and $\rho_{\rm out}$ be the corresponding positions of the intersection of the magnetic surface with the axis $r$ (Fig. 4.8), and $\rho_{\rm in} + \rho_{\rm out} = 2a$. Then

$$\delta\Omega = -4\frac{a}{R} + \Omega^0(\rho_{\rm in}) - \Omega^0(\rho_{\rm out}). \qquad (4.58)$$

The reduction of $|\delta\Omega|$, apparently, leads directly to the reduction of the Pfirsch–Schlüter current. The negative quantity $-4a/R$ in Eq. (4.58) remains the same for any position of a magnetic surface with "half-width" $a$. As can be seen from Eq. (4.58), this negative value could be completely or, at least, partially compensated for only at the expense of the positive additive from $\Omega^0$. For this purpose, it is necessary to make $\rho_{\rm in} > \rho_{\rm out}$, i.e., to displace the magnetic surface inward.

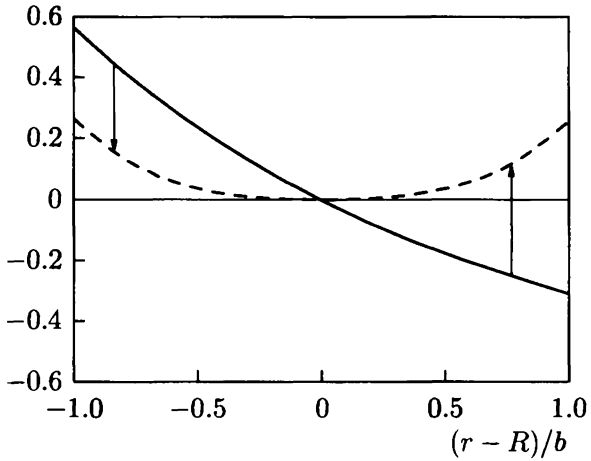


**Fig. 4.7.** Two components of $\Omega$ in a stellarator with CHS parameters: $\mu_0 = 0.3$, $\mu_b = 1$, $R/b = 5$. Solid line: $R^2/r^2 - 1$; dashed line: $\Omega^0$.

The efficiency of such compensation may be low. This can be seen, for example, in Fig. 4.7, where the arrangement of the curves and the scale correspond to the choice of CHS parameters: $R/b = 5$, $\mu_0/\mu_b = 0.3/1$. An appreciable effect could be obtained only if the curve $\Omega^0$ were much closer to $R^2/r^2 - 1$. Large $\Omega^0$ are needed for this. More precisely, it is desirable to have larger $\Omega^0 R/b$.

According to Eq. (3.18), for a parabolic profile of $\mu_h$ we have

$$\frac{R}{b}\Omega^0 = \frac{2}{\ell}\omega^0 \left[\frac{\mu_0}{\mu_b}\xi^2 + \frac{3}{4}\left(1 - \frac{\mu_0}{\mu_b}\right)\xi^4\right], \qquad (4.59)$$

where $\ell$ is the multipolarity of the stellarator, $\omega^0$ is the quantity (3.19) describing the "magnetic hill," and $\xi = \rho/b$ is the dimensionless radius in the transverse cross section. Among real installations the Heliotron E has the largest $\omega^0$. But even in this case very large inward displacements would be required to achieve a significant reduction in $|\delta\Omega|$ (see Fig. 4.9).

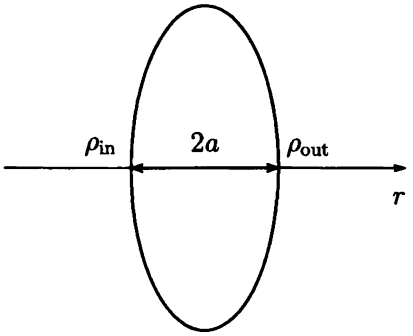


**Fig. 4.8.** The points where the difference in $\Omega$ is taken for the evaluation of the inhomogeneity of $\Omega$ on the magnetic surface.

These reasons are in no way related to the shape of the magnetic surfaces or any plasma characteristic. Hence, it should be a general rule that a large "magnetic hill" [see Eq. (3.11)] and a strong inward shift of the magnetic surface are necessary for the suppression of the Pfirsch–Schlüter current in conventional stellarators. This conclusion follows from the above simple considerations and does not require the solution of an equilibrium problem.

The influence of the magnetic hill and plasma shift on the magnitude of the Pfirsch–Schlüter current has been known about since the formula

$$\bar{j}_\zeta = \frac{2p'(a)}{\mu B_0}\left[1 + B_0^2 V_0''(\Phi)\frac{\Delta}{2}\right]\cos\theta \qquad (4.60)$$

was obtained [137, 139, 144] under the assumption that the magnetic surfaces are circular shifted toroids. Here $\mu$ is the rotational transform, $V_0''(\Phi)$ is the quantity (3.11), $a$ is the minor radius of a magnetic surface, and $\Delta$ and $\theta$ are the shift and poloidal angle from Eq. (3.24) at $K = 1$.

Usually the term with a magnetic hill in Eq. (4.60) is small, and in such cases using Eq. (4.60) does not cause any problems. In particular, the right side of Eq. (3.36) comes from this very

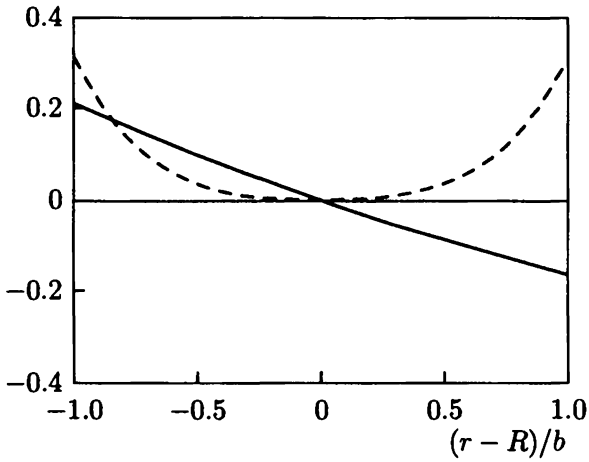


**Fig. 4.9.** Two components of $\Omega$ in a stellarator with Heliotron E parameters: $\mu_0 = 0.5$, $\mu_b = 2.5$, $R/b = 11$. Solid line: $R^2/r^2 - 1$; dashed line: $\Omega^0$.

form of $\bar{j}_\zeta$. However, under "extreme" conditions Eq. (4.60) becomes unreliable.

Indeed, it follows from Eq. (4.60) that for suppression of the Pfirsch–Schlüter current it is necessary to provide [144]

$$B_0^2 V_0''(\Phi)\Delta = -2. \tag{4.61}$$

According to Eqs. (3.10) and (3.11), in an $\ell = 3$ stellarator $V_0''(\Phi) \sim a^2$; therefore, condition (4.61) cannot be fulfilled at the magnetic axis. But then it is impossible to explain the result published by Greene and Johnson back in 1961 [93]: they described the example of an equilibrium configuration in an $\ell = 3$ stellarator without a Pfirsch–Schlüter current.

The result mentioned [93] is unique: for more than 35 years it has neither been confirmed nor refuted. In general, it appeared far from the main stream of stellarator research. Noone made any attempt to explain this extremely unusual numerical result, and so there is nothing strange that the contradiction of

Eq. (4.61) with the unusual prediction of [93] remained unnoticed for a very long time.

The accuracy of Eq. (4.61) was obviously insufficient also for a full explanation of the observed dependence of the plasma shift at finite $\beta$ on the initial conditions in the Heliotron E [240] (Fig. 4.5).

To resolve the contradictions, we should return to the general expression (4.55). The condition of absence of the Pfirsch–Schlüter current is formulated in a general form as

$$\Omega = \Omega(\psi). \tag{4.62}$$

This equality looks simple, but actually it is a rather intricate equation because it is related to the unknown integral characteristic $\psi$. To avoid an integration over magnetic surfaces, instead of Eq. (4.62) we propose to use its differential consequence $\nabla\psi \times \nabla\Omega = 0$, which with account of Eq. (2.84) is transformed into

$$(\mathbf{B}_p + \mathbf{B}^*) \cdot \nabla\Omega = 0. \tag{4.63}$$

Let us assume that this condition is satisfied throughout the whole plasma volume. Then $\bar{j}_\zeta = 0$ everywhere, and, therefore, the poloidal magnetic field $\mathbf{B}_p$ is a purely vacuum field. In the language of equations this appears as follows: in Eq. (2.118) the right-hand side disappears, so that its solution is absolutely independent of the plasma pressure. Then only Eq. (4.63) remains to be solved, where only vacuum fields are present. In such a statement, the problem of complete suppression of the Pfirsch–Schlüter current was considered in [329, 330].

For the given helical field and geometry of installation there remains only one free function in Eq. (4.63), by the choice of which we can try to satisfy Eq. (4.63): the vacuum poloidal field $\mathbf{B}_p$.

For the shift of magnetic surfaces mentioned above, a vertical field is necessary. Thus, as a first step it is natural to consider the simplest case, where $\mathbf{B}_p$ is a uniform vertical field:

$$\mathbf{B}_p = B_\perp \mathbf{e}_z. \tag{4.64}$$

With this field Eq. (4.63) is transformed into

$$\left(B_\perp \mathbf{e}_z + \frac{1}{2\pi}\left[\nabla\psi_V \times \nabla\zeta\right]\right) \cdot \nabla\left(\Omega^0 - 2\frac{\rho}{R}\cos u\right) = 0. \quad (4.65)$$

If $\psi_V = \psi_V(\rho)$, then $\Omega^0 = \Omega^0(\rho)$, so that

$$\left[\nabla\psi_V \times \nabla\zeta\right] \cdot \nabla\Omega^0 = 0, \quad (4.66)$$

and with account of Eq. (3.6) we obtain

$$\frac{1}{2\pi}\left[\nabla\psi_V \times \nabla\zeta\right] \cdot \nabla\Omega = 2B_0\mu_h\frac{\rho}{R^2}\sin u, \quad (4.67)$$

where $\mu_h$, let us recall, is the vacuum rotational transform. With the help of Eq. (3.10) we can also express the term with $B_\perp$ from Eq. (4.65) in a similar form:

$$B_\perp \mathbf{e}_z \cdot \nabla\Omega = B_\perp \mathbf{e}_z \cdot \nabla\Omega^0 = B_\perp \frac{m(\rho^4\mu_h)'}{\ell R^2\rho^2}\sin u. \quad (4.68)$$

In the final account Eq. (4.65) is reduced to

$$2B_0\rho\mu_h + B_\perp\frac{m(\rho^4\mu_h)'}{\ell\rho^2} = 0, \quad (4.69)$$

which can be simply written as $\rho y' + Cy = 0$ with unknown $y = \rho^4\mu_h$.

The solution to Eq. (4.69) is

$$\mu_h = \mu_b\xi^{-(C+4)}, \quad (4.70)$$

where $\xi = \rho/b$, $\mu_b$ is the value of $\mu_h$ at $\rho = b$, and $C = 2\ell B_0/(mB_\perp)$. But such a profile of $\mu_h$ may be unrealizable in real stellarators. Therefore, the existence of the formal solution (4.70) does not yet guarantee the fulfillment of condition (4.63). It is known, however, that in long-period systems ($m\rho/R \ll 1$)

$$\mu_h = \mu_b\xi^{2(\ell-2)}. \quad (4.71)$$

This expression, straightforwardly derived from Eqs. (3.4) and (3.6), coincides with that given by Eq. (4.70) at $C = -2\ell$. Thus, function (4.70) can be considered as a solution of the problem only at

$$B_\perp = -\frac{B_0}{m}. \tag{4.72}$$

Approximation (4.71) is suitable for $\ell = 2$ shearless stellarators and for stellarators with $\ell \geq 3$. Hence, only in such systems may it be possible to achieve complete suppression of the Pfirsch–Schlüter current [329] by the application of a vertical field (4.72).

This surprisingly beautiful and simple result is good, unfortunately, only in theory. The fact is that $B_0/m$ is too large a value for a vertical field. In other words, the vertical field given by (4.72) corresponds to an excessively large shift of the magnetic surfaces. Indeed, substituting (4.72) into Eq. (4.54) gives

$$\frac{\Delta_\perp}{b} = -\frac{1}{\omega^0}, \tag{4.73}$$

where $\omega^0 = \mu_b mb/R$ is the value that determines the "height" of the magnetic hill (see Table 3.1 in Section 3.2). In the Heliotron E, which is characterized by a large value of $\omega^0$, the field (4.72) corresponds to $|\Delta_\perp|/b \simeq 0.2$. Here $\Delta_\perp$, let us recall, is the shift of the outermost magnetic surface, which is restricted in the real installations, at least by the width of the plasma-wall gap. If a shift by 20% of minor radius is still acceptable, although already at the extreme limit of the operational range of the Heliotron E, then 60% or more for the CHS, LHD, and all other installations with $\omega^0 < 2$ is absolutely unrealistic.

These estimates show that an equilibrium state without a Pfirsch–Schlüter current can exist very far from the standard regimes of operation of conventional stellarators. Because of this, suppression of the Pfirsch–Schlüter current has been too weak to be noticed in experiments and calculations for a natural combination of parameters. But two examples of plasma equilibrium with $\bar{j}_\zeta = 0$ are, nevertheless, known [93, 144].

The unusual result already mentioned [93] was obtained numerically for a configuration with the following parameters: $\ell = 3$, $R/b = 16$, $m = 20$, $|B_\perp|/B_0 = 0.05$. At $m = 20$, our formula (4.72) gives the same value of $B_\perp$, which, by the way, does not depend on the aspect ratio. This absolute agreement is remarkable for two reasons. First, until 1996 the result of [93] had not been explained, and formula (4.61) even put it (though, implicitly) in doubt. Second, in [93] a rather complicated problem of plasma equilibrium was solved, whereas our model operates only with a vacuum magnetic field, and all the calculations are elementary.

Let us turn to the second example. According to Eqs. (3.10) and (3.11), in a shearless stellarator $RB_0^2V_0''(\Phi) = 2m\mu$. Equation (4.61) is reduced in this case to

$$\frac{m\Delta}{R} = -\frac{1}{\mu}. \tag{4.74}$$

This is the result obtained by Mikhailov and Shafranov [144]. It does not contradict Eq. (3.36): $\mu\Delta = \text{const}$ and condition (4.61) turn it into an identity. At the plasma boundary the shift $\Delta$ should be subject to the first equality (4.53), so that, finally,

$$\mu\Delta = R\frac{B_\perp}{B_0}. \tag{4.75}$$

Then, apparently, Eq. (4.74) is transformed into Eq. (4.72). Thus, in this particular case our result (4.72) also coincides with the earlier result of [144].

The formally faultless solution (4.74), obtained in two different ways, has, however, a serious latent defect: for a realistic choice of parameters it contradicts the initial assumption $\mu = \text{const}$. Indeed, in a stellarator the shear is small only at $m\rho/R \ll 1$ [see Eq. (3.22)]. Then it should be $m|\Delta|/R \ll 1$ in Eq. (4.74), which could only be possible at $\mu \gg 1$. But in shearless stellarators usually $\mu < 1$, and for $\mu$ of the order of unity the shift $\Delta$ given by Eq. (4.74) displaces the configuration

far beyond the area with $\mu = \text{const}$. In other words, the vertical field (4.72) is unacceptably large.

Actually, all that has been said above means that for typical conditions a vertical field alone is not sufficient for complete suppression of the Pfirsch–Schlüter current (although theoretically it is not forbidden). Because of this it was natural to consider the next problem [330]: whether it might be possible to satisfy condition (4.63) with a smaller vertical field, but with an additional quadrupole field or with poloidal fields of higher multipolarity. The problem was solved by the same scheme as described above, but without restriction (4.64). It appeared that in the general case, also, Eq. (4.63) could be satisfied throughout the operational volume by *only* the vertical field (4.72) and *only* in a stellarator with a rotational transform restricted by Eq. (4.71). If from the very beginning, one considers $\mathbf{B}_p$ arbitrary, only one new solution is added: the shearless stellarator with the same vertical field (4.72), but with an additional current flowing in a ring $R - d$, where

$$d = \frac{R}{m\mu_0}. \tag{4.76}$$

Unfortunately, this solution is doubly unusual: $|B_\perp|$ is too large, and, moreover, $R - d$ is the position of the magnetic axis shifted by the vertical field (4.72). Configurations with conductors placed inside the plasma [331, 332] will, perhaps, sometime become full-fledged members of the fusion family. But for a while we must return to real systems that are not subject to the rigid condition (4.63) with $\mathbf{B}_p$ being a vacuum field.

## 4.5. Integral independence on $\beta$ and "overcompensation"

The discussion in the previous subsection leads to the conclusion that it is impossible to obtain an equilibrium configuration without a Pfirsch–Schlüter current in $\ell = 2$ stellarators with shear. Formally, this means that in such systems Eq. (4.63) can-

not be satisfied everywhere. Indeed, for the parabolic profile of $\mu_h$ (3.6), its consequence (4.69) is transformed into

$$(\mu_b - \mu_0)\left(B_0 + \frac{3m}{\ell}B_\perp\right)\frac{\rho^2}{b^2} + \mu_0\left(B_0 + \frac{2m}{\ell}B_\perp\right) = 0. \quad (4.77)$$

In shearless stellarators $\mu_b = \mu_0$; in $\ell = 3$ systems $\mu_0 = 0$, and then Eq. (4.77) is satisfied at any $\rho$ by the substitution (4.72). But in the most interesting intermediate case at $\ell = 2$ and $\mu_b \neq \mu_0$, condition (4.77) can be fulfilled only at one point along the minor radius:

$$\frac{\rho_0^2}{b^2} = -\frac{\mu_0}{\mu_b - \mu_0}\frac{1 + mB_\perp/B_0}{1 + 1.5mB_\perp/B_0}. \quad (4.78)$$

This solution can be meaningful at $0 \leq \rho_0^2 \leq b^2$, when

$$-1 \leq \frac{mB_\perp}{B_0} \leq -\frac{2\mu_b}{3\mu_b - \mu_0}. \quad (4.79)$$

The right limit in Eq. (4.79) corresponds to $\rho_0 = b$, and the left-hand side to $\rho_0 = 0$. Thus, to obtain $\Omega = \Omega(\psi)$ at the plasma edge in an $\ell = 2$ stellarator with shear a smaller value of $B_\perp$ is required than $B_0/m$. With increasing $|B_\perp|$ the surface where $\Omega = \Omega(\psi)$ moves inside the plasma. On this surface $\bar{j}_\zeta = 0$, and on the left and right sides of this point the Pfirsch–Schlüter current should flow in opposite directions.

To see the change of $\bar{j}_\zeta$ induced by the control vertical field, let us use the model expression (4.60), which can be rewritten in the form

$$\bar{j}_\zeta = j_0 C_{\mathrm{PS}}, \quad (4.80)$$

where

$$j_0 = \frac{2p'(a)}{\mu B_0}\cos\theta \quad (4.81)$$

and $C_{\mathrm{PS}}$ is the multiplier describing the dependence of $\bar{j}_\zeta$ on the shift of the magnetic surface:

$$C_{\mathrm{PS}} = 1 + B_0^2 V_0''(\Phi)\frac{\Delta}{2} = 1 + \frac{m\Delta}{2\ell R}\frac{(a^4\mu_h)'}{a^3}. \quad (4.82)$$

Here $V_0''(\Phi)$ is expressed through $\mu_h$ with the help of Eqs. (3.10) and (3.11).

The ideal case $\bar{j}_\zeta \equiv 0$, which was considered in the previous section, corresponds to $C_{PS} \equiv 0$ in Eq. (4.80). We cannot obtain such a solution for an $\ell = 2$ stellarator with shear, but the even lesser result $|C_{PS}| \ll 1$ would be an appreciable success. At $|C_{PS}| \ll 1$, the Pfirsch–Schlüter current would be suppressed, and the shift $\Delta$ would be determined by the external vertical field only. Then for $C_{PS}$ it would be possible to use the expression [329]

$$C_{PS} = 1 + \frac{1}{2\ell}\left(4 + \frac{a\mu_h'}{\mu_h}\right)\frac{mB_\perp}{B_0}. \tag{4.83}$$

Formally, Eq. (4.83) could be obtained from Eq. (4.82) after substitution of (4.75), which is the solution of Eq. (3.36) with zero right-hand side and with boundary conditions (4.53). But it is necessary to note that both Eq. (4.82) and Eq. (4.75) are not good at $\mu \to 0$, but Eq. (4.83) is already free from this defect. This means that the "good" equality (4.83) can be derived in another, direct way, avoiding the "dangerous" equations (3.36), (4.75), (4.82), and related restrictions.

For shearless ($\mu_h' = 0$) and for $\ell = 3$ ($a\mu_h' = 2\mu_h$) stellarators,

$$C_{PS} = 1 + \frac{mB_\perp}{B_0}. \tag{4.84}$$

This value is a constant over the whole cross section of the plasma column, which decreases with increasing $|B_\perp|$ (at $B_\perp < 0$). Accordingly, the Pfirsch–Schlüter current also decreases, disappearing completely at $mB_\perp = -B_0$.

As can be seen from Eq. (4.83), with the help of a vertical field it is also possible to significantly reduce $C_{PS}$ in a conventional $\ell = 2$ stellarator with shear. But this reduction is radially non-uniform: in the center it is the same as in a shearless stellarator [see Eq. (4.84)], but at the edge it is stronger:

$$C_{PS}(b) = 1 + \left(1 + \frac{\mu_b - \mu_0}{2\mu_b}\right)\frac{mB_\perp}{B_0}. \tag{4.85}$$

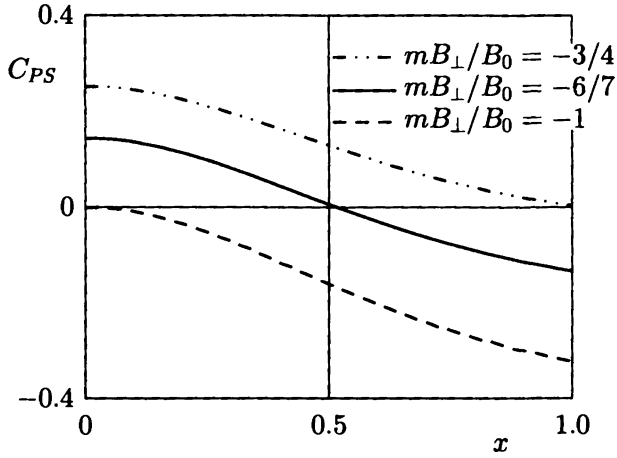


**Fig. 4.10.** Reduction factor for Pfirsch–Schlüter current, $C_{\rm PS}$, in an $\ell = 2$ stellarator with $\mu_0/\mu_b = 1/3$ for different values of $B_\perp/B_0$. The upper curve corresponds to the right-hand end of the interval (4.79), and the lower curve corresponds to the left-hand end. The intermediate solid line corresponds to the choice of $B_\perp$ that makes $C_{\rm PS}$ zero at half of the minor radius.

The value $C_{\rm PS}$ can vanish only at one point along the minor radius, as shown in Fig. 4.10 for $B_\perp$ from the interval (4.79). Most easily $C_{\rm PS} = 0$ can be obtained at the edge of the plasma. But larger $|B_\perp|$ are necessary to turn $C_{\rm PS}$ into zero inside the plasma. Moving a point with $C_{\rm PS} = 0$ toward the plasma center, we obtain an interesting situation: at the left of this point $C_{\rm PS}$ is positive, but at the right it is negative. Thus, together with a reduction of the Pfirsch–Schlüter current, which is simply described by the reduction of $|C_{\rm PS}|$, it is possible, theoretically, to obtain an inversion of the phase of $\bar{j}_\zeta$ somewhere inside the plasma. At much larger $|B_\perp|$ something completely strange happens: $C_{\rm PS}$ becomes negative everywhere, which means a complete change in the direction of the Pfirsch–Schlüter current to the opposite.

In real devices the allowable limits of variation of $B_\perp$ are determined by the value of the admissible plasma shift, which is related to $B_\perp$ by the equality (4.75) with $\mu = \mu_b$. In the family of conventional stellarators, the Heliotron E appears to be the only device where it may be possible to appreciably affect the Pfirsch–Schlüter current with the help of a vertical field (which manifests itself in the fact that both curves on the left side of the vertical axis in Fig. 4.9 are close to each other). The experimentally observed strong reduction of $\Delta_\beta$ for a large initial inward plasma shift [240] (Fig. 4.5), is the consequence of just such a suppression of $\bar{j}_\zeta$.

Qualitatively this conclusion may seem obvious. Therefore, we would like to emphasize that here we are discussing the quantitative characteristics of the effect that for the first time displayed itself so vividly and unexpectedly in experiments in the Heliotron E [240].

The Pfirsch–Schlüter current is the reason for the change of magnetic configuration (see Fig. 4.6), but the observable and practically meaningful characteristic is, after all, the shift $\Delta_\beta$. It is determined by the equality

$$\frac{\Delta_\beta}{b} = -\frac{\beta_0}{2\beta_{\rm eq}^0} \int_0^b \frac{p'(a)}{p_0} \frac{\mu_b}{\mu(a)} \frac{a^2}{b^2} C_{\rm PS}\, da, \qquad (4.86)$$

which differs from Eq. (4.53) in that the multiplier $C_{\rm PS}$, which is close to unity under normal conditions, is added into the integrand.

The reduction of $\bar{j}_\zeta$ and $\Delta_\beta$ is described by the same function $C_{\rm PS}$. The tendency "the greater the $|B_\perp|$, the lesser the $\Delta_\beta$" in Fig. 4.5 is a direct consequence of the dependence (4.83).

At first $C_{\rm PS}$ simply decreases with increasing intensity of the negative field $B_\perp$. But, as soon as $B_\perp$ falls into the interval (4.79), a new quality appears: the function $C_{\rm PS}$ becomes alternating. Therefore, it is possible to imagine a situation where integral (4.86) becomes zero. Then $\Delta_\beta = 0$ irrespective of $\beta$.

Since $\bar{j}_\zeta \not\equiv 0$, such an equilibrium can be called integrally independent of $\beta$.

At much larger $|B_\perp|$ the quantity $C_{PS}$ becomes negative, but $|C_{PS}|$ grows, which means amplification of the Pfirsch–Schlüter current (the regime of "overcompensation"). However, at $C_{PS} < 0$ it should flow "back" [see Eq. (4.80)], and expression (4.86) should change its sign. But this would mean that under these conditions the plasma column should move inward with increasing $\beta$.

These two predictions [329], of the integral independence of $\beta$ and of the complete reverse of the Pfirsch–Schlüter current, look fantastic. At the same time, the estimates of [329, 330] showed that only a small step remained to be done in experiments [240] in the Heliotron E (Fig. 4.5), to observe these effects: it was necessary to increase the control vertical field just a little. Though unusually large values of $|B_\perp|$ had already been discussed, this proposal was realized [333], and experimental results confirmed the expectations (Fig. 4.11). The vacuum configuration, in which the equilibrium was found to be integrally independent of $\beta$, is shown in Fig. 4.12. When it was shifted inward by 1 cm more, on increasing $\beta$ the plasma column moved not outward, as always happens in toroidal systems, but inward (Fig. 4.11).

These unique results are interesting for many reasons. It is enough to note that this is the first demonstration of a beautiful new effect. Moreover, this is direct and convincing confirmation of the reliability of the predictions of the MHD theory of plasma equilibrium. Finally, they show that too large a price would be paid to obtain configurations with a significantly lowered Pfirsch–Schlüter current in conventional stellarators.

In configurations with small $\bar{j}_\zeta$ the equilibrium limit $\beta_{eq}$ is very high, which is their main advantage. But it is well known that both necessary conditions, the large magnetic hill and the strong inward plasma shift, are absolutely unacceptable, since they make equilibrium unstable at very low $\beta$ (see, for example, [159]). For this reason, the area of parameters where an

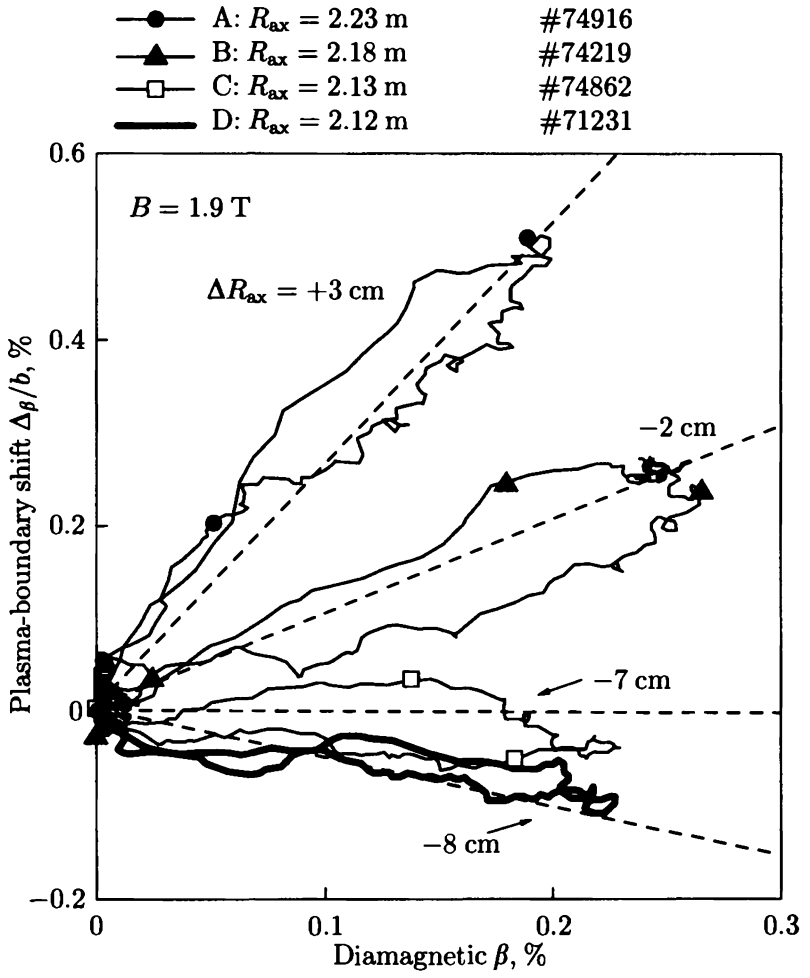


**Fig. 4.11.** Measured finite-pressure-induced plasma boundary shift for various initial positions of the vacuum magnetic axis in the Heliotron E: at $R_{ax}$ = 223 cm (vacuum axis is shifted outward by 3 cm from the geometrical axis $R$ = 220 cm); in a configuration with small inward shift, $R_{ax}$ = 218 cm; in deeply inward shifted configurations with $R_{ax}$ = 213 cm and $R_{ax}$ = 212 cm. Each curve represents one plasma shot, as shown above. Dashed lines are the linear approximation of the measured $\Delta_{ax}$ [333].

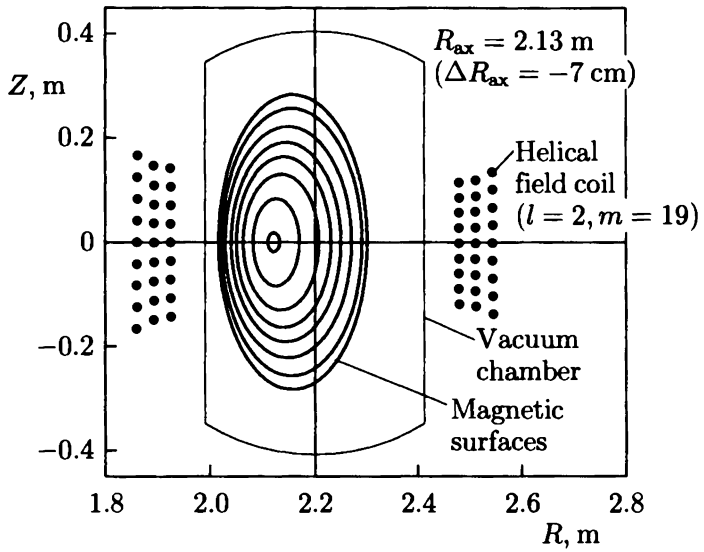


**Fig. 4.12.** Magnetic configuration of Heliotron E at $R_{ax} = 213\,\text{cm}$, $\beta = 0$, which appeared to be integrally independent of $\beta$ at finite plasma pressure.

appreciable suppression of the Pfirsch–Schlüter current can be attained always remained far from the area of search and optimization.

Only one unique example is known [137] where strange behavior of the shift $\Delta_\beta$, similar to that described above, was observed in calculations. It was a numerical simulation of an $\ell = 2$ stellarator with a rather unusual choice of parameters: $R/b = 100$, $m = 100$. It was recently shown [329] that the value of the vertical field calculated by (4.86) at which $\Delta_\beta$ becomes zero coincides with a result described in [137]. Thus, the analytical theory, numerical calculations and experiment appeared in complete harmony. Analytics, as it is supposed to do, has played a uniting role here. Moreover, what is beyond the expectations for plasma physics, its explanations and predictions have appeared to be exact even quantitatively.

Increasing $\beta$ remains one of the main problems of the MHD theory of toroidal systems. Plasma-position control with a vertical field, as was explained in Section 4.3, is a necessary step, but, probably, insufficient. Stronger inward "pushing" of the plasma, as in experiments in the Heliotron E [240, 333], could theoretically give a significant gain in $\beta_{eq}$, but it is accompanied by a dramatic loss of stability. Because of this, such strongly shifted inward configurations can only be of academic interest. But for real optimization of stellarator plasma the position control should be supplemented by the control of the plasma shape.

# 5. The influence of a quadrupole field on the stellarator configuration

## 5.1. Control of the vacuum stellarator configuration using a quadrupole field

We have discussed the problem of control of the plasma column position in stellarators using a vertical field. The next important problem is plasma-shape control. For stellarators, this is still an undeveloped area, but in tokamaks control of the plasma's shape long ago became standard practice. The advantages of a noncircular plasma shape in tokamaks are generally recognized. This is a sufficient reason for the question: what will happen if the plasma cross section in stellarators is made on average noncircular as in tokamaks?

The main characteristic of the plasma shape is its elongation, the ratio of the vertical to the horizontal dimensions. If the boundary cross section is not an ellipse, but, say, D-shaped, additional parameters are necessary for its description: triangularity, etc. The complete optimization of stellarators with respect to the plasma's shape is still a task for the future. As a first step in this direction, we have to ascertain how the equilibrium characteristics of a stellarator plasma would be influenced by its elongation.

Typical values for the plasma-column elongation $K_b$ in tokamaks are 1.5–1.7. This is quite a normal range and it cannot be called large for a tokamak. It is enough to recall, for example, that the ITER tokamak project aims for a plasma with $K_b = 2$ [334]. Such "moderate" and maybe even larger values of $K_b$ seemed attractive, according to estimates of [245, 267], for stellarators also.

However, as we mentioned in the first section, attempts to calculate stellarator equilibrium configurations numerically with $K_b$ of the order of 1.5 failed unexpectedly, although with exactly the same formulation of the problem for a tokamak no difficulty arose. We could easily calculate stellarator equilibria either at $K_b = 1$ [159] or for elongated plasmas when we moved from $K_b = 1$ to somewhat larger elongations by small steps [250]. But then we found an interesting effect: the small increase in $K_b$ was accompanied by a much stronger elongation of the magnetic surfaces in the center of the plasma [250]. As a result, even at $K_b = 1.2-1.3$ the elongation of the near-axis magnetic surfaces became so large that the moment method [254] did not allow the calculations to continue.

The effect of a sharp increase of elongation of the near-axis surfaces in stellarators was not related to the value of $\beta$. Therefore, in order to understand what happened with the $K_b$ increase, it should be sufficient to consider a vacuum configuration. Such an analysis [256] showed that in stellarators with shear the elongation of the magnetic surfaces above some critical level leads to the splitting of the magnetic axis and the emergence of the internal separatrix. This was precisely the reason why we could not advance [250] to $K_b \sim 1.5$: the numerical code allowed the calculation of only one-axial configurations.

It is highly natural to begin the discussion of the problem of plasma-shape control in stellarators with the question of how the vacuum magnetic configuration of a stellarator is changed when its outermost magnetic surface is elongated vertically under the action of the external field.

To elongate the plasma column in tokamaks and stellarators, one needs a quadrupole magnetic field

$$\mathbf{B}_q = -\frac{B_2}{2b}\left[\nabla(\rho^2 \cos 2u) \times \mathbf{e}_\zeta\right]. \tag{5.1}$$

Here $B_2$ is the strength of the field $\mathbf{B}_q$ at a distance $b$ from the axis $\rho = 0$. According to Eq. (2.33), the function $\psi$ describing the averaged magnetic surfaces in a stellarator is a sum of two poloidal magnetic fluxes: the flux $\psi_V$ of the helical field and the flux of the axially symmetric (nonoscillating in $\zeta$) field. Hence, in stellarators with $\psi_V = \psi_V(\rho)$ and a parabolic profile of $\mu_h$ in the presence of the quadrupole field $\mathbf{B}_q$ we have

$$\psi = -\pi B_0 \rho^2 \left[\mu_0 + (\mu_b - \mu_0)\frac{\rho^2}{2b^2} + A\frac{B_2}{B_0}\cos 2u\right]. \tag{5.2}$$

Here $A = R/b$ is the aspect ratio. Expression (5.2), which differs from Eq. (4.35) by the additional term with $B_2$, is valid for vacuum configurations of $\ell = 2$ or $\ell = 3$ stellarators. As will be clearly seen later, the effects we are looking for are not associated with toroidicity; therefore, we have neglected toroidal corrections in Eqs. (5.1) and (5.2).

At $B_2 = 0$, the surfaces $\psi = \text{const}$ are circular. Under the action of the quadrupole field (5.1) they become elongated (Fig. 5.1a, b). In shearless stellarators ($\mu_b = \mu_0$) at $B_2 < B_2^{\text{cr}}$, where

$$B_2^{\text{cr}} = \mu_0 \frac{B_0}{A}, \tag{5.3}$$

the surfaces $\psi = \text{const}$ are nested ellipses with an identical semiaxis ratio

$$K_0 = \left[\frac{1 + B_2/B_2^{\text{cr}}}{1 - B_2/B_2^{\text{cr}}}\right]^{1/2}. \tag{5.4}$$

In stellarators with shear, as can be seen from Eq. (5.2), the influence of the quadrupole field is stronger at the axis and weaker at the periphery, where the role of the second term in the brackets

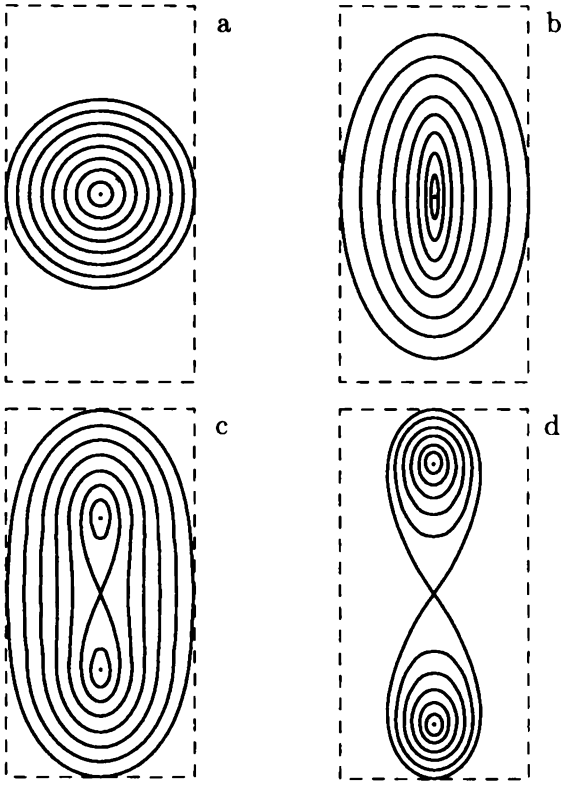


**Fig. 5.1.** Cross sections of the averaged magnetic surfaces in $\ell = 2$ stellarators with a quadrupole field, $\mu_0/\mu_b = 1/3$: a) $B_2 = 0$; b) $B_2 = 0.95B_2^{\rm cr}$; c) $B_2 = 1.35B_2^{\rm cr}$; d) $B_2 = 2B_2^{\rm cr}$. The dashed line is a rectangle with a 1:2 width–height ratio.

[...] is significant. In this case, the quantity $K_0$ is the elongation of the near-axis surfaces.

At $B_2 < B_2^{\rm cr}$, the surfaces $\psi = \text{const}$ remain singly connected (one-axial) up to $K_0 \to \infty$. At $B_2 > B_2^{\rm cr}$, the axis $\rho = 0$ becomes hyperbolic: the lines $\psi = \text{const}$ are not closed in its vicinity. In shearless stellarators, where $\psi_V \sim \rho^2$, no nested surfaces would then remain at all. But in stellarators with shear $\psi_V$ increases faster than $\rho^2$. Because of this, the lines $\psi = \text{const}$,

which the field (5.1) tends to draw away from the axis $\rho = 0$, close up on themselves in the region where the increase in $\psi_V$ becomes stronger than that of the term with $B_2$ in Eq. (5.2). As a result, a configuration with a separatrix like a figure eight is formed (Fig. 5.1c, d).

It is interesting that at the approach to the critical point with $K_0 = \infty$ the elongation of the outer surfaces in stellarators with shear can be quite small.

Indeed, at $B_2 = B_2^{\rm cr}$ the horizontal ($u = 0$) and vertical ($u = \pi/2$) semi-axes $l_x$, $l_z$ of the contour $\psi = \text{const}$ are related by the relationship

$$l_x^2 \left[ 2\mu_0 + (\mu_b - \mu_0) \frac{l_x^2}{2b^2} \right] = (\mu_b - \mu_0) \frac{l_z^4}{2b^2}. \tag{5.5}$$

From this it follows that in this case the elongation $K_b$ of the surface with $l_x = b$, which we shall call the boundary surface, is equal to a value $E$ such that

$$E^4 = 1 + \frac{4\mu_0}{\mu_b - \mu_0}. \tag{5.6}$$

This may be called the critical or limiting elongation: at $K_b < E$ the configuration remains singly connected, whereas at $K_b > E$ a doublet-like structure appears with a two-petal rosette in the center encircled by elongated nested magnetic surfaces (see Fig. 5.1 c, d).

In $\ell = 3$ stellarators, $\mu_0 = 0$ and, accordingly $B_2^{\rm cr} = 0$, $E = 1$. Formally, it then follows that the near-axis magnetic surfaces in such stellarators must be split, turning into the "figures eight" under the action of a vanishingly small quadrupole field. This is the manifestation of the topological instability of the central region in $\ell = 3$ systems, and of their inability to resist external perturbations. The other manifestation of this instability is the splitting of the axis and the formation of an internal separatrix in $\ell = 3$ stellarators owing to their toroidicity [16, 17, 22, 257, 258].

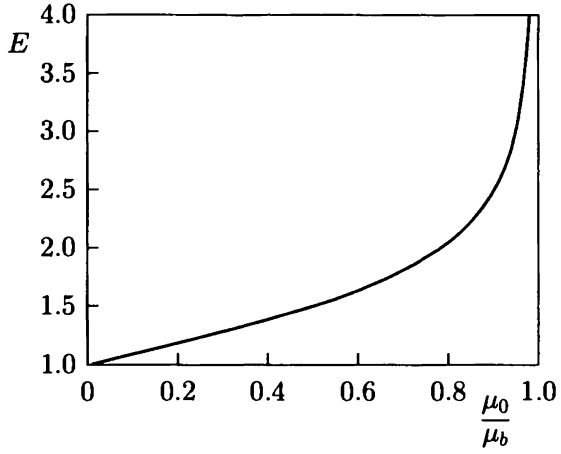


**Fig. 5.2.** Critical elongation in conventional stellarators.

Two-turn ($\ell = 2$) stellarators are better in this respect. The non-zero value of $\mu_0$ makes them more stable topologically, which is a rather important argument in their favor when they are compared with $\ell = 3$ systems [48, 76].

At ratios of $\mu_0/\mu_b$ typical for stellarators, the critical ellipticity $E$ is not large (Fig. 5.2). In the ATF and CHS, for example, $\mu_0/\mu_b \simeq 0.3/1$, and $E \simeq 1.3$. Single-axis configurations with large elongations of the cross section may be obtained only in stellarators with a very small shear: $E \geq 3$ at $\mu_b/\mu_0 \leq 1.05$.

A doublet-like separatrix in the center of a plasma is undesirable, as well as the "usual" magnetic islands at a finite distance from the axis. In both cases, the effective transverse size of the confining volume becomes smaller. Because of this, the problem of suppression of the internal separatrix was rather critical for $\ell = 3$ stellarators [22, 258]. In our case, the condition that the separatrix be absent is reduced to $B_2 < B_2^{\rm cr}$ or $K_b < E$. At the same time, the larger the $K_b$, the higher the $\beta_{\rm eq}$ (this will be discussed in Section 5.4). If working near a limit $E$, high accuracy is necessary in the plasma-shape control, because even a small

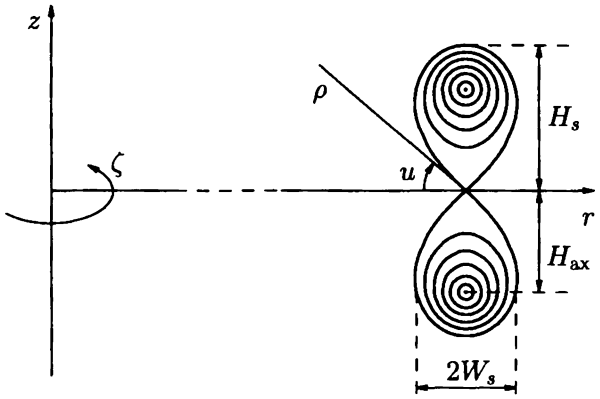


**Fig. 5.3.** Doublet-like magnetic structure in a stellarator with a quadrupole field. Coordinates and main geometric symbols used.

excess in $K_b$ of the value $E$ results in significant readjusting of the magnetic surfaces in the central area.

This is due to the fact that the dimensions of the "figure eight" appearing in a stellarator with shear at $B_2 > B_2^{cr}$ increase rather rapidly with increasing $K_b$. On the separatrix, $\psi = 0$. Given this condition, it is easy to obtain from Eq. (5.2) the height $H_s$ of the separatrix "petal" ($2H_s$ is its full vertical size [see Fig. 5.3]):

$$H_s = b\sqrt{\frac{2}{\mu_b/\mu_0 - 1}\frac{B_2 - B_2^{cr}}{B_2^{cr}}} = b\sqrt{\frac{K_b^4 - E^4}{K_b^2 + 1}}. \qquad (5.7)$$

From this it follows that in a stellarator with $\mu_b/\mu_0 = 3$ (as the ATF or CHS) the separatrix height can already be equal to half of the minor radius, $H_s = 0.5b$, at only $B_2 = 1.25B_2^{cr}$. The dependence (5.7) is shown in Fig. 5.4.

Magnetic fields of higher multipolarity than quadrupole may affect only the outer part of the stellarator plasma column. But a quadrupole field, as can be seen from Eq. (5.2), "penetrates" up to the axis. Hence it turns out to be as strong a

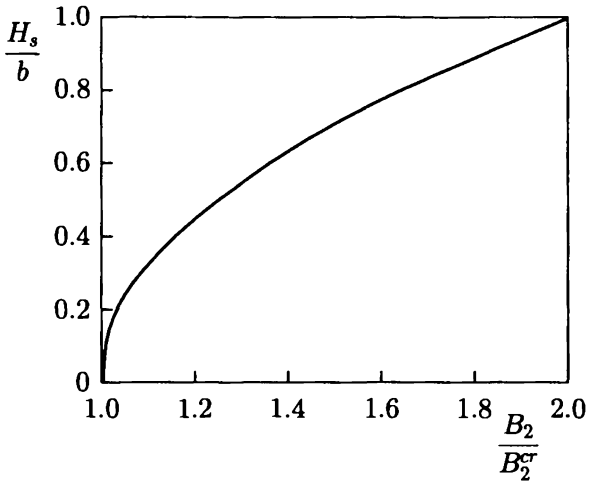


**Fig. 5.4.** Dependence of the height of the doublet-like separatrix on the control quadrupole field in a stellarator with $\mu_0/\mu_b = 1/3$.

means of plasma control in stellarators as the dipole (vertical) field $B_\perp$ (see the previous section).

In the presence of shear, the quadrupole field most strongly affects the near-axis region of a stellarator. On the contrary, in a tokamak the center of the plasma reacts weakly to boundary elongation. This difference is caused by the fact that in stellarators $\mu$ is minimal at the center, whereas in tokamaks the minimum is at the boundary.

The possibility of strong elongation of the magnetic surfaces in the center of the stellarator configuration for moderate deformation of the boundary is a fact of principal importance. Owing to this property, it is possible to control the rotational-transform profile easily and to get an appreciable gain in $\beta_{eq}$ in one-axial configurations in stellarators with shear. This will be discussed in detail later in Sections 5.3 and 5.4. But let us now discuss the more exotic doublet configurations.

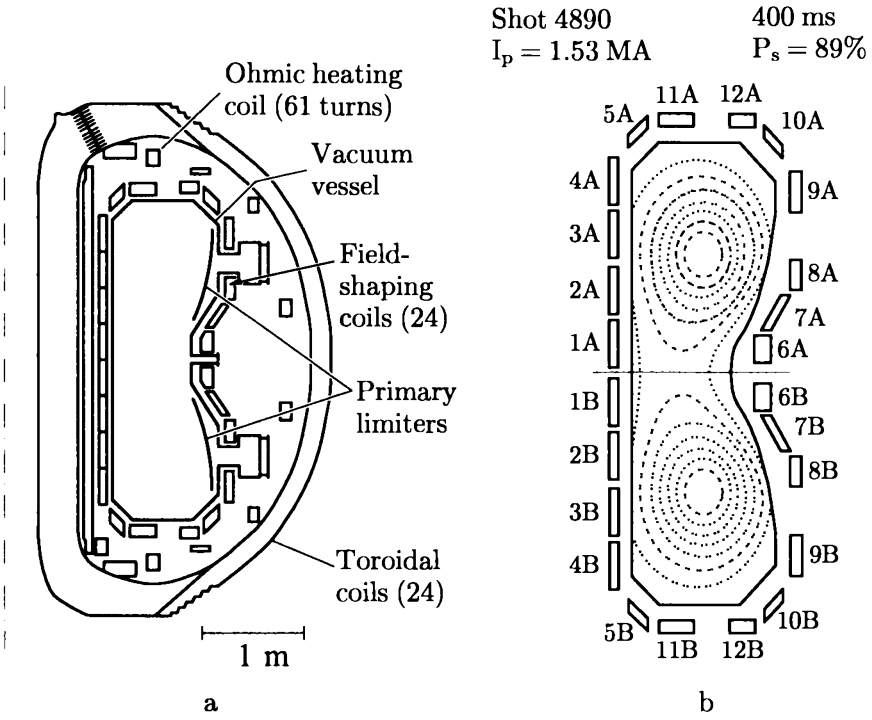


**Fig. 5.5.** Doublet III. (a) Vacuum chamber and magnetic system; (b) typical doublet configuration. Presented by T. Ohkawa at the 9th European Conference on Controlled Fusion and Plasma Physics, Oxford (1979), pp. 321–327.

## 5.2. Doublet-like stellarator configurations

The configurations with a figure-eight separatrix, formed under the action of a quadrupole field in stellarators with shear, look similar to the "doublets" that have been studied for many years in the tokamaks of the Doublet series (Fig. 5.5) [199–202, 259]. If so, it might be worth trying to use the fast growth of the separatrix (5.7) with increasing $B_2$ as an advantage for the creation of doublet configurations in stellarators. It was mentioned in the first section that once a device based on a stellarator with $\ell = 7-9$ (Doublestar) [248] (Fig. 5.6), had already been pro-

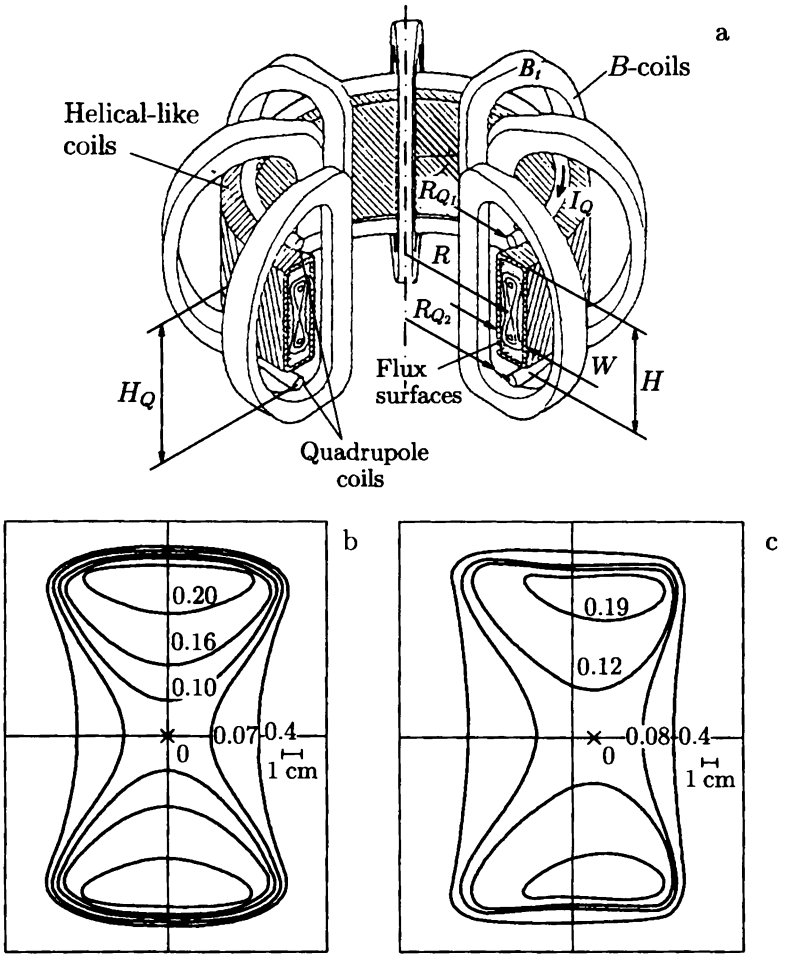


**Fig. 5.6.** Schematic view of a Doublestar stellarator (a) and computed averaged magnetic surfaces (b), (c) for $\ell = 7$ [248]. The numbers on the curves in (b) and (c) are the values of the rotational transform.

posed for the formation of doublet-like configurations. It was shown above that similar triaxial configurations can also be created in conventional stellarators with $\ell = 2$ or $\ell = 3$. What is the difference between them, which of them is better and why,

and how much the doublet-like configurations in stellarators are better in comparison with "tokamak" doublets will all be discussed here.

According to Eq. (5.7), because of the strong dependence of $H_s$ on $B_2$ (at $B_2$ close to $B_2^{cr}$) in stellarators with shear, it is possible to stretch the "figure eight" up to large sizes. In stellarators with $\mu_b/\mu_0 = 3$, for example, a doublet with $H_s = b$ can be produced by a quadrupole field with only $B_2 = 2B_2^{cr}$. The value $B_2^{cr}$ determined by formula (5.3) can itself be relatively small: at $\mu_0 = 0.3$ and $A = 6$ it is only 5% of $B_0$. So, $B_2$ of the order of $2B_2^{cr}$ is quite realistic, and not a large value.

Thus, taking the usual $\ell = 2$ stellarator (or torsatron) as a basis and equipping it with a poloidal field coil system capable of producing a quadrupole field, then varying $B_2$ over the range from zero up to

$$B_2^{max} = \frac{\mu_b/\mu_0 + 1}{2} B_2^{cr} = \frac{\mu_0 + \mu_b}{2} \frac{B_0}{A}, \tag{5.8}$$

it could be possible to obtain configurations of four types [261]: with the usual stellarator geometry at $B_2 = 0$, an elongated one-axial configuration at $B_2 < B_2^{cr}$, an elongated configuration with a small internal separatrix at $B_2$ slightly larger than $B_2^{cr}$, and a doublet-like configuration at $B_2$ of the order of $B_2^{max}$. Figure 5.1 shows all four types of configuration that could be created in such an $\ell = 2$ stellarator with $\mu_b/\mu_0 = 3$.

It should be noted that the construction of the vacuum chamber and magnetic system of the ATF, which was one of the best stellarators of the last generation, allowed operation with $K_b$ even larger than $E$ (see [41, 45]). This gave an opportunity for experimental study of stellarator configurations of three of the types mentioned above, up to configurations with an internal separatrix as shown in Fig. 5.1c. Therefore, a discussion of doublet-like configurations in stellarators is not so far from reality, though now after the termination of experiments with doublets in Doublet devices and after the shut-down of the ATF they remain for the time being the object of theoretical study only.

After many years of operation with doublets in Doublet devices, the program was switched to experiments with one-axial plasma discharges, because it was very difficult to create and sustain doublets in a tokamak. All problems originated from it not being possible to control the currents in the plasma properly, whose fields took an equal part with the external magnetic field in the doublet formation. The doublets created in the Doublet were unstable: the plasma either got divided into two "normal" tokamak columns, or the two halves of the doublet displayed a tendency to merge into a one-axial column. But in stellarators the desired magnetic geometry is produced by external currents only, which is their main advantage. The problem mentioned would simply be absent in stellarators: the creation and sustainment of the necessary magnetic configuration is a completely controllable process.

The doublet configurations produced in stellarators look very similar to tokamak doublets (see Figs. 5.1 and 5.5). Much in common between them is also discovered in a more detailed comparison. The hyperbolic axis of the stellarator doublet (the node of the "figure eight") is the closed field line. This means that the rotational transform on the separatrix is absent. But it is a finite value at the magnetic axis inside the "petal" of the separatrix. Thus, the rotational transform in singly connected one-axial regions divided by the separatrix decreases with distance from the magnetic axis. For stellarators this is quite atypical: the rotational transform $\mu(a)$ in these systems is an increasing function of the radius or, in the extreme case, a constant. The decrease of $\mu(a)$ from the axis toward the boundary is a characteristic feature of tokamaks. It turns out that a configuration with the geometry of a tokamak doublet and with decreasing profile of $\mu(a)$, as in tokamaks, can also be created in a stellarator with a quadrupole field.

Whether $\mu(a)$ is a decaying or growing function of the radius, is significant for plasma stability. It is known that the ballooning modes, whose instability, according to theory [253], limits the growth of $\beta$ in tokamaks ($\mu' < 0$), are not so dan-

gerous in stellarators with $\mu' > 0$ [141, 160]. In our case, at $B_2 < B_2^{\rm cr}$ we have $\mu' > 0$, but at $B_2 > B_2^{\rm cr}$ in the "petals" of the separatrix $\mu' < 0$. Because of this, stellarators with a changeable geometry of the magnetic field, in which it could be possible to obtain all four types of configurations shown in Fig. 5.1 with a transition from positive to negative shear $a\mu'/\mu$, might be interesting for study of the influence of positive and negative shear on plasma stability.

The value of negative shear in singly connected regions inside the separatrix can be evaluated analytically. As follows from Eq. (5.2), the elliptical points (magnetic axes) of the curves $\psi = \text{const}$ lie at a height

$$H_{\rm ax} = \frac{H_s}{\sqrt{2}} = b\sqrt{\frac{1}{\mu_b/\mu_0 - 1}\frac{B_2 - B_2^{\rm cr}}{B_2^{\rm cr}}} \tag{5.9}$$

from the geometrical axis $\rho_0$. Making a transition to coordinates $x, y$ connected with the magnetic axis,

$$x = \rho\cos u, \quad y = \rho\sin u \pm H_{\rm ax}, \tag{5.10}$$

we obtain from Eq. (5.2) an expression for $\psi$ convenient for the analysis of near-axis regions:

$$\begin{aligned}\psi(\rho,u) =& \psi\Big(H_{\rm ax}, \pm\frac{\pi}{2}\Big) - 2\pi A\left[y^2(B_2 - B_2^{\rm cr}) + x^2 B_2\right] \\ &- \pi B_0(\mu_b - \mu_0)\frac{x^2+y^2}{2b^2}\Big(x^2 + y^2 \pm 4H_{\rm ax}y\Big).\end{aligned} \tag{5.11}$$

We have used here a consequence of Eq. (5.9):

$$(\mu_b - \mu_0)\frac{H_{\rm ax}^2}{b^2} = A\frac{B_2}{B_0} - \mu_0. \tag{5.12}$$

It follows from Eq. (5.11) that near the magnetic axis ($x = 0$, $y = 0$) the surfaces $\psi = \text{const}$ are ellipses with elongation (ratio of semi-axes)

$$K_{\rm ax} = \sqrt{\frac{B_2}{B_2 - B_2^{\rm cr}}}. \tag{5.13}$$

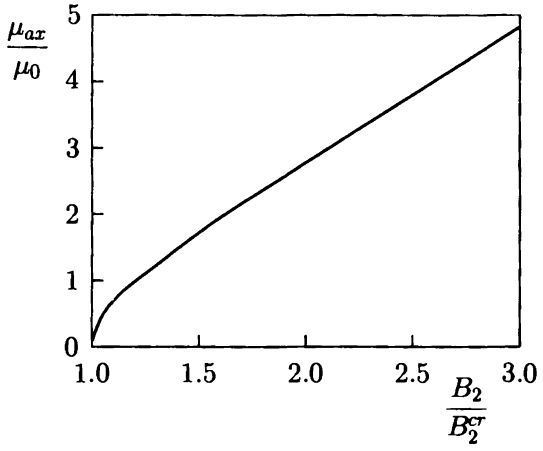


**Fig. 5.7.** Rotational transform at the axis of the stellarator doublet as a function of the control quadrupole field ($\mu_0/\mu_b = 1/3$).

In this geometry, the rotational transform at the axis, $\mu_{ax}$, is calculated using the formula

$$\mu_{ax} = -\frac{1}{2\pi B_0 x K_{ax}} \frac{d\psi(x, y=0)}{dx}. \tag{5.14}$$

With the help of Eq. (5.11) we obtain

$$\mu_{ax} = 2\mu_0 \frac{B_2}{B_2^{cr}} \sqrt{\frac{B_2 - B_2^{cr}}{B_2}} = 2A \frac{B_2}{B_0} \sqrt{\frac{B_2 - B_2^{cr}}{B_2}}. \tag{5.15}$$

Let us recall that here $\mu_0$ is the rotational transform at the magnetic axis of the initial one-axial configuration ($B_2 = 0$), (Fig. 5.1).

The dependence (5.15) of the rotational transform $\mu_{ax}$ at the doublet axis on $B_2$ is shown in Fig. 5.7. At $B_2 = 2B_2^{cr}$, which corresponds to Fig. 5.1d, $\mu_{ax}/\mu_0 \cong 3$. At the usual value for stellarators $\mu_0 = 0.3 - 0.5$, the value $\mu_{ax}$ is of the order of 1–1.5 in this case. These are very good values. If we recall that $\mu = 0$ on the separatrix, they give the total drop of the

rotational transform inside the "petal" of stellarator doublets. In conventional stellarators, $\Delta\mu = \mu_b - \mu_0$ is about half this. Thus, it is possible to obtain a large shear in stellarator doublets, 2–3 times larger than in typical configurations, at quite moderate values of $B_2$.

The comparison of stellarator doublets with those in tokamaks also leads to favorable conclusions. In the Doublet III tokamak operating with triaxial configurations, the typical value was $\mu_{ax} = 1.25$ [259]. But in the example considered above, in the stellarator doublet configuration $\mu_{ax} = 1-1.5$, which is not in the least inferior to the tokamak value.

The expressions derived allow easy comparison of the characteristics of doublets produced with the help of a control quadrupole field in $\ell = 2$ and $\ell = 3$ stellarators. Simply note that in $\ell = 3$ stellarators $\mu_0 = 0$ and, accordingly, $B_2^{cr} = 0$.

It follows from Eqs. (5.11) and (5.13) that in an $\ell = 2$ stellarator the near-axis magnetic surfaces of the doublets are ellipses, whose elongation decreases with increasing $B_2$. But at $B_2 = 2B_2^{cr}$ it is still quite appreciable: $K_{ax} = \sqrt{2}$. In $\ell = 3$ stellarators, the near-axis surfaces in doublets are always circular, more resembling the doublets in tokamaks [259].

Now let us compare the doublets in $\ell = 2$ and $\ell = 3$ stellarators with triaxial configurations in more the exotic Doublestar systems [248] with helical fields of higher multipolarity. Wang and Jensen carried out numerical calculations [248] for $\ell = 7-9$, but analytically we can consider the stellarator doublets at any $\ell$, since the principle of their description is already clear.

According to Eq. (2.33), in a stellarator with a quadrupole field (5.1) we have

$$\psi = \psi_V - \pi A B_2 \rho^2 \cos 2u. \tag{5.16}$$

For a parabolic profile of $\mu_h$ we would obtain Eq. (5.2) from here. But for stellarators with $\ell \geq 3$ we should approximate $\mu_h(\rho)$ by another dependence:

$$\mu_h = \mu_b \left(\frac{\rho}{b}\right)^{2(\ell-2)}, \tag{5.17}$$

where $\mu_b$ is the value of $\mu_h$ at $\rho = b$. The function $\psi_V$ in Eq. (5.16) is related to $\mu_h(\rho)$ by relationship (3.12). Substituting the explicit expression of $\psi_V$ into Eq. (5.16), we obtain the equation for the magnetic surfaces $\psi = \text{const}$ :

$$a \equiv -\frac{\ell-1}{\pi b^2 B_0 \mu_b}\psi = \xi^2\left[\xi^{2(\ell-2)} + h_s^{2(\ell-2)}\cos 2u\right] = \text{const}, \tag{5.18}$$

where $\xi = \rho/b$ is the dimensionless minor radius and

$$h_s^{2(\ell-2)} \equiv \frac{\ell-1}{\mu_b} A \frac{B_2}{B_0}. \tag{5.19}$$

At $B_2 \neq 0$, Eq. (5.18) describes three families of magnetic surfaces, divided by a figure-eight separatrix. On the separatrix, whose node lies at the coordinate axis, $a = 0$. Therefore, as can be seen from Eq. (5.18), $h_s$ is the height of the separatrix expressed in units of $\xi$ ($H_s = bh_s$). Its dimensions grow quickly with an increase in the control quadrupole field. The height $H_s$ reaches the value $b$ (accordingly, $h_s = 1$) at $B_2$ equal to

$$B_2^{\max} = \frac{\mu_b}{\ell-1}\frac{B_0}{A}. \tag{5.20}$$

This is the "extrapolation" of relationship (5.8) to the area $\ell > 3$. At values of $\mu_b$ and $A$ typical for stellarators, the value of $B_2^{\max}$ is not large.

Let us consider the internal area of the doublets described by Eq. (5.18). There are two families of nested surfaces inside the separatrix with magnetic axes located at a distance

$$H_{\text{ax}} = bh_s\left(\frac{1}{\ell-1}\right)^{\frac{1}{2(\ell-2)}} = b\left(\frac{A}{\mu_b}\frac{B_2}{B_0}\right)^{\frac{1}{2(\ell-2)}} = b\left(\frac{B_2}{B^*}\right)^{\frac{1}{2(\ell-2)}} \tag{5.21}$$

from the geometrical axis of the stellarator. Here $B^*$ is the "effective" poloidal field defined by expression (4.47).

In the vicinity of the magnetic axis, the function $a$ (5.18) can be represented as

$$a = a_{\rm ax} + 2\frac{x^2 + (\ell - 2)y^2}{b^2} h_s^{2(\ell-2)} + \cdots, \qquad (5.22)$$

where $a_{\rm ax}$ is a constant and $x$ and $y$ are coordinates attached to the magnetic axis [see Eq. (5.10)]. At $\ell = 3$, the near-axis magnetic surfaces $a = {\rm const}$ are circular (which can also be seen from Eq. (5.11), since Eqs. (5.22) and (5.11) are equivalent at $\ell = 3$). But in stellarators with a helical field of higher multipolarity the surfaces $a = {\rm const}$ are oblate ellipses with a ratio of semi-axes

$$l_x/l_y = \sqrt{\ell - 2}. \qquad (5.23)$$

According to Eq. (5.23), in a stellarator with $\ell = 7$ we would have $l_x/l_y = 2.24$. In the Doublestar configuration with $\ell = 7$ calculated by Wang and Jensen [248], this ratio is somewhat higher, which may be due to the particular way of winding of the helical coils chosen by the authors [248]. Such an elongation in the horizontal direction is undesirable, because in toroidal systems the internal surfaces always move outward and become elongated vertically at a finite plasma pressure. Then, if the external surfaces are oblate, the distance between intersurfaces and the plasma boundary would become too small.

Besides the shape of the near-axis magnetic surfaces, one more important geometrical characteristic of doublets is the location of the magnetic axes. The closer to the outer boundary, the worse from the viewpoint of plasma thermal insulation. The ratio $H_{\rm ax}/(bh_s)$ of the height $H_{\rm ax}$ of the magnetic-axis location above the equatorial plane to the height $bh_s$ of the separatrix "petal" is determined from Eq. (5.21). It appears to be larger for larger $\ell$: $H_{\rm ax}/(bh_s) = 0.71$ at $\ell = 3$, but at $\ell = 8$ this ratio is 0.85.

The geometrical distinctions of the doublets in stellarators with different $\ell$ discussed above are clearly seen in Fig. 5.8, where the magnetic surfaces described by Eqs. (5.2) and (5.18) are shown. Here one can also see that with increasing $\ell$ the

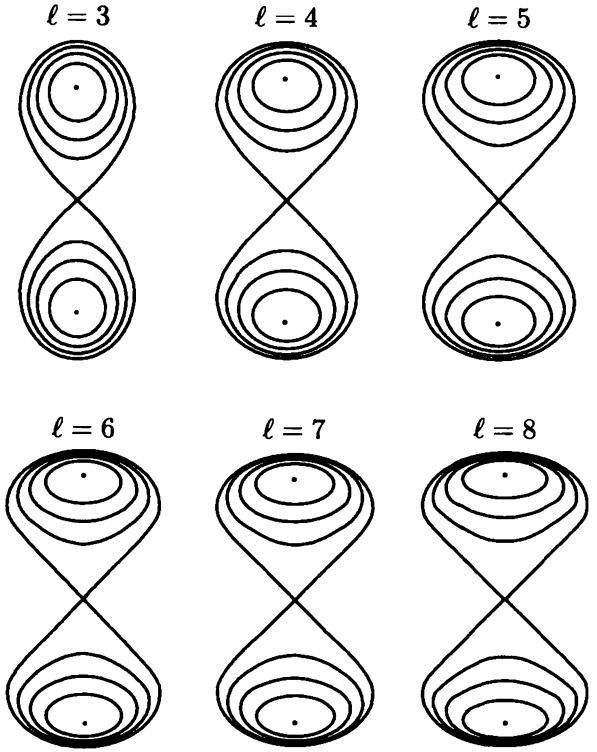


**Fig. 5.8.** Cross sections of the averaged magnetic surfaces in doublet configurations in stellarators with different $\ell$.

separatrix becomes wider and wider. Let us evaluate the ratio of the complete height $2H_s$ of the separatrix to its full width $2W_s$.

At the points of the magnetic surface $a = \text{const}$ that are most remote from the vertical axis passing through its center, the equality $r'_z(a, z) = 0$ should obviously be fulfilled. It is easy to show that these points, whose coordinates $(r, z)$ we denote as $(R + W, z_w)$, lie on the circumference

$$\rho_w^2 \equiv W^2 + z_w^2 = H_{\text{ax}}^2. \tag{5.24}$$

For this purpose, it is sufficient to differentiate Eq. (5.18) with respect to $z$, taking $a'_z = 0$ and $r'_z = 0$. On the separatrix,

$a = 0$. Solving this equation together with Eq. (5.24), we obtain with account of Eq. (5.21)

$$\frac{H_s}{W_s} = \frac{H_s}{H_{ax}}\sqrt{\frac{2(\ell-1)}{\ell-2}} = \sqrt{\frac{2}{\ell-2}}\,(\ell-1)^{\frac{\ell-1}{2(\ell-2)}}. \qquad (5.25)$$

From here it follows that the higher the value of $\ell$, the less the elongation of the doublet. Or, in other words, the wider the "figure eight" $a = 0$. In an $\ell = 3$ stellarator, $H_s/W_s = 2\sqrt{2} = 2.83$; in $\ell = 7$ systems, $H_s/W_s = 1.85$; with increasing $\ell$ the ratio $H_s/W_s$ approaches $\sqrt{2}$.

It is possible to show that in an $\ell = 2$ stellarator with a quadrupole field, the magnetic surfaces of which are described by function (5.2),

$$\frac{H_s}{W_s} = \frac{2\sqrt{2}}{\sqrt{1 - B_2^{cr}/B_2}}. \qquad (5.26)$$

At $B_2$ equal to $B_2^{max}$ (5.8), when $H_s = b$ the ratio (5.26) depends on $\mu_0/\mu_b$ only. For $\mu_0/\mu_b = 0.35/0.95$, which is close to the parameters of the ATF or CHS, $H_s/W_s \cong 4$.

Let us recall that we are talking about dimensions describing the configuration "on average." For restoration of the true three-dimensional geometry one should use the transformation (2.27) or (2.28).

The expressions given above show that the properties of the stellarator doublet configuration greatly depend on the multipolarity $\ell$ of the helical field, which determines the radial dependence of $\mu_h(\rho)$. At larger $\ell$ the strength of the helical field decays faster with distance from the currents that generate it. Consequently, the rotational transform in the central area is small, and this area easily responds to even a weak perturbing field. On the one hand, this is displayed in the fact that a smaller value of the quadrupole field is needed to obtain a doublet with a given size [see Eq. (5.20)]. On the other hand, as is clear from Eq. (5.21), in doublets produced in stellarators with larger $\ell$ the magnetic axes are shifted more strongly toward the

outer boundary. On the whole, the doublets in stellarators with smaller $\ell$ [261, 262] seem more attractive than those that could be produced in the Doublestar [248].

The use of helical fields with smaller $\ell$ than in the Doublestar [248] may improve not only the geometrical, but also the magnetic parameters of doublets. Let us show this by comparing the rotational transform $\mu_{\rm ax}$ on the axes of doublets in stellarators with different $\ell$.

It follows from Eqs. (5.18) and (5.22) that near the elliptical axes of doublets, at $|y| \ll H_{\rm ax}$,

$$\psi(x=0,y) = \psi_{\rm ax} - 2\pi B_0 \frac{\ell-2}{\ell-1} \mu_b\, h_s^{2(\ell-2)} l_y^2, \tag{5.27}$$

where $l_y$ is the vertical semi-axis of the cross section of near-axis surfaces $\psi = \text{const}$. As has been pointed out earlier, these cross sections are ellipses with a ratio of semi-axes given by Eq. (5.23), so that the longitudinal magnetic flux in this area is easily calculated:

$$\Phi(x=0,y) = \pi B_0 \sqrt{\ell-2}\, l_y^2. \tag{5.28}$$

As a result, we obtain for $\ell \geq 3$

$$\mu_{\rm ax} = -\frac{d\psi}{d\Phi} = 2\frac{\sqrt{\ell-2}}{\ell-1}\, \mu_b\, h_s^{2(\ell-2)}. \tag{5.29}$$

One can see from this that at equal $\mu_b$ and at $h_s = 1$ the value $\mu_{\rm ax}$ is larger in stellarators with smaller $\ell$: at $\ell = 3$ it is larger by a factor of 1.43 than that at $\ell = 8$. But at larger $\mu_{\rm ax}$ the configuration should be more stable against external perturbations, and $\beta_{\rm eq}$ should be higher.

Thus, formula (5.29) demonstrates the obvious advantage of systems with lower $\ell$ than those in the Doublestar installation. This advantage is further enhanced by the fact that at smaller $\ell$ it is easier to obtain larger values of $\mu_b$. Let us note that in an $\ell = 2$ stellarator with the parabolic profile of $\mu_h(\rho)$ (3.8) the value of the rotational transform at the axis of a doublet with $H_s = b$ is given by the simple equality

$$\mu_{\rm ax} = \mu_b \sqrt{1 - \mu_0^2/\mu_b^2}, \tag{5.30}$$

which can be easily derived from Eq. (5.15). In the Doublestar configuration calculated in [248], $\mu_{ax} = 0.2$. As is seen from Eq. (5.30), in $\ell = 2$ stellarators $\mu_{ax}$ may be four times larger at the most usual values of $\mu_0$ and $\mu_b$.

The second important magnetic characteristic of stellarator configurations is the magnetic well. It was shown in [248] that a rather deep magnetic well can be easily created in a doublet stellarator with the help of an external vertical field $B_\perp$ shifting the magnetic surfaces into the area of a weaker toroidal field.

To take into account the influence of the vertical field on stellarator doublet configurations, one should substitute $\psi_\perp = -2\pi R B_\perp \rho \cos u$ into the right-hand sides of Eqs. (5.2) and (5.16). In this case, Eq. (5.18) for systems with $\ell \geq 3$ takes the form

$$\xi^{2(\ell-1)} + \xi^2 h_s^{2(\ell-2)} \cos 2u + 2(\ell-1)\frac{AB_\perp}{\mu_b B_0}\xi \cos u = \text{const}. \quad (5.31)$$

At $|B_\perp/B_2| < 2H_{ax}/b$, these surfaces remain triaxial. It is easy to show that under the action of the vertical field $B_\perp$ the magnetic axes of the doublets (5.31) are so shifted that their distance from the geometrical axis $\xi = 0$ is not changed:

$$\Delta_{ax}^2 + z_{ax}^2 = H_{ax}^2, \quad (5.32)$$

while the horizontal displacement (along the $r$ axis) is determined by the formula

$$\Delta_{ax} = \frac{B_\perp}{2B_2} b. \quad (5.33)$$

This dependence of $\Delta_{ax}$ on $B_\perp/B_2$ is the same in systems with different $\ell$. Both equalities are also valid for $\ell = 2$.

Relationships (5.32) and (5.33) show that with increasing $B_\perp$ the magnetic axes of the doublets move along the arc of the circumference of radius $H_{ax}$. Both "petals" of the separatrix bend forward, then merge and disappear at $\Delta_{ax} = H_{ax}$. At $\Delta_{ax} > H_{ax}$, the configuration remains mono-axial despite the presence of the quadrupole field. A similar picture is frequently

observed in $\ell = 3$ stellarators (see [37, 270]). Our consideration gives both a qualitative explanation of these effects and quantitative dependences.

The formation of doublet-like configurations in stellarators under the action of a quadrupole field is not associated with toroidicity. Therefore, in order to avoid superfluous minor details in our description we have neglected the inessential toroidal corrections. In doing so we slightly idealized the picture of the surfaces $\psi = \text{const}$, assuming them to be circular and neglecting their "fine structure" in the near-axis region. The general character of the results of our analysis does not suffer for this, and generalization of them to the case $\psi = \psi(\rho, u)$ is not difficult.

Doublet configurations can also be created in stellarators by other methods. It is known that a two-petal island structure occurs practically always in $\ell = 3$ stellarators and torsatrons if no special steps are taken to suppress it [16, 17, 22, 257, 258, 335]. This effect is usually considered as undesirable. As a means of preventing splitting of the axis and the formation of an internal separatrix, a quadrupole field, in particular, was proposed [258]. In our case, it is used for quite the opposite purpose.

It was shown by Greene and Johnson [93] that doublets can also be created in an $\ell = 2$ stellarator at rather strong corrugation (produced by an additional helical $\ell = 0$ field) with the same pitch in $\zeta$ as that of the main helical field with $\ell = 2$. Triaxial doublet configurations also appear in stellarators with helical conductors wound on a torus of elliptical cross section [247, 267]. In this respect, the Doublestar [248] is close to such systems — its helical windings are placed on a toroidal chamber of rectangular cross section. But it differs from those systems by additional windings for the quadrupole field.

In the examples considered in [16, 17, 247, 257, 258, 267], the main factor that determines the dimensions and the very existence of doublet structures is the arrangement of helical conductors. This method of doublet formation has no flexibility and allows operation only in a narrow range of parameters dependent on the features of the magnetic-system design. In our case,

thanks to control of the magnetic configuration with the help of the external quadrupole field, which appears to be a highly effective means of readjusting the configuration, the possibilities of the device are substantially expanded.

Let us summarize. It is possible to ascertain that by applying a quadrupole field to the usual stellarator configuration it is possible to change its geometry over a very wide range (see Fig. 5.1). The entire variety of configurations, from one-axial up to doublet, can easily be produced in the same installation by changing only the value of the control quadrupole field. The only control parameter is $AB_2/\mu_b B_0 = B_2/B^*$.

With the help of a control quadrupole field, triaxial doublet configurations can be formed in any stellarator with shear. In the presence of shear the outer magnetic surfaces respond to the control quadrupole field much more weakly than the inner surfaces. This is the main reason explaining the formation of doublets in stellarators at $B_2 > B_2^{\rm cr}$ and the efficiency of the influence of the quadrupole field on the one-axial configuration at $B_2 < B_2^{\rm cr}$.

As was shown above, the doublet-like configurations in $\ell = 2$ and $\ell = 3$ stellarators could perfectly compete with doublets in the Doublet tokamaks, winning out overwhelmingly in the simplicity of doublet creation and flexibility of the magnetic geometry control.

Experiments on installations where the transition from the usual one-axial to elongated and then even to doublet configurations could be possible, could give useful information on the influence of elongation on plasma confinement in stellarators, on the influence of shear on plasma stability, and on the behavior of a plasma in systems with an internal separatrix. It could also be interesting to compare stellarator doublet configurations with those in tokamaks.

For already existing stellarators and for installations of the next generation constructed according to the traditional scheme, it is essential to explore the initial range $K_b < E$, where configurations still remain one-axial but the effects of elongation are

already visible. The advantages of elongated one-axial configurations are discussed in the next two sections.

## 5.3. Control of the rotational-transform profile with the help of the quadrupole field

When Oak Ridge theoreticians developed the ATF torsatron project, they discovered [183] that for a circular "on average" plasma boundary, due to the increase of the rotational transform $\mu$ in the center and the decrease in the middle part of the plasma, one of the main advantages of the ATF vacuum magnetic configuration, $\mu(a)$ monotonicity, can be lost (Fig. 5.9). The plasma can then become unstable [181, 183].

The rotational transform $\mu(a)$ in a stellarator is determined by the geometry of the magnetic field only. This is a well-known fact. Formally it follows from the equation

$$J = -\alpha_{22}\psi' + \alpha_{23}\Phi', \tag{5.34}$$

relating the longitudinal current $J$ with the magnetic fluxes, poloidal $\psi$ and toroidal $\Phi$ (Fig. 2.6). Relationship (5.34) is a direct consequence of the Maxwell equation $\mathbf{j} = \mathrm{rot}\,\mathbf{B}$. And the quantities $\alpha_{ik}$ are calculated from the given shape of the magnetic surfaces (see [131]). In a tokamak, $\alpha_{23} = 0$. In this case the rotational transform $\mu(a) = -\psi'/\Phi'$ is also related to the current distribution. But in a current-free stellarator ($J = 0$) the value of $\mu(a)$ on each magnetic surface is unequivocally determined by the shape of the surface: $\mu(a) = -\alpha_{23}/\alpha_{22}$.

The results of numerical calculations [183] (Fig. 5.9), have shown that in the ATF the internal geometry of a plasma column is significantly changed as $\beta$ increases. This change is uncontrollable. But it is possible to counteract it to a certain degree by changing the plasma shape with the help of external poloidal fields. Let us emphasize that here we mean not the traditional "static" correction of the magnetic surface geometry, but "dynamic" control of the plasma shape, when the control fields react to the variation of $\beta$.

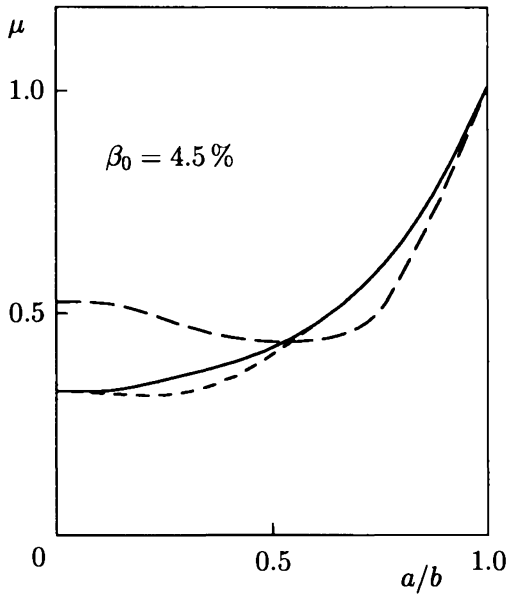


**Fig. 5.9.** Effect of finite pressure and plasma elongation on the rotational-transform profile $\mu$ in the ATF torsatron: solid curve) $\beta = 0$; long-dashed curve) $\beta_0 = 4.5\%$, circular boundary; dashed curve) $\beta_0 = 4.5\%$, elongated boundary [183].

The ATF torsatron had three pairs of ring coils to produce the poloidal field. By changing the currents in them, Carreras et al. [183] succeeded in finding the optimal plasma shape for each value of $\beta$ — optimal in the sense that advancing (in calculations [183]) to large $\beta$ through the sequence of configurations found, it was possible to keep the rotational-transform profile almost unchanged (see Fig. 5.9).

This was a new, unexpected result. Not only the solution, but even the existence of the problem was not known before the publication of [183]. And the proposed solution in [183] was strikingly simple and effective.

With only three parameters at hand (the currents in the control windings of the ATF) it was necessary to sacrifice two

degrees of freedom because of the natural restrictions: the variations of external currents should not, first, result in driving the net longitudinal current in the plasma, and, second, in shifting it from the given position. Under these conditions there remained only one free parameter in the problem. Hence, it was possible to impose only one constraint. For example, the invariability of $\mu$ at the magnetic axis for simultaneous changes of $\beta$ and of the control currents. However, that was enough for a substantial influence on the radial dependence of $\mu$, as is clearly shown in Fig. 5.9.

Numerical calculations [183] have been performed for the ATF only. The results obtained have been considered as dependences on the absolute values of the control currents. And the main statement formulated in the conclusion of [183] was that in torsatrons a vertical field system consisting of three pairs of coils allows independent control of the magnetic well and the rotational transform.

The results of Carreras et al. [183] were extremely interesting both in the theoretical and practical respect. Actually, they showed that in the ATF for a circular (on average) plasma boundary, which was natural for conventional stellarators, it was impossible to advance to large $\beta$. Simultaneously an elegant radical solution was offered [183]. The doubtless importance of the results [183] required a deeper and wider study of the problem.

In the numerical calculations of [183] the only control parameter was the quadrupole moment. By its variation the plasma shape was changed. Therefore, the problem considered for specific constructive restrictions of the ATF [183] could be formulated in more general terms as the influence of the plasma shape on the rotational-transform profile in a stellarator. The problem was considered in such a formulation in [249–251].

To obtain an analytical expression for $\mu(a)$, it is necessary to prescribe the plasma shape and then to calculate $\alpha_{ik}$ in Eq. (5.34). The values $\alpha_{ik}$ in Eq. (5.34) are most simply expressed through the metric coefficients of the flux coordinates with straight field lines (see [162, 131, 147, 251]). However,

the transition to these coordinates and the intermediate calculations appear bulky. Following [280], we offer here another, non-traditional way of calculating $\mu$ for stellarators, whose simplicity and clarity make any comment unnecessary.

To calculate $\mu$, one can use relationship (2.118), which allows $\psi'$ to be expressed in terms of the longitudinal current $J$ and the poloidal flux of the helical field, $\psi_V$:

$$J = \int \frac{\mathbf{j}\cdot\nabla\zeta}{2\pi}\,d\tau = -\oint \frac{\nabla a}{|\nabla a|}\cdot\frac{\nabla(\psi-\psi_V)}{4\pi^2 r^2}\,dS_n = -\frac{V_0'}{4\pi^2}\Big\langle\frac{\nabla a\cdot\nabla(\psi-\psi_V)}{r^2}\Big\rangle_0. \tag{5.35}$$

Here we integrate over the axially symmetric "quasi-tokamak" volume, and the surface integral is calculated over its boundary, the toroidal surface $\psi = \text{const}$, the brackets $\langle\ldots\rangle_0$ designating averaging (2.42). It is clear that Eq. (5.35) is a particular case of Eq. (5.34).

To take into account the combined effect of the plasma pressure and the external control field on the profile $\mu(a)$, let us use the model of magnetic elliptical surfaces (3.24) (Fig. 3.4). Usually more simple models are used in analytical calculations: with $K = 1$ (circular surfaces) or with very small ellipticity arising near the magnetic axis at finite $\beta$. But we shall consider $K$ as arbitrary. This is absolutely necessary for the description of the behavior of $\mu(a)$ for variations of the plasma shape, since in stellarators with shear the elongation of near-axis surfaces becomes large even for a rather moderate ellipticity of the boundary $K_b$. This was discussed in Section 5.1.

If the geometry of the magnetic surfaces is explicitly prescribed by expressions (3.24), the averaging $\langle\ldots\rangle_0$ in Eq. (5.35) is reduced to integration (3.35), where $D$ is the function (3.34). For the first term on the right-hand side of Eq. (5.35) we obtain in this case

$$\alpha_{22} = \frac{V_0'}{4\pi^2}\Big\langle\frac{|\nabla a|^2}{r^2}\Big\rangle_0 = \frac{a}{R_c}\frac{K^2+1}{2K}f_{22}, \tag{5.36}$$

where $R_c = R + \Delta(a)$ is the position of the magnetic-surface center, $f_{22}$ is a quantity of the order of unity,

$$f_{22} = \frac{1}{2\pi} \int_0^{2\pi} \frac{1 + (K^2 - 1)(K^2 + 1)^{-1} \cos 2\theta}{(1 - a/R_c \cos\theta)(1 - \Delta' \cos\theta + 2d \sin^2\theta)} d\theta, \quad (5.37)$$

and $d \equiv aK'/(2K)$. Note that the quantity $\alpha_{22}$ in Eq. (5.36) is determined only by the shape of the magnetic surfaces. It does not depend on the helical field and turns out to be the same for stellarators and tokamaks.

If $\psi_V = \psi_V(\rho)$, then

$$\nabla a \cdot \nabla \psi_V = -2\pi B_0 \mu_h \frac{Ka}{D} (a - \Delta \cos\theta), \quad (5.38)$$

where $D$ is function (3.34). This is obtained with account of

$$\rho \mathbf{e}_\rho \cdot \nabla a = \frac{Ka}{D} (a - \Delta \cos\theta), \quad (5.39)$$

which, according to Eq. (3.32), is valid for shifted elliptical magnetic surfaces, and $\psi_V'(\rho)$ is expressed through $\mu_h$ with the help of Eq. (3.6). Now, addressing once again Eq. (3.35), for a parabolic profile $\mu_h$ we obtain

$$\frac{V_0'}{4\pi^2} \left\langle \frac{\nabla a \cdot \nabla \psi_V}{r^2} \right\rangle_0 = -\frac{2\pi B_0 K a^2}{R_c} \times \left[ \mu_0 + \frac{\mu_b - \mu_0}{b^2} \left( a^2 \frac{K^2 + 1}{2} + 2\Delta^2 \right) \right]. \quad (5.40)$$

Actually, the condition $\psi_V = \psi_V(\rho)$ may be valid to within the toroidal corrections; therefore, we disregard them in Eq. (5.40). Stellarators are systems with a rather large aspect ratio, so no serious mistake arises after that.

Equality (5.35), which can be written in the form

$$-\alpha_{22}\psi' + \frac{V_0'}{4\pi^2} \left\langle \frac{\nabla a \cdot \nabla \psi_V}{r^2} \right\rangle_0 = J, \quad (5.41)$$

allows $\psi'$ to be expressed through the calculated quantities. To

complete the calculations of $\mu = -\psi'/\Phi'$, we have to find the remaining value $\Phi'$.

Expressions (2.51), and (2.53), together with Eq. (3.35), yield in our case (elliptical shifted magnetic surfaces)

$$\frac{1}{F}\frac{d\Phi}{da} \cong \frac{Ka}{R_c}(1+d). \tag{5.42}$$

It is possible to put $F \cong 2\pi R B_0$ here. With the help of the last two equalities we finally obtain

$$\mu = \mu_{\rm st} + \mu_J, \tag{5.43}$$

where $\mu_{\rm st}$ is the "stellarator" part of the rotational transform,

$$\mu_{\rm st}(a) = \frac{2K}{K^2+1}\left[\mu_0 + \frac{\mu_b - \mu_0}{b^2}\left(a^2\frac{K^2+1}{2} + 2\Delta^2\right)\right](1-\delta), \tag{5.44}$$

$\mu_J$ is the rotational transform due to the longitudinal current,

$$\mu_J(a) = \frac{2}{K^2+1}\frac{RJ}{2\pi a^2 B_0}(1-\delta), \tag{5.45}$$

and $\delta$ is a non-negative quantity which is expressed through the derivatives of $\Delta$ and $K$ [251]:

$$\delta = \frac{1}{2}\left[\Delta'^2 + d^2 + \frac{K^2-1}{K^2+1}\left(\frac{\Delta'^2}{2} + d - d^2\right)\right]. \tag{5.46}$$

At $\Delta'^2 \ll 1$, $|d| \ll 1$, the value of $\delta$ is much smaller than unity.

Let us recall that $d \equiv aK'/(2K)$. In stellarators with shear $K' < 0$, therefore, $|d| \ll 1$ is really a very weak condition. Indeed, since $K$ is multiplied by $a$ in $d$, the growth of ellipticity of the magnetic surfaces $K$ toward the axis is practically not limited by the condition $|d| \ll 1$. For an illustration we can give two simple examples: $f = 1/a$, $af'/(2f) = -0.5$; $f = 1 - \ln a$, $af'/(2f) = -0.5/(1-\ln a)$. In both cases, the condition $|af'/(2f)| \le 0.5$ does not hinder the infinite growth of $f$ at $a \to 0$.

This positive quality of our analytical model is supplemented by the fact that the absolute value of the shift always decreases with increasing $K$. Accordingly, the value $\Delta'^2$ also becomes smaller. As a whole, the analytical model of elliptical shifted magnetic surfaces appears quite adequate to the physical character of the problem.

There is a lot of information in formula (5.44), since the shear, shift, and ellipticity of the magnetic surfaces are taken into account there, and the dependences $\Delta(a)$ and $K(a)$ still remain free. To see and to evaluate various effects hidden in expression (5.44), let us consider different factors separately.

The effect of the magnetic surface shift is described by the term with $\Delta^2$, and, moreover, $\delta$ contains the derivative $\Delta'$.

The term with $\Delta^2$ in Eq. (5.44) describes the increase in $\mu$ on a magnetic surface when it is shifted from the initial position. Under the action of the external vertical field or owing to the finite $\beta$, the magnetic axis is the most strongly shifted. Hence, according to Eq. (5.44), the increase in $\mu(a)$ due to the shift $\Delta$ appears maximal at the axis. At the axis $\Delta' = 0$; therefore at $K = 1$

$$\mu_{\rm st}(0) = \mu_0 + 2(\mu_b - \mu_0)\frac{\Delta_{\rm ax}^2}{b^2}. \qquad (5.47)$$

At $\beta$ close to the equilibrium limit $\beta_{\rm eq}$ the shift of the axis $\Delta(0)$ can be of the order of $b/2$. In the ATF torsatron $\mu(0)$ should increase then (if $K(0)$ does not vary) almost twice in comparison with the initial value $\mu_0$.

The effect of increasing $\mu(0)$ at finite plasma pressure was repeatedly noticed both in numerical and in analytical calculations [147, 150, 153, 155, 156, 222, 336]. But only Carreras et al. [183] clearly pointed out its potential danger.

As can be seen from Eq. (5.44), the increase in $\mu$ in the center because of the magnetic-axis shift is aggravated by the simultaneous reduction of $\mu$ at a finite distance from the axis where $\Delta$ becomes smaller but $\Delta'^2$, on the contrary, increases. To show it more clearly, let us again put $K = 1$ in Eq. (5.44).

Then we obtain

$$\mu_{st}(a) = \left[\mu_0 + (\mu_b - \mu_0)\frac{a^2 + 2\Delta^2}{b^2}\right]\left(1 - \frac{\Delta'^2}{2}\right). \qquad (5.48)$$

At small $\beta$ the quantity $\Delta'^2$ is also small, but approaching $\beta_{eq}$ it increases. By definition $\Delta'^2 < 1$; therefore, even at the limit of the applicability of the model the multiplier $1 - \Delta'^2/2$ cannot become smaller than 0.5. But if in a stellarator with $\mu_0 = 0.3$, $\mu_b - \mu_0 = 0.6$ at $\Delta_{ax}/b = 0.5$ the value of $\mu(0)$ can increase by a factor of two in comparison with $\mu_0$, then an even smaller decrease in $\mu$ in the middle part of the plasma column (for example, by 30%) is already sufficient to make the derivative $\mu'_{st}$ negative, as in Fig. 5.9.

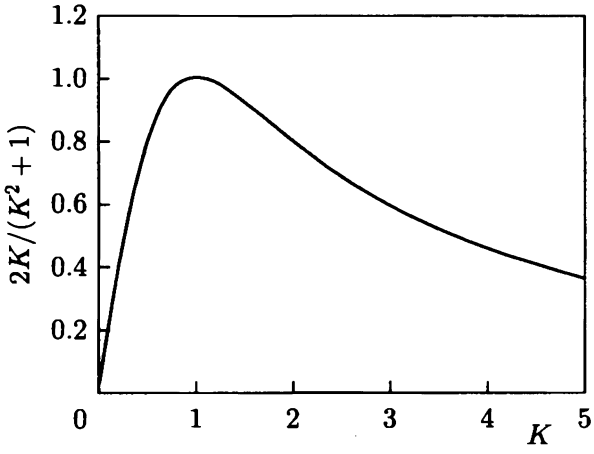


**Fig. 5.10.** Rotational-transform reduction factor owing to elongation of the magnetic surfaces in a stellarator.

The main effect of the elongation is described by the multiplier $2K/(K^2+1)$ in Eq. (5.44). At $K \neq 1$, it is always smaller (see Fig. 5.10) than unity (including the range $K < 1$). This is exactly what is needed to hinder the growth of $\mu(0)$ accompanying the Shafranov shift. However, the quantity $2K/(K^2+1)$, as seen in Fig. 5.10, decreases very slowly for deviation from

$K = 1$: the reduction in $\mu$ by a factor of two owing to elongation is reached only at $K \cong 4$. By tokamak measures this value is large. But large $K$ are required *only* in the plasma center. Fortunately, it is not difficult to strongly elongate the near-axis region of a plasma in stellarators with shear. As was explained in Section 5.1, in stellarators with shear the large values of $K$ in the center are reached for a rather moderate elongation of the plasma column $K_b$ [250, 256]. According to Eq. (5.4), values of the elongation $K_0$ of near-axis surfaces as large as necessary are easily obtained when the increasing $B_2$ comes close to the value $B_2^{\rm cr}$. Then $K_b$ remains smaller than the critical elongation $E$ defined by Eq. (5.6), whose dependence on $\mu_0/\mu_b$ is shown in Fig. 5.2.

The "pure" controlling impact of the quadrupole field on the value of $\mu(0)$ is described by the relationship

$$\mu(0) = \frac{2K_0}{K_0^2 + 1}\mu_0 = \mu_0\sqrt{1 - (B_2/B_2^{\rm cr})^2}. \qquad (5.49)$$

It is derived from Eq. (5.44) at $\Delta = 0$ with account of Eq. (5.4), which gives the relation between $K_0$ and $B_2$.

We repeatedly mentioned shear, because control of the $\mu(a)$ profile in a stellarator with the help of a quadrupole field appears effective only in the presence of shear. This unequivocally follows from Eq. (5.44). Actually, for such a conclusion we have to know the behavior of $K(a)$. But in stellarators with shear, as was already explained, this dependence is highly favorable.

On the basis of the above it is possible to conclude that the effect of control of the rotational-transform profile, shown for the first time in numerical calculations [183] for the ATF, is not associated with specific features of the ATF but can be used in any stellarator with shear. The presence of shear allows the value of $\mu(0)$ to be easily controlled (reduced to zero) with the help of a quadrupole field. At the same time, it is significant that the effect of this field on the configuration becomes weaker at larger distances from the axis.

But in shearless stellarators this is not so. As is clear from Eq. (5.2), in stellarators with $\mu_b = \mu_0$ all surfaces $\psi = \text{const}$ are identically elongated under the action of the quadrupole field. In this case, $K = K_0 = \text{const}$ [see Eq. (5.4)], $K' = 0$, and so Eq. (5.44) is transformed into

$$\mu_{\text{st}} = \frac{2K}{K^2+1}\mu_0 \left[1 - \frac{3K^2+1}{2(K^2+1)}\frac{\Delta'^2}{2}\right]. \tag{5.50}$$

It follows from here that due to the relative shift of magnetic surfaces a small shear appears at finite plasma pressure in stellarators with $\mu_h = \text{const}$, which are called shearless. According to Eq. (5.50), the rotational transform in shearless stellarators always decreases because of the shift. At the axis, $\Delta' = 0$, hence, at any pressure profile, a negative shear should always arise near the axis. The elongation of surfaces allows it to be reduced, but it is impossible to suppress it completely, as can be done in systems with shear.

In a shearless stellarator, for a parabolic pressure profile $\Delta' = -a\beta/(b\beta_{\text{eq}})$ at any $K$ [280]. Therefore, at $\beta \neq 0$ the $\mu$ profile also becomes parabolic in this case:

$$\mu = \frac{2K}{K^2+1}\mu_0 \left[1 - \frac{3K^2+1}{2(K^2+1)}\frac{\beta^2}{2\beta_{\text{eq}}^2}\frac{a^2}{b^2}\right]. \tag{5.51}$$

This effect is unpleasant for two reasons. First, at $\mu' < 0$ the ballooning modes can become dangerous [141, 143, 144, 160]. Second, decreasing with increasing pressure, $\mu(b)$ can reach the resonant value $m/n$ with small $m$ and $n$, which is extremely undesirable. Experiments in the W VII-A stellarator have shown [70, 77, 337, 338] that the best confinement of a plasma is provided when $\mu$ is close to a resonance $m/n$ $(1/2, 1/3, 2/3, \ldots)$, but does not coincide with it. At $\mu(b) = m/n$ the plasma confinement is much worsened. It follows from Eq. (5.51) that it cannot be avoided: with increasing $\beta$ the value of $\mu(b)$ can vary by a factor of 1.5–2 in comparison with the chosen vacuum value $\mu_0$. The elongation of the plasma does not help in this case.

It can be seen from Eq. (5.50) that the $\mu(a)$ profile in shearless stellarators should be distorted at any $p(a)$. The impossibility of keeping $\mu = \text{const}$ at finite $\beta$ in the "usual" shearless stellarators is a serious defect of these systems. No simple ways are known to overcome it. The problem can be partially solved by a transition to more complex configurations like the W VII-AS [38, 70] or W VII-X [52, 57, 101, 228].

The radial dependence of $\mu$ is determined by the quantity $\Delta'$ depending on the pressure distribution $p(a)$. For a current-free plasma ($\mu_J = 0$) in a shearless stellarator ($\mu_h = \mu_b = \text{const}$), it follows from Eq. (3.36) that

$$\Delta' = \frac{b}{a}\frac{\beta(a) - \bar{\beta}(a)}{\beta^0_{\text{eq}}}, \tag{5.52}$$

where $\beta^0_{\text{eq}} = \mu_b^2 b/R$ is the quantity (3.15), $\beta(a) = 2p(a)/B_0^2$ is the local value of $\beta$, and $\bar{\beta} = 2\bar{p}/B_0^2$ is averaged over the cross section $a = \text{const}$,

$$\bar{p}(a) \equiv \frac{2}{a^2}\int_0^a p(a)a\,da. \tag{5.53}$$

At peaked $p(a)$ the function $\Delta'(a)$ is nonmonotonic. Accordingly, $\mu(a)$ must also be nonmonotonic (Fig. 5.11). For example, for a plasma with a pressure given by

$$p = p_0\left(1 - \frac{a^2}{b^2}\right)^2 \tag{5.54}$$

we have $\bar{p} = p_0\left(1 - a^2/b^2 + a^4/(3b^4)\right)$ and, according to Eq. (5.52),

$$\Delta' = -3\frac{\beta}{\beta^0_{\text{eq}}}\frac{a}{b}\left(1 - \frac{2}{3}\frac{a^2}{b^2}\right). \tag{5.55}$$

In this case the quantity $|\Delta'|$ reaches its maximum at $a^2/b^2 = 0.5$. The profiles $\mu(a)$ with a minimum at $a/b = 0.7$, similar to

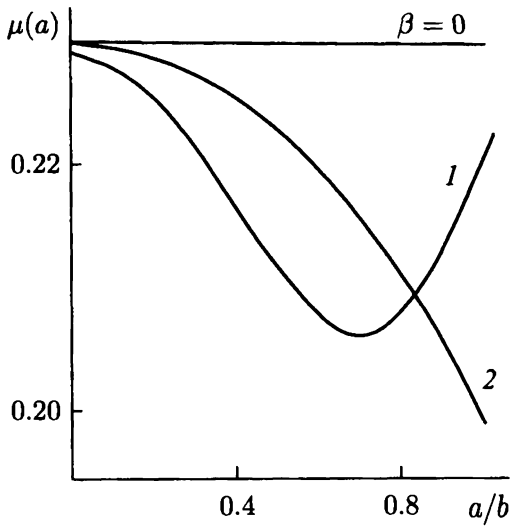


**Fig. 5.11.** Effect of pressure distribution on the rotational-transform profile in shearless stellarators: *1)* $p = p_0(1 - a^2/b^2)^2$; *2)* $p = p_0(1 - a^2/b^2)$.

that shown in Fig. 5.11, are very frequently encountered in numerical calculations of equilibrium [42, 61, 156, 183, 222, 337], including those for stellarators with shear. Expressions (5.50) and (5.55) show that the "drop" in $\mu$ at $a/b = 0.7$ should be associated with the choice of $p(a)$ in the form (5.54). Accordingly, in problems where the distortion of the $\mu$ profile is important, it is necessary to bear in mind that this distortion is determined not only by the value of $\beta$, but also by the pressure profile $p(a)$.

## 5.4. Elongation of the plasma column as a means of increasing $\beta_{eq}$ in stellarators

If it were possible to create a stellarator configuration where the equilibrium plasma currents did not have the component $\bar{j}_\zeta$, this could be the ideal solution of the equilibrium problem. However, in conventional stellarators configurations

without the Pfirsch–Schlüter current are found to be in that area of parameters where the plasma equilibrium is unstable. Moreover, this area lies so far from the acceptable ranges [329, 330] that progress in that direction as a way of at least partial suppression of the Pfirsch–Schlüter current is hardly suitable for real experiment.

These questions have been discussed in Sections 4.4 and 4.5. Formally, the desired goal was the reduction of the difference $\Omega - \langle\Omega\rangle$ and, by that, the reduction of the right-hand side of Eq. (2.118):

$$\frac{2\pi\bar{j}_\zeta}{r} = 4\pi^2 \frac{dp}{d\psi}\left(\Omega - \langle\Omega\rangle\right). \tag{5.56}$$

It is clear that at smaller $\bar{j}_\zeta$ the deviation of $\psi$ from the vacuum solution to Eq. (2.118) is also smaller, and, accordingly, the equilibrium limit $\beta_{\text{eq}}$ is higher. It may seem that the reduction of $\Omega - \langle\Omega\rangle$ is the only way of decreasing $\bar{j}_\zeta$. But this is not so. There is another multiplier in $\bar{j}_\zeta$. Let us take a new look at it:

$$\left|\frac{dp}{d\psi}\right| = \frac{|\nabla p|}{|\nabla\psi|}. \tag{5.57}$$

On the plasma boundary, $p = 0$; therefore, at a given minor radius, $\beta$ is higher at larger allowable $|\nabla p|$. The presence of $|\nabla\psi|$ in the denominator of Eq. (5.57) suggests that for getting larger $|\nabla p|$ at fixed $|p'(\psi)|$ it is necessary to increase $|\nabla\psi|$.

This can be done by driving the net current through the plasma or by placing a conductor with a current inside the plasma. Mentioning this for completeness, we are obliged, first of all, to consider the main, more simple and attractive variant: the control of $\psi$ by the fields of external currents. Some examples have already been discussed above, and in general the effectiveness of such control is determined by the relationship

$$\psi = \psi_V + \psi_{\text{ext}} + \psi_{\text{pl}}, \tag{5.58}$$

which corresponds to Eqs. (2.33) and (2.37). Naturally, the poloidal flux $\psi_{\text{ext}}$ of the external (vacuum) control field must

satisfy the equation

$$\operatorname{div} \frac{\nabla \psi_{\text{ext}}}{r^2} = 0. \tag{5.59}$$

Therefore, the next condition must be valid for an arbitrary closed contour on the plane $(r, z)$:

$$\oint_\Gamma \frac{1}{r} \frac{\partial \psi_{\text{ext}}}{\partial n} \, dl = 0. \tag{5.60}$$

This directly follows from Eq. (4.6). The last equality shows that the increase in $|\nabla \psi|$ owing to $\psi_{\text{ext}}$ is not possible in all the directions from the magnetic axis. This is perfectly illustrated by the functions (3.31), which are the particular solutions to Eq. (5.59).

For such restrictions the choice should be unequivocally made for the benefit of the horizontal direction, along the $r$ axis, which is the direction of the maximal inhomogeneity of the magnetic field. This inhomogeneity does not allow the transverse dimension of the plasma column to be increased: the "fatter" the magnetic surface, the larger $\Omega - \langle \Omega \rangle$ [see Eq. (4.58)]. But in the vertical direction the toroidal field is homogeneous; therefore, the reduction in $|\nabla \psi|$ and the accompanying stretching of magnetic surfaces in the vertical direction are not dangerous.

Using this method of reduction of the Pfirsch–Schlüter current, we have to ensure the increase in $|\mathbf{e}_r \cdot \nabla \psi|$ on both sides of the center of the configuration. A homogeneous vertical field $B_\perp \mathbf{e}_z$ cannot be used for this purpose, but a quadrupole field is quite suitable. To see that, it is enough to look at expression (5.2) for the function $\psi$ in a stellarator with an additional quadrupole field.

It follows from Eq. (5.2) that in the equatorial plane

$$\frac{\psi(b)}{\psi_V(b)} = 1 + \frac{2B_2}{B_2^{\text{cr}} + B^*}, \tag{5.61}$$

where $B_2$ is the quadrupole field at the distance $\rho = b$, $B_2^{\text{cr}} =$

$\mu_0 B_0/A$ is the value given by Eq. (5.3), and

$$B^* = \mu_b \frac{B_0}{A} = \frac{\mu_b}{\mu_0} B_2^{\rm cr}. \tag{5.62}$$

At the geometrical axis $\psi = \psi_V = 0$, therefore, the ratio (5.61) can be considered as a quantitative measure of the change in $|\mathbf{e}_r \cdot \nabla\psi|$ under the action of the control quadrupole field. The larger the $B_2$, the better the result given by Eq. (5.61). However, at $B_2 = B_2^{\rm cr}$ the internal separatrix appears (see Fig. 5.1). At $B_2 = B_2^{\rm cr}$ we have

$$\frac{\psi(b)}{\psi_V(b)} = 1 + \frac{2\mu_0}{\mu_b + \mu_0}. \tag{5.63}$$

This is the upper limit for single-axial configurations. It is clear that

$$0 \le \frac{2\mu_0}{\mu_b + \mu_0} \le 1. \tag{5.64}$$

Therefore, at $B_2 < B_2^{\rm cr}$ the gain in $|\nabla\psi|$ at the expense of the quadrupole field cannot be very large. However, at typical parameters of a stellarator (for example, $\mu_0/\mu_b = 1/3$), the 1.5-fold increase in $|\nabla\psi|$ is quite real. Then it is possible also to expect a similar increase in $\beta_{\rm eq}$.

This simple consideration shows how and why it is possible to control the magnitude of the current $\bar{j}_\zeta$ without shifting the plasma. Because of the utmost simplicity of the given arguments, the conclusion that the positive effect is possible (though only up to a certain level) is beyond doubt.

The reduction of the Pfirsch–Schlüter current associated with plasma elongation can be shown explicitly, having calculated the right-hand side of Eq. (5.56) at a given geometry of the magnetic surfaces. Using the model (3.24) of shifted ellipses (Fig. 3.4), we obtain

$$\bar{j}_\zeta = \frac{2p'(a)}{\mu_{\rm st} B_0 K}\left[\cos\theta + \frac{\Delta'}{2} + \frac{R}{2a}\left(\langle\Omega^0\rangle - \Omega^0\right)\right], \tag{5.65}$$

where $K$ is the elongation of the magnetic surfaces and $\mu_{st}$ is function (5.44). According to Eq. (5.44), with increasing $K$ the rotational transform $\mu_{st}$ decreases, but the product $K\mu_{st}$ nevertheless becomes larger with increasing $K$, which gives the reduction of $\bar{j}_\zeta$.

In the elementary case of a shearless stellarator we have

$$\bar{j}_\zeta = \frac{2p'(a)}{\mu_0 B_0} \frac{K^2+1}{2K^2} \left( \cos\theta + \frac{\Delta'}{2} \right), \tag{5.66}$$

where $\mu_0$ is the rotational transform at $K = 1$. Small terms with $\Omega^0$ were disregarded here. It follows from Eq. (5.66) that the vertical elongation of magnetic surfaces ($K > 1$) results in a reduction, and the "squeezing" ($K < 1$) results in an increase in $\bar{j}_\zeta$. Already at $K = 1.5$ the current amplitude is 1.4 times smaller, and at $K = 0.75$ it is 1.4 times larger than the corresponding value for the circular surfaces ($K = 1$).

The last two equations, as well as Eq. (5.63), show that the possible gain in $\beta_{eq}$ due to elongation of the plasma cross section could be, unfortunately, not very large. To use the effect at full scale, large elongations $K$ are needed. But in stellarators with shear large values of $K$ are easily obtained in the center of the plasma for rather moderate elongations of the boundary $K_b$. Therefore, this way of increasing $\beta_{eq}$ (though twofold) may be perfectly recommended for experiment.

We have presented only analytical estimates, but they are clear, reliable, and rather informative. The exact results obtained by the numerical solution of the equilibrium problem [183, 250, 268, 269, 280] confirm that up to a double increase in $\beta_{eq}$ by means of plasma-shape control is quite realistic in conventional stellarators.

*February 1998*
*Russian Research Centre*
*"Kurchatov Institute"*
*Moscow*

# List of main symbols

$a$ — Magnetic surface label

$A$ — Aspect ratio, $A = R/b$

$A_t$ — Toroidal component of the vector potential, $A_t = A_{\text{ext}} + A_{\text{pl}}$

$A_{\text{ext}}$ — The part of $A_t$ created by the external current

$A_{\text{pl}}$ — The part of $A_t$ created by the plasma currents

$b$ — Minor radius of a plasma

$\mathbf{B}$ — Magnetic vector field, $\mathbf{B} = \bar{\mathbf{B}} + \tilde{\mathbf{B}}$

$\bar{\mathbf{B}}$ — Axially symmetric part of $\mathbf{B}$, $\bar{\mathbf{B}} = B_t \mathbf{e}_\zeta + \mathbf{B}_p$

$\mathbf{B}_p$ — Poloidal component of the field $\bar{\mathbf{B}}$

$\tilde{\mathbf{B}}$ — Helical magnetic field

$\tilde{\mathbf{B}}_p$ — Poloidal component of the field $\tilde{\mathbf{B}}$

$\mathbf{B}_q$ — Quadrupole magnetic field

$\mathbf{B}^*$ — "Effective poloidal field"

$B_J$ — Net-current magnetic field on the plasma boundary

$B_t$ — Toroidal component of the field $\bar{\mathbf{B}}$

$B_0$ — Toroidal magnetic field on the geometrical axis of a stellarator

$B_2$ — Value of the quadrupole magnetic field $\mathbf{B}_q$ at $\rho = b$

$B_2^{\text{cr}}$ — Critical value of $B_2$, $B_2^{\text{cr}} = \mu_0 B_0 / A$

$B_\perp$ — Value of the vertical magnetic field

$C_{\text{PS}}$ — Reduction factor of the Pfirsch–Schlüter current

$d\tau$ — Volume element

$E$ — Critical elongation

$\mathbf{e}_\zeta$ — Unit vector along $\nabla\zeta$

$F$ — External poloidal current

$G$ — Green's function

$G_0$ — Cylindrical approximation of the Green's function $G$

$H_{\text{ax}}$ — Distance between the geometrical and magnetic axes of the doublet

$H_s$ — Height of the "petal" of the doublet-like separatrix

$J$ — Longitudinal (toroidal) current
$\mathbf{j}$ — Current density
$\bar{j}_\zeta$ — Axially symmetric part of $\mathbf{j} \cdot \mathbf{e}_\zeta$
$K$ — Average elongation (ratio of the axes) of averaged magnetic surfaces
$K_b$ — Elongation of the boundary magnetic surface
$K_0$ — Elongation of near-axis magnetic surfaces
$l, \alpha$ — Quasi-cylindrical coordinates with origin at the center of the plasma column
$\ell$ — Multipolarity of a stellarator
$m$ — Number of helical magnetic field periods
$\mathbf{n}$ — Normal to the "averaged" plasma boundary
$p$ — Plasma pressure
$R$ — Major radius of a stellarator
$R_c$ — Radial position of the center of a magnetic surface, $R_c = R + \Delta(a)$
$r, \zeta, z$ — Usual cylindrical coordinates
$V$ — Volume inside a magnetic surface $\Psi = \text{const}$
$V_0$ — Volume inside a surface $\psi = \text{const}$
$\alpha$ — Local characteristic of the longitudinal component of $\mathbf{j}$, $\alpha = \mathbf{j} \cdot \mathbf{B}/\mathbf{B}^2$
$\alpha_0$ — Integral characteristic of the longitudinal component of $\mathbf{j}$, $\alpha_0 = \langle \mathbf{j} \cdot \mathbf{B} \rangle / \langle \mathbf{B}^2 \rangle$
$\beta$ — Ratio of plasma pressure to magnetic pressure (average over plasma cross section)
$\beta_{\text{eq}}$ — Equilibrium limit of $\beta$
$\beta^0_{\text{eq}}$ — Value determining the scale of $\beta_{\text{eq}}$, $\beta^0_{\text{eq}} = \mu_b^2 b/R$
$\beta(a)$ — Value of $\beta$ on a magnetic surface, $\beta(a) = 2p(a)/B_0^2$
$\beta_0$ — Local value of $\beta$ on a magnetic axis, $\beta(0) = 2p(0)/B_0^2$
$\Gamma_p$ — Boundary of the plasma "averaged" cross section
$\delta\mathbf{r}$ — Vector of deformation $3D \to 2D$
$\Delta(a)$ — Shift of the center of a magnetic surface
$\Delta_\beta$ — Shift of the plasma caused by its pressure

$\Delta_b$ — Shift of the plasma column (plasma-boundary shift), $\Delta_b = \Delta_\beta + \Delta_\perp$

$\Delta_\perp$ — Shift of the plasma owing to the external vertical field

$\zeta$ — Toroidal angle

$\mu$ — Rotational transform

$\mu_h$ — Vacuum rotational transform

$\mu_0$ — Vacuum rotational transform at a geometrical axis

$\mu_b$ — Vacuum rotational transform at $\rho = b$

$\mu_{st}$ — "Stellarator" part of the rotational transform

$\mu_J$ — Rotational transform due to the longitudinal current

$\xi$ — Dimensionless minor radius, $\xi = \rho/b$

$\rho, u, \zeta$ — Quasi-cylindrical coordinates with origin at the geometrical axis of the stellarator $r = R$

$\Phi$ — Toroidal magnetic flux

$\varphi_h$ — Potential of the helical magnetic field

$\varphi_{\ell m}$ — Components of the Fourier decomposition of $\varphi_h$

$\Psi$ — Flux function (poloidal magnetic flux), $\Psi = \psi + \tilde{\psi}$

$\tilde{\psi}$ — Rapidly oscillating part of $\Psi$, $\tilde{\psi} = -\delta\mathbf{r} \cdot \nabla\psi$

$\psi$ — Axially symmetric part of $\Psi$

$\psi_V$ — Poloidal flux of the helical field $\tilde{\mathbf{B}}$

$\Omega$ — Characteristic of the inhomogeneity of $\mathbf{B}^2$, $\Omega = 1 + \left(\langle\tilde{\mathbf{B}}^2\rangle_\zeta - B_t^2\right)/B_0^2$

$\Omega^0$ — Contribution to $\Omega$ due to the helical field, $\Omega^0 = \langle\tilde{\mathbf{B}}^2\rangle_\zeta/B_0^2$

$\omega^0$ — Value characterizing the "magnetic hill," $\omega^0 = \mu_b m b/R$

$\langle\ldots\rangle_\zeta$ — Averaging over $\zeta$

$\langle\ldots\rangle$ — Averaging over the volume between the neighboring magnetic surfaces

$\langle\ldots\rangle_0$ — "Quasi-tokamak" averaging over the volume between the neighboring surfaces $\psi(r, z) = \text{const}$

$\tilde{f}$ — Rapidly oscillating part of $f$, $\tilde{f} = f - \langle f\rangle_\zeta$

$\hat{\tilde{f}}$ — rapidly oscillating part of the integral $\int \tilde{f}\, d\zeta$

## REFERENCES


1. L. A. Artsimovich and K. B. Kartashev, *Dokl. Akad. Nauk SSSR*, **146**, 1305–1308 (1962). English translation: *Sov. Phys. Dokl.*, **5** (1962).
2. V. D. Shafranov, *At. Energ.*, **13**, 521–529 (1962).
3. V. D. Shafranov, in: *Reviews of Plasma Physics* (edited by M. A. Leontovich), Vol. 2, Gosatomizdat, Moscow (1963), pp. 92–131. English translation: Consultants Bureau, New York (1966), pp. 103–151.
4. V. S. Mukhovatov and V. D. Shafranov, *Nucl. Fusion*, **11**, 605–633 (1971).
5. L. A. Artsimovich, *Closed Plasma Configurations* [in Russian], Nauka, Moscow (1969).
6. L. A. Artsimovich, *Nucl. Fusion*, **12**, 215–252 (1972).
7. V. S. Mukhovatov, in: *Itogi Nauki i Tekhniki: Fizika Plazmy* (Advances in Science and Technology: Plasma Physics) [in Russian, edited by V. D. Shafranov], Vol. 1, Part 1, VINITI, Moscow (1980), pp. 6–118.
8. L. I. Artemenkov, I. N. Golovin, P. I. Kozlov, et al., in: *Proc. 4th Int. Conf. Plasma Phys. and Controlled Nuclear Fusion Research, Madison, 1971*, Vol. 1, IAEA, Vienna (1971), pp. 359–367,
9. L. Spitzer, *Phys. Fluids*, **1**, 253–264 (1958).
10. A. S. Bishop, *Project Sherwood*, Addison–Wesley, Massachusetts (1958).
11. L. M. Kovrizhnykh, *Zh. Tekh. Fiz.*, **31**, 888–890 (1961). English translation: *Sov. Phys. Tech. Phys.*, **6**, 643 (1962).
12. L. V. Korablev, A. I. Morozov, and L. S. Solov'ev, *Zh. Tekh. Fiz.*, **31**, 1153–1163 (1961). English translation: *Sov. Phys. Tech. Phys.*, **6**, 845–851 (1962).
13. I. M. Gel'fand, M. I. Graev, N. M. Zueva, A. I. Morozov, and L. S. Solov'ev, *Zh. Tekh. Fiz.*, **31**, 1164–1168 (1961). English translation: *Sov. Phys. Tech. Phys.*, **6**, 852 (1962).
14. L. M. Kovrizhnykh, *Zh. Tekh. Fiz.*, **32**, 526–535 (1962). English translation: *Sov. Phys. Tech. Phys.*, **7**, 383 (1962).
15. D. W. Kerst, *Plasma Phys. C*, **4**, 253–262 (1962).

16. V. F. Aleksin, in: *Plasma Physics and Problems of Controlled Thermonuclear Fusion* [in Russian], Vol. 3, the Ukrainian Academy of Sciences, Kiev (1963), pp. 216–224.
17. L. M. Kovrizhnykh, *Zh. Tekh. Fiz.*, **33**, 377–381 (1963). English translation: *Sov. Phys. Tech. Phys.*, **8**, 281 (1963).
18. V. K. Mel'nikov, *Dokl. Akad. Nauk SSSR*, **149**, 1056–1059 (1963). English translation: *Sov. Phys. Dokl.*, **8**, 176 (1963).
19. A. P. Popryadukhin, *Zh. Tekh. Fiz.*, **34**, 658–665 (1964). English translation: *Sov. Phys. Tech. Phys.*, **9** (1964).
20. A. I. Morozov and L. S. Solov'ev, in: *Reviews of Plasma Physics* (edited by M. A. Leontovich), Vol. 2, Gosatomizdat, Moscow (1963), pp. 3–91. English translation: Consultants Bureau, New York (1966), pp. 1–101.
21. L. S. Solov'ev and V. D. Shafranov, in: *Reviews of Plasma Physics* (edited by M. A. Leontovich), Vol. 5, Atomizdat, Moscow (1967), pp. 3–208. English translation: Consultants Bureau, New York (1970), pp. 1–247.
22. E. D. Volkov, V. A. Suprunenko, and A. A. Shishkin, *The Stellarator* [in Russian], Naukova Dumka, Kiev (1983).
23. M. S. Berezhetskii, S. E. Grebenshchikov, A. P. Popryadukhin, and I. S. Shpigel', *Zh. Tekh. Fiz.*, **35**, 2167–2175 (1965). English translation: *Sov. Phys. Tech. Phys.*, **10**, 1662, (1966).
24. A. Gibson and J. Hugill, *Phys. Rev. Lett.*, **21**, 1052–1055 (1968).
25. M. A. Ivanovskii, S. N. Popov, A. P. Popryadukhin, and M. S. Rabinovich, in: *Proc. 4th Int. Conf. Plasma Phys. and Controlled Nuclear Fusion Research, Madison, 1971*, Vol. 3, IAEA, Vienna (1971), pp. 63–77.
26. O. I. Fedyanin, "Studies of the magnetic configuration of an $\ell = 2$ stellarator," Preprint CLM-R 142, Culham (1975).
27. D. K. Akulina, Eh. D. Andryukhina, M. S. Berezhetskij, et al., in: *Proc. 6th Int. Conf. Plasma Phys. and Controlled Nuclear Fusion Research, Berchtesgaden, 1976*, Vol. 2, IAEA, Vienna (1977), pp. 115–126.
28. T. Mizuuchi, S. Morimoto, A. Iiyoshi, and K. Uo, *Nucl. Fusion*, **22**, 247–253 (1982).
29. R. P. Doerner, D. T. Anderson, F. S. B. Anderson, et al., *Phys. Fluids*, **29**, 3807–3812 (1986).

30. R. Takahashi, H. Matuura, T. Mizuuchi, et al., in: *Proc. Int. Stellarator/Heliotron Workshop, Kyoto University, 1986*, Vol. 1, Kyoto (1986), pp. 220–232.

31. K. Nishimura, K. Matsuoka, M. Fujiwara, et al., in: *Proc. 15th Symposium on Fusion Technology, Utrecht, 1988*, Vol. 1, Elsevier, North-Holland (1989), pp. 398–401.

32. R. Jaenicke, K. Schworer, E. Ascasibar, et al., in: *Proc. 16th Europ. Conf. on Controlled Fusion and Plasma Physics*, Vol. 13B, Part II, Venice (1989), pp. 627–630.

33. R. J. Colchin, F. S. B. Anderson, A. C. England, et al., *Rev. Sci. Instrum.*, **60**, 2680–2689 (1989).

34. J. H. Harris, T. C. Jernigan, F. S. B. Anderson, et al., *Fusion Technol.*, **17**, 51–61 (1990).

35. H. Yamada, K. Matsuoka, S. Okamura, K. Ida, and K. Nishimura, *Rev. Sci. Instrum.*, **61**, 686–692 (1990).

36. M. Murakami, S. C. Aceto, E. Anabitarte, et al., *Phys. Fluids*, **B3**, 2261–2269 (1991).

37. G. G. Lesnyakov, E. D. Volkov, A. V. Georgievskij, et al., *Nucl. Fusion*, **32**, 2157–2176 (1992).

38. U. Brossman, W. Dommaschk, F. Herrnegger, et al., in: *Proc. 9th Int. Conf. Plasma Phys. and Controlled Nuclear Fusion Research, Baltimore, 1982*, Vol. 3, IAEA, Vienna (1983), pp. 141–156.

39. B. A. Carreras, H. R. Hicks, J. A. Holmes, et al., *Phys. Fluids*, **26**, 3569–3579 (1983).

40. J. R. Cary, *Phys. Fluids*, **27**, 119–128 (1984).

41. L. Garcia, B. A. Carreras, J. H. Harris, H. R. Hicks, and V. E. Lynch, *Nucl. Fusion*, **24**, 115–129 (1984).

42. T. C. Hender, B. A. Carreras, L. A. Charlton, et al., *Nucl. Fusion*, **25**, 1463–1473 (1985).

43. J. R. Cary and J. D. Hanson, *Phys. Fluids*, **29**, 2464–2473 (1986).

44. P. Merkel, *J. Comput. Phys.*, **66**, 83–98 (1986).

45. J. F. Lyon, B. A. Carreras, K. K. Chipley, et al., *Fusion Technol.*, **10**, 179–226 (1986).

46. N. T. Besedin, Yu. K. Kuznetsov, and I. M. Pankratov, in: *Voprosy Atomnoi Nauki i Tekhniki: Termoyaderny Sintez* (Atomic Science and Technology: Thermonuclear Fusion) [in Russian], No. 3, Kurchatov Institute, Moscow (1987), pp. 18–20.

47. P. Merkel, *Nucl. Fusion*, **27**, 867–871 (1987).

48. I. S. Danilikin and O. E. Khadin, in: *Voprosy Atomnoi Nauki i Tekhniki: Termoyaderny Sintez* (Atomic Science and Technology: Thermonuclear Fusion) [in Russian], No. 1, Kurchatov Institute, Moscow (1988), pp. 41–45.

49. V. E. Bykov, A. V. Georgievskii, V. V. Demchenko, et al., in: *Voprosy Atomnoi Nauki i Tekhniki: Termoyaderny Sintez* (Atomic Science and Technology: Thermonuclear Fusion) [in Russian], No. 1, Kurchatov Institute, Moscow (1988), pp. 46–50.

50. M. A. Henderson, R. F. Gandy, J. D. Hanson, G. J. Hartwell, and D. G. Swanson, *Nucl. Fusion*, **28**, 1099–1104 (1988).

51. B. A. Carreras, N. Dominguez, L. Garcia, et al., *Nucl. Fusion*, **28**, 1195–1207 (1988).

52. G. Grieger, C. Beidler, E. Harmeyer, et al., in: *Proc. 12th Int. Conf. Plasma Phys. and Controlled Nuclear Fusion Research, Nice, 1982*, Vol. 2, IAEA, Vienna (1989), pp. 369–387.

53. Y. Nakamura, K. Ichiguchi, M. Wakatani, and J. L. Johnson, *J. Phys. Soc. Jpn.*, **58**, 3157–3174 (1989).

54. V. E. Bykov, A. A. Shishkin, J. Kisslinger, and F. Rau, "On vacuum field properties of the Uragan-2M torsatron standard configuration," Preprint IPP 2/301, Garching (1989).

55. S. M. Hamberger, B. D. Blackwell, L. E. Sharp, and D. B. Shenton, *Fusion Technol.*, **17**, 123–130 (1990).

56. C. Alejaldre, J. J. A. Gozalo, J. B. Perez, et al., *Fusion Technol.*, **17**, 131–139 (1990).

57. C. Beidler, G. Grieger, F. Herrnegger, et al., *Fusion Technol.*, **17**, 148–168 (1990).

58. A. Iiyoshi, M. Fujiwara, O. Motojima, N. Ohyabu, and K. Yamazaki, *Fusion Technol.*, **17**, 169–187 (1990).

59. Y. Nakamura, M. Wakatani, J. N. Leboeuf, et al., *Fusion Technol.*, **19**, 217–233 (1991).

60. K. Harafuji, T. Hayashi, and T. Sato, *J. Comput. Phys.*, **81**, 169–192 (1989).

61. T. Hayashi, T. Sato, and A. Takei, *Phys. Fluids*, **B2**, 329–337 (1990).

62. T. Hayashi, A. Takei, N. Ohyabu, et al., in: *Proc. 13th Int. Conf. Plasma Phys. and Controlled Nuclear Fusion Research, Washington, 1990*, Vol. 2, IAEA, Vienna (1991), pp. 143–150.

63. T. Hayashi, A. Takei, N. Ohyabu, and T. Sato, *Nucl. Fusion*, **31**, 1767–1770 (1991).

64. T. Hayashi, A. Takei, and T. Sato, *Phys. Fluids*, **B4**, 1539–1546 (1992).

65. T. Hayashi, T. Sato, W. Lotz, et al., in: *Proc. 14th Int. Conf. Plasma Phys. and Controlled Nuclear Fusion Research, Würzburg, 1992*, Vol. 2, IAEA, Vienna (1993), pp. 29–34.

66. T. Hayashi, T. Sato, P. Merkel, J. Nuhrenberg, and U. Schwenn, *Phys. Plasmas*, **1**, 3262–3268 (1994).

67. T. Hayashi, T. Sato, N. Nakajima, et al., in: *Proc. 15th Int. Conf. Plasma Phys. and Controlled Nuclear Fusion Research, Seville, 1994*, Vol. 3, IAEA, Vienna (1996), pp. 309–312.

68. H. Grad, *Phys. Fluids*, **10**, 137–154 (1967).

69. J. R. Cary and M. Kotschenreuther, *Phys. Fluids*, **28**, 1392–1401 (1985).

70. G. Grieger, H. Renner, and H. Wobig, *Nucl. Fusion*, **25**, 1231–1242 (1985).

71. K. Uo, *Nucl. Fusion*, **25**, 1243–1248 (1985).

72. J. Fujita and K. Matsuoka, *Nucl. Fusion*, **25**, 1253–1257 (1985).

73. D. J. Lees, *Nucl. Fusion*, **25**, 1259–1265 (1985).

74. S. Yoshikawa and T. H. Stix, *Nucl. Fusion*, **25**, 1275–1279 (1985).

75. UW/TSL Group, *Nucl. Fusion*, **25**, 1281–1284 (1985).

76. L. M. Kovrizhnykh and I. S. Shpigel', *Nucl. Fusion*, **25**, 1285–1288 (1985).

77. B. A. Carreras, G. Grieger, J. H. Harris, et al., *Nucl. Fusion*, **28**, 1613–1694 (1988).

78. J. L. Johnson, C. R. Oberman, R. M. Kulsrud, and E. A. Frieman, *Phys. Fluids*, **1**, 281–296 (1958).

79. A. Lenard, *Phys. Fluids*, **7**, 1875–1877 (1964).
80. J. L. Johnson, *Phys. Fluids*, **7**, 2015–2016 (1964).
81. J. B. Taylor, *Phys. Fluids*, **8**, 1203–1205 (1965).
82. H. P. Furth, in: *Plasma Physics, Trieste, 1964*, IAEA, Vienna (1965), pp. 391–409.
83. H. P. Furth, J. Killen, M. N. Rosenbluth, and B. Coppi, in: *Proc. 2nd Int. Conf. Plasma Phys. and Controlled Nuclear Fusion Research, Culham, 1965*, Vol. 1, IAEA, Vienna (1966), pp. 103–125.
84. R. M. Kulsrud, in: *Proc. 2nd Int. Conf. Plasma Phys. and Controlled Nuclear Fusion Research, Culham, 1965*, Vol. 1, IAEA, Vienna (1966), pp. 127–143.
85. B. McNamara, K. J. Whiteman, and J. B. Taylor, in: *Proc. 2nd Int. Conf. Plasma Phys. and Controlled Nuclear Fusion Research, Culham, 1965*, Vol. 1, IAEA, Vienna (1966), pp. 145–167.
86. L. S. Solov'ev and V. D. Shafranov, in: *Proc. 2nd Int. Conf. Plasma Phys. and Controlled Nuclear Fusion Research, Culham, 1965*, Vol. 1, IAEA, Vienna (1966), pp. 169–190.
87. V. D. Shafranov, *Plasma Phys.*, **13**, 349–352 (1971).
88. T. Coor, S. P. Cunningham, R. A. Ellis, M. A. Heald, and A. Z. Kranz, *Phys. Fluids*, **1**, 411–420 (1958).
89. W. Stodiek, R. A. Ellis, Jr., and J. G. Gorman, *Nucl. Fusion*, Supplement, Part 1, 193–198 (1962).
90. R. M. Sinclair, S. Yoshikawa, W. L. Harries, and J.O. Kessler, *Phys. Fluids*, **6**, 937–945 (1963).
91. K. Bol, *Phys. Fluids*, **7**, 1855–1863 (1964).
92. K. M. Young, *Plasma Phys.*, **16**, 119–152 (1974).
93. J. M. Greene and J. L. Johnson, *Phys. Fluids*, **4**, 875–890 (1961).
94. M. D. Kruskal and R. M. Kulsrud, *Phys. Fluids*, **1**, 265–274 (1958).
95. D. V. Bartlett, G. Cannici, G. Cattanei, et al., in: *Proc. 8th Int. Conf. Plasma Phys. and Controlled Nuclear Fusion Research, Brussels, 1980*, Vol. 1, IAEA, Vienna (1981), pp. 185–196.
96. A. Iiyoshi, M. Sato, O. Motojima, et al., *Phys. Rev. Lett.*, **48**, 745–748 (1982).

97. M. Fujiwara, K. Matsuoka, K. Yamazaki, et al., in: *Proc. 14th Europ. Conf. on Controlled Fusion and Plasma Physics*, Vol. 11D, Part I, Madrid (1987), pp. 404–404C.

98. V. E. Bykov, A. V. Georgievskij, V. V. Demchenko, et al., *Fusion Technol.*, **17**, 140–147 (1990).

99. K. Nishimura, K. Matsuoka, M. Fujiwara, et al., *Fusion Technol.*, **17**, 86–100 (1990).

100. O. Motojima, K. Akaishi, M. Asao, et al., in: *Proc. 13th Int. Conf. Plasma Phys. and Controlled Nuclear Fusion Research, Washington, 1990*, Vol. 3, IAEA, Vienna (1991), pp. 513–523.

101. G. Grieger, W. Lotz, P. Merkel, et al., *Phys. Fluids*, **B4**, 2081–2091 (1992).

102. I. S. Danilkin, L. M. Kovrizhnykh, and I. S. Shpigel', in: *Voprosy Atomnoi Nauki i Tekhniki: Termoyaderny Sintez* (Atomic Science and Technology: Thermonuclear Fusion) [in Russian], No. 3, Kurchatov Institute, Moscow (1990), pp. 31–38.

103. K. Matsuoka, S. Okamura, K. Nishimura, et al., *Fusion Eng. Design*, **26**, 135–140 (1995).

104. S. Okamura, K. Matsuoka, K. Nishimura, et al., *Nucl. Fusion*, **35**, 283–296 (1995).

105. H. Yamada, K. Ida, H. Iguchi, et al., *Nucl. Fusion*, **32**, 25–32 (1992).

106. K. Miyamoto, *Nucl. Fusion*, **18**, 243–284 (1978).

107. V. D. Shafranov, *Nucl. Fusion*, **20**, 1075–1083 (1980).

108. J. L. Shohet, in: *Fusion* (edited by E. Teller), Vol. 1, part A, Academic Press, New York (1981), pp. 243–289.

109. D. J. Lees, in: *Plasma Physics and Nuclear Fusion Research* (edited by R. D. Gill), Academic Press (1981), pp. 385–399.

110. J. L. Johnson, G. Grieger, D. J. Lees, M. S. Rabinovich, J. L. Shohet, and K. Uo, *IEEE Transactions on Plasma Science*, PS-9, 142–149 (1981).

111. M. S. Rabinovich, in: *Itogi Nauki i Tekhniki: Fizika Plazmy* (Advances in Science and Technology: Plasma Physics) [in Russian, edited by V. D. Shafranov], Vol. 2, VINITI, Moscow (1981), pp. 6–79.

112. J. L. Johnson, *Nucl. Technology/Fusion*, **2**, 340–361 (1982).

113. B. B. Kadomtsev and V. D. Shafranov, *Usp. Fiz. Nauk*, **139**, 399–434 (1983). English translation: *Sov. Phys. Uspekhi*, **26**, 207 (1983).

114. V. D. Shafranov, in: *Itogi Nauki i Tekhniki: Fizika Plazmy* (Advances in Science and Technology: Plasma Physics) [in Russian, edited by V. D. Shafranov], Vol. 8, VINITI, Moscow (1988), pp. 131–171.

115. A. Gibson, in: *Proc. Conf. on Nuclear Fusion Reactors, Culham, 1969*, UKAEA Culham Laboratory (1970), pp. 233–241.

116. V. N. Pyatov and A. A. Shishkin, *Nucl. Fusion*, **6**, 937–941 (1976).

117. I. S. Danilkin, *Fiz. Plazmy*, **4**, 1033–1043 (1978). English translation: *Sov. J. Plasma Phys.*, **4**, 576–581 (1978).

118. N. S. Gorbachev, Yu. K. Kuznetsov, and I. B. Pinos, *Nucl. Fusion*, **20**, 341–347 (1980).

119. P. J. Fielding and W. N. G. Hitchon, "Plasma equilibrium in toroidal $\ell = 3$ stellarators," Preprint CLM–P605, Culham (1980).

120. P. J. Fielding and W. N. G. Hitchon, *J. Plasma Phys.*, **24**, 453–478 (1980).

121. P. J. Fielding and W. N. G. Hitchon, *Nucl. Fusion*, **21**, 775–785 (1981).

122. The T.F.R. Group, in: *Proc. 6th Europ. Conf. on Controlled Fusion and Plasma Physics*, Vol. 2, Moscow (1973), pp. 20–36.

123. J. Hugill and A. Gibson, *Nucl. Fusion*, **14**, 611–619 (1974).

124. O. Kluber, S. Corti, J. Gernhardt, et al., in: *Proc. 6th Int. Conf. Plasma Phys. and Controlled Nuclear Fusion Research, Tokyo, 1974*, Vol. 1, IAEA, Vienna (1975), pp. 179–189.

125. M. Fujiwara, S. Itoh, K. Matsuoka, et al., *Jpn. J. Appl. Phys.*, **14**, 675–690 (1975).

126. J. L. Anderson, R. S. Booth, R. J. Colchin, R. V. Miskell, and J. M. Bailey, *Nucl. Fusion*, **16**, 629–637 (1976).

127. D. Grove, V. Arunasalam, K. Bol, et al., in: *Proc. 6th Int. Conf. Plasma Phys. and Controlled Nuclear Fusion Research, Berchtesgaden, 1976*, Vol. 1, IAEA, Vienna (1977), pp. 21–32.

128. F. Schneider, in: *Proc. 10th Symposium on Fusion Technology, Padova, 1978*, Vol. 2, Pergamon Press (1979), pp. 1013–1018,

129. V. D. Shafranov, in: *Proc. 2nd Int. Conf. Plasma Theory, Kiev, 1974* [in Russian], Naukova Dumka, Kiev (1976), pp. 43–48.

130. L. E. Zakharov and V. D. Shafranov, in: *Reviews of Plasma Physics* (edited by M. A. Leontovich and B. B. Kadomtsev), Vol. 11, Energoizdat, Moscow (1982), pp. 118–235. English translation: Consultants Bureau, New York (1986), pp. 153–302.

131. V. D. Pustovitov and V. D. Shafranov, in: *Reviews of Plasma Physics* [in Russian], (edited by B. B. Kadomtsev), Vol. 15, Energatomoizdat, Moscow (1987), pp. 146–291. English translation: Consultants Bureau, New York (1990), pp. 163–326.

132. V. D. Shafranov, *Zh. Eksp. Teor. Fiz.*, **33**, 710–722 (1957). English translation: *Sov. Phys. JETP*, **6**, 545 (1958).

133. H. Grad and H. Rubin, in: *Proc. of Second United Nations International Conference on the Peaceful Uses of Atomic Energy, Geneva, 1958*, Vol. 31, United Nations, New York (1958), pp. 190–197.

134. R. Lust and A. Schluter, *Z. Naturforsch.*, **12a**, 850–854 (1957).

135. J. M. Greene and J. L. Johnson, *Phys. Fluids*, **4**, 1417–1426 (1961).

136. J. L. Johnson, J. M. Greene, and K. E. Weimer, *Nucl. Fusion*, **2**, 16–22 (1962).

137. J. M. Greene, J. L. Johnson, and K. E. Weimer, *Plasma Phys.*, **8**, 145–155 (1966).

138. J. L. Johnson, "Comments concerning a numerical model for studying MHD properties of stellarators," Preprint IPP 6/162, Garching (1977).

139. M. I. Mikhailov, *Fiz. Plazmy*, **6**, 45–54 (1980). English translation: *Sov. J. Plasma Phys.*, **6**, 25–30 (1980).

140. L. M. Kovrizhnykh and S. V. Shchepetov, *Fiz. Plazmy*, **6**, 976–986 (1980). English translation: *Sov. J. Plasma Phys.*, **6**, 533–538 (1980).

141. L. E. Zakharov, M. I. Mikhailov, V. I. Pistunovich, et al., in: *Proc. 8th Int. Conf. Plasma Phys. and Controlled Nuclear Fusion Research, Brussels, 1980*, Vol. 1, IAEA, Vienna (1981), pp. 313–328.

142. M. I. Mikhailov and V. D. Shafranov, in: *Proc. 10th Europ. Conf. on Controlled Fusion and Plasma Physics*, Vol. 1, Moscow (1981), pp. 393–396.

143. M. I. Mikhailov and V. D. Pustovitov, *Pis'ma Zh. Eksp. Teor. Fiz.*, **34**, 388–391 (1981). English translation: *JETP Lett.*, **34**, 368–370 (1981).

144. M. I. Mikhailov and V. D. Shafranov, *Plasma Phys.*, **24**, 233–242 (1982).

145. V. D. Pustovitov, *Fiz. Plazmy*, **8**, 473–483 (1982). English translation: *Sov. J. Plasma Phys.*, **8**, 265–271 (1982).

146. M. I. Mikhailov, V. D. Pustovitov, and V. D. Shafranov, *Pis'ma Zh. Eksp. Teor. Fiz.*, **35**, 152–154 (1982). English translation: *JETP Lett.*, **35**, 186–188 (1982).

147. V. D. Pustovitov, *Fiz. Plazmy*, **9**, 575–584 (1983). English translation: *Sov. J. Plasma Phys.*, **9**, 335–340 (1983).

148. Eh. D. Andryukhina, M. S. Berezhetskij, M. A. Blokh, et al., in: *Proc. 8th Int. Conf. Plasma Phys. and Controlled Nuclear Fusion Research, Brussels, 1980*, Vol. 1, IAEA, Vienna (1981), pp. 199–207.

149. L. M. Kovrizhnykh and S. V. Shchepetov, *Fiz. Plazmy*, **7**, 419–427 (1981). English translation: *Sov. J. Plasma Phys.*, **7**, 229–233 (1981).

150. L. M. Kovrizhnykh and S. V. Shchepetov, *Fiz. Plazmy*, **7**, 965–967 (1981). English translation: *Sov. J. Plasma Phys.*, **7**, 527–528 (1981).

151. L. M. Kovrizhnykh and S. V. Shchepetov, *Pis'ma Zh. Eksp. Teor. Fiz.*, **33**, 441–444 (1981). English translation: *JETP Lett.*, 33, 427–430 (1981).

152. I. S. Danilkin, L. M. Kovrizhnykh, and S. V. Shchepetov, in: *Proc. 10th Europ. Conf. on Controlled Fusion and Plasma Physics*, Vol. 1, Moscow (1981), pp. 397–400.

153. L. M. Kovrizhnykh and S. V. Shchepetov, *Nucl. Fusion*, **23**, 859–867 (1983).

154. L. M. Kovrizhnykh, *Plasma Phys. Contr. Fusion*, **26**, 195–207 (1984).

155. H. R. Strauss, *Plasma Phys.*, **22**, 733–745 (1980).

156. H. R. Strauss and D.A. Monticello, *Phys. Fluids*, **24**, 1148–1155 (1981).

157. D. Lortz and J. Nuhrenberg, *Z. Naturforsch.*, **37a**, 876–878 (1982).

158. V. D. Pustovitov, *Nucl. Fusion*, **23**, 1079–1088 (1983).

159. V. D. Pustovitov, V. D. Shafranov, L. E. Zakharov, et al., in: *Proc. 9th Int. Conf. Plasma Phys. and Controlled Nuclear Fusion Research, Baltimore, 1982*, Vol. 2, IAEA, Vienna (1983), pp. 541–556.

160. V. D. Shafranov, *Phys. Fluids*, **26**, 357–364 (1983).

161. L. M. Kovrizhnykh and S. V. Shchepetov, *Usp. Fiz. Nauk*, **148**, 637–670 (1986). English translation: *Sov. Phys. Uspekhi*, **29**, 343 (1986).

162. V. D. Shafranov and E. I. Yurchenko, *Nucl. Fusion*, **8**, 329–339 (1968).

163. C. Mercier, *Suppl. Nucl. Fusion*, Part 2, 801–808 (1962).

164. C. Mercier and H. Luc, "The MHD approach to the problem of plasma confinement in closed magnetic configurations," in: *Lectures in Plasma Physics*, EUR 5127e, Commission of European Communities, Luxembourg (1974).

165. J. M. Greene and J. L. Johnson, *Phys. Fluids*, **5**, 510–517 (1962).

166. L. S. Solov'ev, *Zh. Eksp. Teor. Fiz.*, **53**, 626–643 (1967). English translation: *Sov. Phys. JETP*, **26**, 400 (1968).

167. G. Bateman, *MHD Instabilities*, MIT Press, Cambridge, MA (1978).

168. L. S. Solov'ev, *Zh. Eksp. Teor. Fiz.*, **53**, 2063–2069 (1967). English translation: *Sov. Phys. JETP*, **26**, 1167 (1968).

169. L. S. Solov'ev, in: *Reviews of Plasma Physics* (edited by M.A. Leontovich), Vol. 6, Atomizdat, Moscow (1972), pp. 210–290. English translation: Consultants Bureau, New York (1975), pp. 239–331.

170. V. D. Shafranov and E. I. Yurchenko, *Nucl. Fusion*, **9**, 285–289 (1969).

171. D. Lortz and J. Nuhrenberg, *Nucl. Fusion*, **17**, 125–133 (1977).

172. A. B. Mikhailovskii and V. D. Shafranov, *Zh. Eksp. Teor. Fiz.*, **66**, 190–199 (1974). English translation: *Sov. Phys. JETP*, **39**, 88–92 (1974).

173. B. A. Carreras, *Sov. J. Plasma Phys.*, **16**, 722–729 (1990).

174. L. A. Charlton and J.-N. Leboeuf, *Phys. Fluids*, **B5**, 2989–2998 (1993).

175. G. H. Neilson, F. S. B. Anderson, D. B. Batchelor, et al., in: *Proc. 15th Europ. Conf. on Controlled Fusion and Plasma Heating*, Vol. 12B, Part II, Dubrovnik (1988), pp. 486–489.

176. J. H. Harris, M. Murakami, B. A. Carreras, et al., *Phys. Rev. Let.*, **63**, 1249–1252 (1989).

177. M. Murakami, B. A. Carreras, J. H. Harris, et al., in: *Proc. 16th Europ. Conf. on Controlled Fusion and Plasma Physics*, Vol. 13B, Part II, Venice (1988), pp. 575–579.

178. J. H. Harris, E. Anabitarte, G. L. Bell, et al., *Phys. Fluids*, **B2**, 1353–1358 (1990).

179. J. H. Harris, L. A. Charlton., G. L. Bell, et al., in: *Proc. 13th Int. Conf. Plasma Phys. and Controlled Nuclear Fusion Research, Washington, 1990*, Vol. 2, IAEA, Vienna (1991), pp. 677–684.

180. N. Dominguez and V. E. Lynch, "Absence of second stability in ATF", Report ORNL/TM-13040, Oak Ridge National Laboratory, Oak Ridge, USA (1995).

181. G. Rewoldt and J. L. Johnson, *Nucl. Fusion*, **24**, 733–738 (1984).

182. J. L. Johnson, *Comput. Phys. Rep.*, **4**, 37–70 (1986).

183. B. A. Carreras, H. R. Hicks, J. A. Holmes, et al., *Nucl. Fusion*, **24**, 1347–1355 (1984).

184. Yu. K. Kuznetsov, M. I. Mikhailov, V. K. Pashnev, and V. M. Tonkopryad, *Nucl. Fusion*, **23**, 15–23 (1983).

185. J. P. Friedberg, P. A. Politzer, and Ph. Rosenau, *Phys. Fluids*, **27**, 2093–2100 (1984).

186. D. K. Akulina, Eh. D. Andryukhina, G. S. Voronov, et al., in: *Proc. 7th Int. Conf. Plasma Phys. and Controlled Nuclear Fusion Research, Innsbruck, 1978*, Vol. 2, IAEA, Vienna (1979), pp. 287–301.

187. P. H. Rebut, D. V. Bartlett, G. Baumel, et al., in: *Proc. 10th Int. Conf. Plasma Phys. and Controlled Nuclear Fusion Research, London, 1984*, Vol. 1, IAEA, Vienna (1985), pp. 11–27.

188. L. A. Artsimovich and V. D. Shafranov, *Pis'ma Zh. Eksp. Teor. Fiz.*, **15**, 72–76 (1972). English translation: *JETP Lett.*, **15**, 51–54 (1972).

189. A. V. Bortnikov, Yu. T. Baiborodov, N. N. Brevnov, et al., in: *Proc. 6th Europ. Conf. on Controlled Fusion and Plasma Physics*, Vol. 1, Moscow (1973), pp. 165–168.

190. W. Feneberg and K. Lackner, in: *Proc. 6th Europ. Conf. on Controlled Fusion and Plasma Physics*, Vol. 1, Moscow (1973), pp. 209–212.

191. G. Laval and R. Pellat, in: *Proc. 6th Europ. Conf. on Controlled Fusion and Plasma Physics*, Vol. 2, Moscow (1973), pp. 64–74.

192. A. V. Bortnikov, N. N. Brevnov, S. N. Gerasimov, et al., in: *Proc. 6th Int. Conf. Plasma Phys. and Controlled Nuclear Fusion Research, Tokyo, 1974*, Vol. 1, IAEA, Vienna (1975), pp. 147–159.

193. M. Okabayashi and G. Sheffild, *Nucl. Fusion*, **14**, 263–265 (1974).

194. G. Laval, R. Pellat, and J. S. Soule, *Phys. Fluids*, **17**, 835–845 (1974).

195. P. Noll, in: *Proc. 7th Europ. Conf. on Controlled Fusion and Plasma Physics*, Vol. 2, Lausanne (1973), pp. 91–101.

196. H. Toyama, S. Inoue, K. Itoh, et al., in: *Proc. 6th Int. Conf. Plasma Phys. and Controlled Nuclear Fusion Research, Berchtesgaden, 1976*, Vol. 1, IAEA, Vienna (1977), pp. 323–334.

197. G. Cima, D. C. Robinson, C. L. Thomas, and A. J. Wootton, in: *Proc. 6th Int. Conf. Plasma Phys. and Controlled Nuclear Fusion Research, Berchtesgaden, 1976*, Vol. 1, IAEA, Vienna (1977), pp. 335–350.

198. M. S. Chu, D. R. Dobrott, G. E. Guest, et al., in: *Proc. 6th Int. Conf. Plasma Phys. and Controlled Nuclear Fusion Research, Berchtesgaden, 1976*, Vol. 2, IAEA, Vienna (1977), pp. 387–394.

199. T. Ohkawa and H. G. Voorhies, *Phys. Rev. Lett.*, **22**, 1275–1277 (1969).

200. T. Ohkawa and T. H. Jensen, *Plasma Phys.*, **12**, 789–797 (1970).

201. T. Ohkawa, C. C. Baker, N. H. Brooks, et al., in: *Proc. 6th Int. Conf. Plasma Phys. and Controlled Nuclear Fusion Research, Tokyo, 1974*, Vol. 1, IAEA, Vienna (1975), pp. 281–290.

202. R. L. Freeman, S. J. Adcock, J. F. Baur, et al., in: *Proc. 6th Int. Conf. Plasma Phys. and Controlled Nuclear Fusion Research, Berchtesgaden, 1976*, Vol. 1, IAEA, Vienna (1977), pp. 317–322.

203. S. V. Mirnov, *Physical Processes in the Tokamak Plasma* [in Russian], Energoatomizdat, Moscow (1983).

204. J. Wesson, *Tokamaks*, Clarendon Press, Oxford (1987).

205. L. M. Degtyarev, V. V. Drozdov, and S. Yu. Medvedev, *Numerical Modeling of Equilibrium and Stability of Toroidal Plasmas* [in Russian], Keldysh Institute of Applied Mathematics, the USSR Academy of Sciences, Moscow (1989).

206. B. B. Kadomtsev, in: *Itogi Nauki i Tekhniki: Fizika Plazmy* (Advances in Science and Technology: Plasma Physics) [in Russian, edited by V. D. Shafranov], Vol. 10, Part 1, VINITI, Moscow (1991), pp. 5–147.

207. T. Takeda and S. Tokuda, *J. Comput. Phys.*, **93**, 1–107 (1991).

208. E. Bertolimi, P. L. Mondino, and P. Noll, *Fusion Technol.*, **11**, 71–119 (1987).

209. F. Hofmann and S. C. Jardin, *Nucl. Fusion*, **30**, 2013–2022 (1990).

210. R. E. Bell, N. Asakura, S. Bernabei, et al., *Phys. Fluids*, **B2**, 1271–1279 (1990).

211. E. A. Lazarus, M. S. Chu, J. R. Ferron, et al., *Phys. Fluids*, **B3**, 2220–2229 (1991).

212. F. Hofmann, N. Pomphrey, and S. C. Jardin, *Nucl. Fusion*, **32**, 897–902 (1992).

213. F. Hofmann, J. B. Lister, M. Anton, et al., *Plasma Phys. Contr. Fusion*, **36**, B277–B287 (1994).

214. F. J. Helton and J. M. Greene, *J. Comput. Phys.*, **66**, 458–468 (1986).

215. R. Toschi, M. Chazalon, F. Engelmann, J. Nihoul, J. Raeder, and E. Salpietro, *Fusion Technol.*, **14**, 19–29 (1988).

216. F. Najmabadi and R. W. Conn, in: *Proc. 14th Int. Conf. Plasma Phys. and Controlled Nuclear Fusion Research, Wurzburg, 1992*, Vol. 3, IAEA, Vienna (1993), pp. 295–310.

217. Yu. A. Sokolov, *Fusion Eng. Design*, **25**, 159–167 (1994).

218. D. A. Humphreys, J. A. Leuer, A. G. Kellman, et al., *Fusion Technol.*, **26**, 331–339 (1994).

219. G. H. Neilson, D. B. Batchelor, D. N. Hill, et al., *Fusion Eng. Design*, **26**, 563–574 (1995).

220. R. J. Colchin, M. Murakami, E. Anabitarte, et al., *Phys. Fluids*, **B2**, 1347–1352 (1990).

221. J. F. Lyon, in: *Proc. 8th Int. Workshop on Stellarators, Kharkov, 1991*, IAEA, Vienna (1991), pp. 7–15.

222. G. Anania, J. L. Johnson, and K. E. Weimer, *Phys. Fluids*, **26**, 2210–2218 (1983).

223. G. Anania and J. L. Johnson, *Phys. Fluids*, **26**, 3070–3078 (1983).

224. V. E. Lynch, B. A. Carreras, L. A. Charlton, L. Garcia, T. C. Hender, H. R. Hicks, and J. A. Holmes, *J. Comput. Phys.*, **66**, 411–444 (1986).

225. M. Wakatani, Y. Nakamura, and K. Ichiguchi, *Fusion Eng. Design*, **15**, 395–413 (1992).

226. J. Nuhrenberg and R. Zille, *Phys. Lett.*, **A114**, 129–132 (1986).

227. J. Nuhrenberg and R. Zille, *Phys. Lett.*, **A129**, 113–117 (1988).

228. G. Grieger, C. Beidler, E. Harmeyer, et al., *Fusion Technol.*, **21**, 1767–1778 (1992).

229. O. Motojima, F. Sano, M. Sato, et al., *Nucl. Fusion*, **25**, 1783–1787 (1985).

230. V. D. Shafranov and L. E. Zakharov, *Nucl. Fusion*, **12**, 599–601 (1972).

231. Yu. V. Gutarev, Yu. K. Kuznetsov, V. K. Pashnev, and N. P. Ponomarnenko, *Fiz. Plazmy*, **14**, 286–291 (1988). English translation: *Sov. J. Plasma Phys.*, **14**, 164–167 (1988).

232. V. D. Pustovitov, in: *Proc. 15th Europ. Conf. on Controlled Fusion and Plasma Heating*, Vol. 12B, Part II, Dubrovnik (1988), pp. 502–505.

233. V. D. Pustovitov, *Fiz. Plazmy*, **14**, 1436–1443 (1988). English translation: *Sov. J. Plasma Phys.*, **14**, 840–844 (1988).

234. V. D. Pustovitov, *Nucl. Fusion*, **30**, 1523–1531 (1990).

235. V. D. Pustovitov, in: *Proc. 13th Int. Conf. Plasma Phys. and Controlled Nuclear Fusion Research, Washington, 1990*, Vol. 2, IAEA, Vienna (1991), pp. 301–310.

236. J. M. Greene, J. L. Johnson, and K. E. Weimer, *Phys. Fluids*, **14**, 671–683 (1971).

237. L. E. Zakharov and S. V. Putvinskii, in: *Itogi Nauki i Tekhniki: Fizika Plazmy* (Advances in Science and Technology: Plasma Physics) [in Russian, edited by V. D. Shafranov], Vol. 7, VINITI, Moscow (1985), pp. 4–79.

238. V. V. Bakaev, S. P. Bondarenko, V. V. Bronnikov, et al., in: *Proc. 10th Int. Conf. Plasma Phys. and Controlled Nuclear Fusion Research, London, 1984*, Vol. 2, IAEA, Vienna (1985), pp. 397–407.

239. S. Besshou, K. Ogata, K. Kondo, et al., in: *Proc. 21st Europ. Conf. on Controlled Fusion and Plasma Physics*, Vol. 18B, Part I, Montpellier (1994), pp. 420–423.

240. S. Besshou, K. Ogata, K. Kondo, et al., *Nucl. Fusion*, **35**, 173–182 (1995).

241. S. Besshou, K. Ogata, K. Kondo, et al., *Trans. Fusion Technol.*, **27**, 219–222 (1995).

242. S. P. Hirshman, W. I. van Rij, and P. Merkel, *Comput. Phys. Comm.*, **43**, 143–155 (1986).

243. R. N. Morris, J. C. Glowienka, G. H. Neilson, S. P. Hirshman, and P. Merkel, *Nucl. Fusion*, **29**, 2115–2123 (1989).

244. H. J. Gardner and K. Ichiguchi, "Free-boundary equilibrium studies for the Large Helical Device," Preprint NIFS–231, National Institute for Fusion Science, Nagoya, Japan (1993).

245. I. S. Danilkin and L.M. Kovrizhnykh, *Pis'ma Zh. Eksp. Teor. Fiz.*, **19**, 193–197 (1974). English translation: *JETP Lett.*, **19**, 119–121 (1974).

246. I. S. Danilkin and L. M. Kovrizhnykh, in: *Proc. 6th Int. Conf. Plasma Phys. and Controlled Nuclear Fusion Research, Tokyo, 1974*, Vol. 2, IAEA, Vienna (1975), pp. 163–175.

247. J. L. Shohet, D. T. Anderson, and J. A. Tataronis, *Nucl. Fusion*, **16**, 441–445 (1976).

248. T. S. Wang and T. H. Jensen, *Nucl. Fusion*, **18**, 1459–1465 (1978).

249. E. A. Matveeva and V. D. Pustovitov, *Pis'ma Zh. Eksp. Teor. Fiz.*, **45**, 216–219 (1987). English translation: *JETP Lett.*, **45**, 268–271 (1987).

250. E. A. Matveeva and V. D. Pustovitov, *Fiz. Plazmy*, **14**, 151–160 (1988). English translation: *Sov. J. Plasma Phys.*, **14**, 81–87 (1988).

251. V. D. Pustovitov, *Fiz. Plazmy*, **14**, 522–528 (1988). English translation: *Sov. J. Plasma Phys.*, **14**, 305–309 (1988).

252. A. B. Mikhailovskii, *Plasma Instabilities in Magnetic Confinement Systems* [in Russian], Atomizdat, Moscow (1978).

253. O. P. Pogutse and E. I. Yurchenko, in: *Reviews of Plasma Physics* (edited by M. A. Leontovich and B. B. Kadomtsev), Vol. 11, Energoizdat, Moscow (1982), pp. 56–117. English translation: Consultants Bureau, New York (1986), pp. 65–151.

254. L. E. Zakharov, V. D. Pustovitov, S. B. Semenov, A. A. Subbotin, and J. Peralto, "Simplified models for plasma equilibrium in a tokamak" [in Russian], Preprint IAE-4115/6, Kurchatov Institute, Moscow (1985).

255. V. D. Pustovitov, "Unified approach for the description of plasma equilibrium in tokamaks and stellarators" [in Russian], Preprint IAE-4474/6, Kurchatov Institute, Moscow (1987).

256. V. D. Pustovitov, *Fiz. Plazmy*, **14**, 101–104 (1988). English translation: *Sov. J. Plasma Phys.*, **14**, 63–65 (1988).

257. A. Gibson, *Phys. Fluids*, **10**, 1553–1560 (1967).

258. V. N. Kalyuzhnyj, V. V. Nemov, and A. A. Shishkin, *Nucl. Fusion*, **22**, 347–361 (1982).

259. J. C. Wesley, T. Angel, C. J. Armentrout, et al., in: *Proc. 8th Int. Conf. Plasma Phys. and Controlled Nuclear Fusion Research, Brussels, 1980*, Vol. 1, IAEA, Vienna (1981), pp. 35–42.

260. R. W. Moore, L. C. Bernanrd, V. S. Chan, et al., in: *Proc. 8th Int. Conf. Plasma Phys. and Controlled Nuclear Fusion Research, Brussels, 1980*, Vol. 1, IAEA, Vienna (1981), pp. 283–290.

261. V. D. Pustovitov, *Fiz. Plazmy*, **15**, 756–760 (1989). English translation: *Sov. J. Plasma Phys.*, **15**, 437–440 (1989).

262. V. D. Pustovitov, *Nucl. Fusion*, **30**, 1079–1086 (1990).

263. R. Chodura and A. Schlüter, *J. Comput. Phys.*, **41**, 68–88 (1981).

264. T. Ohkawa, *Kakuyugo Kenkyu*, **20**, 557–570 (1968).

265. T. Ohkawa, *Kakuyugo Kenkyu*, **22**, 395–404 (1969).

266. D. Yu. Sychugov and S. V. Shchepetov, in: *Proc. 8th Int. Workshop on Stellarators, Kharkov, 1991*, IAEA, Vienna (1991), pp. 313–316.

267. I. S. Danilkin and S. V. Shchepetov, *Fiz. Plazmy*, **13**, 392–402 (1987). English translation: *Sov. J. Plasma Phys.*, **13**, 220–228 (1987).

268. V. V. Drozdov and V. D. Pustovitov, in: *Voprosy Atomnoi Nauki i Tekhniki: Termoyaderny Sintez* (Atomic Science and Technology: Thermonuclear Fusion) [in Russian], No. 2, Kurchatov Institute, Moscow (1989), pp. 16–19.

269. V. V. Drozdov, M. Yu. Isaev, M. I. Mikhailov, V. D. Pustovitov, and V. D. Shafranov, in: *Proc. 12th Int. Conf. Plasma Phys. and Controlled Nuclear Fusion Research, Nice, 1988*, Vol. 2, IAEA, Vienna (1989), pp. 611–621.

270. G. G. Lesnyakov and V. I. Petrenko, in: *Proc. 8th Int. Workshop on Stellarators, Kharkov, 1991*, IAEA, Vienna (1991), pp. 99–102.

271. V. I. Perevozchikov, *Fiz. Plazmy*, **18**, 946–950 (1992). English translation: *Sov. J. Plasma Phys.*, **18**, 492–494 (1992).

272. M. V. Malyshev and V. D. Pustovitov, in: *Proc. 20th Europ. Conf. on Controlled Fusion and Plasma Physics*, Vol. 17C, Part I, Lisboa (1993), pp. 429–432.

273. D. L. Grekov and A. V. Zolotukhin, in: *Proc. IAEA Tech. Committee Meeting on Stellarators and Other Helical Confinement Systems*, Garching (1993), pp. 158–163.

274. J. F. Lyon, G. Grieger, F. Rau, et al., *Nucl. Fusion*, **30**, 1695–1715 (1990).

275. N. N. Bogolyubov and Yu. A. Mitropolskii, *Asymptotic Methods in the Theory of Nonlinear Oscillations*, Gordon and Breach, New York (1961).

276. A. I. Morozov and L. S. Solov'ev, in: *Reviews of Plasma Physics* (edited by M. A. Leontovich), Vol. 2, Gosatomizdat, Moscow (1963), pp. 177–261. English translation: Consultants Bureau, New York (1966), pp. 201–297.

277. T. C. Hender and B. A. Carreras, *Phys. Fluids*, **27**, 2101–2109 (1984).

278. J. Todoroki, *J. Phys. Soc. Jpn.*, **56**, 128–138 (1987).

279. J. Todoroki, *J. Phys. Soc. Jpn.*, **58**, 3979–3992 (1989).

280. V. D. Pustovitov, in: *Itogi Nauki i Tekhniki: Fizika Plazmy* (Advances in Science and Technology: Plasma Physics) [in Russian, edited by V. D. Shafranov], Vol. 13, VINITI, Moscow (1993), pp. 3–84; V. D. Pustovitov, *J. Plasma Fusion Res.*, (formerly Kakuyugo Kenkyu), **70**, 943–991 (1994).

281. A. B. Kuznetsov, Yu. K. Kuznetsov, D.Yu. Sychugov, and S. V. Shchepetov, in: *Voprosy Atomnoi Nauki i Tekhniki: Termoyaderny Sintez* (Atomic Science and Technology: Thermonuclear Fusion) [in Russian], No. 3, Kurchatov Institute, Moscow (1991), pp. 69–75.

282. E. D. Andryukhina and O. I. Fedyanin, *Fiz. Plazmy*, **3**, 792–798 (1977). English translation: *Sov. J. Plasma Phys.*, **3**, 447–450 (1977).

283. F. Herrnegger, P. Merkel, and J. L. Johnson, *J. Comput. Phys.*, **66**, 445–457 (1986).

284. A. A. Shishkin, in: *Voprosy Atomnoi Nauki i Tekhniki: Termoyaderny Sintez* (Atomic Science and Technology: Thermonuclear Fusion) [in Russian], No. 2, Kurchatov Institute, Moscow (1987), pp. 15–19.

285. V. D. Pustovitov, *Fiz. Plazmy*, **21**, 1027–1038 (1995). English translation: *Plasma Phys. Rep.*, **21**, 969–980 (1995).

286. V. D. Pustovitov, *Fiz. Plazmy*, **16**, 732–737 (1990). English translation: *Sov. J. Plasma Phys.*, **16**, 424–427 (1990).

287. F. Herrnegger and E. K. Maschke, *Nucl. Fusion*, **14**, 119–121 (1974).

288. D. Pfirsch and E. Rebhan, *Nucl. Fusion*, **14**, 547–551 (1974).

289. H. Oshiyama and Y. Fukutani, *Nucl. Fusion*, **14**, 793–796 (1974).

290. J. P. Christiansen and J. B. Taylor, *Nucl. Fusion*, **22**, 111–115 (1982).

291. M. S. Chu, *Nucl. Fusion*, **27**, 611–615 (1987).

292. N. A. Madden and R. J. Hastie, *Nucl. Fusion*, **34**, 519–526 (1994).

293. A. B. Mikhailovskii, *Fiz. Plazmy*, **22**, 1111–1118 (1996). English translation: *Plasma Phys. Rep.*, **22**, 1009 (1996).

294. D. J. Braams, "The interpretation of tokamak magnetic diagnostics: status and prospects," Preprint IPP 5/2, Garching (1985).

295. I. S. Danilkin, in: *Stellarators, Trudy Fiz. Inst. Akad. Nauk SSSR* [in Russian], Vol. 65, Moscow (1973), pp. 26–49. English translation: *Proc. Lebedev Phys. Inst. Acad. Sci. USSR*, Vol. 65 (1973).

296. D. K. Lee, J. H. Harris, S. P. Hirshman, and G. H. Neilson, *Nucl. Fusion*, **28**, 1351–1364 (1988).

297. W. A. Cooper, S. P. Hirshman, and D. K. Lee, *Nucl. Fusion*, **29**, 617–627 (1989).

298. Y. Nakamura, M. Wakatani, and J. L. Johnson, "Choice of LHD stellarator equilibrium for the comparison of stability property calculations with KSTEP and other MHD stability codes," Preprint PPLK-R-58, PPL Kyoto University, Kyoto (1992).

299. Y. Nakamura, T. Matsumoto, M. Wakatani, et al., *J. Comput. Phys.*, **128**, 43–57 (1996).

300. N. Nakajima, J. Todoroki, and M. Okamoto, *Kakuyugo Kenkyu*, **68**, 395–403 (1992).

301. R. B. White, A. H. Boozer, and R. Hay, *Phys. Fluids*, **25**, 575–576 (1982).

302. A. H. Boozer, *Phys. Fluids*, **27**, 2441–2445 (1984).

303. J. R. Cary, C. L. Hedrick, and J. S. Tolliver, *Phys. Fluids*, **31**, 1586–1600 (1988).

304. J. Todoroki, *J. Phys. Soc. Jpn.*, **62**, 1562–1582 (1993).

305. K. C. Shaing and J. D. Callen, *Phys. Fluids*, **26**, 3315–3326 (1983).

306. N. Nakajima, M. Okamoto, J. Todoroki, Y. Nakamura, and M. Wakatani, *Nucl. Fusion*, **29**, 605–616 (1989).

307. K. Y. Watanabe, N. Nakajima, M. Okamoto, K. Yamazaki Y. Nakamura, and M. Wakatani, *Nucl. Fusion*, **35**, 335–345 (1995).

308. H. E. Mynick, T. K. Chu, and A. H. Boozer, *Phys. Rev. Lett.*, **48**, 322–326 (1982).

309. K. C. Shaing and S. A. Hokin, *Phys. Fluids*, **26**, 2136–2139 (1983).

310. L. M. Kovrizhnykh, *Nucl. Fusion*, **24**, 851–936 (1984).

311. V. E. Bykov, A. V. Georgievskii, V. G. Peletminskaya, Yu. F. Sergeev, A. V. Khodyachikh, and A. A. Shishkin, in: *Voprosy Atomnoi Nauki i Tekhniki: Termoyaderny Sintez* (Atomic Science and Technology: Thermonuclear Fusion) [in Russian], No. 4, Kurchatov Institute, Moscow (1984), pp. 19–29.

312. V. E. Bykov, A. V. Georgievskij, V. G. Peletminskaya, A. V. Khodyachikh, and A. A. Shishkin, *Nucl. Fusion*, **24**, 1195– 1203 (1984).

313. L. M. Kovrizhnykh, *Nucl. Fusion*, **25**, 1391–1397 (1985).

314. C. D. Beidler, W. N. S. Hitchon, W. I. van Rij, S. P. Hirshman, and J. L. Shohet, *Phys. Rev. Lett.*, **58**, 1745–1747 (1987).

315. C. D. Beidler, W. N. S. Hitchon, D. L. Grekov, and A. A. Shishkin, *Nucl. Fusion*, **30**, 405–411 (1990).

316. A. Kato, Y. Nakamura, and M. Wakatani, *J. Phys. Soc. Jpn.*, **60**, 494–511 (1991).

317. I. S. Danilkin and O. E. Khadin, in: *Voprosy Atomnoi Nauki i Tekhniki: Termoyaderny Sintez* (Atomic Science and Technology: Thermonuclear Fusion) [in Russian], No. 3, Kurchatov Institute, Moscow (1992), pp. 39–44.

318. M. S. Smirnova and A. A. Shishkin, *Nucl. Fusion*, **32**, 1147–1160 (1992).

319. G. H. Neilson and J. H. Harris, *Nucl. Fusion*, **27**, 711–724 (1987).

320. L. D. Landau and E. M. Lifshitz, *Electrodynamics of Continuous Media*, Pergamon, New York (1960).

321. V. D. Shafranov, *At. Energ.*, **19**, 175 (1965).

322. V. D. Pustovitov, *J. Plasma Fusion Res.* (formerly *Kakuyugo Kenkyu*), **69**, 34–40 (1993).

323. I. S. Gradshtein and I. M. Ryzhik, *Tables of Series, Products and Integrals*, Plenum Press, New York (1963).

324. R. D. Woolley, M. Bell, J. Coonrod, et al., *Fusion Technol.*, **8**, 1807–1812 (1985).

325. W. Woyke, J. Gernhardt, O. Gruber, et al., in: *Proc. 19th Europ. Conf. on Controlled Fusion and Plasma Physics*, Vol. 16C, Part I, Innsbruck (1992), pp. 455–458.

326. K. Kurihara, *Nucl. Fusion*, **33**, 399–412 (1993).

327. J. B. Lister, F. Hofmann, J.-M. Moret, et al., *Fusion Technol.*, **32**, 321–373 (1997).

328. A. Portone, R. Albanese, Yu. V. Gribov, et al., *Fusion Technol.*, **32**, 374–389 (1997).

329. V. D. Pustovitov, *Nucl. Fusion*, **36**, 583–591 (1996).

330. V. D. Pustovitov, *Nucl. Fusion*, **36**, 1281–1290 (1996).

331. A. I. Morozov, *Pis'ma Zh. Tekh. Fiz.*, **16**, No. 15, 86–89 (1990). English translation: *Sov. Tech. Phys. Lett.*, **16**, (1990).

332. A. I. Morozov, *Fiz. Plazmy*, **18**, 305–316 (1992). English translation: *Plasma Phis. Rep.*, **18**, (1992).

333. S. Besshou, V. D. Pustovitov, N. Fujita, et al., *Phys. Plasmas*, **5**, 481–485 (1998).

334. K. Tomabechi, J.R. Gilleland, Yu. A. Sokolov, R. Toschi, and the ITER Team, *Nucl. Fusion*, **31**, 1135–1224 (1991).

335. O. Motojima, K. Y. Watanabe, A. Sagara, et al., *Trans. Fusion Technol.*, **27**, 264–269 (1995).

336. N. A. Manzyuk, V. N. Pyatov, A. M. Rozhkov, and V. P. Sebko, *Fiz. Plazmy*, **3**, 14–17 (1977). English translation: *Sov. J. Plasma Phys.*, **3**, 7–9 (1977).

337. D. Dorst, A. Elsner, G. Grieger, et al., *Plasma Phys. Contr. Fusion*, **26**, 183–194 (1984).

338. G. Cattanei, D. Dorst, A. Elsner, et al., in: *Proc. 12th Europ. Conf. on Controlled Fusion and Plasma Physics*, Vol. 9F, Part I, Budapest (1985), pp. 393–396.

# FUNDAMENTALS OF STATIONARY PLASMA THRUSTER THEORY

A. I. Morozov and V. V. Savelyev

## Introduction

This review is devoted to very specific processes in stationary plasma propulsion devices with poloidal magnetic and electric fields and a dielectric channel (Fig. 1) [1–3]. At present, these accelerators with closed-drift electrons and an extended acceleration region (also called Hall thrusters) generate quasi-neutral multi-ampere ($\sim 1-50$ A) streams of ions of different species (from hydrogen to xenon) with particle energies of 50–1000 eV. They are mostly known as electric propulsion thrusters for spacecraft (see the Appendix for more details). Therefore, such devices are more frequently called "stationary plasma thrusters" (SPTs). We will use this term throughout the paper. SPTs were designed in 1960s from the basic idea of A. I. Morozov at the Kurchatov Atomic Energy Institute (AEI) (G. Ya. Shchepkin's laboratory). They were first launched into space in 1971 [4] and have since (most recently in 1997) been mounted onboard more than 50 Russian satellites. From 1999, these thrusters should be used on USA satellites and then perhaps on the satellites of other countries.

In addition, SPTs are now used in some countries in technological systems for processing the surface layers of different products (such as optical lens refining, magnetic memory formation, corrosion endurance enhancement, etc.).

SPTs are worthy of serious study. However, in the course of research it has become clear that the physical processes in SPTs are extremely complicated, despite the simple construction of the devices. This is primarily due to the principal role that the electron interactions with the channel walls play together with volume processes. As a result, SPT performance is affected by both the state of the wall surface (micro- and macroshape and chemical composition of the surface layers) and the properties of plasma structures on Debye and electron-Larmor scales. Therefore, the construction of a self-consistent theory of SPT processes requires a kinetic description of not only heavy particles (atoms and ions), but of electrons as well.

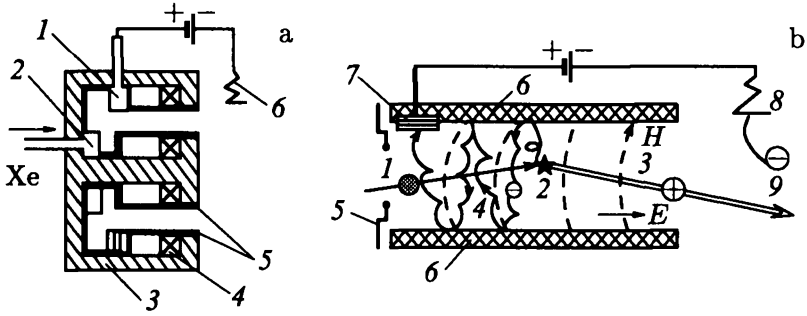


**Fig. 1.** (a) Principal scheme of an SPT. SPT units: *1* – anode, *2* – gas-distributor, *3* – magnetodriver with a ring and disk poles, *4* – coil, *5* – ring dielectric channel, *6* – gas-discharge source of electrons – the cathode. (b) Scheme of SPT processes. *1* – trajectory of a neutral atom, *2* – ionization, *3* – ion trajectory in the electric field, *4* – electron motion in the crossed fields, *5* – gas-distributor, *6* – dielectric channel's walls, *7* – anode, *8* – emitting cathode, *9* – electron escaping from the SPT together with the accelerated ion.

The major contribution to the SPT physics studies has been made by the Shchepkin–Morozov laboratory at the AEI,

as well as by A. I. Bugrova's laboratory at the Moscow Institute of Radiotechnics, Electronics, and Automatics (MIREA) with which the authors have collaborated for many years. In addition to these two groups, some important results were obtained earlier by Fishgoit–Melikov's group at the Central Institute for Avia-Motor Construction (CIAM), by Kim's group at the Moscow Aviation Institute (MAI), and by the "Fakel" Enterprise in Kaliningrad. At present, experimental, analytical, and numerical studies of SPT processes make them relatively clear. However, it seems that a quantitative theory (without adjustable coefficients) is still far off. Intensive joint efforts of theoreticians, specialists on numerical modeling, and experimenters are required.

Below we shall try to present a sufficiently complete description of the physical processes in SPTs. For this purpose, while focusing on theoretical models, we shall supplement them briefly with existing experimental data if necessary.

It should be stressed from the very beginning that SPTs are not the only type of electric propulsion thrusters (EPTs) that have been designed or flown in space. Nevertheless, they are the favorite among EPTs and are the only ones to have been systematically operated in space. One more note — SPTs have many "relatives." These include ion magnetrons [5, 6], anodic layer thrusters (ALTs) [7–9], multi-lens accelerators [10], etc. We will not, however, deal with all of them here; neither will we be concerned with the engineering aspects of EPTs in general or of SPTs in particular (see, for example, [11]).

This review paper reflects the experience of the authors and their colleagues in theoretical and experimental studies of processes in SPTs. Some of these works have been performed with the financial help of the Russian Fund for Fundamental Research (RFFR) and the French SEP Enterprise.

A. I. Bugrova and her colleagues actively assisted in the preparation of this review. The authors deeply acknowledge them all. We also sincerely thank B. B. Kadomtsev, who initiated this review.

# 1. General picture of processes in SPTs

## 1.1. Principal scheme of an SPT

SPT schemes are presented in Fig. 1. A magnetic system creates a quasi-radial magnetic field increasing to the outlet of the thruster. The magnetic force lines are convex toward the anode (Fig. 1.1a, b). The field strength is chosen such that the electron Larmor radius $\rho_e$ is much smaller than the discharge gap length $L$ (usually $L/\rho_e \sim 20-30$, $\langle\rho_i\rangle/L \sim 100$), and the ion radius $\rho_i$ is much larger than $L$:

$$\rho_e \ll L \ll \rho_i. \tag{1.1}$$

The actual magnetic field strength at maximum is $\sim$150–300 Oe; the channel length is $\sim$2–3 cm. When the magnetic field strength increases toward the outlet, the plasma configuration is macrostable (see the next section and Section 6.1 for more details), and so a sufficiently stable electric field distribution is formed within the channel. To a high accuracy, the longitudinal electric field strength $E_z$ in the main part of the channel is proportional to the radial magnetic field component:

$$E_z \sim H_r. \tag{1.2}$$

Consider the "skeletal" scheme of SPT processes shown in Fig. 1b. In the presence of crossed $E$ and $H$ fields, electrons drift in the azimuthal direction, forming an azimuthal current. The interaction of this current with the radial magnetic field creates the Ampere force

$$\mathbf{f} = \frac{1}{c}\left[\mathbf{j}, \mathbf{H}\right], \tag{1.3}$$

which accelerates the plasma. The processes in such electric and magnetic fields allow the following interpretation in terms of two-liquid plasmodynamics. The magnetic force lines with spiral-like electron trajectories wound around them can be considered as some "electron system" transparent for ions, resembling to the

electron system of an ion source. Such filaments are equipotentials in the zone with constant plasma density, as follows from Ohm's law (see Section 2). The presence of the azimuthal drift in this model is the azimuthal "rotation" of the magnetic line system as a whole.

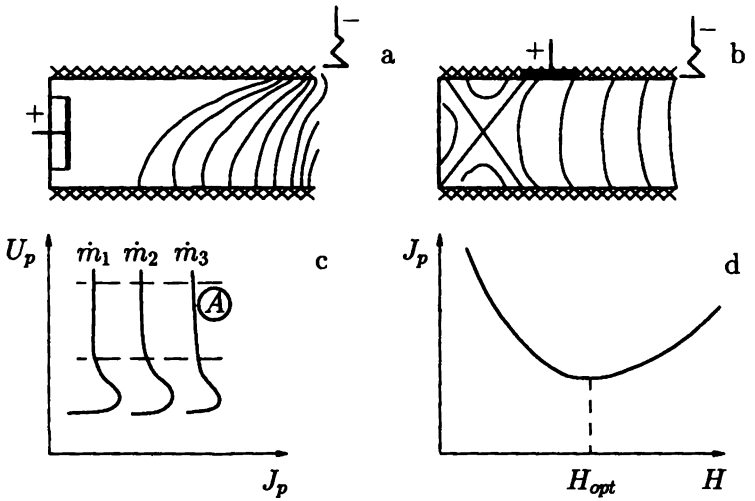


**Fig. 1.1.** SPT characteristics. (a) Morphology of the magnetic force lines in a first-generation SPT (EOL-1, M-70, M-100). (b) Morphology of the magnetic force lines in a second-generation SPT (SPT-ATON). (c) The typical shape of the volt-ampere characteristics of an SPT at $\dot{m}_3 > \dot{m}_2 > \dot{m}_1$ (A – working region). (d) The magneto-ampere characteristics of an SPT. The optimal magnetic field provides a minimum discharge current for given $\dot{m}$ and $U_p$.

Neutral atoms come from the gas distributor into the rotating cloud of electrons and are ionized close to the anode (Fig. 1b).

Since the neutral atom density in this zone is $\sim 3 \times 10^{13}\,\mathrm{cm}^{-3}$ and the ion density is $\sim 10^{12}\,\mathrm{cm}^{-3}$, collisions of atoms and ions with each other can be neglected, which is not the case for electrons. Thus, an ion formed at a point with potential $\Phi^*$,

if it does not collide with the walls and is not secondarily ionized, is accelerated by the $E$-field and leaves the channel with energy

$$\mathcal{E}_i = e\Phi^*. \tag{1.4a}$$

Experiment shows that the mean ion energy in the outgoing flux is

$$\langle \mathcal{E}_i \rangle \approx (2/3-3/4)eU_p, \tag{1.4b}$$

where $U_p$ is the potential difference between the cathode and anode. The degree of ionization of the xenon atom flux, which is the main propellant used in the SPT channel, is very high ($\sim 95-98\%$), especially in view of the very large effective thickness of the ionization zone of $\sim 4-5$ mm.

Electrons formed during the ionization, although appearing in the magnetic field, must come to the anode. There are several factors that help this. First, the ionization occurs in a region of relatively weak (in comparison with $H_{\max}$) field, so their Larmor radius is relatively large. Second, the density of the neutral ionization gas is sufficiently high in the near-anode region, and the ratio of the ion elastic collision cross-section to the ionization cross-section is about 10 at typical SPT energies $\langle \mathcal{E}_e \rangle$. Lastly, a significant role in electron supply to the anode is played by the "near-wall" conductivity (see Section 1.2).

After coming to the anode, electrons pass through the outer circuit and are then emitted from the cathode (Fig. 1), thus forming an ion flux leaving the SPT. This provides not only bulk, but also "current" neutralization of the ion flux.

It is seen from the above that three regions can be distinguished inside the SPT channel (Fig. 1b). In the near-anode region (A), the ionization is low and the current is carried here mostly by electrons. In the ionization zone (I), the current is maintained both by electrons going to the anode and ions going to the SPT outlet. Finally, in the acceleration zone (U) between the ionization zone and the channel outlet, the current in the channel is carried predominantly by ions. There is clearly an

approximate equality (provided that singly ionized ions prevail)

$$(J_e)_{\mathrm{A}} \approx (J_e + J_i)_{\mathrm{I}} \approx (J_i)_{\mathrm{U}} \approx J_p, \tag{1.5}$$

where $J_p$ is the discharge current in the external chain.

It follows from the above that in a well-organized process, i.e., for practically total ionization of the propellant and low destruction of ions on the walls,

$$J_p \approx \frac{e}{M}\dot{m}(1 + \alpha_2), \tag{1.6}$$

where $e$ and $M$ are the elementary charge and ion mass, respectively, $\dot{m}$ is the propellant mass rate, and $\alpha_2$ is the fraction of doubly ionized ions. In currently used SPTs, this fraction may be as high as 10–15% and comparatively weakly depends on the voltage. Thus, the discharge current is determined by the propellant consumption to a high accuracy. Indeed, the volt-ampere characteristics shown in Fig. 1.1c clearly indicate the discharge current saturation at a given mass rate $\dot{m}$. Here the saturation current is directly proportional to $\dot{m}$ in full agreement with Eq. (1.6).

Clearly, a change in the propellant rate proportionally alters the propulsion and the discharge current, and a change in the discharge voltage also alters the propulsion but due to the increase in the velocity of the outflowing ions (1.4). Instead of (1.4) one can write that the outflow velocity is

$$V_M = \sqrt{\frac{2e}{M}(1 + \alpha_2)(U_p - \Delta)}. \tag{1.7}$$

Here $\Delta$ is the "expense" of the voltage to ionization. At $\Delta = 0$ and $V_M \sim 20\ \mathrm{km\,s^{-1}}$, we have $U_p \approx 250\ \mathrm{V}$.

The propulsion efficiency (including losses in the magnetic system and the cathode) is calculated as

$$\eta_T = \frac{F^2}{2\dot{m}_\Sigma U_p J_p} \tag{1.8}$$

and is typically of the order of 50–60% (the highest efficiency relates to the second-generation SPT). This formula takes into account that the magnetic coils turn on consecutively with the discharge and the cathode works in the "autoregime," i.e., due to the potential difference ($\sim 10$ V) between the cathode and the plasma flow with a positive potential which is being neutralized. The quantity $\dot{m}_\Sigma$ is the total propellant mass rate in the thruster $\dot{m}_D$ and in the cathode $\dot{m}_K$. Typically $\dot{m}_K \sim 0.1\dot{m}_D$. Finally, $U_p$ is the voltage between the anode and cathode plus the voltage on the magnetic field coils ($U_{\text{coil}} \leq 10$ V).

## 1.2. Specifics of physical processes in SPTs

From the physical point of view, an SPT is a totally novel gas-discharge system that is unlike any other classical or recent discharge device (tokamak, MHD-generator, etc.). We do not wish to present here a full review of SPT processes (see below for more details), and will only be concerned with two principal points: the macrostability of the plasma configuration and the role of electron collisions with the dielectric channel walls.

### *1.2.1. The discharge stability in SPTs*

In the 1910s, it was apparently Taundsen who first derived the formula for the electronic plasma conductivity across a magnetic field:

$$\sigma_\perp = \frac{\sigma_0}{1 + (\omega_e \tau_e)^2} \propto \frac{1}{H^2}. \tag{1.9}$$

Here $\omega_e$ is the electron gyrofrequency, $\tau_e$ is the electron free-path time, and $\sigma_0$ is the plasma conductivity in the absence of a magnetic field.

Equation (1.9) implies that the plasma conductivity must rapidly decrease with the magnetic field strength.

However, this dependence of $\sigma_\perp$ on $H$ was not confirmed for almost over 50 years. At the beginning of the 1940s, D. Bohm

suggested a formula for the "real" plasma conductivity across a magnetic field based on experimental data:

$$\sigma^B = \theta \frac{enc}{H}. \tag{1.10}$$

Here $n$ is the electron concentration, and $\theta \sim 1/16$ is the numerical coefficient. The appearance of Bohm's formula convinced practically all gas-discharge physicists that $\sigma_\perp \sim 1/H$. However experiments carried out at the Kurchatov AEI in 1963–64 in the Shchepkin–Morozov laboratory showed that this is not the case. The value of $\sigma_\perp$ proved to be at least an order of magnitude smaller than that given by Bohm's formula. Several years later the same result was obtained in tokamaks.

The "Bohm barrier" has been overcome because in the SPT channel a large-scale azimuthal asymmetrical instability, the so-called "spike" that "shorted" the anode with the cathode, was suppressed. It was later found that the "spike" disappears if the magnetic field increases from the anode to the outlet, more precisely if

$$(\mathbf{V}_i, \nabla)\frac{n}{H} < 0. \tag{1.11}$$

But a magnetic field increasing toward the outlet was initially suggested for the SPT (see Fig. 1.1). This is explained by the fact that at the beginning of 1960s magnetic-force-line equipotentialization became known, and the chosen geometry of force lines (convex toward the anode) provided repulsion of ions from the walls by the electric field, thus reducing the channel erosion. This geometry of force lines of a curl-free magnetic field corresponds to condition (1.11).

### *1.2.2. Electron collisions with the channel walls in SPTs*

The principal features of SPTs are: a long free path for electrons in the presence of the magnetic force lines set against the channel walls, and also the presence of a bulk longitudinal electric field and a high electron temperature ($T_e > 15\,\text{eV}$). The

combination of these four factors gives rise to at least four specific phenomena.

1. First of all, the electron distribution inside the channel is principally non-Maxwellian. This is due to the fact that the electrons inside the channel are separated into three groups. The first group includes electrons that do not directly reach the walls (here we suppose smooth walls with roughness much lower than the electron Larmor radius) due to the much higher potential in the middle of the channel than on the walls and also due to Debye layers. The second group is formed by electrons that reach the walls and scatter inelastically off them. Finally, the electrons scattered elastically by the wall belong to the third group (Section 3.2).

2. Because of the high electron temperature, the near-wall Debye layers can lose stability due to the increase of the secondary electron emission coefficient and convert from static into dynamic structures occupying a notable part of the channel.

3. Scattering of electrons on the walls leads to an additional electron transfer across the magnetic field. The efficiency of this mechanism, called "near-wall conductivity" (NWC), depends (on a sufficiently smooth wall) on the Debye voltage jump near the wall. (However, if there are sufficiently high azimuthal asymmetric prominences in the system, the NWC will be determined by these prominences and may weakly depend on the Debye voltage jump.) The higher the jump, the smaller the number of electrons that reach the dielectric surface and the smaller the electron current, and vice versa. This autoregulation improves the thruster's characteristics.

4. In the very first experiments, it was found that parts of the insulator adjacent to the outlet are dispersed by ion bombardment, which restricts the thruster resource. The general shape of the surface formed under the action of ion bombardment is well known. Such a surface either remains smooth, or small-scale prominences oriented mostly across the incident ion flux form on the surface (the so-called "pike's tongue").

However, a long-term ($> 1000$ h) endurance test of an SPT performed at the "Fakel" Enterprise (Kaliningrad) revealed something quite different. A periodic structure oriented not across but along the ion flux appeared on the insulator. The period was of the order of the electron Larmor radius or of the cycloid height in the existing magnetic fields. Although the mechanism of such anomalous erosion formation is not yet fully understood, there is no doubt that electrons play a major role here, with their impacts on the insulator ultimately leading to its "dissociation" and the tearing-off of separate atoms or small clusters (see Section 4.2 for more details).

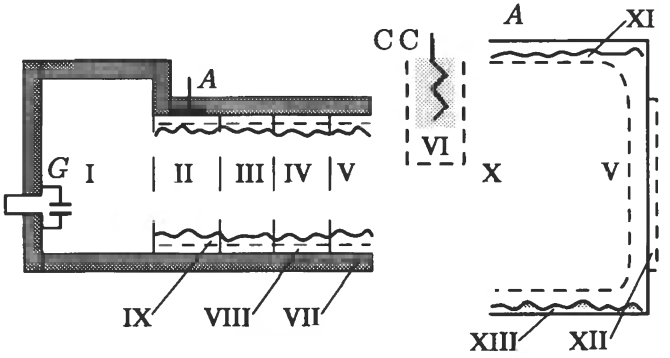


**Fig. 1.2.** Quasi-autonomous functional units of the SPT-ATON. G – gas-distributor, A – anode, V – vacuum chamber, CC – cathode-compensator, I–IX – see the text, X – plasma stream in the vacuum chamber, XI – a plasma boundary layer at the chamber walls, XII – a sputtered "target," XIII – powdering on the chamber walls.

## 1.3. Quasi-autonomous functional units of SPTs

As noted above, the picture of physical processes in SPTs is very complicated. At the same time, the working region in the thruster can be subdivided into quasi-autonomous units with a simpler functional scheme. For a second-generation SPT these blocks are shown in Fig. 1.2. (In the first-generation SPTs a

clearly distinguished buffer space was absent.) Let us list them and note the characteristic processes in each of them separately.

(I) — Buffer space. The propellant is supplied here from the gas-distributor G. The density of Xe here is about $10^{13}-10^{14}\,\mathrm{cm}^{-3}$. Some electrons penetrate into this region from the channel and cause weak ionization. The magnetic field strength is about $10-20\,\mathrm{Oe}$. In the optimal regime, the electric field in the buffer volume focuses the forming ions into the acceleration channel (Fig. 5.1). Powdering of the rear wall in some cases is indicative of the formation of negative ions in the vacuum chamber (see Section 8).

(II) — Near-anode zone. This is a natural continuation of the buffer space. Here the degree of ionization is also relatively small ($\sim 10\%$ of the rate). The motion of electrons across the magnetic field occurs mostly due to their collisions with the walls (the near-wall conductivity). Binary collisions with heavy particles notably, although lessso, contribute to the electron transfer process.

(II-A) — The anode and the Debye layer (DL) near it. So far there is no data about the near-anode DL properties under working conditions. However, if the target is made of the wrong material (see Section 8), the anode can become covered with a non-conducting layer, and then micro-arcs may induce anode fracturing through this coating.

(III) — Ionization zone. In optimal regimes, this is a comparatively small (when using Xe) region with a thickness of $\sim 4\,\mathrm{mm}$, in which most of the propellant is ionized. As a rule, the electron temperature here is maximal $\left(\langle T_e\rangle \sim 20\,\mathrm{eV}\right)$, and the electron density reaches a maximum at the end of this zone. In many cases, a significant (up to 20%) fraction of the doubly ionized ions ($\mathrm{Xe}_e^{++}$) is formed in the ionization zone. A high level of UHF noise is typical of this zone.

(IV) — Main acceleration zone. In this zone, the ions acquire most of their final energy. Here it is important to provide an electric equipotential configuration convex toward the anode. In this case the ions will be focused to the middle of the chan-

nel, which drastically reduces the erosion of insulators. In SPTs currently in use, the ions are not pushed totally away from the walls. This is connected with xenon ionization in the acceleration zone and the necessity of providing contact between the flux and the channel walls to reduce the excessive electrons due to NWC. Some contact of the plasma flux with the wall is needed to clean the surface of the insulators (channel walls) of modified surface layers formed due to both the inflow of "contaminating" particles from the vacuum chamber and reactions between active mixtures in the propellant (although in tiny amounts) and the insulator materials.

(V) — Output region. Here some very complicated processes occur, which are related to three factors: (1) Injection of electrons into the magnetic field from the cathode-compensator (CC), near which there is no magnetic field. (2) The simultaneous change of the ion flux neutralization mechanism. While the neutralization was initially due to the channel electrons drifting mostly in the azimuthal direction, after passing the input zone this neutralization is accomplished by the CC electrons dragged by the ion flux. (3) An important feature is that the magnetic field does not increase along the ion motion and, on the contrary, decreases. This stimulates the development of azimuthally asymmetric macro-oscillations, since the fundamental condition (1.11) is violated. It is also evident that the injection of electrons from the CC zone into the magnetic field is an intrinsically dissipative process. Since the plasma density here, as well as in the whole system, is low, the dissipation is caused not by particle collisions but by UHF oscillations. This fact has also been confirmed experimentally (see Section 3.5). The capture of electrons by the outgoing ion flux is also a dissipative process and is accompanied by UHF-noise as well.

(VI) — The neutralization unit, including the CC, the "plasma bridge" that connects the working space of the CC (in the existing models it is an empty cathode with the propellant flowing through it), and the plasma flow. The plasma bridge is needed to get rid of the influence of the bulk electron charge on

their transport into the flux outgoing from the SPT. Apart from numerous papers devoted to empty cathodes as such, the processes occurring in the neutralization block VI have been poorly studied, since this unit does not cause difficulties in practical performance. Now we wish to consider the "small-scale" functional units VII–IX.

(VII) — Surface layer of a small-crystal insulator (at present, smooth insulators are used in SPTs). The insulator should, in addition to the natural requirements of being mechanically strong, thermally resistant, and erosion resistible, have an appropriate dependence of the secondary electron emission coefficient $\sigma$ on the electron energy $\varepsilon_p$. Namely, the value of $\sigma^*$ at which $\sigma(\varepsilon^*) = 1$ must be $\sim 2kT_e$, since otherwise either the NWC or the Debye layer is broken (see block VIII). Therefore, insulators with a high boron content with $\varepsilon^* \sim 30 - 40\,\mathrm{eV}$ are used in SPTs.

(VIII) — Debye (non-quasi-neutral) layers close to the insulators. In plasma systems with a low electron temperature (for example, in glow discharges), where $kT_e \ll \varepsilon^*$, the potential jump on the DL is determined from the condition of equality of local ion and electron fluxes to a given element of the wall surface:

$$j_{i,n} = j_{0e}(1 - \sigma_0) \exp\left(-\frac{eU_d}{kT_e}\right), \quad U_d > 0. \tag{1.12}$$

However, in SPTs $\sigma$ is of order unity and, especially during oscillations, can much exceed unity. Under such conditions a dynamic structure is formed instead of the "reliable" and "quiet" DL, which is discussed below in Section 3.3. The presence of such a structure that adjusts to the parameters of the flux core is an important SPT feature.

(IX) — Region of relaxation of the electron flux "reflected" from the walls (ERR). To a large extent the ERR is the NWC zone. The electron flux scattered either by a vibrating DL or by collisions with the insulator surface has parameters (in particular, the mean drift velocity) differing from those in the flux

core. This naturally gives rise to the formation of complex structures near the walls, generates spatial oscillations of the current density, and enhances the UHF-oscillations.

Finally, regions X, XI, and XII are related to the intrinsic chamber processes, and we shall be concerned with these in Section 8. If the SPT performs in space, the processes outside the thruster are mainly due to the interaction of the plasma flux with the terrestrial magnetic field and ionospheric plasma (Section 8).

## 1.4. General system of equations and boundary conditions for SPT processes

From the brief description of the main processes in SPTs, it is seen that self-consistent modeling can be done only using the kinetics of the atoms, ions, and electrons, and Maxwell's equations

$$\frac{Df_{0\alpha}}{Dt} = S_{0\alpha}, \quad \frac{Df_{i\beta}}{Dt} = S_{i\beta}, \quad \frac{Df_e}{Dt} = S_e, \qquad \hat{M}\,[\mathbf{E}, \mathbf{H}] = \mathbf{J}\,[f_{i\alpha}, f_e]. \tag{1.13}$$

Here the last equality symbolically represents the system of Maxwell equations. The indices $\alpha$ and $\beta$ refer to the numbers of excited levels of atoms and ions. To system (1.13) must be added boundary conditions for the distribution functions such as

$$f_k^+(\mathbf{V}, \mathbf{P}, t) = \sum_{k_1} \hat{S}_{k,k_1}(\mathbf{V}, \mathbf{V}_1', \mathbf{P}, t, \mathbf{P}_1', t')\, f_{k_1}^-(\mathbf{V}_1', \mathbf{P}_1', t'). \tag{1.14}$$

Here $f_{k_1}^-(\mathbf{V}_1', \mathbf{P}_1', t')$ is the distribution function of particles of type $k_1$ incident on the surface at the time $t'$ near the point $\mathbf{P}'$, $f_k^+(\mathbf{V}, \mathbf{P}, t)$ is the distribution function of the "secondary" particles, and $\hat{S}_{k,k_1}$ is the operator for the process $f_{k_1}^- \to f_k^+$.

Under the general formulation used, the boundary conditions imposed on $\mathbf{E}$ and $\mathbf{H}$ are, in general, traditional.

But system (1.13) does not describe all processes to be taken into account when studying and optimizing SPTs. This

system must be completed with the transfer equation of radiation in atomic lines in the buffer and near-anode zones. This is connected with the fact that for small neutral atom velocities ($1-3\times10^4\,\mathrm{cm\,s^{-1}}$) and low charged particle densities ($\sim10^{12}\,\mathrm{cm^{-3}}$), the Doppler and Stark spectral line broadenings are small. So the Lorentz line profile broadening starts playing a major role when the photon free-path length is determined by a very large cross-section:

$$\sigma_L = \pi\lambda^2, \tag{1.15}$$

where $\lambda$ is the radiation wavelength.

One of the most important SPT characteristics is the lifetime, which in reality is determined both by erosion (change in the geometry $\Gamma$) of insulators and by their secondary-emission characteristics $\sigma$. This generates additional systems of equations, which can be symbolically written in the form

$$\frac{\partial\Gamma}{\partial t} = A(f_0, f_i, f_e, \chi), \tag{1.16a}$$

$$\frac{\partial\sigma}{\partial t} = B(f_0, f_i, f_e, \chi), \tag{1.16b}$$

$$\frac{\partial\chi}{\partial t} = C(f_0, f_i, f_e, \chi). \tag{1.16c}$$

Here $\chi$ is the set of crystal-chemical characteristics of the near-surface layers.

In this review, of the three equations (1.16) we will consider only the first (Section 5).

Broadly, the problem of the total description of real processes in SPTs is very complicated. In addition, at present we ignore many terms both in the operator $\hat{S}_{k,k_1}$ and in Eq. (1.16), since processes occurring on the surface in the presence of strong ion and electron bombardment are not studied.

Under such circumstances, a necessary condition for effective development of SPT theory includes, on the one hand, a close connection with experiment, and on the other hand, the development of a theory for the separate local units described above. At this stage of research, one should try to

exploit the most simplified models by minimizing their dimension, using hydrodynamic models where possible (see Section 7). One should also thoroughly analyze quasi-autonomous ("non-consistent") models for the dynamics of separate components by considering other models as some "background," whose parameters are taken from experiment, from "other" theories, or *a priori*.

# 2. Magnetic and electric fields in SPTs

## 2.1. Magnetic fields in SPTs

As noted above, the main requirement on the magnetic field in the SPT channel is that its strength must increase toward the outlet. This requirement is consistent with all experimental data. Simple theoretical considerations in favor of this fact will be considered below in Sections 2.3 and 7.3.

However, within the framework of this requirement the choice of specific force line configurations is very broad, and depending on the regimes, the channel size, and the vacuum conditions, the optimal magnetic configurations can substantially differ from one another. Now this choice is mainly made experimentally, in particular based on the fact that the highest performance characteristics are obtained using the "symmetrical" (with respect to the middle channel surface) configurations with a real zero of the magnetic field. The simplest analytical expressions for the scalar magnetic potential $\phi_m(r, z)$ that satisfy the two conditions mentioned above are given by the formula ($\mathbf{H} = \nabla\phi_m$)

$$\phi_m = H_0 R(1 + qz/L)\ \ln(r/R). \tag{2.1}$$

Note that this expression was used by A. I. Morozov for construction of the first theoretical schemes in 1962–1963. One should stress, however, that the real optimal fields are described by more complex expressions.

The magnetic field strength for a given configuration is characterized by its maximal value which is usually reached at

the channel outlet and is $H_m = 200$–$300$ Oe. The choice of $H_m$ is made by measuring the magneto-ampere characteristic (MAC), i.e., the dependence of the discharge current on $H_m$. A typical MAC is shown in Fig. 1.1d. It is seen that in the beginning $J_p$ sharply drops with $H_m$ as $J_p \sim H^{-2}$; then "saturation" occurs, followed by a slow increase with oscillations. The optimal value $H_m^{\text{opt}}$ of $H_m$ is such, that the discharge current is minimal. The interpretation of the MAC is obvious: for $H_m < H_m^{\text{opt}}$, the electron transfer in the channel is close to the classical value, and for $H_m > H_m^{\text{opt}}$ it is anomalous.

One more remark about the SPT magnetic field is the following. The reaction from the momentum given to the flux is passed to the magnetic field. In the one-dimensional case we may write the equation

$$\frac{H^2}{8\pi} + \rho V^2 = \text{const.} \tag{2.2}$$

It follows from here that the maximum thrust density produced by an SPT is

$$f_{\max} = (\rho V^2)_{\max} = \frac{H_m^2}{8\pi}. \tag{2.3}$$

Substituting $H_m = 300$ Oe into this equation, we obtain $f_{\max} \approx 3.6\,\text{g}\,\text{cm}^{-1}$. The real maximum value of $f$ obtained by the SPT A-4 without overloading the insulators was $\sim 0.4\,\text{g}\,\text{cm}^{-2}$. Given Eq. (1.3), we find the azimuthal drift current, which for the SPT A-4 with a mean channel radius of $R_0 = 2.5$ cm (see Fig. A.1, the Appendix) in the regime $\dot{m} = 3\,\text{mg}\,\text{s}^{-1}$, $U_p = 400$ V, and for a thrust of $F = 8$ g is

$$(J_\theta)_A = e \int n \frac{cE}{H}\, dS_\theta = \frac{10F}{2\pi R_0 H_C} = 28.5\,\text{A}. \tag{2.4}$$

This azimuthal current is almost an order of magnitude higher than the discharge current $J_p \sim 3$ A. In Eq. (2.4), the integration is performed over the area $\mathbf{S}_\theta$ — the $(r, z)$-section of the zone occupied by the plasma. $H_C$ is the mean magnetic field strength, which we accepted to be $H_C = 200$ Oe.

It is easy to see that the azimuthal current $J_\theta$ used above produces a magnetic field $H_J \sim 15\,\mathrm{Oe}$ inside the channel. This is a significant value, especially for diagnostic purposes. In particular, if coils are put on the insulator, appropriately joined and connected with an oscillograph, then by turning on and off the discharge (keeping the power at the magnetic coils constant), one can obtain signals on the oscillograph screen that are proportional to $J_\theta$. Moreover, in this way one can estimate the size of the region occupied by this current [12].

## 2.2. "Equipotentialization" of the magnetic force lines. Magnetic drift surfaces

As mentioned above, the acceleration of ions in SPTs is due to a volume superthermal electric field. The main factor preventing the creation of such a field is the high mobility of electrons. Thus, in order to study the electrostatic field in a plasma one should first of all consider the equations of electron dynamics. The situation is simplest in a hydrodynamic model for an ideal barotropic electron gas:

$$\frac{\partial n}{\partial t} + \operatorname{div}(n\mathbf{u}) = 0, \quad \mathbf{u} \equiv \mathbf{v}_e, \tag{2.5a}$$

$$m_e n \frac{d\mathbf{u}}{dt} + \nabla P_e = e\left(\mathbf{E} + \frac{1}{c}[\mathbf{u}, \mathbf{H}]\right), \tag{2.5b}$$

$$P_e = P_e(n). \tag{2.5c}$$

Here we have neglected ohmic resistance, i.e., the term $\mathbf{j}/\sigma$, with respect to $\mathbf{E}$. Indeed, by assuming typical values $j \sim 0.1\,\mathrm{A\,cm^{-2}}$ and Coulomb conductivity at $T_e \sim 10\,\mathrm{eV}$, we obtain $\sigma \sim 3\times10^{14}$ (in absolute units), and, consequently, $j/\sigma \sim 3\times10^{-4}\,\mathrm{V\,cm^{-1}} \ll 100\,\mathrm{V\,cm^{-1}}$.

In real SPTs, the electron inertia may be neglected, and so instead of the Euler–Lorentz equation (2.5b) one can use the "ohmic approximation" to study stationary and low-frequency

processes, i.e., the equation

$$\frac{\nabla P_e}{en_e} - \mathbf{E} = \frac{1}{c}[\mathbf{u}, \mathbf{H}]. \tag{2.6}$$

The barotropic condition (2.5c) enables us to introduce the thermal enthalpy $W = \int dP(n)/n$, and the assumption of quasi-stationarity of processes — the electric potential $\Phi$. Ultimately, Ohm's law takes the form

$$\nabla\left(\Phi + \frac{W_e(n)}{e}\right) = \frac{1}{c}[\mathbf{u}, \mathbf{H}]. \tag{2.7}$$

It is seen from here that the function

$$\Phi_T = \Phi + W_e(n)/e \tag{2.8}$$

is constant along the magnetic field lines. At present, $\Phi_T$ is referred to as a "thermalized potential." Ascribing an index $\gamma$ to the magnetic force lines, one can write [13]

$$\Phi_T = \Phi_T(\gamma). \tag{2.9}$$

Thus, the "equipotentialization" of the force lines (in the sense of $\Phi_T$, not $\Phi$) occurs in the plasma (Fig. 2.1a).

For an isothermal Maxwellian distribution

$$P = nkT_0, \quad T_0 = \text{const}, \tag{2.10a}$$

the thermalized potential is

$$\Phi_T(\gamma) = \Phi - \frac{kT_0}{e} \ln \frac{n}{n_0}. \tag{2.10b}$$

It is seen that the electron density is distributed according to Boltzmann's law along each force line. For barotropic conditions, the drift lines $\delta$ are also equipotentials:

$$\Phi_T = \Phi_T(\delta). \tag{2.11}$$

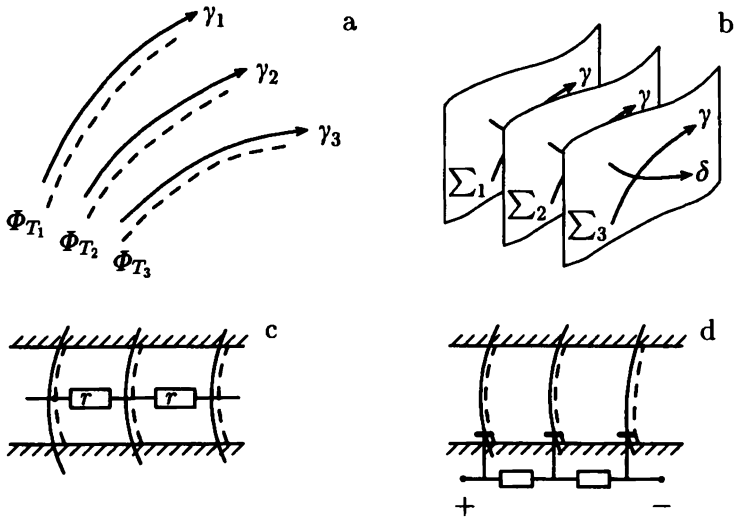


**Fig. 2.1.** Superthermal electrostatic fields in plasma. (a) Equipotentialization of the magnetic force lines. (b) Magnetic drift surfaces. (c) Fixing of the magnetic force line potential due to the internal plasma resistivity $r$. (d) Fixing of the magnetic force line potential using a system of near-wall electrodes.

Introducing "magnetic drift surfaces" (MDS) $\Sigma = (\gamma, \delta)$, using Eqs. (2.9) and (2.11) one can write (Fig. 2.1b)

$$\Phi_T = \Phi_T(\Sigma), \tag{2.12}$$

which implies the constancy of the thermalized potential on the magnetic drift surfaces. This statement, as well as Eq. (2.11), is valid only for barotropic conditions, when $\nabla P_e/n$ is the gradient of some function, or in some particular case when electron pressure can be neglected. The situation is quite different for the magnetic field line equipotentiality condition (2.9). Here a much weaker condition must be fulfilled:

$$P_e = P_e(n, \gamma). \tag{2.13}$$

However, as will be shown below in Section 3.2, in SPTs the conditions are barotropic for the main fraction of electrons outside the ionization zone. In addition, apart from a small number of exceptions, modern SPTs are axially symmetric, and in this case in the stationary regime $\Phi_T$ does not depend on the azimuth automatically. Thus, in such an SPT one can always consider the magnetic drift surfaces as being equipotential.

In another case of negligibly low electron temperature one can also use MDS. Under this condition

$$\Phi_T \approx \Phi_T(\Sigma) = \Phi(\mathbf{r}). \tag{2.14}$$

The magnetic drift surfaces are the basic "structural elements" of SPTs, and so it is important to study their stability. In this connection, we introduced above condition (1.11) of the MDS stability relative to the formation of azimuthal asymmetric "folds" on them. We shall return to this point in Section 6 in more detail. Equation (2.9) describes the change of the electric potential only along a magnetic field line. But it remains unclear how it alters from one line to another, i.e., the dependence of $\Phi_T$ on $\gamma$ remains undetermined. In principle, one can consider two schemes of "potential fixing" [14]. The first is connected with dissipative processes in the channel which cause the electron flux to thread all the plasma volume under study. An example is given by an SPT in which the electron flux passes from the outlet to the anode due to oscillations, collisions, and the near-wall conductivity. Different parts of the channel produce different resistance for the flux, and so a specific potential distribution accordingly sets in inside the channel (Fig. 2.1c).

The second potential-fixing scheme employs special emitting electrodes that are set on the channel walls (Fig. 2.1d). This method is based on the fact that the $\Phi$ jump near the electrode is of the order of $kT_e/e$ provided that the plasma processes do not lead to an anomalously high ("turbulent") conductivity. Thus when $\delta\varphi$ (the potential difference in the plasma) is much higher than $kT_e/e$, it may be fixed with special electrodes. It may ap-

pear at first glance that an arbitrary potential distribution may be created using such electrodes of greater or lesser complexity. However, this is not the case. It turns out that a given plasma density distribution in a given magnetic field unambiguously selects "natural" equipotential (in the sense $\Phi_T = \text{const}$) surfaces. To make "unnatural" surfaces equipotential costs appreciable energetic (more precisely, "current") losses.

## 2.3. The "loading" of magnetic force lines

So what is the "cost" of creating one or another potential relief in the plasma system with given $\mathbf{H}(\mathbf{r})$ and $n(\mathbf{r})$, and in particular of the "free" potential distribution? We assume "free" or "natural" potential distributions to be the potential reliefs such that no continuous (neglecting dissipation) exchange of electrons between the fixators and plasma occurs. In these cases, the electrons in plasma can be considered "autonomous," and their motion is reduced to oscillations along the magnetic field lines and drift transitions from one line to another. Therefore, a "natural" potential distribution is self-sustaining to the accuracy of small dissipative losses. In this section, we are interested in the equilibrium of the systems considered.

Let the process be stationary and the system have magnetic drift surfaces (2.7):

$$\operatorname{div}(n\mathbf{u}) = 0, \tag{2.15a}$$

$$\nabla\Phi_T = \frac{1}{c}[\mathbf{u}, \mathbf{H}]. \tag{2.15b}$$

In these equations, $n$ and $\mathbf{H}$ are considered known and $\Phi_T$ and $\mathbf{u}$ unknown. In order to obtain equations describing the "natural" potential distribution, let us suppose, in the first instance, that it is possible to introduce a system of orthogonal coordinates $(x_1, x_2, x_3)$ such that the $x_3$ axis coincides with the magnetic lines while $x_1$ and $x_2$ are perpendicular to them (Fig. 2.2a). Then it is possible to express the magnetic invariant

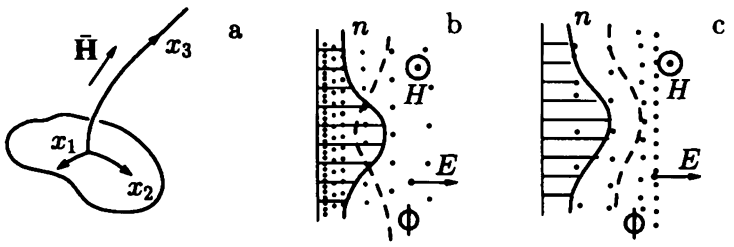


**Fig. 2.2.** "Loading" of magnetic force lines. (a) The coordinate axes. (b) Perturbation of equipotentials in a density-inhomogeneous plasma in a magnetic field decreasing along **E** (see also Fig. 6.2e). (c) The same, for an increasing magnetic field.

$\Phi_T$ in the form

$$\Phi_T(\gamma) = \Phi_T(x_1, x_2). \tag{2.16}$$

The metric form in an arbitrary orthogonal reference frame can be written as

$$ds^2 = h_1^2 dx_1^2 + h_2^2 dx_2^2 + h_3^2 dx_3^2.$$

From (2.15b) we derive

$$u_1 = -\frac{c}{Hh_2}\left(\frac{\partial \Phi_T}{\partial x_2}\right), \quad u_2 = -\frac{c}{Hh_1}\left(\frac{\partial \Phi_T}{\partial x_1}\right). \tag{2.17}$$

To find the component $u_3$, we substitute Eq. (2.17) into the continuity equation and integrate along the force line to obtain [15, 16]

$$u_3(x_3) - u_3(0) = \frac{1}{h_1 h_2 n}\frac{D(\omega, \Phi_T)}{D(x_1, x_2)}. \tag{2.18}$$

Here

$$\omega(x_3) = \int_{x_3(0)}^{x_3} \frac{nh_3}{H}\, dx_3, \tag{2.19}$$

where $x_3(0)$ is the coordinate of the "beginning" of the force line and $D(f,g)/D(\alpha,\beta)$ is the Jacobian. If the plasma volume is autonomous, then the velocity $u_3$ vanishes not only at the beginning but also at the "end" of the magnetic field line. In this case, the equation relating $\Phi_T$ to the plasma density and the magnetic field distribution can be written in the form

$$\frac{D(\Phi_T, W)}{D(x_1, x_2)} = 0, \tag{2.20a}$$

where

$$W \equiv \int_{x_3(0)}^{x_3(\infty)} \frac{n\,dl}{H}. \tag{2.20b}$$

Here $x_3(\infty)$ is the coordinate of the magnetic field line end; $dl = h_3\,dx_3$ is the element of the magnetic line length. We shall call the quantity $W$ the "loading" of the force line. Equation (2.20) implies that the plasma volume is autonomous if the distribution $\Phi_T$ is uniquely defined by the loading, i.e.,

$$\Phi_T = F(W). \tag{2.21}$$

If the plasma volume is not autonomous, then Eq. (2.18) yields the density of current coming from the fixator to a given force line:

$$j = en\left[u_3(\infty) - u_3(0)\right] = \frac{e}{h_1 h_2}\frac{D(W, \Phi_T)}{D(x_1, x_2)}. \tag{2.22}$$

Equations (2.20b) and (2.21) have the following consequences.

Firstly, the expression for $W$ can be considered as a generalization of the freezing condition for plane streams across the magnetic field, which is known in magnetohydrodynamics,

$$\kappa = \frac{n}{H} = \text{const}, \tag{2.23}$$

and the formula for the "specific magnetic tube volume,"

which is known from the equilibrium plasma configuration theory:

$$U = \int \frac{dl}{H}. \tag{2.24}$$

The relation between $W$ and $\kappa$ is obvious. As to the relation between $W$ and $U$, one should take into account the hydrodynamic equilibrium equation

$$\nabla P = \frac{1}{c}[\mathbf{j}, \mathbf{H}], \tag{2.25}$$

which suggests constancy of the density along the magnetic force line. Thus under the natural condition $T_e = T_e(\gamma)$ one can take $n$ outside integral (2.20b) for the loading to obtain expression (2.24) for the specific magnetic tube volume.

Secondly, the relation between $W$ and $\Phi$ is easily seen in the ordinary one-liquid magnetohydrodynamics. Indeed, equality (2.23) takes place along the matter stream line, since in one-liquid magnetohydrodynamics the ion and electron velocities differ by an infinitesimally small value. At the same time, an ideal conductivity plasma flows along the equipotentials according to Ohm's law:

$$\mathbf{E} + \frac{1}{c}[\mathbf{v}, \mathbf{H}] = 0, \quad \mathbf{v} = \mathbf{u}.$$

The conservation of $\kappa$ and $\Phi$ along the stream lines is clearly equivalent to Eq. (2.21).

Thirdly, a "hint" as to the instability of the plasma flux in the SPT channel follows from Eq. (2.21) if the magnetic field strength decreases along the ion motion. Conversely, there are conditions for stability if $H$ increases. This can be seen from Fig. 2.2b, c, which shows distributions of the $H$-field (the density of points — traces of the force lines), of the plasma density in some sections $z = \text{const}$, and, as a consequence, the distribution of the potential $\Phi(x, z)$ according to Eq. (2.21). It can be seen that in the first case the azimuthal $x$-components of the electric field enhance an inhomogeneity, and in the second case they attenuate it.

## 2.4. Plasma electric field for the quasi-Maxwellian electron component

Above we have analyzed the electric plasma field based on a sufficiently arbitrary (at first glance) model of a non-dissipative (ideal) electron component with a barotropic distribution $P_e = P_e(n)$. In the next section, as mentioned in Section 2.2, we shall present arguments for the validity of the barotropic law. Nevertheless, it appears worthwhile to consider the above questions of the $E$-field properties using the traditional electron hydrodynamics of S. I. Braginskii [15], which is based on the assumption of a quasi-Maxwellian distribution of electron velocities. We consider three main questions: (a) What are the real values of the dissipative terms with respect to the non-dissipative ones? (b) What is the general relation of the thermalized potential $\Phi_T(\gamma)$ to the electric potential $\Phi(\mathbf{r})$? (c) What is the form of the relation $\Phi_T(\gamma)$ to the "loading" $W = \int ndl/H$?

### *2.4.1. The system of equations for the electrons*

The equations initially used by S. I. Braginskii have the following form:

$$\frac{\partial n}{\partial t} = -\mathrm{div}\,(n\mathbf{u}_e), \tag{2.26a}$$

$$mn\frac{d\mathbf{u}_e}{dt} + \nabla P_e = -\mathrm{div}\,\overleftrightarrow{\pi}_e - en\left(\mathbf{E} + \frac{1}{c}[\mathbf{u}_e, \mathbf{H}]\right) + \mathbf{R}, \tag{2.26b}$$

$$\frac{3}{2}n\frac{dkT_e}{dt} = -P_e\mathrm{div}\,\mathbf{u} - \mathrm{div}\,\mathbf{q}_e - (\overleftrightarrow{\pi}_e\,\nabla\mathbf{u}_e) + Q. \tag{2.26c}$$

Here $P_e = nkT_e$, $\overleftrightarrow{\pi}_e$ is the viscosity tensor, $\mathbf{R} = \mathbf{R}_u + \mathbf{R}_T$ is the total friction force between the electrons and ions that takes into account the Ohmic resistance $\mathbf{R}_u$ and the thermoforce caused by the electron temperature gradient, $\mathbf{q}_e = \mathbf{q}_u + \mathbf{q}_T$ is the total electron heat flux, and $Q$ is the heat given to ions during

collisions. For singly ionized ions, we have ($\mathbf{u} = \mathbf{j}/en$)

$$\mathbf{R}_u = en\left(\frac{\mathbf{j}_{\text{II}}}{\sigma_{\text{II}}} + \frac{\mathbf{j}_\perp}{\sigma_\perp}\right), \quad \sigma_\perp = \sigma_1 T^{3/2}, \quad \sigma_{\text{II}} \approx 2\sigma_\perp, \tag{2.27a}$$

$$\mathbf{R}_T = -0.7 n_e \nabla_{\text{II}}(kT_e) - \frac{3}{2}\frac{n_e}{\omega_e \tau_e}\left[\mathbf{h}^0, \nabla kT_e\right], \tag{2.27b}$$

$$\mathbf{q}_u = 0.7 n (kT_e)\mathbf{u}_{\text{II}} + \frac{3}{2} n \frac{kT_e}{\omega_e \tau_e}\left[\mathbf{h}^0, \mathbf{u}\right], \tag{2.27c}$$

$$\mathbf{q}_T = -\kappa_{\text{II}} \nabla(kT_e) - \kappa_\perp \nabla_\perp (kT_e) - \frac{5}{2}\frac{cnkT_e}{eH}\left[\mathbf{h}^0, \nabla kT_e\right], \tag{2.27d}$$

$$\kappa_{\text{II}} = 3.2\frac{nkT_e}{m}\tau_e, \quad \kappa_\perp = 4.7\frac{nkT_e}{m\omega_e^2 \tau_e}, \tag{2.27e}$$

$$\tau_e = \frac{3.5 \cdot 10^4}{(\Lambda/10)}\frac{T_e^{3/2}}{n}, \tag{2.27f}$$

where $\sigma = \text{const}$, $\mathbf{h}^0 = \mathbf{H}/H$, and $\Lambda$ is the Coulomb logarithm.

### *2.4.2. The evaluation of dissipative terms in modern SPT models*

The characteristic temperature and density are $T_e \approx 20\,\text{eV}$ and $n \approx 10^{12}\,\text{cm}^{-3}$, respectively. Then $\Lambda = 2$, $\tau_e \approx 1.6 \times 10^{-6}\,\text{s}$. The characteristic thermal conductivity $\theta$ time-scale over the length $L \sim 1\,\text{cm}$ across and along the magnetic field (here we take the channel width to be $b \sim 1/3$ of its length $L$) is

$$\begin{aligned} \theta_{\text{II}} &\approx \frac{L^2 m}{kT\tau_e} = 2 \times 10^{-11}\,\text{s}, \\ \theta_\perp &\approx \theta_{\text{II}}(\omega_e \tau_e)^2 = 5 \times 10^{-4}\,\text{s}. \end{aligned} \tag{2.28}$$

Here the characteristic magnetic field is $H = 200\,\text{Oe}$ and $\omega_e \tau_e = 5 \times 10^3$. The value of $\theta_{\text{II}}$ is unnaturally small, which indicates that the hydrodynamical approach cannot be applied to its evaluation. At the same time the value of $\theta_\perp$ appears to be very

large, since the real lifetime of electrons formed inside the channel is $\sim 10^{-6}$ s. Thus, the plasma of a "given line of force" must be considered isothermal (in the framework of S. I. Braginskii's "quasi-Maxwellian" hydrodynamics), and the thermal conductivity across the magnetic field ($\sim \kappa_\perp$) can be neglected altogether. Clearly, the amount of energy transferred from electrons to ions due to elastic collisions is negligibly small. Of course, inelastic energy losses (through excitation and ionization) may be significant.

Now we wish to consider transport phenomena due to the motion of ions with velocity $\mathbf{u}$ relative to the electrons.

We start with the force $\mathbf{R}_u$. The maximum current density in an SPT occurs in the azimuthal drift. Its value is

$$j_\theta = encE/H \sim 20\,\mathrm{A\,cm^{-2}}. \tag{2.29a}$$

Here the values of $n$ and $H$ are taken as above, and $E = 300\,\mathrm{V\,cm^{-1}}$. Correspondingly,

$$R_u/en \sim j/\sigma_1 \sim 3 \cdot 10^{-2}\,\mathrm{V\,cm^{-1}} \ll E. \tag{2.29b}$$

Therefore, the term $\mathbf{R}_u$ can be neglected from the very beginning. The thermoforce $\mathbf{R}_T$ in SPT conditions is also small under the assumptions made. The first term in Eq. (2.27b) is small due to the effective smoothing of the electron temperature along the force line, the second one — due to the large value of $(\omega_e \tau_e)$.

Now we consider the viscosity term. An accurate evaluation can be made only for specific systems because of the complexity of the formulas. However, it is known (see Section 4 below for more details) that the electron component in the SPT acceleration zone can be considered as a solid body rotating with a constant angular velocity. Thus, as the first approximation it is natural to neglect the viscosity in this zone. As to the ionization zone, a big role here is played by kinetic UHF-oscillations (see Section 3.5), and a hydrodynamic analysis is hardly worth doing.

The quantity $\mathbf{q}$ can be considered in the same way as $\mathbf{R}$. Thus, the electron dynamic equations in the acceleration zone

in the quasi-Maxwellian hydrodynamics can be written in the form

$$\frac{\partial n}{\partial t} + \operatorname{div} n\mathbf{u}_e = 0, \tag{2.30a}$$

$$mn\frac{d\mathbf{u}_e}{dt} + \nabla P_e = -en\left(\mathbf{E} + \frac{1}{c}[\mathbf{u}_e, \mathbf{H}]\right), \tag{2.30b}$$

$$\frac{3}{2}nk\frac{dT_e}{dt} + P_e \operatorname{div} \mathbf{u}_e = \operatorname{div} \overleftrightarrow{\kappa}\, \nabla T_e, \tag{2.30c}$$

$$P_e = nkT_e(\gamma), \tag{2.30d}$$

$$\kappa_{\text{II}} \to \infty, \qquad \kappa_{\perp} \to 0. \tag{2.30e}$$

Here $\gamma$ is the magnetic force line number (index). Clearly, the system (2.30) could have be written from the very beginning by rejecting *a priori* dissipative terms, but we considered it worth evaluating them in advance. For SPTs one can neglect the electron inertia in the Euler–Lorentz equation (2.30) since the cycloid height is $h \equiv 2cE/(H\omega_{eL}) \ll R$, where $R$ is the mean channel radius. Thus, restricting the study to the frequencies $\omega \ll c/R$, we can consider the electric field to be the potential $E = -\nabla\Phi$, and Eq. (2.30b) under these simplifying assumptions takes the form

$$-\nabla\Phi = \frac{\nabla kT_e(\gamma)n}{en} + \frac{1}{c}[\mathbf{u}_e, \mathbf{H}]. \tag{2.31}$$

### *2.4.3. Equipotentialization of the magnetic force lines*

The projection of Eq. (2.31) onto the magnetic field direction yields

$$\frac{\partial\Phi}{\partial l} - \frac{kT_e(\gamma)}{e}\frac{1}{n}\frac{\partial n}{\partial l} = 0. \tag{2.32}$$

Here $dl$ is an element of the magnetic field line arc. Equation (2.32) implies the conservation law

$$\Phi - \frac{kT_e(\gamma)}{e}\ln\left(\frac{n}{n_0}\right) \equiv \Phi_T(\gamma). \tag{2.33}$$

Clearly, relationship (2.33) means nothing but the presence of a "self" Boltzmann electron distribution along each force line:

$$n = n_1(\gamma) \exp\left\{\frac{e\Phi}{kT_e(\gamma)}\right\}, \quad n_1 = n_0 \exp\left\{-\frac{e\Phi_T}{kT_e(\gamma)}\right\}, \qquad (2.34)$$

As to the drift lines, in contrast to the barotropic hydrodynamics (in the absence of symmetry) the thermalized potential is not conserved since

$$(\mathbf{u}_e, \nabla)\Phi_T = -\frac{(\mathbf{u}_e, \nabla)}{e} kT_e(\gamma). \qquad (2.35)$$

## 2.5. Remarks

1. From what has been said in this section, it is clear that the formation of a magnetic field with convex lines toward the anode is insufficient to provide ion focusing to the middle of the channel. This is due to the fact that the thermalized potential $\Phi_T$, not the electric potential $\Phi$, is conserved along the force lines. At the same time, the electron dynamics are determined by the electric potential. To avoid ion flux defocusing due to the thermal effect, it is necessary to try to bend the magnetic force lines more strongly and to decrease the mean electron energy as much as possible. (See Section 3.2 below for more details).

2. Let the thermal correction be small so the magnetic force lines are equipotential in the usual sense: $\Phi = \Phi(\gamma)$. Then by choosing different magnetic field configurations, one can form reliefs of superthermal potential in the plasma of various shapes and thus construct different "magnetoelectric" plasma devices. Figure 2.3 shows schematically the main types of stationary devices using only poloidal fields [16].

Thrusters with azimuthal drift, including SPTs, are of the type of engine shown in Fig. 2.3a.

If an energetic quasi-neutral ion flux is directed against the electric field, as shown in Fig. 2.3b, it will be retarded by giving energy to the electric field source. Such braking systems are usually called recuperators.

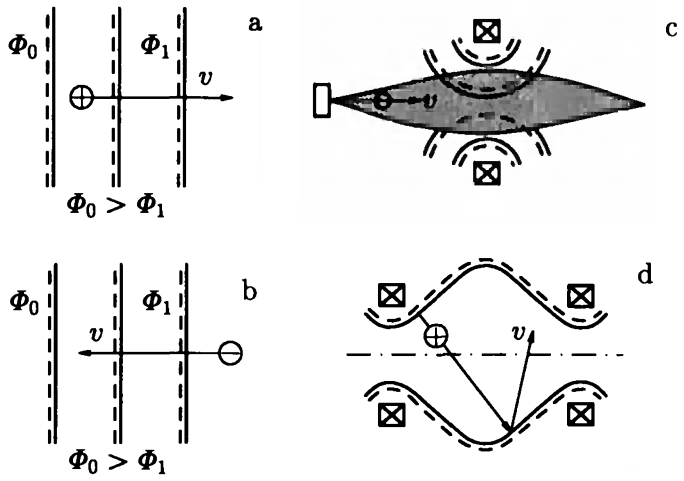


**Fig. 2.3.** "Magnetoelectric" plasma devices. (a) Accelerators of compensated ion fluxes (CIF). (b) Energy recuperators of CIF. (c) Focusing lenses of CIF. (d) Magnetoelectric plasma traps (the equipotentials are shown by solid lines, the magnetic force lines by dotted lines).

Using the same principle, one can also design devices for static focusing of strong-current quasi-neutral fluxes, for example, "plasma lenses," separators, energy-analyzers, etc. (Fig. 2.3c). Moreover, magnetoelectric plasma traps can be constructed in this way (Fig. 3.6d). All these possibilities have been experimentally realized [16, 18–21].

## 3. Electron kinetics in the SPT channel

As noted in Section 1, in the SPT channel there are numerous structures of the electron scale that play a large role in the thruster performance. To describe them, the electron distribution function (EDF) $f_e(\mathbf{v}, \mathbf{r}, t)$ must be known. But at present the determination of this function by directly solving the kinetic equation with all the factors affecting the SPT's per-

formance is impossible. In this situation, one should construct simplified fragmented models reflecting some real features by using very general properties of the electron dynamics in the SPT (in particular, the dominance of collisions with the walls) and experimental data.

## 3.1. Characteristics of particle collisions with each other and with the surfaces

To analyze the points considered below in Sections 3.2–3.4, we shall need to know the particle collision cross-sections, as well as the secondary electron emission (SEE) coefficients, the coefficients of sputtering of surfaces by heavy particles, and the secondary particle distribution functions. Most of these data can be taken from handbooks, but we wish to list them here for the reader's convenience for typical plasma parameters in the mostly well-studied SPT models with a channel outer diameter of 70 mm of both the first (R-70 model, the prototype of the M-70 model) and second generation (A-4 model, ATON, Fig. A.1b). We consider regimes with a xenon rate of $\dot{m} = 3\,\mathrm{mg\,s^{-1}}$ ($J_{\dot{m}} \approx 2.3\,\mathrm{A}$) and a discharge voltage of $U = 300\,\mathrm{V}$. In these regimes, the characteristic atomic density before the ionization zone is $\sim 3 \times 10^{13}\,\mathrm{cm^{-3}}$, while the ion and electron densities in the ionization zone are about $2 \times 10^{12}\,\mathrm{cm^{-3}}$ and then smoothly decrease to $5 \times 10^{11}\,\mathrm{cm^{-3}}$ (Fig. 3.1a). (At present, first-generation SPTs are operating in space. SPTs of this type remain the most studied. The second-generation SPTs with better process organization have been studied less systematically. Thus, below we shall often refer to the first-generation model experiments, but only when they do not strongly differ from the second generation SPT data.) The electron temperature distribution is shown in Fig. 3.1b. Its characteristic values lie within the range $10 < T_e < 20\,\mathrm{eV}$. However, it is important to stress that in the "normal" regimes the parameter variation level is of the order of $\sim 10-15\%$ of the mean values presented in Fig. 3.1.

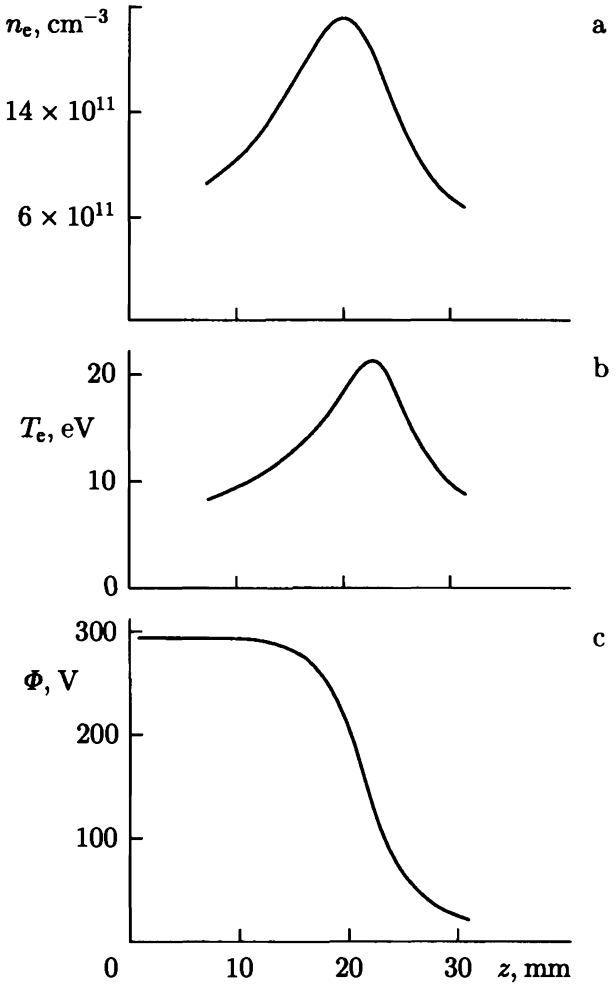


**Fig. 3.1.** Distributions of the electron concentration (a), the electron temperature (b), and the plasma potential (c) along the accelerator's length for $\dot{m} = 3\,\mathrm{mg\,s^{-1}}$, $U_p = 300\,\mathrm{V}$ in the SPT-ATON.

After these introductory remarks, let us pass to the description of elementary processes in SPTs and the estimation of their role in the working process.

### *3.1.1. Space collisions*

*Electron–electron collisions.* The cross-section is estimated according to Eq. (2.27):

$$\sigma_{ee} \approx 10^{-3} \frac{1}{(T_e)^2(\mathrm{eV})} \,(\mathrm{cm}^2), \tag{3.1}$$

and for $T_e = 15\,\mathrm{eV}$ the collisional cross-section, free-path length relative to electron collisions, and free-path time are, respectively,

$$\begin{aligned} &\sigma_{ee} \sim 4 \cdot 10^{-6}\,\mathrm{cm}^2, \quad \tau_{ee} \sim \frac{\lambda_{ee}}{V_{T_e}} \sim 10^{-6}\,\mathrm{s}, \\ &\lambda_{ee} \sim \lambda_{ei} \sim \frac{1}{n_{ee}\sigma_{ee}} \sim 2 \cdot 10^3\,\mathrm{cm}. \end{aligned} \tag{3.2}$$

It is seen from here that $\tau_{ee} \sim \tau_{i0}$, the time of presence of an ion inside the SPT channel ($L \sim 2\,\mathrm{cm}$, $V_{i,\max} \sim 2 \times 10^6\,\mathrm{cm\,s^{-1}}$). However, the mean lifetime of an electron inside the channel $\tau_{e0}$ must be equal to that of an ion $\tau_{i0}$. Thus it is clear that the Coulomb collisions shifting electrons toward the anode by a distance of the order of the electron Larmor radius have no significant effect on their transport across the magnetic field.

*Elastic collisions of electrons with neutral Xe atoms.* The cross-section of these collisions is comparatively weakly dependent on the electron energy and for Xe with energies $\sim 10\,\mathrm{eV}$ is about [22]

$$\sigma_{e0} \sim 3 \cdot 10^{-15}\,\mathrm{cm}^2. \tag{3.3}$$

Thus, in the region before the ionization zone where $n_0 \sim 3 \times 10^{13}\,\mathrm{cm}^{-3}$, the free-path length is

$$\lambda_{e0} \sim 10\,\mathrm{cm}, \tag{3.4}$$

and in this region such collisions partially determine the electron transport across the magnetic field, although, as we shall see below, the main role here is played by the collisions of electrons with the walls yielding the near-wall conductivity.

*Collisions of electrons with ions.* Coulomb scattering of electrons on ions is important for energies $\mathcal{E}_e < 15\,\mathrm{eV}$ and for higher electron energies when their interaction with the ion base becomes dominant. In this case, the cross-section of elastic electron–ion collisions is close to that of electron–neutral atom collisions.

*Excitation and ionization of atoms by electrons.* Here the situation is much more complicated, because a large number of atomic levels can be involved, with some of them being metastable and thus in the excited state being capable of "waiting" for the next collision to become an ion. Finally, a new component appears in the plasma — the photons, part of which turn out to be essentially locked.

The ionization potentials for atoms and ions of Xe are

$$\begin{aligned} I_0(\mathrm{Xe}) &= 12.13\,\mathrm{eV}, \\ I_1(\mathrm{Xe}^+) &= 21.2\,\mathrm{eV}, \\ I_2(\mathrm{Xe}^{++}) &= 32.1\,\mathrm{eV}. \end{aligned} \tag{3.5}$$

The dependences of cross-sections of the ionization of the atom on the electron energy are shown in Fig. 3.2 [23].

*Photon absorption.* As is well known, the absorption coefficient $\kappa_\omega$ (inversely proportional to the free-path length) of a photon with a frequency $\omega$ close to the frequency $\omega_{kl} = (E_k - E_l)/\hbar$ is given by the expression

$$\kappa_\omega = n_0 \frac{f_{kl} e^2}{mc} \pi\, P(\omega). \tag{3.6}$$

Here $n_0$ is the atomic concentration in the ground state, $f_{kl}$ is the oscillation strength, $P(\omega)$ is the line profile which has a maximum at the frequency $\omega_{kl}$. Denoting the characteristic spectral line width by $\delta\omega$, one can put $P(0) \sim 1/\delta\omega$ (considering the normalization $\int_0^\infty P(\omega)d\omega = 1$). Consequently, the estimate of the absorption coefficient $\kappa_\omega(\omega_0)$ at the central frequency $\omega_0$ is

$$\kappa_\omega(\omega_0) \approx n_0 f_{kl} \frac{\pi e^2}{mc} \frac{1}{\delta\omega}. \tag{3.7}$$

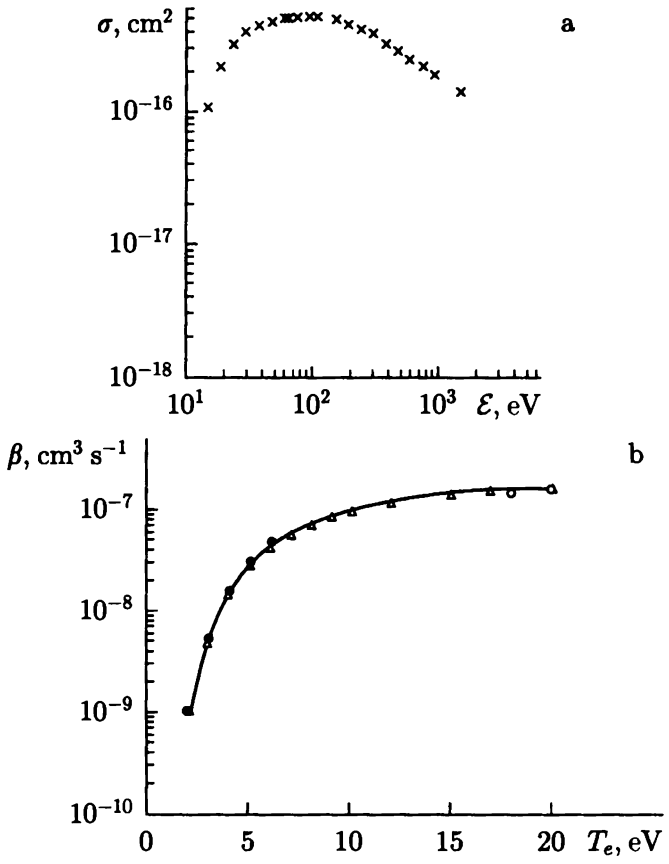


**Fig. 3.2.** The effective Xe ionization cross-section (a) and ionization coefficient (b) dependences on the electron energy.

The smallest possible line width is determined by the natural (Lorentz) decay at which

$$P(0) = 3\frac{mc^2}{\pi e^2 \omega_0^2}, \tag{3.8}$$

so for the Lorentz broadening we have

$$\kappa_\omega^L(\omega_0) \equiv n_0 \sigma_{kl}^L, \quad \sigma_{kl}^L \equiv f_{kl}\frac{3\lambda_0^2}{(4\pi)^2}, \tag{3.9}$$

and $\lambda_0 = 2\pi c/\omega_0$. Substituting $f_{kl} = 1$, $\lambda_0 = 5000\,\text{Å}$ into Eq. (3.9), we obtain the estimate of the photon free-path length

$$L_\omega = 1/\kappa_\omega \approx 0.5 \cdot 10^{10}/n_0. \tag{3.10}$$

Thus, for natural broadening the photon free path would be $L_\omega < 1\,\text{cm}$ at $n_0 = 10^{10}\,\text{cm}^{-3}$. However, in SPTs the natural broadening is much smaller than the more powerful Doppler broadening. For the Doppler broadening,

$$\delta\omega = V_T\omega_0/c. \tag{3.11}$$

Assuming neutral Xe velocity $V_T = 2 \times 10^4\,\text{cm s}^{-1}$, $\lambda = 5000\,\text{Å}$, $f_{kl} = 1$, we obtain using Eq. (3.7)

$$L_\omega \sim 10^{10}/n_e. \tag{3.12}$$

This estimate shows that in the buffer and near-anode zones, where the neutral atom density is $\geq 3 \times 10^{13}\,\text{cm}^{-3}$, their radiation is strongly locked. It is also strongly locked in the ionization zone, in which the neutral atom density decreases from $\sim 5 \times 10^{13}$ to $\sim 10^{11}\,\text{cm}^{-3}$. However, the radiation of ions is weakly locked in this zone. This is due to both much smaller $n_i \sim 10^{12}\,\text{cm}^{-3}$ and higher velocities $\sim 5 \times 10^5\,\text{cm s}^{-1}$. In the acceleration zone, where $n_0 \sim 10^{11}\,\text{cm}^{-3}$ and $n_i \sim 10^{12}\,\text{cm}^{-3}$, the radiation of neutral atoms and ions is practically unlocked due to the low density of the former and the high chaotic velocity of the latter.

In this respect, it is worthwhile to speak of single atoms and ions only in the acceleration zone, where the radiation is practically unlocked. It has been shown both theoretically and experimentally that the most powerful excitation and radiation processes are mainly of a "coronal" character. In other words, an atom (or ion) is excited by electrons from the ground state and returns back to the ground state by emitting one photon or a photon cascade. Correspondingly, the total cross-section of such a collision of an electron with an atom (ion) will be

$$\sigma_e^{(z)} = \sum_k \sigma_{e,0k}^{(z)}. \tag{3.13}$$

Here $z = 0, 1$ is the heavy particle charge, and $k$ are the quantum numbers of the excited state.

*The ion cost.* It is seen from the above that because of radiation locking the ion cost in SPTs can be substantially lower than the usually accepted value of three ionization potentials and approach one ionization potential, $eI_1$. Unfortunately, radiation locking in the SPT channel has not yet been studied appropriately.

Clearly, for a sufficiently high electron temperature in the SPT channel the ion cost $\zeta$ in the absence of locking is

$$\zeta = eI + \theta \frac{\sigma_{01}}{\sigma_{\text{ion}}} \varepsilon_{01}. \tag{3.14}$$

Here $\theta \sim 1.5$, $\sigma_{01}$ is the cross-section of electron transition from the ground to the first excited level in an atom (ion), $\varepsilon_{01}$ is the required energy, and $\sigma_{\text{ion}}$ is the ionization cross-section.

### *3.1.2. Interaction of electrons with surfaces*

Due to the free access of electrons to the surface of the dielectric walls in SPTs, the secondary electron emission coefficient $\sigma_{\text{SEE}}(\mathcal{E}_p)$ and the secondary electron spectrum $\eta(\mathcal{E}, \mathcal{E}_p)$ have a significant effect on the SPT performance. Here $\mathcal{E}_p$ is the energy of incident electrons. The typical dependence $\sigma_{\text{SEE}}(\mathcal{E}_p)$ is shown in Fig. 3.3a [24]. There are five parameters here: (1) the value of $\sigma_0$ at small ($\mathcal{E}_p \sim 1\,\text{eV}$) energies of the incident electrons. Usually $\sigma_0 \sim 1/2$. (2) The energy $\mathcal{E}_p = \mathcal{E}^*$ at which $\sigma_{\text{SEE}} = 1$. This energy is called the "first multiplication threshold." For dielectrics with boron, $\mathcal{E}^* \sim 30-40\,\text{eV}$. Outside these energetic limits, the operation of the SPT is accompanied by a high level of oscillations. (3), (4) — maximal value $\sigma_{\text{SEE}} = \sigma_m$, which is within the range of $\sim 2-4$ for these insulators; the corresponding energy is $\mathcal{E}_p = \mathcal{E}_m \sim 500\,\text{eV}$. (5) $\mathcal{E}^{**}$ is the "second multiplication threshold," which in our case is $\sim 1-2\,\text{keV}$.

As to the secondary electron energy distribution function (Fig. 3.3b), there are two groups of particles: one with low en-

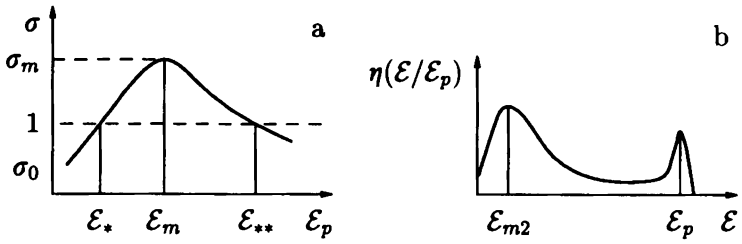


**Fig. 3.3.** The secondary electron emission. (a) A qualitative dependence of the secondary electron emission coefficient $\sigma$ on the incident electron energy $\mathcal{E}_p$. (b) The characteristic energy spectrum of the secondary electrons.

ergy (3–5 eV), which weakly depends on $\mathcal{E}_p$, and another consisting of the elastically reflected electrons. In the case of boron-containing dielectrics, the fraction of the elastically reflected electrons (in the region $\mathcal{E}_p \leq 100$ eV) can be as high as $\sim 70\%$ of the total number of secondary electrons (see Section 3.2). Experiments with SPTs (see Section 5.2 below) have revealed a specific insulator erosion clearly stimulated by electrons. However, the question is still open as to whether electron collisions fully detach heavy particles from the insulator or only weaken their bonds with the main insulator body, and the ions ultimately separate them off.

### *3.1.3. Interaction of heavy particles with surfaces*

In Section 6, we shall consider the sputtering of the channel dielectric walls by incident ions, and in Section 8 we shall deal with problems connected with the interaction of the flux leaving the SPT with various "targets," including the chamber walls.

We shall be interested in two problems: the sputtering coefficient of the irradiated material and the characteristics of the secondary (emitted as a result of the bombardment) particles, including their chemical and energetic spectra. Here we shall

consider the bombardment of surfaces by $Xe^+$ and $Ar^+$ ions with energies of $\sim 100$–$400$ eV. We should stress the rich variety of processes occurring during the bombardment, and so the simple relationships described below reflect the real situation very fragmentarily. This is especially true for the system under study and is mainly due to the formation of coatings from the sputtering products that settle onto both the channel walls and the vacuum chamber walls. Thus, one should be cautious in comparing parameters of the particle interaction with surfaces obtained with the use of low-intensity ion beams under sterile laboratory conditions with the real parameters of a working SPT in a vacuum chamber.

*Accommodation.* In analyzing the interaction of fluxes from an SPT with a target and the vacuum chamber as a whole, it is important to know the accommodation coefficient:

$$\kappa = \left\langle \frac{\mathcal{E}_W}{\mathcal{E}_p} \right\rangle. \tag{3.15}$$

Here $\mathcal{E}_W$ is the energy passed to the wall by an incident particle with energy $\mathcal{E}_p$. This coefficient significantly depends on the mass ratio

$$M = \frac{M_w - M_p}{M_w + M_p}, \tag{3.16}$$

where $M_w$ is the wall particle mass and $M_p$ is the incident particle mass. If $M > 0$, one can consider, to the first approximation, the interaction of the incident particle with the wall particle as a binary collision so that obviously the energy of a reflected atom (ion) lies in the range [25]

$$\mathcal{E}_p^R = \mu^2 \mathcal{E}_p - \mu \mathcal{E}_p. \tag{3.17}$$

This estimate reasonably correlates with experiment, and in this case the accommodation coefficient is comparatively small.

If $\mu < 0$, the model of binary collisions does not apply. A heavy incident particle rams some wall particles deep into the wall material and the accommodation coefficient is very large.

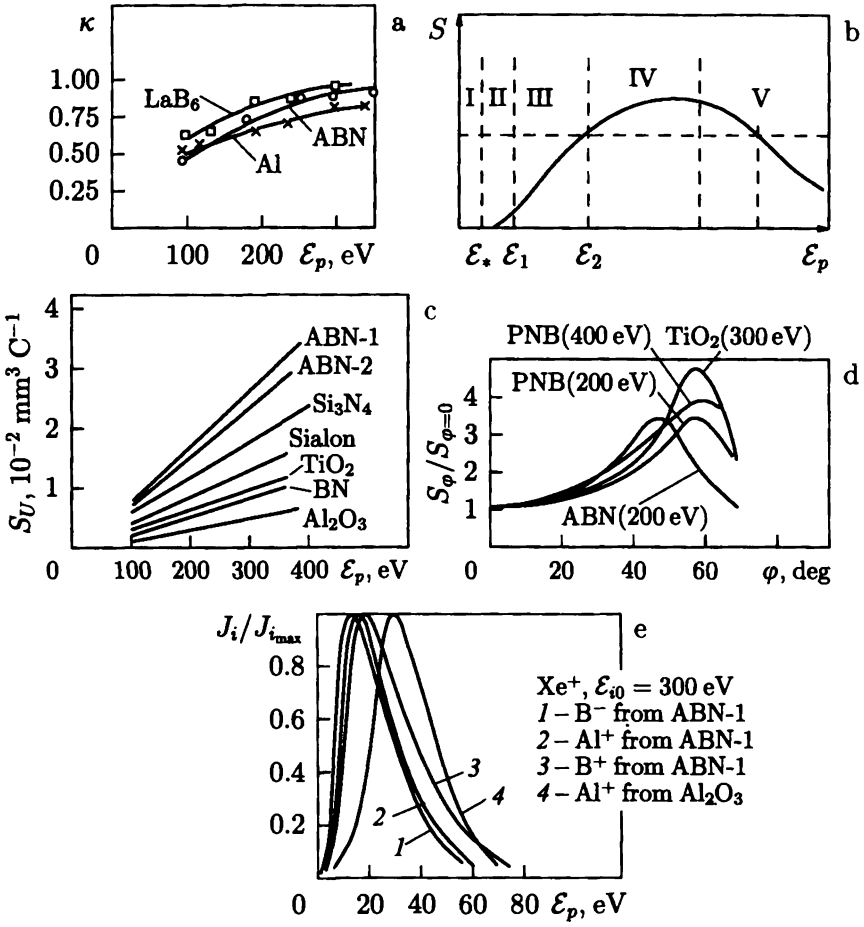


**Fig. 3.4.** Interaction of heavy particles with surfaces. (a) The accommodation coefficient. (b) A qualitative dependence of the sputtering coefficient $S$ on the incident particle energy $\mathcal{E}_p$. (c) The volume sputtering coefficients of different dielectrics. (d) The dependence of the sputtering coefficient on the ion incidence angle. (e) Energy distribution of the sputtering products.

In Fig. 3.4a, taken from [26], we plot the accommodation coefficients for coating ions for two interesting materials from the

point of view of SPTs — a dielectric ABN (amomonium boronitride) and a high-efficiency $LaB_6$ emitter — and aluminum (for comparison).

*Surface sputtering by ions.* When the incident particle energy $\mathcal{E}_p$ exceeds the binding energy $\mathcal{E}_b$ of particles forming the solid body surface, surface sputtering begins. If $\mathcal{E}_p \geq (3-5)eI$, where $I$ is the ionization potential of the incident atom, the difference between the sputtering action of atoms and ions is small as a rule, and so we shall consider the sputtering caused by ions.

Although during SPT performance in many cases coatings of various origins are being sputtered, the data we need for our analysis are absent, and we restrict ourselves to considering only uniform material sputtering.

The main characteristic of the sputtering is the sputtering coefficient. For simple materials it is usually defined as

$$S = N_n/N_p, \tag{3.18a}$$

i.e., as the ratio of the number of particles knocked out of the surface $N_n$ to the number of ions incident onto it $N_p$. However, for SPT channel wall sputtering it is convenient to use another definition:

$$S = \delta V/q, \tag{3.18b}$$

where $\delta V$ is the volume of the insulator sputtered by ion incidence of total charge $q$.

The typical shape of the dependence of $S$ on $\mathcal{E}_p$ is shown in Fig. 3.4b. Here five regions are shown. In region I sputtering is absent. Region II is the vicinity of the sputtering threshold ($\mathcal{E}^* \sim$ 10–30 eV). In region III, the coefficient $S$ increases almost linearly with the characteristic values $\mathcal{E}_1 \sim 30-50$ eV, $\mathcal{E}_2 \sim$ 0.5–1 keV. Then the growth of $S$ slows down, $S$ passes through a maximum (region IV), and in region V ($V_p \geq 10^8\,\mathrm{cm\,s^{-1}}$) $S$ drops continuously. Below we shall need some specific data. In Fig. 3.4c, we plot the dependences $S(\mathcal{E}_p)$ for insulators and some metals irradiated by $Xe^+$. Figure 3.4d shows the dependence of $S$ on the ion incident angle with respect to the surface [26].

The mass and charge composition of the sputtered particles is very different. Whereas during the sputtering of metals mostly neutral atom fluxes are observed, during the sputtering of insulators the fraction of ions in the outgoing flux can reach tens of percents. Finally, it is important to emphasize that among the sputtered particles there are negative ions as well. The energetic spectrum of particles is presented in Fig. 3.4e [26].

## 3.2. Electron distribution functions in the SPT channel

In the vast majority of discharges, the electron distribution functions are formed mostly due to volume processes, either classical (elastic or inelastic particle collisions with each other or with photons) or collective ("anomalous").

In SPTs, volume processes are dominating from the point of view of EDF formation in the ionization zone and near the channel outlet. In both zones, collective UHF-oscillations, which we address in Section 3.5, play a major role. At present, we are far from constructing a quantitative theory of such oscillations, and so below we mainly restrict ourselves to a brief review of experimental data. At the same time, in the acceleration and near-anode zones the role of oscillations is comparatively small, and there the main factor affecting the EDF is essentially classical collisions of particles with the walls. This allows us to construct analytical models for EDFs.

### *3.2.1. Qualitative characteristics of EDFs*

As follows from a very general consideration, in those parts of the SPT channel where collisions with the walls are important, three groups of electrons should appear, which we shall refer to as "locked," "escaping," and "intermediate" (Fig. 3.5a). The appearance of these three groups is due to the central part ("core") of the flux having a higher potential than the surface of the walls. The Debye layers near the walls also contribute to this.

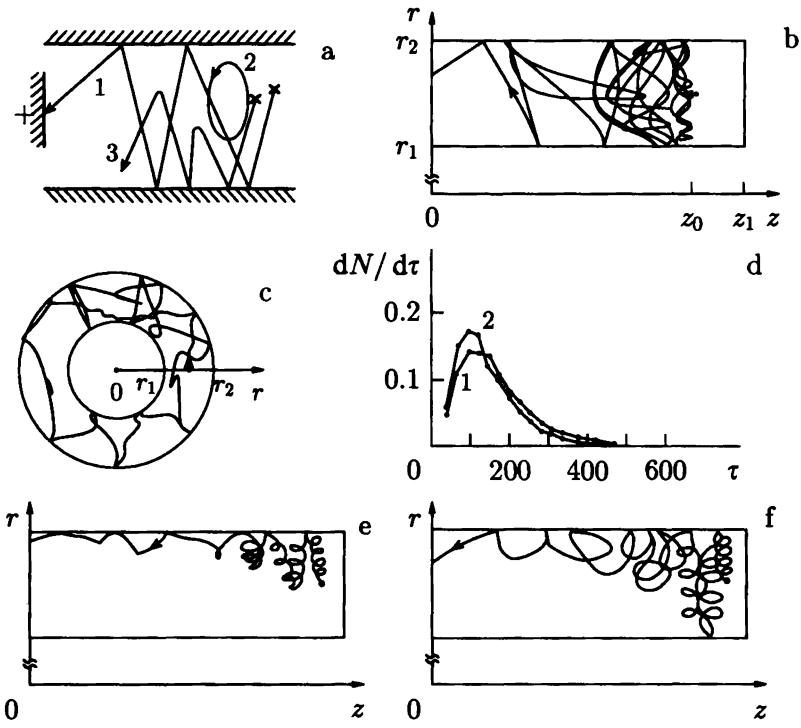


**Fig. 3.5.** Motion of electrons in the SPT channel. (a) Three types of trajectories: *1* – "escaping," *2* – "locked," *3* – "intermediate." (b), (c) The projections of a "typical" escaping electron trajectory for $\alpha = 0.03$. (d) The distribution of the escaping electrons over the lifetime inside the channel, $\alpha = 0.03$: *1* – the number of trajectories $N = 2000$, *2* – $N = 4000$, 5000. (e) The trajectory of an intermediate electron ($\alpha = 0.03$) in the presence of a Debye layer ($U_d = 0.02$) and inelastic scattering on the walls. (f) The same, with the radial electric field component present.

The group of "locked" electrons consists of those prevented from striking the wall by the radial electric field. This action is not of course absolute. Collisions of electrons with each other and with heavy particles, as well as oscillations of different fre-

quencies, provide a constant renewal of electrons in this group. The electrons that elastically collide systematically with the wall belong to the "escaping" group. Clearly, the energy of these particles must increase close to the anode, $\mathcal{E}_p \approx e(\Phi - \Phi_*)$, where $\Phi_*$ is the potential at which the "birth" occurs. By approaching the anode the amplitude of the distribution function of these particles must naturally decrease because of losses near the walls due to inelastic collisions. This is confirmed by experiment.

Finally, the "intermediate" group is formed by electrons with energy sufficient for them to reach the walls, but the collisions are inelastic. Correspondingly, the intermediate particle energy lies between the maximum energy of the locked particles $\mathcal{E}_{\max}^{\mathrm{Loc}}$ and the minimum energy of the escaping electrons $\mathcal{E}_{\min}^{\mathrm{Esc}}$

$$\mathcal{E}_{\max}^{\mathrm{Loc}} < \mathcal{E}^{\mathrm{Int}} < \mathcal{E}_{\min}^{\mathrm{Esc}}.$$

The intermediate electron distribution function has a maximum close to $\mathcal{E}_{\max}^{\mathrm{Loc}}$.

Very useful information on the electron behavior in the SPT channel is obtained from numerical calculations of the trajectories of these particles in given fields. The trajectories of captured particles are sufficiently obvious; therefore below we reproduce only trajectories of the "escaping" and "intermediate" particles.

*Escaping electrons.* Since the energy of these electrons is assumed to be sufficiently high, we shall neglect the potential thermalization and Debye layers, i.e., the radial electric field component $E_r$. In Section 3.2.3, we shall show that outside the ionization zone and the channel outlet the relation between the electric potential and the magnetic flux can be taken in the form:

$$\Phi = \kappa\Psi, \tag{3.19}$$

and the magnetic flux function can be written in the simplest form

$$\Psi = r_1 \left\{ H_1(z_1 - z) + \frac{H_0 - H_1}{3z_1^2}(z_1^3 - z^3) \right\}. \tag{3.20}$$

Here $r_1$ is the internal channel radius; $z = 0$ and $z_1$ correspond to the position of the anode and outlet, respectively. The expression for $\Psi$ does not take into account the magnetic line bending, which is insignificant here, but instead accounts for the magnetic field strength increase toward the channel outlet and decrease along the radius since

$$H_r = -\frac{1}{r}\frac{\partial \Psi}{\partial z} = \frac{r_1}{r}\left(H_1 + \frac{H_0 - H_1}{z_1^2} z^2\right). \tag{3.21}$$

Then the electron dynamics are described by the equations [27]

$$\begin{gathered} m\ddot{r} = -\frac{\partial U}{\partial r}, \quad m\ddot{r} = -\frac{\partial U}{\partial z}, \\ U = -e\Phi + \frac{1}{2mr^2}\left(D + \frac{e}{c}\Psi\right)^2, \quad D = mrV_\theta - \frac{e}{c}\Psi, \end{gathered} \tag{3.22}$$

with the initial conditions $r = r_0$, $z = z_0$, $V_r = V_{r0}$, $V_z = V_{z0}$, $V_\theta = V_{\theta 0}$. Calculations of trajectories in the given fields show that electrons can reach the channel wall ($r = r_1$ or $r = r_2$). They have been assumed to reflect inward without energy losses but move diffusively, i.e., the velocity vector of an individual electron is a random value randomly distributed on the hemisphere. The main dimensionless parameters are

$$\alpha = \frac{cE_0}{H_0 r_1}\frac{mc}{eH_0} = \frac{1}{2}\frac{h}{r_1}, \quad \gamma = \frac{H_1}{H_0}. \tag{3.23}$$

where $h$ is the cycloid height in the fields $E_0 = kH_0 r_1$ and $H_0$. For $H_0 = 100\,\mathrm{Oe}$, $E = 100\,\mathrm{V\,cm^{-1}}$, one obtains $\alpha = 0.03$, $\gamma = 0.1$.

The projections of the "typical" trajectory on the $(r, z)$ and $(r, \theta)$ planes for $\alpha = 0.03$ are shown in Fig. 3.5b, c. Here the bold point marks the electron starting point (the inner insulator radius is taken as the unit of length, i.e., $r_1 = 1$). With increasing $\alpha$ the "complexity" of the trajectory strongly increases [28].

For $\alpha = 0.03$, some statistical characteristics of a large number of particle trajectories born inside the limits

$$1 < r < r_2 = 2, \quad 2.5 < z < z_1 = 3$$

have been studied. Figure 3.5d shows the particle lifetime distributions calculated for 5000 trajectories. Time is measured in units of the Larmor turn time $t_0 = mc/eH_0$ ($\approx 10^{-9}$ s). It is seen that the minimum lifetime is $\tau_{\min} \approx 22\,(2.5 \times 10^{-8}\,\mathrm{s})$, $\tau_{\max} \approx 700$, $\langle\tau\rangle \approx 143\,(1.7 \times 10^{-7}\,\mathrm{s})$. The minimum and mean lifetime for given $\alpha$ and $\gamma$ rapidly stabilize with the number of trajectories calculated. $\tau_{\max}$ appears unbounded and tends to infinity as $N \to \infty$ [28].

The mean lifetime is of special interest. Clearly, the mean lifetime $\tau_{e0}$ of all electrons formed during ionization must be exactly equal to that of the formed ions $\tau_{i0}$. The quantity

$$\tau_{i0} = \int_0^{z_0} \frac{dz}{\sqrt{\frac{e}{M}\Phi(z)}} \approx 10^{-6}\,\mathrm{s}. \tag{3.24}$$

The mean lifetime of the escaping electrons $\langle\tau^{\mathrm{Esc}}\rangle$ must be less than $\tau_{i0}$. This is the case, since most electrons coming to the anode belong to the intermediate group.

*Intermediate electrons.* The intermediate electrons are mainly formed due to inelastic collisions with the channel walls. Thus, for single particle modeling we need to specify the Debye jump and also the secondary electron energy distribution function $\eta(\mathcal{E}, \mathcal{E}_p)$. In our calculations, we have taken DL to be infinitely thin such that the potential difference is determined by the parameter $U_d$ and the distribution function $\eta(\mathcal{E}, \mathcal{E}_p)$ has been taken in the "triangle" form

$$\eta\left(\frac{\mathcal{E}}{\mathcal{E}_p}\right) = \begin{cases} \dfrac{2}{\mathcal{E}^2}\left(\mathcal{E}_{\max} - \dfrac{\mathcal{E}}{\mathcal{E}_p}\right), & 0 < \dfrac{\mathcal{E}}{\mathcal{E}_p} < \mathcal{E}_{\max}, \\ 0, & \dfrac{\mathcal{E}}{\mathcal{E}_p} > \mathcal{E}_{\max}. \end{cases} \tag{3.25}$$

Here $\mathcal{E}_{\max} \geq 1$ is a parameter of this function.

The initial calculations were carried out with the $E$ and $H$ fields taken from the above equations (3.19) and (3.20). We have found that in this case the trajectory "adheres" to the external insulator (Fig. 3.5e) after some collisions due to the radial magnetic field gradient. To detach the trajectory from the wall two steps have been made. First of all, a random electron velocity orientation in the plasma volume was introduced. Such an isotropization models, on the one hand, particle collisions, and on the other, particle scattering on the UHF-oscillations of the $E$-field. However, considering the estimates of Section 3.1, classical collisions very rarely provide an effective detachment of the trajectories from the insulator surfaces. Thus, here we only need to rely on collective processes, which are much less clear.

The second mechanism is very natural and effectively reduces to an account of the thermalization of the potential, i.e., to an account of the "radial" electric field which is due to the higher potential at the "core" of the flux relative to the walls. Instead of Eq. (3.19), the expression for the electric potential takes the form

$$\Phi = \kappa\Psi(z) + \Phi_T(r), \quad \Phi_T(r) = \Phi_0(1 - \xi^2/a^2),$$

where $\xi = r - r_0$, $r_0 = (r_1 + r_2)/2$, $a = (r_2 - r_1)/2$. Calculations of trajectories in such an electric field at $E_r \sim 20\,\mathrm{V\,cm^{-1}}$, close to real conditions, have confirmed the expected effect (Fig. 3.5f).

*Experimental data on the EDF in an SPT channel.* In 1980–1996, A. I. Bugrova and colleagues performed detailed studies of the EDF in the channel of the SPT R-70 and the ATON (A-4) [29–31]. For this purpose, oriented Langmuir probes were used with take-up surfaces $\sim 0.2 \times 0.2\,\mathrm{mm^2}$ attached at alundum tubes $\sim 1\,\mathrm{mm}$ in diameter. The measurements were made at different points in the channel (the maximum number of points was 20) in different regimes for three orientations of the take-up surfaces. The signals were registered by static devices and so were averaged over time. Using the probe characteristics

$$J_{x,y,z}(P, \Phi) = \int V_{x,y,z} f_e(P, \mathbf{V}, \Phi)\, d\mathbf{V}\, S_{PR},$$

where $P$ is the point at which measurements were made, one can recover the electron distribution function $f_e = f_e(\mathbf{v}, \mathbf{r})$. The following main results were obtained.

(1) In the generation zone of "channel" electrons (the ionization zone and the entrance zone of electrons from the cathode-compensator into the channel), a "one-humped" EDF exists. This fact correlates with the high level of UHF-noise in these zones (Fig. 3.6a).

(2) As electrons come toward the anode from the generation zones, the EDF starts separating into three components corresponding to the locked, escaping, and intermediate particles (Fig. 3.6b).

(3) The distribution function of the locked particles is well described (Fig. 3.6c) by a linear spline ("Bugrova's distribution"):

$$f_e^{\mathrm{Loc}}(\mathbf{v}) = \frac{1}{N}\begin{cases} \mu - \mathcal{E}_*, & \mathcal{E}_* < \mu, \\ 0, & \mathcal{E}_* > \mu. \end{cases} \tag{3.26}$$

Here $\mathcal{E}_* = m\left[v_r^2 + (v_\theta - u)^2 + v_z^2\right]/2$, $u = cE/H = \Omega r$, $\Omega = \mathrm{const}$. It is seen from here that the locked electrons rotate as a solid body (the "isodriftness") [30].

(4) The distribution function of escaping particles is characterized by the following features:

(a) to experimental accuracy, $f_e^{\mathrm{Esc}}$ depends only on the total energy:

$$f_e^{\mathrm{Esc}}(\mathbf{v}, \mathbf{r}) = F(\mathcal{E}). \tag{3.27}$$

(b) this function has a maximum at

$$\mathcal{E} = e(\Phi - \Phi_*), \tag{3.28}$$

where $\Phi_*$ is some average potential corresponding to the electron generation zone;

(c) the amplitude $f_e$ decreases nearly exponentially toward the anode;

(d) the energetic width $\Delta$ of the distribution function is practically independent of $\mathbf{r}$.

Thus, these experimental data imply

$$f_e^{\mathrm{Esc}}(\mathbf{v},\mathbf{r}) = \frac{e^{-x/\Lambda}}{N} \times \begin{cases} 1 - \left(\dfrac{\mathcal{E} + e\Phi - \Phi_*)}{\Delta}\right)^2, & \Delta > \left|\mathcal{E} - e(\Phi - \Phi_*)\right| \\ 0, & \Delta < \left|\mathcal{E} - e(\Phi - \Phi_*)\right|. \end{cases} \quad (3.29)$$

Here $\Lambda$ and $\Delta$ are some constants. Approximation (3.29) is in full agreement with the qualitative characteristics given above (Fig. 3.6e).

(5) The intermediate electrons, which mainly provide the near-wall conductivity, are very difficult to reveal by probe diagnostics [31]. This is due to both their relatively small number and the fact that their localization zone lies close to the external insulator, while the energy distribution function is concentrated toward the high energy part of the locked particles (Fig. 3.6d).

Let us estimate the density of these electrons in the near-anode zone in the SPT R-70 for a standard regime ($\dot{m} = 3\,\mathrm{mg\,s^{-1}}$, $U_p = 300\,\mathrm{V}$, Xe) assuming the total current in this zone ($J_p = 3\,\mathrm{A}$) is carried by the intermediate electrons. The mean velocity of the electrons toward the anode $\langle V_{ez}^{\mathrm{Int}}\rangle$ can be taken as $\sim 0.1 V_{Te} \sim 3 \times 10^7\,\mathrm{cm\,s^{-1}}$. (Such a choice for $\langle V_{ez}^{\mathrm{Int}}\rangle$ corresponds to numerical calculations of the intermediate electron dynamics which demonstrate that they make $\sim$3 turns between collisions). The result is

$$n_e^{\mathrm{Int}} = \frac{J_p}{eS\langle V_{ez}^{\mathrm{Int}}\rangle} \approx 3 \cdot 10^{10}\,\mathrm{cm^{-3}}. \quad (3.30)$$

At the same time, in the zone considered the total electron density measured by the probe method is $n_e \sim 3 \times 10^{11}\,\mathrm{cm^{-3}}$, i.e., an order of magnitude higher. In regard to the acceleration zone located between the two generation zones of "channel" electrons, the fraction of the electron current $J_e$ here is at least an order of magnitude smaller than $J_p$, whereas the estimate for $\langle V_{ez}^{\mathrm{Int}}\rangle$ remains the same. Finally, the oscillations inside the channel

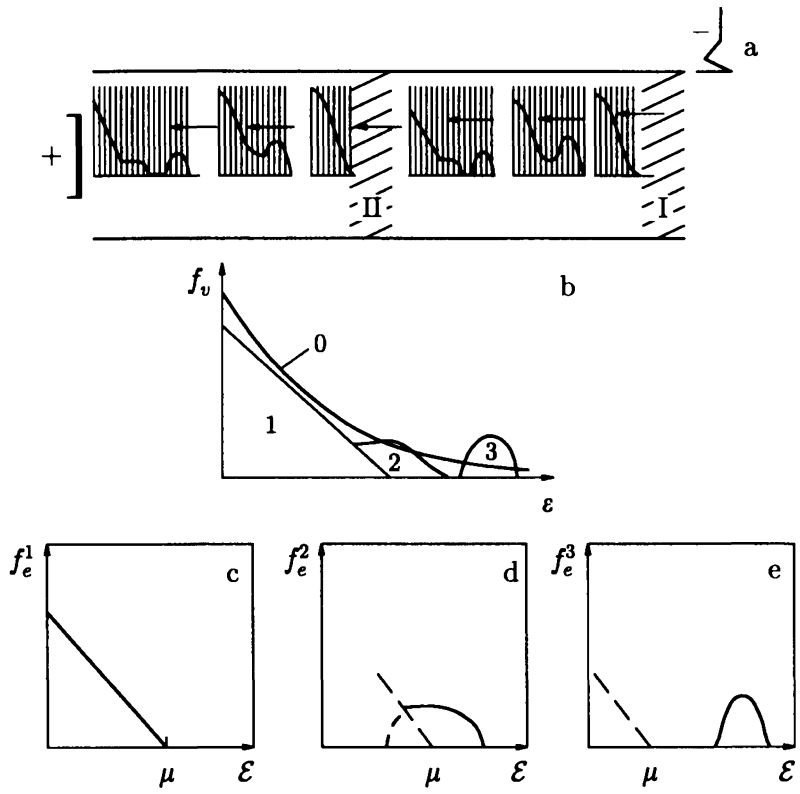


**Fig. 3.6.** Electron distribution in the SPT channel. (a) Evolution of the EDF $f$ in the channel. The "generation regions" of electrons (input zone I) and the ionization zone II are hatched. (b) The general shape of an EDF in velocity space: *0* – a Maxwellian function, *1* – the locked electrons, *2* – the intermediate electrons, *3* – the escaping electrons. (c), (d), (e) EDFs of the main groups of electrons.

somehow mix the high-energy fraction of the locked particles with the intermediate ones.

This explains the worse accuracy and completeness of experimental data on the intermediate component. Nevertheless, experiments clearly indicate that the distribution function of

these electrons has nearly a "table"-like shape. This also follows from the solution of the kinetic equation (see Section 3.4).

### *3.2.2. Kinetics of the escaping electrons*

In this section and below, we semi-empirically derive the distribution functions of the escaping and locked electrons. A similar problem for the intermediate component will be considered in Section 3.4, devoted to the near-wall conductivity.

An approximation for $f_e^{\mathrm{Esc}}$ in the form of a quadratic spline (3.29) was given above. The basic elements of this formula can be obtained from the stationary one-dimensional equation

$$V_z \frac{\partial f^{\mathrm{Esc}}}{\partial z} - \frac{e}{m}\frac{\partial \Phi}{\partial z}\frac{\partial f^{\mathrm{Esc}}}{\partial V_z} = -\frac{f^{\mathrm{Esc}}}{\tau_c}. \tag{3.31}$$

Here $\tau_c$ is the effective time between collisions when the amplitude decreases $e$ times. The natural choice for $\tau_c$ may be

$$\tau_c = b/V_\perp \sim b/\alpha V_z. \tag{3.32}$$

Here $V_\perp$ is the "radial" component of the electron velocity, which can be taken to be proportional to $V_z$ because of the scattering isotropy:

$$V_\perp \approx \alpha V_z, \quad \alpha = \mathrm{const}. \tag{3.33}$$

In this case, the general solution of (3.31) has the form

$$f_e^{\mathrm{Esc}} = A(\mathcal{E} - e\Phi)\, e^{-x/b}. \tag{3.34}$$

The distribution function $A(\varepsilon)$ is determined by conditions inside the fast electron generation zone. Experiments show that $A(\varepsilon)$ is well approximated by a quadratic spline.

### *3.2.3. The distribution function $f_e^{\mathrm{Loc}}$ of captured electrons*

The captured component is formed from the intermediate and escaping components due to rare collisions and not too high noise. Thus, its calculation by the relaxation method is now

hardly possible. However, there is an important point that allows one to determine $f_e^{\mathrm{Loc}}$ to the accuracy of the shape of a function of one argument, which can be taken from experiment. This key point is the already mentioned "isodriftness" of the electron cloud, i.e., its solid rotation in the SPT channel (extended systems with poloidal fields seem to isodrift over a wide range of parameters):

$$u_\theta = c\frac{[\mathbf{E}_T, \mathbf{H}]_\theta}{H^2} = \Omega r, \quad \Omega = \mathrm{const}. \tag{3.35}$$

Here, in accordance with Eq. (2.6),

$$\mathbf{E}_T = -\nabla\Phi_T = \mathbf{E} + \frac{\nabla P_e}{en}.$$

Equation (3.35) automatically yields the relation between the thermalized potential $\Phi_T$ and the flux function:

$$\Phi_T = \Omega(\Psi + \mathrm{const}). \tag{3.36}$$

Experiments directly demonstrate that the isodriftness is a property of the locked electron component. The reason for the isodriftness is the viscosity and building up of various diocotronic oscillations.

Now consider how the isodriftness can be used to determine $f_e^{\mathrm{Loc}}$. If collisions are scarce, $f_e^{\mathrm{Loc}}$ satisfies, to the first approximation, the Liouville kinetic equation

$$\mathbf{v}\frac{\partial f_e^{\mathrm{Loc}}}{\partial \mathbf{r}} - \frac{e}{m}\left(\mathbf{E} + \frac{1}{c}[\mathbf{v}, \mathbf{H}]\right)\frac{\partial f_e^{\mathrm{Loc}}}{\partial \mathbf{v}} = 0. \tag{3.37}$$

This equation in the axially symmetric case allows five integrals:

$$\begin{aligned} &\mathcal{E} = \mathcal{E}_k - e\Phi = \mathrm{const}, \quad \mathcal{P} = mrV_\theta - \frac{e}{c}\Psi = \mathrm{const}, \\ &Y_\alpha(r, z, \mathbf{v}) = \mathrm{const}, \quad \alpha = 1, 2, 3, \end{aligned} \tag{3.38}$$

so that the general solution of Eq. (3.37) can be written in the form

$$f_e^{\mathrm{Loc}} = F(\mathcal{E}, \mathcal{P}, Y_1, Y_2, Y_3). \tag{3.39}$$

Functions $\Phi(\mathbf{r})$ and $\Psi(\mathbf{r})$ are assumed to be known. Integrals $\mathcal{E}(\mathbf{r},\mathbf{v})$ and $\mathcal{P}(\mathbf{r},\mathbf{v})$ are local in the sense that they depend only on the phase space coordinates $(\mathbf{r},\mathbf{v})$. At the same time, integrals $Y_\alpha$ are determined by the entire shape of functions $\Phi(\mathbf{r})$ and $\Psi(\mathbf{r})$, i.e., by particle trajectories in this space. Hence the distribution function of the ejecting and intermediate electrons, which start moving along a new trajectory after each collision with the wall, must be described by a function $F$ depending on all five integrals $(\mathcal{E},\mathcal{P},Y_\alpha)$. In particular, this is why $f_e^{\mathrm{Loc}}$ depends explicitly on $\mathbf{r}$ in Eq. (3.34), which effectively reflects integrals $Y_\alpha$.

The situation is different for the locked electrons. They stay in one place and are affected by relatively weak but mixing perturbations, which must ultimately lead to the loss of the initial parameters of the trajectories. (Apparently, the most characteristic forgetfulness time is that of the transverse adiabatic invariant.) This means that some time after a given group of locked particles has been formed, their distribution function depends on only two local integrals:

$$f_e^M = F(\mathcal{E},\mathcal{P}). \tag{3.40}$$

Now it is almost evident that the isodriftness condition leads to a one-argument function:

$$f_e^M = F(\chi), \quad \chi = \mathcal{E} - \Omega\mathcal{P} + A, \tag{3.41}$$

where $A$ is some constant, since the functions $\Phi(\mathbf{r})$ and $\Psi(\mathbf{r})$ are determined to the accuracy of a constant.

The argument $\chi$ can be recast in the form

$$\chi = \theta - \bar{\mathcal{E}}, \tag{3.42a}$$

where

$$\begin{aligned} \bar{\mathcal{E}} &\equiv \frac{m}{2}\left[V_r^2 + V_z^2 + (V_\theta - u)^2\right], \\ \theta &= e\left(\Phi - \frac{1}{c}\psi\right) + \frac{m}{2}\Omega^2 r^2 + A, \\ u &= \Omega r. \end{aligned} \tag{3.42b}$$

The interpretation of the quantities $\bar{\mathcal{E}}$ and $u$ is clear.

Now we need to relate the general analysis given above with specific SPT conditions. As noted above, here we are dealing with an isodrift regime outside the ionization zone and relatively thin near-wall layers (see Section 3.5). To determine the function $F(\chi)$ either an experiment or a detailed analysis of a specific situation in the channel is required. It is easier to use the experimental data given above, which shows that the function $F(\chi)$ can be approximated by a linear spline (3.26):

$$F = \frac{1}{N}\begin{cases} \mu - \bar{\mathcal{E}}, & \bar{\mathcal{E}} < \mu, \\ 0, & \bar{\mathcal{E}} > \mu. \end{cases} \tag{3.43a}$$

The quantity

$$\mu = \mu_0 + e\left[\left(\Phi - \frac{1}{c}\Psi\right) - \left(\Phi_0 - \frac{1}{c}\Psi_0\right)\right] + \frac{m}{2}\Omega^2(r^2 - r_0^2) \tag{3.43b}$$

has the sense of maximal electron energy at a point of the channel with given $\Phi$, $\Psi$, $r$. The constant $\mu_0$ is determined experimentally and is equal to the maximum electron energy at some "reference" point $(\Phi_0, \Psi_0, r_0)$. The density of the locked electron component in the channel is given by the expression

$$n = \int_{-\infty}^{+\infty} f^M \, d\mathbf{v} = \frac{8\pi}{15N}\left(\frac{2}{m}\right)^{3/2} \mu^{5/2}. \tag{3.44}$$

Considering that $N$ is constant over the entire channel volume under study, we can write

$$N = \frac{8\pi}{15 n_0}\left(\frac{2}{\pi}\right)^{3/2} \mu_0^{5/2}, \tag{3.45}$$

so that

$$n = n_0 \left(\frac{\mu}{\mu_0}\right)^{5/2}. \tag{3.46}$$

From here and Eq. (3.43) the relation between $\Phi$, $\Psi$, and $n$

follows like Eq. (2.8) for the thermalized potential $\Phi_T$:

$$\Phi - \frac{1}{c}\Psi + \frac{m\Omega^2 r^2}{2e} = b + a\left(\frac{n}{n_0}\right)^{2/5}, \qquad a = \frac{\mu_0}{e}, \quad b = -\frac{\mu_0}{e} + \xi_0. \tag{3.47}$$

Now we turn to the pressure tensor for the locked isodrift electrons. First of all, it must be diagonal: $P_{ik} = P\delta_{ik}$. Clearly,

$$P = \frac{8\pi}{3N}\frac{m}{35}\left(\frac{2}{m}\right)^{5/2}\mu^{7/2}, \tag{3.48a}$$

i.e.,

$$\frac{P}{P_0} = \left(\frac{\mu}{\mu_0}\right)^{7/2}. \tag{3.48b}$$

Comparing Eq. (3.48) and (3.46), we arrive at the "adiabatic equation"

$$\frac{P}{P_0} = \left(\frac{n}{n_0}\right)^{7/5}. \tag{3.49}$$

Hence the effective adiabatic index for the locked electrons is

$$\gamma_{\text{eff}} = 7/5, \tag{3.50}$$

and consequently the effective number of degrees of freedom $i$, which is determined as

$$\gamma = \frac{i+2}{i},$$

is $i = 5$. We stress that for the isothermal case (2.10) $\gamma = 1$ and $i = \infty$, respectively. One more important point with regard to Eq. (3.47) should be emphasized. This equation implies that the plasma can be pushed off the channel walls without any singularities. That is, for a given $\Psi$ (force line) and $n \to 0$ the function $\Phi$ has no singularities. Meanwhile, the thermalized potential has a logarithmic singularity for $n \to 0$ and a Maxwellian distribution.

## 3.3. Debye layers on the SPT channel walls

### *3.3.1. Features of DLs in the SPT channel*

Debye layers, which practically always appear near solid surfaces touching plasma, seem to be such "robust" structures that in most cases they remain outside the scope of investigators. As a result (quite paradoxically), the behavior of DLs in real conditions is known much worse than that of many very exotic formations.

It could appear that the DL problem for dielectric surfaces is fully described by the expressions (see, e.g., [17])

$$j_{in} = j_{en}(1-\sigma)\, e^{-\frac{eU_D}{kT_e}}, \tag{3.51a}$$

$$q_\Gamma = j_{en}\, e^{-\frac{eU_D}{kT_e}} \left[(1-\sigma)(2kT_e + e\chi) - \sigma(\bar{\mathcal{E}}_\eta + e\chi)\right]. \tag{3.51b}$$

Here $j_{in}$ and $j_{en}$ are the ion and electron normal flux densities on the surface, respectively, $U_D$ is the absolute value of the near-wall ("Debye") potential jump, $q_\Gamma$ is the density of the energy flux inside the wall, $\chi$ is the surface work function of electrons, $\bar{\mathcal{E}}_\eta$ is the mean energy of secondary electrons leaving the surface, and $\sigma$ is the integral coefficient of the secondary electron emission.

However, in the SPT case the picture becomes much more complicated. Firstly, the distribution function of electrons incident onto the surface is essentially non-Maxwellian. Secondly, the electron component in the SPT channel contains many particles for which $\sigma(\mathcal{E}) > 1$, and here Eqs. (3.51) become invalid. Thirdly, the insulator surfaces surrounding the channel are principally non-smooth. This is due to both the roughness of the insulator material and the erosion by energetic particles which leads to the formation of millimeter-scale structures on the surfaces, which are an order of magnitude larger than the DL thickness estimated by $\mathbf{V}_{Te}$ and $\omega_0$. It should be added that these non-smoothnesses have sharp edges and protuberances.

The construction of adequate DL models taking into account these features is required first of all to determine the scale

of the near-wall conductivity and of the heat flux onto the surface. Both require that the secondary electron distribution function be known. For the given incident particle distributions, a DL theory must be based on the system of Vlasov's equations

$$\begin{aligned} &\frac{\partial f_e}{\partial t} + \mathbf{v}\frac{\partial f_e}{\partial \mathbf{r}} + \frac{e}{m}\left(\nabla\Phi - \frac{1}{c}[\mathbf{v},\mathbf{H}]\right)\frac{\partial f_e}{\partial \mathbf{v}} = 0, \\ &\Delta\Phi = -4\pi e\left(n_i - \int f_e\, d\mathbf{v}\right) \end{aligned} \tag{3.52}$$

and a boundary condition such as (1.14). In the case of a stationary (static) DL, the magnetic field effect on electrons can be neglected since the Debye radius in SPTs is an order of magnitude smaller than the Larmor electron radius. However, as will be shown below (Sections 3.3.4, 3.5.3), in SPT conditions the classical DL seems to disappear and form a highly noisy structure with a thickness much higher than the Debye radius $r_D$. Thus, the calculations of such a dynamical DL must be carried out in a region with size $\gg r_D$ and accounting for the magnetic field. In view of the many uncertainties in the case of a "developed" dynamical DL, here we consider how a thin quasistatic DL can be calculated taking into account the above-mentioned three features of this problem in the SPT channel.

Due to the large mass $M$ and small Debye radius, the ion distribution function within the DL can be considered fully determined by its value $f_{i0}$ at the "outer boundary" $x = x_0 = 0$ (Fig. 3.7), so that

$$f_i(\mathbf{v},\mathbf{r}) = f_{i0}\left(V_x - \sqrt{\frac{2e|\Phi|}{M}}, V_y, V_z, \mathbf{r}\right). \tag{3.53}$$

Here we have assumed that the outer boundary potential $\Phi_0 = 0$. While it is not difficult to find a "likely" shape for $f_{i0}$ (for example, a quadratic spline), the situation with a "likely" EDF at $x = x_0$

$$f_e = f_{e0}\big(V_x, V_y, V_z, x_0, y, z\big)\Big|_{V_x<0} \tag{3.54}$$

is more complicated. This is mainly due to the lack of knowledge about the intermediate electron distribution function $f_e^{\text{Int}}$.

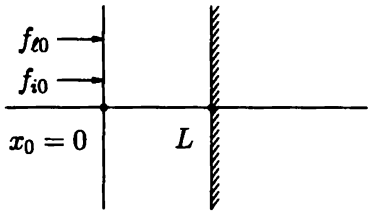


**Fig. 3.7.** The region $0 \leq x \leq L$ of DL calculations.

The setting of boundary conditions on the insulator surface also has some distinctive features.

It is expedient to determine an adequate surface relief using profilograms of the insulators used.

More complex is the question on the distribution of the surface charge density $\gamma$ formed by the "adhering" electrons and ions. Neglecting the insulator surface conductivity, we have

$$\frac{\partial \gamma}{\partial t}(t, \mathbf{x}) = j_{in}(t, \mathbf{x}) - j_{en}(t, \mathbf{x}). \tag{3.55}$$

Here $\mathbf{x}$ are two-dimensional surface coordinates.

If the electric field were not to penetrate deep inside the dielectric, the boundary condition for the $E$-field would be taken as

$$E_n = -\frac{\partial \Phi}{\partial \mathbf{n}} = 4\pi\gamma. \tag{3.56a}$$

Here $\mathbf{n}$ is the normal to the surface. However, such a field penetration surely occurs in the case of an inhomogeneous density $\gamma(\mathbf{x})$. Then one should also solve Laplace's equation inside the insulator with the boundary condition at $x_1 \to +\infty$:

$$\frac{\partial \Phi}{\partial x_1} = 0. \tag{3.56b}$$

However, it may well happen that the surface conductivity is of importance. In such a case, using Ohm's law

$$\mathbf{i} = \Sigma \mathbf{E}_t, \tag{3.57a}$$

instead of Eq. (3.55) we obtain

$$\frac{\partial \gamma}{\partial t} + \mathrm{div}_{\mathbf{x}} \mathbf{i} = j_{in} - j_{en}. \tag{3.57b}$$

Here $\mathbf{i}$ is the surface current density and $\Sigma$ is the surface conductivity. However, at present there are no data about $\Sigma$ in realistic SPT conditions.

As for the secondary electron distribution function immediately close to the surface, it is determined by the distribution function of the incident electrons near the wall and the functions $\sigma(\mathcal{E}_p)$ and $\eta(\mathcal{E}, \mathcal{E}_p)$. (As was recently found, for the ion flux density that falls onto SPT walls, intensive dislocation generation occurs, which may substantially change $\sigma(\mathcal{E}_p)$ and other surface insulator properties.)

### *3.3.2. Stationary one-dimensional DL (general relations) [33]*

In this case, the system of equations (3.52) takes the form

$$f_i = F_i\Big(M\frac{V^2}{2} + e\Phi\Big), \tag{3.58a}$$

$$f_e = F_e\Big(m\frac{V^2}{2} - e\Phi\Big), \tag{3.58b}$$

$$\frac{d^2\Phi}{dx^2} = -4\pi e(n_i - n_e). \tag{3.58c}$$

Since in the one-dimensional case there is no direct dependence on $V_y$ and $V_z$, we shall use the function

$$f_{i,e} \leftarrow \int_{-\infty}^{+\infty} f_{i,e}\, dV_y\, dV_z \tag{3.59}$$

and the notation $V_x = V$.

The underlying assumption of the simplest stationary DL model is naturally that the electron component in the layer consists of a system of three fluxes, one of which ($f_{e1}$) comes from the plasma volume toward the wall and other two of which ($f_{e2}$ and $f_{e3}$) come from the wall. The first of them ($f_{e2}$) is due to elastically reflected electrons whose energy is not sufficient to overcome the potential barrier in the DL. The other ($f_{e3}$) is due to the secondary electrons "knocked out" by the primary electrons that reached the wall.

The functions $f_{e2}$ and $f_{e3}$ are automatically determined by specifying

$$f_{e0} \equiv F_{e0}^{+}\left(m\frac{V_0^2}{2}\right)\Big|_{x=x_0,\,V_x>0} \tag{3.60}$$

at $x = x_0$, where $\Phi = \Phi_0 = 0$ is set. Thus,

$$f_{e1} = F_{e0}^{+}\left(m\frac{V^2}{2} + e\Phi\right), \quad m\frac{V_0^2}{2} > eU_D, \tag{3.61a}$$

$$f_{e2} = 2F_{e0}^{+}\left(m\frac{V^2}{2} + e\Phi\right), \quad m\frac{V_0^2}{2} < eU_D. \tag{3.61b}$$

Here the factor 2 takes into account the presence of incident and reflected particles. The component $f_{e3}$ is then

$$f_{e3}\left(m\frac{V^2}{2} - e\Phi\right) = \int_{U_D}^{\infty} \eta\left(m\frac{V^2}{2} - e(U_D + \Phi), \mathcal{E}_p\right) \times \sigma(\mathcal{E}_p)\, F_{e0}^{+}(\mathcal{E}_p - eU_D)\, d\mathcal{E}_p. \tag{3.62}$$

Here $\mathcal{E}_p$ is the kinetic energy of the electron reaching the surface. At $\Phi = -U_D$ we denote

$$f_{e3} \equiv F_{e3}^{-}\left(m\frac{V_0^2}{2}\right). \tag{3.63}$$

We shall take into account only the incident ion flux:

$$f_i\Big|_{x\to-\infty} = F_i^{+}\left(M\frac{V_0^2}{2}\right)\Big|_{V>0}, \tag{3.64a}$$

and hence

$$f_i(x,V) = V_0 F_i^+ \left(M\frac{V_0^2}{2}\right)\left(V_0^2 - \frac{2e}{M}\Phi\right)^{-1/2}. \qquad (3.64b)$$

Using Eqs. (3.60), (3.62), and (3.64), we arrive at the potential distribution equation

$$\frac{d^2\Phi}{dx^2} = -4\pi e\left[\int_0^\infty \frac{V_0 F_i^+(\frac{1}{2}MV_0^2)}{\sqrt{V_0^2 - \frac{2e}{M}\Phi}}\,dV_0 - \int_{\sqrt{\frac{2e}{m}|\Phi|}}^\infty \frac{V_0 F_e^+(\frac{1}{2}mV_0^2)}{\sqrt{V_0^2 + \frac{2e}{m}\Phi}}\,dV_0 - 2\int_0^{\sqrt{\frac{2e}{m}|\Phi|}} \frac{V_0 F_e^+(\frac{1}{2}mV_0^2)}{\sqrt{V_0^2 + \frac{2e}{m}\Phi}}\,dV_0 - \int_0^\infty \frac{V_0 F_e^-(\frac{1}{2}mV_0^2)}{\sqrt{V_0^2 - \frac{2e}{m}(\Phi + U_D)}}\,dV_0\right] \equiv Q(\Phi). \qquad (3.65)$$

For the given functions $F_i^+$ and $F_e^+$, using Eq. (3.62) we can find $F_e^-$ so that Eq. (3.65) can be solved in quadratures. This equation has two integration constants, which are determined by the potential value at $x = x_0$ and the ion flux density $j_{i0}$ falling on the walls. The latter should be equal to the electron flux "adhering" to the wall to satisfy the stationarity condition (we assume that $j_{ex} > 0$)

$$j_{in} = j_{en}. \qquad (3.66)$$

At the left boundary ($x_0$), we assume that $\Phi_0 = 0$, and by the natural requirement that the main plasma volume is quasi-neutral, we obtain [see Eq. (3.51b)] $Q(0) = 0$.

At small $\Phi$, for many functions $F_i^+$, $F_e^+$ we can write

$$Q\Big|_{\Phi\to 0} = \lambda\Phi.$$

If $\lambda \equiv \kappa^2 > 0$, we obtain the solution with an oscillating electric field distribution (see Section 3.4). A particular case of such

solutions is represented by Bernstein–Kruscal–Greene waves. A detailed analysis of Eq. (3.65) is given in [34]. Here we shall restrict ourselves to considering integral characteristics such as (3.51) for non-Maxwellian distribution functions and $\sigma(\mathcal{E}_p) \sim 1$.

### *3.3.3. Integral relations for a stationary DL on smooth surfaces [33]*

*Electron–ion flux balance on dielectric surfaces.* Let us assume that all the DL parameters depend on only one coordinate, $x$, the dielectric surface lies at $x_1 = L$, and the ion flux is incident from the left ($x_0 \to -\infty$). For visual purposes we set the electron current $j_e$ positive. Then the current balance at $x_1 = L$ can be written as $j_{ex} = j_{ix}$. The value of $j_{ix}$ considered is given at $x = x_0$ and

$$j_{ex} = e \int \left[1 - \sigma(\mathbf{v})\right] V_x f_\Gamma(\mathbf{v})\, d\mathbf{v}. \tag{3.67}$$

Here $f_\Gamma(\mathbf{v})$ is the EDF immediately before the wall. Later we shall take into account that near the first multiplication threshold, $\mathcal{E}^*$, the secondary emission coefficient can be approximated by a linear function:

$$\sigma = \sigma_0 + (1 - \sigma_0)\frac{\mathcal{E}}{\mathcal{E}^*}. \tag{3.68}$$

Since collisions in the DL are assumed to be infrequent and the conditions stationary, we have

$$f_\Gamma(\mathbf{v}) = F_0\left(V_x + \sqrt{2eU_D/m}, V_y, V_z\right). \tag{3.69}$$

Here $F_0(\mathbf{v})$ is the EDF near the DL; also, we assume that the wall's potential is $\Phi_c = -U_D < 0$. Substituting Eq. (3.68) and (3.69) into (3.67), we get the flux balance equation

$$j_{ix} = e(1 - \sigma_0) \int\limits_{V_x > 0}^{\infty} V_x \left(1 - \frac{\mathcal{E}}{\mathcal{E}^*}\right) \times F_0\left(V_x + \sqrt{2eU_D/m}, V_y, V_z\right) d\mathbf{v}. \tag{3.70}$$

We shall speak of the existence of a "classical DL" if Eq. (3.70) for a given EDF $F_0(\mathbf{v})$ and given constants $j_{ix}$, $\mathcal{E}^*$, $\sigma_0$ has a solution

$$U_D = -\Phi_c > 0, \tag{3.71a}$$

and

$$\frac{dj_{ex}}{d\Phi_c} = -\frac{dj_{ex}}{dU_D} > 0. \tag{3.71b}$$

Clearly, the dependence

$$j_{ex}(\Phi_c) = e(1-\sigma_0) \int\limits_{V_x>0}^{\infty} V_x \left(1 - \frac{\mathcal{E}}{\mathcal{E}^*}\right) \times F_0\left(V_x + \sqrt{2e\,|\Phi_c|\,/m}, V_y, V_z\right) d\mathbf{v} \tag{3.72}$$

represents the volt-ampere characteristic (VAC) of the DL and condition (3.71b) implies that this characteristic is increasing. Otherwise the DL will be "roughly unstable."

*Druvestein relations.* If $F_0(\mathbf{v})$ is a function of only the total electron energy $\mathcal{E}_0 = \mathcal{E} - e\Phi$, then for a given VAC of the Debye layer, i.e., the function $j_{ex}(\Phi)$, one can find $F_0(\mathcal{E}_0)$ in a way similar to Druvestein's double integration method. Consider two simple models.

(1) Let $F_0$ depend on only one velocity component $V$. Then

$$j_{ex}(\Phi_c) = \frac{e(1-\sigma_0)}{m} \int\limits_0^{\infty} d\mathcal{E} \left(1 - \frac{\mathcal{E}}{\mathcal{E}^*}\right) F_0\left(\mathcal{E} - e\Phi_e\right) \equiv \frac{e(1-\sigma_0)}{m} I(\Phi_c), \tag{3.73a}$$

and after the differentiation we obtain the equation for $F_0$ :

$$F_0'(-e\Phi_c) + \frac{1}{\mathcal{E}^*} F_0(-e\Phi_c) = -\frac{1}{e^2} \frac{d^2 I(\Phi_c)}{d\Phi_c^2}. \tag{3.73b}$$

Here the prime means differentiation with respect to the entire argument.

(2) Let $F_0$ depend on $\mathcal{E} - e\Phi_c$ as before, but the velocity space be three-dimensional:

$$\mathcal{E} = \frac{m}{2}\left(V_x^2 + V_y^2 + V_z^2\right);$$

then

$$j_{ex}(\Phi_c) = 4\pi e \frac{1-\sigma_0}{m^2} \int_0^\infty \mathcal{E}\, d\mathcal{E} \left(1 - \frac{\mathcal{E}}{\mathcal{E}^*}\right) F_0(\mathcal{E} - e\Phi_c)$$

$$\equiv \frac{4\pi e}{m^2}(1-\sigma_0)\, Y(\Phi_c), \tag{3.74a}$$

and the equation for $F_0$ has the form

$$F_0'(-e\Phi_c) + \frac{2}{\mathcal{E}^*} F_0(-e\Phi_c) = -\frac{Y'''(\Phi_c)}{e^3}. \tag{3.74b}$$

At $\mathcal{E}^* \to \infty$, Eq. (3.74b) reduces to Druvestein's formula connecting the EDF with the VAC of the probe.

*Volt-ampere characteristics for a one-dimensional EDF.* The general relations (3.72) can be illustrated by a one-dimensional EDF when $f = F_0(V_x)$. A DL with a three-dimensional EDF can be considered in a similar way.

For analysis of Eq. (3.73a) it is advantageous to consider two shapes of $F(V_x)$: Maxwellian distributions with unbounded change of $V_x$ and "truncated" EDFs that are not zero in the interval $0 \le V_x < V_M$.

For a one-dimensional Maxwellian distribution,

$$f(V_x) = n_0 \left(\frac{m}{2\pi k T_e}\right)^{1/2} \exp\left(-\frac{\mathcal{E} - e\Phi}{kT_e}\right). \tag{3.75a}$$

Using Eq. (3.73a), we find

$$I(\Phi_c) = n_0 \left(\frac{m}{2\pi k T_e}\right)^{1/2} kT_e \left(1 - \frac{kT_e}{\mathcal{E}^*}\right) \exp\left(\frac{e\Phi_c}{kT_e}\right). \tag{3.75b}$$

Thus, a classical DL can exist only at

$$kT_e < \mathcal{E}^*. \tag{3.76a}$$

It is interesting that at $kT_e = \mathcal{E}^*$ the electron flux incident on the wall vanishes independently of $\Phi_c$. Should a three-dimensional Maxwellian distribution be taken, a more rigorous DL existence condition would appear instead of (3.76a):

$$kT_e < \mathcal{E}^*/2. \tag{3.76b}$$

The situation is different for "truncated" EDFs. Here always a range of $\Phi_c < 0$ exists where $I(U_D) > 0$, $dI(\Phi_c)/d\Phi_c > 0$. Indeed, let the truncation of the EDF occur at $\mathcal{E}_M$. Then if

$$-e\Phi_c < \mathcal{E}_1 = \mathcal{E}_M - \mathcal{E}^*, \tag{3.77}$$

the quantity $(1 - \mathcal{E}/\mathcal{E}^*) > 0$ in the integrand (3.73a) and hence $I(\Phi_c) > 0$. It is also evident that $I'(\Phi_c) > 0$ if condition (3.77) is satisfied.

Thus, for truncated EDFs there are always conditions for a classical DL to form. But for their realization one more condition should be met:

$$(j_{ex})_{\max} = e\frac{1-\sigma_0}{m} \max I(\Phi_c) \geq j_{ix}^0. \tag{3.78}$$

This condition is not always fulfilled.

To be more specific, consider three types of the "truncated" EDF.

Figure 3.8a shows an EDF $F_0$ in which most particles have an energy $\mathcal{E} < \mathcal{E}^*$. Clearly, the VAC corresponding to this distribution (Fig. 3.8d) is similar, to the accuracy of the ion component, to that of ordinary Langmuir probes.

In the second case (Fig. 3.8b) the mean energy of electrons $\langle\mathcal{E}\rangle > \mathcal{E}^*$ and the VAC of the DL (Fig. 3.8e) has nothing in common with the probe VAC.

Finally, the third distribution has two humps (Fig. 3.8c). Here the main low-energy group of particles has $\langle\mathcal{E}\rangle < \mathcal{E}^*$, and the relatively scarce high-energy electrons have $\langle\mathcal{E}\rangle > \mathcal{E}^*$. The corresponding VAC is shown in Fig. 3.8f. In all three cases, classical DL can appear. In case (b), two layers corresponding to $\Phi_c^{(1)}$ and $\Phi_c^{(2)}$ could be formed.

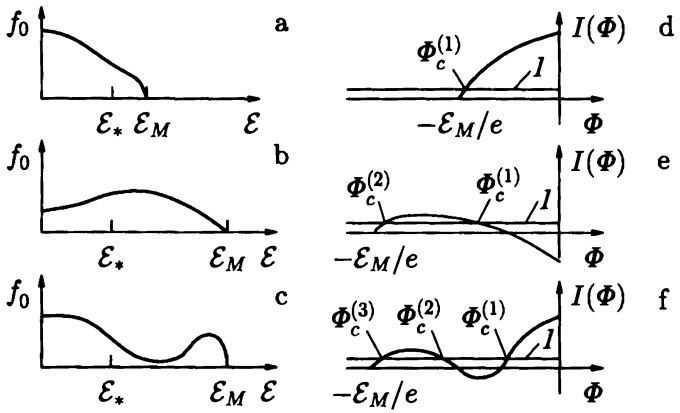


**Fig. 3.8.** Electron distribution functions (1) and the corresponding volt-ampere characteristics of the stationary Debye layers (2).

However, the DL with $\Phi_c^{(1)}$ is "roughly" unstable since this value lies on the decreasing part of the VAC. In case (c), there are two roughly stable values $\Phi_c^{(1)}$ and $\Phi_c^{(3)}$. However, the DL with $\Phi_c^{(2)}$ in case (b) and with $\Phi_c^{(3)}$ in case (c) can turn out to be unrealizable if the ion current is strong enough and condition (3.78) is not met.

To conclude this section, consider the VAC of a DL formed when the EDF resembles that of the intermediate component and has a "table" shape:

$$F_0(\mathcal{E}) = \begin{cases} 0, & \mathcal{E} < \mathcal{E}_1, \\ A, & \mathcal{E}_1 < \mathcal{E} < \mathcal{E}_2, \\ 0, & \mathcal{E} > \mathcal{E}_2. \end{cases} \tag{3.79}$$

In this case, the dependence $I(\Phi)$ defined by Eq. (3.73a) has the form $(\Phi_c < 0)$

$$I(\Phi_c) = \int d\mathcal{E} \left(1 - \frac{\mathcal{E}}{\mathcal{E}^*}\right) F_0(\mathcal{E} - e\Phi_c) \tag{3.80}$$

$$= \begin{cases} (\mathcal{E}_2 - \mathcal{E}_1 + e\Phi_c)\left(1 - \dfrac{\mathcal{E}_2 + \mathcal{E}_1 - e\Phi_c}{2\mathcal{E}^*}\right), & \mathcal{E}_1 - e\Phi_c \le \mathcal{E} \le \mathcal{E}_2, \\ 0, & \mathcal{E}_2 - \mathcal{E}_1 \le -e\Phi_c. \end{cases}$$

Here

$$I(0) = (\mathcal{E}_2 - \mathcal{E}_1)\left(1 - \frac{\mathcal{E}_2 + \mathcal{E}_1}{2\mathcal{E}^*}\right). \tag{3.81a}$$

This quantity is positive at

$$\mathcal{E}_2 + \mathcal{E}_1 < 2\mathcal{E}^*. \tag{3.81b}$$

Next, the stability condition $(dI/d\Phi > 0)$ takes the form

$$\frac{dI}{d\Phi} = \left(1 - \frac{\mathcal{E}_1}{\mathcal{E}^*}\right) + \frac{e\Phi_c}{\mathcal{E}^*} > 0, \tag{3.82a}$$

and hence requires

$$e\Phi_c > \mathcal{E}_1 - \mathcal{E}^*. \tag{3.82b}$$

This implies that the smaller the $\mathcal{E}_1$, the more stable the DL. The value of $\Phi_c$ is in turn determined by the ion flux, and so for specific $\mathcal{E}_1$ and $\mathcal{E}^*$ inequality (3.82b) can be invalid if the value of $\Phi_c$ is a large negative number.

*The energy given to the wall by electrons in the stationary regime.* An electron incident on the wall brings its kinetic and potential (the surface work function $e\chi$) energy. The knocked-out particle, in turn, carries away the surface work and some kinetic energy.

A constructive calculation of such fluxes can clearly be performed only for a classical DL. This results in formulas such as Eq. (3.51). Its derivation is obvious and we omit it here.

### *3.3.4. Dynamical DL*

If $\langle\sigma(\mathcal{E})\rangle \geq 1$, then the monotonic static DL disappears and we are dealing with quite a new situation. The potential in a DL cannot be monotonic for sure, even if it is static, and must rather have a dynamic structure.

Let us consider one of the possible one-dimensional settings of the problem of DL studies near a dielectric wall. This is a local consideration. Let $x$ be the coordinate across the layer (in this section $x = 0$ and $x = L$ correspond to a remote point

in the plasma and to the wall position, respectively); $V$ is the electron velocity component along the $x$-axis. Then the kinetic equation for the EDF has the form [35, 36]

$$\frac{\partial f_e}{\partial t} + V\frac{\partial f_e}{\partial x} - \frac{e}{m}E\frac{\partial f_e}{\partial V} = 0, \tag{3.83}$$

where $E$ is the electric field with the potential $\Phi(x)$ satisfying Poisson's equation

$$\frac{\partial^2 \Phi}{\partial x^2} = -4\pi e(n_{i0} - n_e). \tag{3.84}$$

Here we shall assume the ion density across the layer to be constant: $n_{i0} = \text{const}$. Thus, if $j_{i0} = en_{i0}V_{i0} = \text{const}$ is the ion flux on the wall, we can write the following equation for the wall surface charge density $\rho$:

$$\frac{d\rho}{dt} = j_{i0} - e\int_0^\infty V f_e(t, L, V)\big(1 - \sigma(V)\big)\, dV. \tag{3.85}$$

Let the electric field inside the dielectric be zero. Then the boundary condition on the wall (the relation between $E$ and $\rho$) is

$$E(L) = -4\pi\rho.$$

The potential is normalized such that

$$\Phi(0) = 0.$$

To complete the mathematical setting of the problem, some boundary conditions on $f_e$ should be specified. Let the electrons at $x = 0$ and for $V > 0$ be Maxwellian:

$$f_e(t, 0, V) = n_{e0}\left(\frac{m}{2\pi k T_{e0}}\right)^{1/2} \exp\left(-\frac{mV^2}{2T_{e0}}\right), \tag{3.86}$$

where $n_{e0}$, $T_{e0}$ are the density and temperature of the incident electrons.

Now we should formulate a condition on $f_e$ at $x = L$. To this end, we assume that one of three possible events may occur during the collision of an electron of energy $\mathcal{E}_p$ with the wall: (1) the electron disappears; (2) the electron knocks one secondary electron with energy $\mathcal{E}$ out of the wall; (3) the electron knocks out two secondary electrons with energies $\mathcal{E}_1$ and $\mathcal{E}_2$. In the last case, we assume for simplicity that the secondary electron energies are always the same: $\mathcal{E}_1 = \mathcal{E}_2 = \mathcal{E}$. Let $P_0(\mathcal{E}_p)$, $P_1(\mathcal{E}, \mathcal{E}_p)$, and $P_2(\mathcal{E}, \mathcal{E}_p)$ be the probability of the first, second, and third event, respectively. We also introduce the following quantities: $W_0(\mathcal{E}_p) = P_0(\mathcal{E}_p)$, $W_1(\mathcal{E}_p) = \int P_1(\mathcal{E}, \mathcal{E}_p)\, d\mathcal{E}$ — the probability of the birth of one secondary electron, $W_2(\mathcal{E}_p) = \int P_2(\mathcal{E}, \mathcal{E}_p)\, d\mathcal{E}$ — the probability of the birth of two secondary electrons. Then by definition we have the following secondary electron emission coefficient $\sigma$ :

$$\sigma(\mathcal{E}_p) = W_1(\mathcal{E}_p) + 2W_2(\mathcal{E}_p). \tag{3.87}$$

The normalization condition reads

$$W_0(\mathcal{E}_p) + W_1(\mathcal{E}_p) + W_2(\mathcal{E}_p) = 1.$$

It is also convenient to introduce the following functions (the conditional probabilities):

$$\begin{aligned} &\eta_1(\mathcal{E}, \mathcal{E}_p) = P_1(\mathcal{E}, \mathcal{E}_p)/W_1(\mathcal{E}_p), \quad \int_0^\infty \eta_1(\mathcal{E}, \mathcal{E}_p)\, d\mathcal{E} = 1, \\ &\eta_2(\mathcal{E}, \mathcal{E}_p) = P_2(\mathcal{E}, \mathcal{E}_p)/W_2(\mathcal{E}_p), \quad \int_0^\infty \eta_2(\mathcal{E}, \mathcal{E}_p)\, d\mathcal{E} = 1. \end{aligned} \tag{3.88}$$

It is natural to suppose that the secondary electron energy does not exceed the progenitor electron energy. To take this point into account, below we set $\eta_1(\mathcal{E}, \mathcal{E}_p) \equiv 0$ for $\mathcal{E} \geq \mathcal{E}_p$ and $\eta_2(\mathcal{E}, \mathcal{E}_p) \equiv 0$ for $\mathcal{E} \geq \mathcal{E}_p/2$.

Now we can write the boundary condition at $x = L$. To this end, we count the number of secondary electrons (below we

denote the energy distribution of primary and secondary electrons through $F^{\pm}(\mathcal{E})$ respectively)

$$\sqrt{2\mathcal{E}}F^{-}(\mathcal{E}) = \int_0^\infty P_1(\mathcal{E},\mathcal{E}_p)\sqrt{2\mathcal{E}_p}\,F^{+}(\mathcal{E}_p)\,d\mathcal{E}_p + 2\int_0^\infty P_2(\mathcal{E},\mathcal{E}_p)\sqrt{2\mathcal{E}_p}\,F^{+}(\mathcal{E}_p)\,d\mathcal{E}_p$$

or

$$\sqrt{2\mathcal{E}}F^{-}(\mathcal{E}) = \int_0^\infty \left[\eta_1(\mathcal{E},\mathcal{E}_p)W_1(\mathcal{E}_p) + 2\eta_2(\mathcal{E},\mathcal{E}_p)W_2\mathcal{E}_p)\right]\sqrt{2\mathcal{E}_p}F^{+}(\mathcal{E}_p)\,d\mathcal{E}_p. \tag{3.89}$$

The specific choice of functions $W_0$, $W_1$, $W_2$, $\eta_1$, and $\eta_2$ has been made as follows:

$$\begin{aligned}
W_0(\mathcal{E}_p) &= \begin{cases} \dfrac{W_{00}}{1+W_{01}(\mathcal{E}_p/\mathcal{E}_1)^4}, & \mathcal{E} < \mathcal{E}_1, \\ 0, & \mathcal{E} > \mathcal{E}_1, \end{cases} \\
W_2(\mathcal{E}_p) &= \begin{cases} (\mathcal{E}_p/\mathcal{E}_2)^4, & \mathcal{E} < \mathcal{E}_2, \\ 1, & \mathcal{E} > \mathcal{E}_2, \end{cases} \\
W_1(\mathcal{E}_p) &= 1 - W_0(\mathcal{E}_p) - W_2(\mathcal{E}_p), \\
\eta_1(\mathcal{E},\mathcal{E}_p) &= \begin{cases} \dfrac{2}{\mathcal{E}_p}\left(1-\dfrac{\mathcal{E}}{\mathcal{E}_p}\right), & \mathcal{E} < \mathcal{E}_p, \\ 0, & \mathcal{E} > \mathcal{E}_p, \end{cases} \\
\eta_2(\mathcal{E},\mathcal{E}_p) &\equiv \eta_1(\mathcal{E},\mathcal{E}_p/2).
\end{aligned} \tag{3.90}$$

Here $W_{00}$, $W_{01}$, $\mathcal{E}_1$, $\mathcal{E}_2$ are the model parameters: $W_{00} = W_0(0)$, $\mathcal{E}_1$ is the energy corresponding to the first multiplication threshold, $\mathcal{E}_2$ is the energy of the second threshold.

Thus, we have a closed system of equations for determining $f_e$, $\Phi$, and $\rho$.

The calculations were performed for the following parameters: the velocity of the incident ions $V_{i0} = 3 \times 10^5$ cm s$^{-1}$; the

ion density $n_{i0} = 10^{12}\,\mathrm{cm}^{-3}$ ($n_{i0} = n_{e0}$). The temperature of the incident electrons $T_{e0}$ has been varied. Below, we shall use units appropriate to this problem. As a unit of density we take $n_{e0}$, the velocity is measured in units of the characteristic thermal velocity $V_{T0} = \left(T_{e0}/m\right)^{1/2}$, the Debye radius $r_{D0} = \left(T_{e0}/4\pi e^2 n_{e0}\right)^{1/2}$ serves as a unit of length, the time is in units of $t_0 = r_{D0}/V_{T0}$, the energy unit is $T_{e0}$, and the electric field unit is $4\pi e n_{e0} r_{D0}$.

If the electron temperature is $T_{e0} \sim 10\,\mathrm{eV}$, the ratio of the ion to electron fluxes onto the wall is of order $10^{-3}$ and the first term in Eq. (3.85) can be neglected. Three essentially dimensionless parameters remain: the length of the system in units of the Debye radius $x_0$, and the multiplication threshold energies $\varepsilon_1 = \mathcal{E}_1/T_{e0}$ and $\varepsilon_2 = \mathcal{E}_1/T_{e0}$. We also set $W_{00} = 0.8$ and $W_{01} = 20$.

The general picture appears as follows. We found three different types of solutions changing into each other as the temperature increases. As an illustration, consider the results of three calculations.

Let $x_0 = 15$ and consider the case of "low" temperature $\varepsilon_1 = 1$, $\varepsilon_2 = 2$. Calculations show that in this case the solution comes to a stationary regime. The plots shown in Fig. 3.9a present the distributions of the electron density $n_e(x)$ and the potential $\Phi(x)$ in the range $(0, x_0)$ and the electron distribution function $f_e$ in different outlets ($x = 0$; $x_0/2$; $x_0$). The electron density on the wall is small $n_e(x_0) = 0.07$; the potential and the charge of the wall are negative $\Phi(x_0) = -3.0$, $\rho(x_0) = -1.9$. Thus, at low temperatures we obtain a classical Debye layer that prevents slow electrons from falling onto the wall. Its thickness is of the order of several Debye radii.

A qualitatively new behavior of the main parameters arises at high temperatures. Figure 3.9b shows the results of calculations for $\varepsilon_1 = 0.5$, $\varepsilon_2 = 1$, i.e., at twice the temperature. A stationary solution can be obtained in this case as well (the approach of the stationary solution here is accompanied by intense oscillations), but the "autonomous" layer is no longer pos-

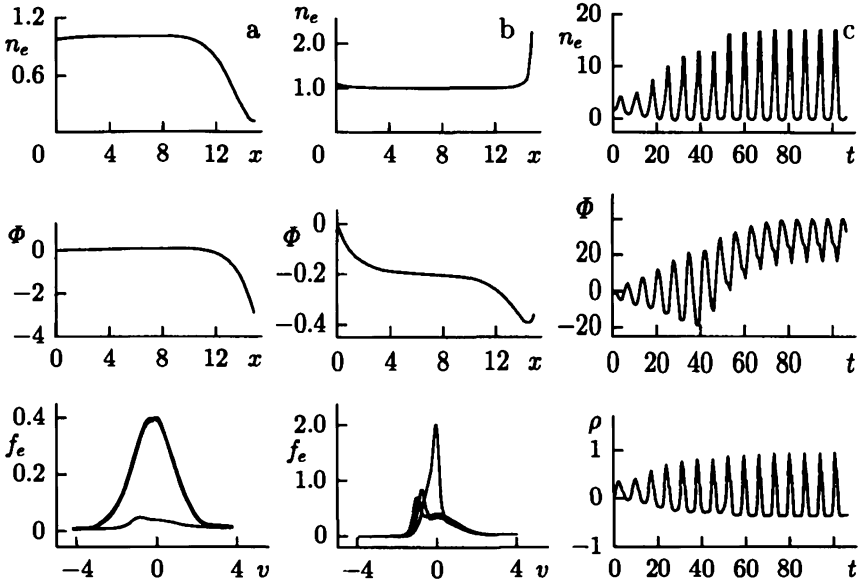


**Fig. 3.9.** Change of the DL structure with increasing electron temperature. (a) A stationary regime ($\varepsilon_1 = 1, \varepsilon_2 = 2$). Distributions of the density $n_e(x)$, potential $\Phi(x)$, and $f_e(v)$ inside three outlets $x = 0, 0.5x_0, x_0$. (b) The same for $\varepsilon_1 = 0.5, \varepsilon_2 = 1$. (c) $\varepsilon_1 = 0.35, \varepsilon_2 = 0.7$. The temporal behavior of the electron density $n_e$ and potential $\Phi$ on the wall ($x = x_0$), and also of the wall's charge $\rho$.

sible. The wall charge is positive [$\rho(x_0) = 0.14$], and the density $n_e(x_0) = 2.2$ is twice as high as in the plasma. In addition, the near-wall layer expands and the perturbation covers the entire region considered ($0 \leq x \leq x_0$). The potential drops at first and then slightly increases toward the wall.

At higher temperatures the stationary regime is not obtained and strong oscillations with a frequency of the order of several Langmuir frequencies appear. Consider the case with $\varepsilon_1 = 0.35$, $\varepsilon_2 = 0.7$. In Fig. 3.9c, we present time plots for the potential, the electron density, and the charge on the wall. Such

behavior has been obtained for other parameters. The mean wall charge is $\rho(x_0) \cong 0.25$, the potential $\Phi(x_0) \cong 25$, and the density $n_e(x_0) \cong 8$. Close to the wall, the storage of slow electrons begins, while the potential increases starting from $x = 0$.

The calculations suggest that the dynamical layer thickness increases with the mean electron energy. This restricts the possibility of DL study in this model. The discovered density growth near the wall also requires modification of the model considered and sewing it to the entire azimuthally drifting electron flux.

### 3.4. The near-wall conductivity (NWC)

The trajectories discussed in Section 3.2 clearly demonstrate that electron collisions with the wall allow the electrons to move across the magnetic field toward the anode. Such a transfer, as already noted, has been called near-wall conductivity [37]. NWC is an essentially classical effect. This is one more "neoclassic" conductivity.

Without a magnetic field, the corresponding effective bulk conductivity is

$$\sigma_{\text{eff},0} \frac{e^2 n \tau_{\text{eff}}}{m}, \tag{3.91}$$

where $\tau_{\text{eff}} = \alpha b / V_T$ is the characteristic time between two electron collisions with the walls, $b$ is the transverse size of the plasma volume, $V_T$ is the thermal particle velocity, and $\alpha < 1$ is a numerical factor of the collision efficiency. From Eq. (3.91) it follows that the equation of electron dynamics ("Ohm's law")

$$\frac{\mathbf{j}_e}{\sigma_{\text{eff}}} = \mathbf{E}^* + \frac{1}{c} [\mathbf{v}_e, \mathbf{H}] \tag{3.92}$$

leads to the classical expression for the conductivity across the magnetic field

$$\sigma_{\perp}^{\text{NWC}} = \frac{\sigma_{\text{eff},0}}{1 + \left(\frac{\sigma_{\text{eff},0} H}{enc}\right)^2} \propto \frac{1}{H^2}. \tag{3.93}$$

In Eq. (3.92), collisions with heavy particles are neglected and $\mathbf{E}^* = \mathbf{E} + \nabla P_e/(en)$.

Expression (3.93) is analogous to a "purely" classical formula that implies electron collisions with heavy particles (atoms and ions). By contrast, NWC is caused by collisions with a "superheavy particle" — the surface of the insulator (wall) — and Eqs. (3.91) and (3.93) are averaged inside the plasma volume.

Both the classical transport across the $\mathbf{H}$-field and NWC are due to collision-induced "breakdown" of the electron drift in crossed $(\mathbf{E}, \mathbf{H})$-fields. However, while sharing some properties with classical transfer, NWC has some unique features.

(a) Firstly, there is a clear space localization of collisions. If, in the classical case, points of the drift breakdown are located chaotically throughout the whole space, during NWC the drift breakdown occurs either on the surface itself or immediately nearby. A specific breakdown "space synchronization" emerges, which leads to the formation of near-wall currents with a thickness of the order of the electron Larmor radius as a rule:

$$\delta \propto \rho_e \propto \frac{V_{Te}}{\omega_H}. \tag{3.94}$$

This is explained by the fact that electric drift restoration occurs over such a scale length.

(b) Secondly, the current density due to near-wall conductivity changes non-monotonically, as a rule. This property of NWC, which is its diagnostic feature, can be illustrated as follows. Imagine a channel formed by two scattering parallel planes covered with an infinitesimally thin Debye surface (Fig. 3.10). Let the secondary emission coefficient be $\sigma = 1$ and the accommodation coefficient be $\kappa = 1$. The magnetic field is assumed to be homogeneous and directed along the $z$-axis and the electric field also homogeneous and directed along the $x$-axis. Then electrons incident, for example, on the bottom plane pass through the Debye layer on the surface, lose practically all energy and, after being reflected from the surface, pass through the DL again and, having the same energy, go with velocity $V_{\text{II}} = \sqrt{2eU_D/m}$

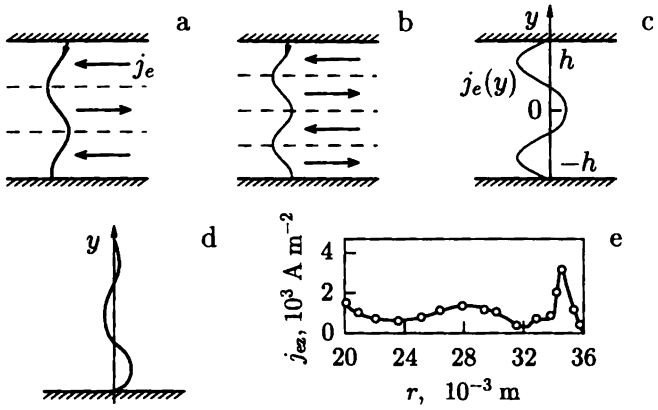


**Fig. 3.10.** NWC on a microrough surface. (a), (b) Separation of the channel into layers with different directions of the mono-velocity electron current density: (a) the total electron current $J_e \neq 0$; (b) the total electron current $J_e = 0$; (c) the current density in a plane channel [Eq. (3.112)]; (d) plot of the function $Y(k)$; (e) the experimental distribution $j_{ez}(r)$ [40].

toward the upper plane, tracing a cycloid. In Fig. 3.10, the trajectory projection on the plane $(x, z)$ is shown. It is clear that the space between layers is separated into layers with interchanging directions of the electron current $\mathbf{j}_e = -en\mathbf{V}_e$. The thickness of a layer with one current direction is

$$\lambda = V_{\text{II}} \frac{\pi}{\omega_H}. \tag{3.95}$$

Depending on the distance $L$ between the planes and on the ratio $L/V_{\text{II}}$, a different number of current layers can appear between the planes. If there is an equal number of oppositely directed current layers, the total current between the layers vanishes (Fig. 3.10a). In the general case, the total current can have an arbitrary sign but its absolute value cannot exceed the current in one layer (Fig. 3.10b). This picture is, of course, ideal. But it obviously shows the feasibility of formation of spatially oscillat-

ing current distributions inside the SPT channel. The effect of "transversal quantization" of the current density described is still to be studied systematically. It seems that an optimal system of layers is observed in experiments when the oscillations practically disappear and the efficiency coefficient increases. Usually, a non-monotonic structure $j_{ez}(r)$ (Fig. 3.10c) is observed, which can be treated as a superposition of distributions like that shown in Fig. 3.10a, b but with different $V_{\text{II}}$.

Note further two NWC features — the effect of surface geometry and DL thickness. We shall call a surface "microharsh" if the DL thickness

$$\delta_D \gg \delta\Gamma, \tag{3.96a}$$

where $\delta\gamma$ is the height of irregularities on the plane surface. Oppositely, if

$$\delta_D \ll \delta\Gamma \tag{3.96b}$$

the surface is called "macroharsh" (Fig. 3.11).

In the first case, most incident particles are mirror-reflected due to the DL, and the drift breakdown occurs only for those particles that penetrate this layer and are diffusion scattered by the surface itself. In the second case, the drift breakdown can occur without piercing the DL, i.e., due to mirror reflection by surface elements tilted in the drift direction $(\mathbf{n}^0, \mathbf{u}_d) \neq 0$. Here $\mathbf{n}^0$ is the normal to the surface. In SPTs, both mechanisms actually occur (see Section 4).

Some words about the history of the problem. The possibility of near-wall conductivity in SPT conditions was first noted by A. I. Morozov in 1968 [37] (later the author was informed that a similar phenomenon takes place in solids, where it was called a "static skin-effect" [38]). The principal content of this paper is presented in Section 3.4.1. The first experiments with artificial inhomogeneities were carried out at the Kurchatov AEI and at MIREA, as well as at MAI. Systematic experimental studies of NWC features based on probe measurements of the electron current in the channel began in 1978 in the laboratory headed by A. I. Bugrova (MIREA). Their results will be briefly described in Section 3.4.5.

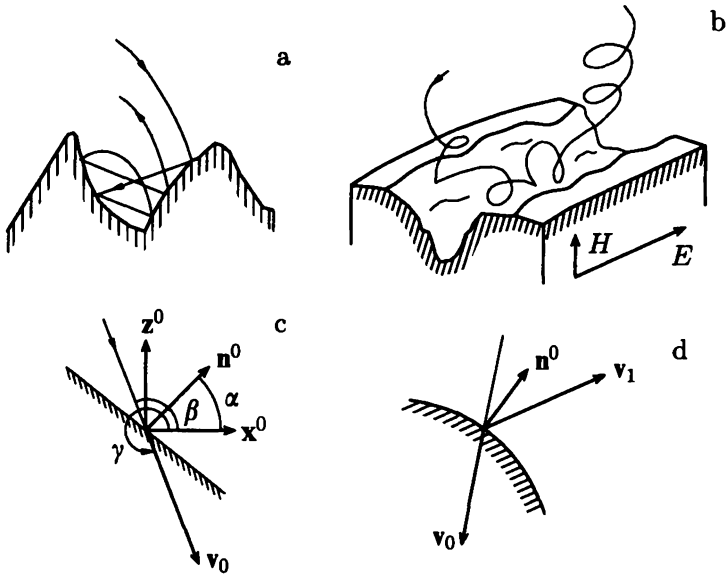


**Fig. 3.11.** NWC on a macroinhomogeneous surface. (a) The scheme of a multiple reflection. (b) The "run" of an electron toward the anode in a slit oriented along the $E$-field. (c) Explanations for the two-dimensional case. (d) Explanations for the three-dimensional case.

As for the development of the NWC theory, the papers by A. I. Morozov and A. P. Shubin in which sufficiently general kinetic equations for NWC were studied should be noted (see below, Sections 3.4.6 and 3.4.7).

### *3.4.1. NWC in a semi-infinite plasma near a microrough surface*

The simplest example is provided by an NWC near a microrough surface that restricts a semi-infinite plasma volume in the presence of a magnetic field (axis $x$) perpendicular to the surface and an electric field parallel to the surface (axis $z$). We also assume the Debye layer to be much thinner than the layer

due to NWC so that in calculations its thickness can be neglected. In such a case, both the incident and reflected particles undergo trochoidal motion:

$$\begin{aligned} z &= a + \frac{A}{\omega_e}\cos(\omega_e t + \alpha), \quad V_z = A\sin(\omega_e t + \alpha), \\ x &= V_x t, \quad V_x = V_{x0} = \text{const}, \quad u = cE/H, \\ y &= b + ut + \frac{A}{\omega_e}\sin(\omega_e t + \alpha), \quad V_y = u + A\cos(\omega_e t + \alpha). \end{aligned} \tag{3.97}$$

When considering static problems, the time should be excluded from Eq. (3.97) with the aid of the equation $x = V_x t$. Given the distribution functions $f^+(V', 0, y, z)$ and $f^-(V', 0, y, z)$ of incident and reflected particles on the surface of the wall, one can find their values at any $x$ using the substitution

$$\begin{aligned} V_x' &\to V_x, \\ V_y' &\to u + (V_y - u)\cos\left(\omega_e \frac{x}{V_x}\right) + V_z \sin\left(\omega_e \frac{x}{V_x}\right), \\ V_z' &\to V_z \cos\left(\omega_e \frac{x}{V_x}\right) - (V_y - u)\sin\left(\omega_e \frac{x}{V_x}\right), \\ y' &\to y - u\frac{x}{V_x} + \frac{V_z}{\omega_e} \\ &\quad - \frac{1}{\omega_e}\left[V_z \cos\left(\omega_e \frac{x}{V_x}\right) - (V_y - u)\sin\left(\omega_e \frac{x}{V_x}\right)\right], \\ z' &\to z + \frac{V_y - u}{\omega_e} \\ &\quad - \frac{1}{\omega_e}\left[V_z \sin\left(\omega_e \frac{x}{V_x}\right) + (V_y - u)\cos\left(\omega_e \frac{x}{V_x}\right)\right]. \end{aligned} \tag{3.98}$$

The distribution function of incident particles $f^+$ is assumed to be Maxwellian with a velocity shift equal to the drift velocity $u$:

$$f^+ = \frac{1}{N^+}\exp\left(-\frac{1}{c_{T0}^2}\left[V_x^2 + (V_y - u)^2 + V_z^2\right]\right). \tag{3.99}$$

The distribution function of reflected particles (at $x = 0$) is taken as an "immobile" Maxwellian function:

$$f^- = \frac{1}{N^-} \exp\left(-\frac{1}{c_{T1}^2}\left[V_x^2 + V_y^2 + V_z^2\right]\right). \tag{3.100}$$

The normalization coefficients are

$$N^+ = \frac{\pi^{3/2} C_{T0}^3}{2n^+}, \quad N^- = \frac{\pi^{3/2} C_{T1}^3}{2n^-},$$

where $n^+$ and $n^-$ are the densities of incident and reflected particles. If $\sigma_e$ is the secondary electron emission coefficient, then

$$n^+ c_{T0} \sigma_e = n^- c_{T1}. \tag{3.101}$$

Substituting (3.97) into (3.98), it is easy to obtain that the function (3.99) remains unchanged while Eq. (3.100) takes the form

$$f^- = \frac{1}{N^-} \exp\left\{-\frac{1}{c_{T1}^2}\left[V_x^2 + V_z^2 + (V_y - u)^2 + u^2 + 2u(V_y - u)\cos\left(\omega_e \frac{x}{V_x}\right) + 2uV_z \sin\left(\omega_e \frac{x}{V_x}\right)\right]\right\}. \tag{3.102}$$

It is interesting to note that $n^- = \int f^- d\mathbf{v}$ is independent of $x$.

In our case, only the $x$-component of the current is of interest, and so we restrict ourselves to calculating this. By the evenness of the function $f^+(V_z)$, we have (the negative sign is omitted before the integral)

$$j_z = e \int_{V_x=-\infty}^{0} \iint V_z f^- d\mathbf{v}. \tag{3.103}$$

Substituting Eq. (3.102), we arrive at

$$j_z = e \frac{2n^-}{\sqrt{\pi}} c \frac{E}{H} \int_{-\infty}^{0} \sin\left(\frac{x\omega_e}{c_{T1}\alpha}\right) \exp\left(-\alpha^2\right) d\alpha. \tag{3.104}$$

It is seen from here that the current density distribution near the wall is determined by the function

$$Y(k) \equiv \int_0^\infty \sin\left(\frac{k}{\alpha}\right) \exp\left(-\alpha^2\right) d\alpha, \quad k \equiv \frac{x\omega_e}{c_{T1}} \equiv \frac{x}{\rho_e}, \quad \alpha = \frac{V_x}{c_{T1}}. \tag{3.105}$$

To clarify the dependence $Y(k)$, one can use a third-order equation for this function

$$(kY' - Y)'' = 2Y,$$

or for the function $z = Y/k$

$$\left(k^2 z'\right)'' = 2zk. \tag{3.106}$$

From the integral representation of the function $Y(k)$ it follows that of the three solutions (3.106) we need only the one that is an odd function of $k$ and has the properties

$$\begin{aligned} &Y(0) = 0, \\ &Y'(k) \to \infty \quad \text{at} \quad k \to 0, \\ &Y'(k) \to 0 \quad \text{at} \quad k \to \infty. \end{aligned} \tag{3.107}$$

Without making a detailed study of this function, we restrict ourselves to finding its asymptotic at $k \to 0$ and $k \to \infty$. It is easy to see that at $k \to 0$ the solutions are approximated by the functions $Y_1 \sim k \ln|k|$, $Y_2 \sim \text{const}$, $Y_3 \sim k$. Taking into account Eq. (3.107), we see that

$$Y(k)\Big|_{k\to\infty} \approx k \ln|k| \approx x \ln\frac{x}{\rho_e}. \tag{3.108}$$

This means that the current density vanishes at $x = 0$ and increases somewhat faster than linearly with the distance from the wall.

At $k \to \infty$ solutions (3.106) can be approximated by the functions

$$Y_n \approx k \exp\left(|k|^{2/3} a_n\right), \quad a_n = \frac{3}{2^{2/3}} \exp\left(\frac{2\pi i n}{3}\right), \quad n = 1, 2, 3. \tag{3.109}$$

Conditions (3.107) imply $Y = c_1 Y_2 + c_2 Y_3$, where $c_1$ and $c_2$ are constants. Thus

$$Y(k) \approx k \exp\left(-\frac{3}{2^{5/3}}|k|^{2/3}\right) \cos\left(\frac{3\sqrt{3}}{2^{5/3}}|k|^{2/3} + \text{const}\right). \quad (3.110)$$

The general shape of the dependence $j_z(x)$ is shown in Fig. 3.10d. As expected, the current is indeed localized in the layer $\sim \rho_e$. The total current in a layer of thickness 1 cm along the $z$-axis is

$$i = \int_{-\infty}^{0} j_z \, dx.$$

Substituting Eq. (3.104) into this expression yields

$$i = \sigma_e j_{e0} \frac{u}{\omega_e} = \sigma_e j_{e0} \frac{h}{2}. \quad (3.111a)$$

Here $h$ is the height of the cycloid. The physical meaning of the formula is evident. Using the expressions for $j_{e0} = en^+ c_{T0}/\sqrt{\pi}$ and $u = cE/H$, we can recast Eq. (3.111a) in the form of Ohm's law:

$$i = \sigma_e \frac{n^+ c_{T0}}{\sqrt{\pi}} \frac{mc^2}{H^2} E. \quad (3.111b)$$

Now we wish to evaluate the scale $i$ for parameters similar to those of the current onto the wall (at present we do not know them exactly): $\sigma_e = 1$, $n^+ = 0.5 \times 10^{11}\,\text{cm}^{-3}$, $c_{T0} = 2 \times 10^8\,\text{cm s}^{-1}$, which correspond to $T_+ = 10\,\text{eV}$, $E = 100\,\text{V cm}^{-1}$, $H = 150\,\text{Oe}$. Substituting them into Eq. (3.111b), we find $i = 0.14\,\text{A cm}^{-1}$. Considering that the NWC generally appears near the external insulator, we obtain the total current $J_e = 2\pi Ri \approx 2.8\,\text{A}$ for the R-70 model, which is in reasonable agreement with the experimental data.

### *3.4.2. NWC of electron plasma in a plane layer*

A natural generalization of the problem considered is the problem of the NWC of electron plasma in a finite plane layer.

Omitting the rather lengthy calculations, here we present the final results. Let the thickness of the layer be $2b$ and the distribution functions of electrons reflected from the wall be Maxwellian functions with parameters $n^+$, $T^+$, $n^-$, $T^-$, respectively. Then the longitudinal current is

$$j_z(x) = \frac{eu}{\sqrt{\pi}} \left\{ n^+ S\left[\frac{b}{\rho_L^+}\left(1+\frac{x}{b}\right)\right] + n^- S\left[\frac{b}{\rho_L^-}\left(1-\frac{x}{b}\right)\right]\right\}. \tag{3.112}$$

Here $\rho_L^{\pm} = \left(2kT^{\pm}/m\right)^{1/2}/\omega_e$ are the Larmor radii calculated for the temperatures of the upper and lower walls, respectively. In particular, for $n^+ = n^-$, $T^+ = T^-$ the density of the current on the wall (at $x = \pm b$) is

$$j_z(\pm b) = \frac{enu}{\sqrt{\pi}} S\left(\frac{2b}{\rho_L}\right). \tag{3.113}$$

One more comment should be made. We have considered examples with the simplest reflection model when the secondary electrons are Maxwellian. Clearly, similar calculations can be carried out for any scattering function $S(\mathbf{v}, \mathbf{v}')$.

### *3.4.3. NWC due to surface macroinhomogeneities*

At present, there are no systematic calculations of NWC in SPTs due to the macroinhomogeneities of the insulators. This is explained, on the one hand, by the difficulties of such calculations (they can be most effectively done only numerically), and on the other hand, by the fact that today there are no insulator surface profiles that would be of much interest for many readers.

Worth studying could be specially designed profiles providing a given NWC and lifetime, or those formed due to insulator erosion during thruster operation (see Section 4).

The artificial (pre-formed) profiles working in the mirror reflection regime (i.e., having a large Debye jump) would have some important advantages: their properties would be practically independent of the insulator material and the anomalous

erosion would be radically suppressed (Section 4.2). Here, however, the question arises of the effective energy loss by electrons heated due to the motion toward the anode. The problem of maintaining the initial ("optimal") profile under the conditions of inevitable ion bombardment also emerges. Thus, the problem of artificial macroinhomogeneities is very complicated and requires large complex studies, and we shall not be concerned with them here.

The second class of problems is related to NWC caused by profiles formed during particle bombardment of the insulator surface. This question will be partially considered in Section 4 in connection with the "anomalous" erosion problem.

Completing these introductory remarks, we should note that the main methodical difficulty in constructing a theory of NWC on macroinhomogeneous surfaces relates to the inevitable appearance of "multiple collision chains" (Fig. 3.11a, b), which are practically absent on microharsh surfaces.

*NWC on a tilted "mirror" plane.* To obtain a more concrete understanding of the situation on a macroinhomogeneous surface, we consider the incidence of electrons onto an inclined mirror-reflecting plane. For this purpose, we write down expressions connecting the velocity of an electron after reflection $\mathbf{V}_1$ with the incidence velocity $\mathbf{V}_0$ and the orientation of the normal to the surface determined by the unit vector $\mathbf{n}^0$. This relation can be obtained in two forms: first in a two-dimensional representation, then in a three-dimensional form.

*The two-dimensional case.* Let the $z$-axis be along the magnetic field, the $x$-axis lie in the $(\mathbf{n}^0, \mathbf{z}^0)$ plane, and the $y$-axis be normal to this plane. Let the velocity $\mathbf{V}_0$ lie in the plane $(\mathbf{n}^0, \mathbf{z}^0)$. Then (Fig. 3.11c)

$$\begin{aligned} \gamma &= \pi + \beta, \\ V_{1x} &= V\cos\gamma = -V\cos\beta, \\ V_{1y} &= V\sin\gamma = -V\sin\beta. \end{aligned} \tag{3.114}$$

Here $V = |\mathbf{V}_0| = |\mathbf{V}_1|$. The velocity components of the reflected

electron are

$$V_{1x} = V\cos(2\alpha - \beta), \quad V_{1y} = V\sin(2\alpha - \beta). \tag{3.115}$$

The last expression is especially important for us. It demonstrates that $V_{1z} > 0$ only for

$$\beta < 2\alpha. \tag{3.116}$$

If $\alpha$ is sufficiently small, then $V_{1z} < 0$ and hence an electron continues to move downward after the collision with the plane, which must mean the appearance of multiple collisions.

*The three-dimensional case.* Let us introduce a coordinate plane pulled over the vectors $\mathbf{n}^0$ and $\mathbf{V}_0$ (Fig. 3.11d). Constructing now a unit vector $\mathbf{w}^0$ orthogonal to $\mathbf{n}^0$ and lying in this plane, we obtain, from the mirror symmetry, that

$$\mathbf{V}_1 = -(\mathbf{V}_0, \mathbf{n}^0)\mathbf{n}^0 + (\mathbf{V}_0, \mathbf{w}^0)\mathbf{w}^0. \tag{3.117a}$$

In turn, $\mathbf{w}^0$ is determined by

$$\mathbf{w}^0 = \frac{\mathbf{V}_0 - (\mathbf{V}_0, \mathbf{n}^0)\mathbf{n}^0}{|\mathbf{V}_0 - (\mathbf{V}_0, \mathbf{n}^0)\mathbf{n}^0|}. \tag{3.117b}$$

From Eqs. (3.117) we find

$$\begin{aligned} \mathbf{V}_0 &= -(\mathbf{V}_1, \mathbf{n}^0) + (\mathbf{V}_1, \mathbf{w}^0)\mathbf{w}^0, \\ \mathbf{w}^0 &= \frac{\mathbf{V}_1 - (\mathbf{V}_1, \mathbf{n}^0)\mathbf{n}^0}{|\mathbf{V}_1 - (\mathbf{V}_1, \mathbf{n}^0)\mathbf{n}^0|}. \end{aligned} \tag{3.118}$$

Here we have taken into account that

$$|\mathbf{V}_0| = |\mathbf{V}_1|, \quad (\mathbf{V}_0, \mathbf{n}^0) = -(\mathbf{V}_1, \mathbf{n}^0). \tag{3.119}$$

Knowing the velocities of the reflected particles and the EDF of the incident ones, one can find the EDF of the reflected particles. Namely, if

$$f_e^+ = F_0(\mathbf{V}_0) \tag{3.120a}$$

is the incident electron distribution function, then assuming them to survive after colliding with the wall, the conservation law is

$$(\mathbf{V}_0, \mathbf{n}^0) F_0(\mathbf{V}_0)\Big|_\Gamma = -(\mathbf{V}_1, \mathbf{n}^0) F_1(\mathbf{V}_1)\Big|_\Gamma .$$

From here and using Eqs. (3.118), (3.119) we arrive at

$$F_1(\mathbf{V}_1)\Big|_\Gamma = F_0\Big(\mathbf{V}_1 - 2(\mathbf{V}_1, \mathbf{n}^0)\Big)\Big|_\Gamma . \tag{3.120b}$$

Here the index $\Gamma$ means that the functions are taken on the wall surface.

By assuming that the $\mathbf{E}$ and $\mathbf{H}$ fields are homogeneous, one can use Eq. (3.98):

$$\mathbf{V}(\mathbf{r}_0) = \hat{K}(\mathbf{r} - \mathbf{r}_0)\Big[\mathbf{V}(\mathbf{r})\Big]. \tag{3.121}$$

Here $\hat{K}$ is a matrix, $\mathbf{V}_0$ is the velocity, and $\mathbf{r}_0$ is the initial coordinate of a particle on the reflecting surface. Thus, the distribution function of the reflected electrons will be

$$f_e^-(\mathbf{r}, \mathbf{V}) = F_1\left(\hat{K}(\mathbf{r} - \mathbf{r}_0)\Big[\mathbf{V}(\mathbf{r})\Big]\right), \tag{3.122}$$

and consequently the electron current density across the magnetic field for a single mirror reflection from a unitary tilted surface is

$$\mathbf{j}_\perp(\mathbf{r}) = \int \mathbf{V}_\perp f_e^+(\mathbf{r}, \mathbf{V})\, d\mathbf{V}. \tag{3.123}$$

An analytical calculation of the integral on the right-hand side is generally very complicated. In addition, the accuracy of this integral is in principle limited by taking into account single scatterings only.

### *3.4.4. The inverse problem of NWC theory for semi-infinite space [39]*

As shown in Section 3.4.1, in a semi-infinite space the density of the $z$-component of the electric current decreases nonmonotonically, in an oscillatory way, with the distance from the

wall. It was these oscillations $j_{ez}(x)$ that allowed the experimental discovery of NWC. However, the dependence of $j_{ez}$ on $x$, if known, permits us to go further and, assuming stationarity and homogeneity of the fields, to determine in some cases the distribution of the $V_x$ component of the reflected particles:

$$F^-(V_x) = \int f^-(\mathbf{v})\, dV_y\, dV_z. \tag{3.124}$$

Although the above assumptions in real SPT conditions are not strictly fulfilled, the behavior of $j_{ez}(x)$ provides much useful information. In particular, as mentioned above in the section on the DL, the distinctive features of $j_{ez}(x)$ pointed to the mosaic structure of the Debye layer and to the possibility of breakdown of the DL.

Now let us find an explicit form of the relation between $F(V_x)$ and $j_{ez}(x)$. One more assumption should be made, namely, that the scattering is isotropic in the $y, z$-directions on the wall surface and the function $f^-(\mathbf{v})$ can be presented in the form

$$f^-(\mathbf{v}, x) = G\left(V_z^2 + V_y^2\right) B(V_x). \tag{3.125}$$

The functions $G$ are assumed to be normalized to unity.

In such a case, substitution of Eq. (3.98) yields for arbitrary $x$

$$f^-(\mathbf{v}, x) = G\left[\left(V_z + u \sin\frac{\omega_e x}{V_x}\right)^2 + \left(V_y - u + u\cos\frac{\omega_e x}{V_x}\right)^2\right] B(V_x).$$

From here we find

$$\begin{aligned} j_z(x) &= e \int_{-\infty}^{0} dV_x \int_{-\infty}^{+\infty} V_z\, dV_z\, dV_y\, G\left(V_y, V_z, \frac{x}{V_x}\right) B(V_x) \\ &= -eu \int_{-\infty}^{0} \sin\frac{\omega_e x}{V_x}\, B(V_x)\, dV_x. \end{aligned} \tag{3.126}$$

Introducing the new variable $\xi = \omega_e/V_x$, we can rewrite Eq. (3.126) as the Fourier integral

$$j_z(x) = eu\omega_e \int_0^{-\infty} \sin \xi x \, B\left(\frac{\omega_e}{\xi}\right) \frac{d\xi}{\xi^2}, \tag{3.127}$$

and hence

$$B(V_x) = \frac{1}{\pi}\left(\frac{\omega_e^2}{eV_x^2}\right) \int j_z(x) \sin \frac{\omega_e x}{V_x} \, dx. \tag{3.128}$$

### *3.4.5. Experimental studies of NWC [30, 40, 41]*

The first arguments favoring the existence of NWC had an integral character (Kurchatov AEI, MIREA, MAI). Here are some of them:

— When a ceramic stick is introduced into the channel from the side of the outlet (for instance, the probe holder), the discharge current increases significantly.

— The discharge current, propulsion, and efficiency coefficient of the thruster are very sensitive to the insulator material and contamination of the surface (see Section 8 for a discussion of the latter).

— If longitudinal scratches are made on the insulator surface, the discharge current $J_p$ and electron temperature $T_e$ do not change significantly unless the depth of the scratch exceeds some value of the order of the Debye radius calculated by $\langle \mathcal{E}_e \rangle$ and $n_e$.

Systematic experimental studies of NWC began in 1978 at MIREA in A. I. Bugrova's laboratory. Here distributions of the $z$-component of the current density $j_z(r)$ were measured using directed probes [40]. The first experiments already showed these distributions to be oscillatory. Since then, numerous studies have been carried out [30, 41]. The distributions $j_z(r)$ were measured for different discharge voltages and magnetic fields, as well as at different braking potentials on the probe. Some expected effects

such as the decrease in distance between oscillations with increasing magnetic field or the disappearance of peaks near the external insulator with increasing braking potential, etc. have been found. But some unexpected results were discovered as well. These include, primarily, the asymmetry of the distribution $j_z(r)$ with respect to the external and internal insulators and especially the presence of a sharp peak near the external insulator, which is due to "too" low-energy electrons. That this peak is due to just such electrons follows not only from its disappearance with the braking potential on the probe but also the following estimate in the spirit of the inverse problem described above. Clearly, the maximum of the current density formed by a group of electrons with close values of $V_{\text{II}}$ will be located at a distance

$$\delta r_{\max} = V_{\text{II}} \frac{\pi}{2\omega_{He}} \tag{3.129}$$

from the wall. By knowing $\delta r_{\max} \approx 2\,\text{mm}$, $H \approx 50\,\text{Oe}$, we find

$$V_{\text{II}} \approx \frac{2\delta r_{\max}\omega_{He}}{\pi} = 7 \cdot 10^7\,\text{cm}\,\text{s}^{-1}.$$

This velocity corresponds to $\mathcal{E}_{\text{II}}^{(peak)} \sim 1\,\text{eV}$, which is far below the Debye jump estimated using the characteristic energy of the same locked electrons ($\mathcal{E}_{\text{II}}^{(\text{Loc})} \sim 15\,\text{eV}$). It is this difference between the two energies that gave rise to the hypothesis on "DL breakdown," which was later confirmed experimentally (see Section 3.5 below).

As for the asymmetry of the distribution $j_z(r)$ relative to the external and internal insulator surfaces, this was explained by electron trajectory calculations (Fig. 3.5), which showed the major role of the radial inhomogeneity of the magnetic field and the transversal adiabatic invariant.

### *3.4.6. Integral equation for the EDF in NWC conditions*

The dynamics of electrons in the NWC regime can be considered as a generalization of Knudsen's flow of a neutral gas in

tubes. In such a flow the motion of a particle consists of interchanging "regular" flights by inertia and diffuse scatterings during collisions with the wall. In the case of NWC we also have two phases: collisions (now they can be not only diffusive but also reflective) and regular motion in the electromagnetic field. The general description of the electron behavior in the NWC regime with given $(\mathbf{E}, \mathbf{H})$-fields reduces to solving the Liouville equation

$$\frac{\partial f}{\partial t} + \mathbf{v}\frac{\partial f}{\partial \mathbf{r}} - \frac{e}{m}\left(E + \frac{1}{c}[\mathbf{v}, \mathbf{H}]\right)\frac{\partial f}{\partial \mathbf{v}} = 0 \qquad (3.130a)$$

with the boundary condition

$$V_n f^-(\mathbf{v}, P) = \int S(\mathbf{v}, \mathbf{v}'|P)\, V_n f^+(\mathbf{v}', P)\, d\mathbf{v}'. \qquad (3.130b)$$

Should the fields be known, the trajectory of a particle can be analytically calculated in many cases with sufficient accuracy for our purposes. This is true first of all for homogeneous $(\mathbf{E}, \mathbf{H})$-fields, as well as for sufficiently strong magnetic fields when trajectories and velocities of particles can easily be found in the drift approximation. Thus, we shall assume that the analytical expressions for the "kinetic" operator

$$K \equiv \hat{K}(\mathbf{x}_1, \mathbf{v}_1|\mathbf{x}_0, \mathbf{v}_0) \qquad (3.131)$$

are known. This operator determines the coordinate $\mathbf{x}_1$ and the velocity $\mathbf{v}_1$ of an electron on the wall provided that it has collided with the wall at a point $\mathbf{x}_0$ and been given a velocity $\mathbf{v}_0$ during the scattering. By knowing the scattering function $S(\mathbf{v}, \mathbf{v}')$ in addition, we are able to fully calculate the evolution of the EDF in the channel by solving an integral equation of the form

$$V_n f^-(\mathbf{v}_1, \mathbf{x}_1) = \tilde{S}\hat{K}\left[V_n' f^-(\mathbf{v}', \mathbf{x}')\right]. \qquad (3.132)$$

Unfortunately, this equation can hardly be used as a basis for analytical calculations of the EDF due to the extremely varied shapes of trajectories in the SPT channel, i.e., due to the very

complicated character of the operator $K$ even for the simplest field configurations, since, as was shown in Section 3.2, particles can either travel from one wall to another or cannot reach the other wall and return. This fact strongly complicates the structure of Eq. (3.122).

Thus, in the published papers [42, 43] mainly the simplest case of two parallel walls is considered. In this case, electrons are passed from one insulator to another after the collision, while the $(\mathbf{E}, \mathbf{H})$-fields are homogeneous (the case with a drift description of trajectories was considered in [44]). These assumptions were added with two more narrow presuppositions: the scattering was assumed to be isotropic and elastic, although some fraction of the particles $\nu = 1 - \sigma$ dies out in each collision. Clearly, these additional conditions correspond to the group of escaping electrons.

Under the assumptions made it is expedient to introduce two pairs of functions $f_1^{\pm}$ and $f_2^{\pm}$ corresponding to each of the walls. Considering the above, we can write down the balance equation for a given point of the surface:

$$\int |V_n| f_\alpha^-\left(\mathbf{V}^2, z, \pm h\right) d\Omega = \sigma \int |V_n'| f_\alpha^+\left(\mathbf{V}, z, \pm h\right) d\Omega. \quad (3.133)$$

Here $V_n = V\cos\theta$, $d\Omega = \sin\theta\, d\theta\, d\varphi$, $\alpha = 1, 2$. A system of two equations at $x = \pm h$ follows from Eq. (3.133):

$$f_\alpha^-\left(\mathbf{V}^2, z, \pm h\right) = \frac{\sigma}{\pi} \int |\cos\theta'|\, f_\alpha^+\left(\mathbf{V}', z, \pm h\right) d\Omega'. \quad (3.134)$$

Because of the elastic character of the collisions, both parts of Eq. (3.134) were divided by $V$. Since both equations (3.134) are similar, we shall rearrange one of them for $f_1^-$. The function $f_1^+$ entering the right-hand side of this equation can be expressed through $f_2^-\left(\mathbf{V}'', z'', -h\right)$ because

$$f_1^+\left(\mathbf{V}', z, +h\right) = \hat{K} f_2^-\left(\mathbf{V}'', z'', -h\right). \quad (3.135)$$

The operator $K$ expresses $(\mathbf{V}'', z'')$ at $x = -h$ through $(\mathbf{V}', z)$ — the phase coordinates of the point to which an electron comes after reaching $x = h$. Using Eq. (3.98), we then have

$$(V'')^2 = V^2 + 2u\xi,$$
$$\xi = V_z \sin\frac{2h}{\omega_e|V_x'|} + (V_y - u)\left(1 - \cos\frac{2h}{\omega_e|V_x'|}\right). \tag{3.136}$$

$z''$ is also expressed through $\xi$ :

$$z'' = z - \frac{\xi}{\omega_e}. \tag{3.137}$$

Ultimately, we arrive at the result

$$f_1^-(V^2, z) = q_1(V^2, z) + \frac{\sigma}{\pi}\int \cos\theta''\, d\Omega' f_2^-\left(V^2 + 2u\xi, z - \frac{\xi'}{\omega_e}\right), \tag{3.138a}$$

$$f_2^-(V^2, z) = q_2(V^2, z) + \frac{\sigma}{\pi}\int \cos\theta''\, d\Omega' f_1^-\left(V^2 + 2u\xi, z - \frac{\xi'}{\omega_e}\right). \tag{3.138b}$$

If $q_1 = q_2$ and the initial conditions are symmetrical with respect to both walls, then $f_1^- = f_2^-$. By knowing these functions, the EDF inside the channel can be found:

$$f_e(\mathbf{V}, x, z) = \hat{K}_1 f_1^- + \hat{K}_2 f_2^-. \tag{3.139}$$

Unfortunately, exact solutions of Eq. (3.138) in a compact form (i.e., not in the form of an infinite series) are as yet unknown. However, approximate solutions can be constructed using different assumptions. We shall not consider them here, since Eq. (3.138) is obtained using a large number of assumptions and thus has restricted practical value. A review of some approximate solutions of this equation is published in [43].

*3.4.7. Model kinetic equations (MKE) [45]*

Here we wish to use a somewhat different approach to calculate the NWC, which is based on a simplified (model) kinetic equation. It relies upon only one assumption — that the electrons are strongly magnetized. To understand clearly the essence of this assumption, let us consider the above equations (3.138). Taking into account that at

$$\frac{h}{\rho_e} \equiv \omega_e \frac{h}{|V|} \to \infty$$

the harmonic terms in $\xi$ rapidly oscillate, averaging over these oscillations we get in the first approximation

$$\bar{\xi} = -(u - V_y'). \tag{3.140}$$

As a result, we obtain a simplified kinetic equation

$$\bar{f}^-(V^2, z) = q(V^2, z) + \frac{\sigma}{\pi} \int \bar{f}^- \left( V^2 - 2u(u - V_y'), z + \frac{u - V_y'}{\omega_e} \right) \cos\theta' \, d\Omega. \tag{3.141}$$

But we can simplify it further by taking into account the interchangeable sign of $V_y'$ and writing down directly a simple "model" kinetic equation

$$\bar{f}^-(V^2, z) = q(V^2, z) + \sigma \bar{f}^- \left( V^2 - 2u^2, z + u/\omega_e \right). \tag{3.142}$$

In a similar way, we now wish to construct a model kinetic equation for an arbitrary character of the "reflection" ("secondary emission") of electrons and for arbitrary fields inside the channel. However, we shall assume, as before, that the channel walls represent parallel planes and the EDF is symmetrical relative to these planes. Thus, we shall use the distribution function $f \equiv F(\mathcal{E}_k, z)$ depending only on the kinetic energy $\mathcal{E}_k$ of a particle and its coordinate $z$. We shall also assume that the **E**-field is directed along the $z$-axis and the electrons shift toward decreasing $z$. The function of interaction of an electron with the wall

$S$ is taken as a product of two terms: $\sigma\left(\mathcal{E}_p^D\right)$, the secondary electron emission coefficient, and $\eta\left(\mathcal{E}, \mathcal{E}_p^D\right)$, the normalized to unity distribution function of secondary electrons generated by an incident electron with energy $\mathcal{E}_p^D$. Thus,

$$\int \eta(\mathcal{E}, \mathcal{E}_p^D)\, d\mathcal{E} = 1, \quad S = \sigma(\mathcal{E}_p^D)\, \eta(\mathcal{E}, \mathcal{E}_p^D). \tag{3.143}$$

Here the index $D$ implies that $\mathcal{E}_p^D = \mathcal{E}_p - eU_D$, where $\mathcal{E}_p$ is the energy of an electron before the DL. However, we shall omit this index below. The equation sought is formulated for the flux $g = Vf$ using the following basic scheme of processes. The flux of electrons $g_f(\mathcal{E}_p', z)$ with energy $\mathcal{E}_p'$ at the point $z'$ is reflected as a flux

$$g_r(\mathcal{E}', z') = \int \eta(\mathcal{E}', \mathcal{E}_p'')\, \sigma(\mathcal{E}_p'')\, g_f(\mathcal{E}_p'', z')\, d\mathcal{E}_p''. \tag{3.144}$$

After reflection from the wall, the electrons shift along the **E**-field by a distance of the order of a semi-height of the cycloid:

$$l \approx \frac{cE}{H}\frac{1}{\omega_e} \tag{3.145a}$$

and acquire an energy of

$$W \approx eEl = mu^2, \quad u = cE/H. \tag{3.145b}$$

As a result of this shift, the "reflected" particles pass (in the framework of this simplified model) into the category of "incident" particles

$$g^-(\mathcal{E}', z') = g^+(\mathcal{E}' + W, z' - l). \tag{3.146}$$

By introducing a "new" energy $\mathcal{E} = \mathcal{E}'' + W$ and a coordinate $z = z' - l$, we obtain the equation sought:

$$g(\mathcal{E}, z) = q(\mathcal{E}, z) + \int \eta(\mathcal{E} - W, \mathcal{E}_p)\, \sigma(\mathcal{E}_p)\, g_f(\mathcal{E}', z + l)\, d\mathcal{E}',$$
$$\mathcal{E}_p = \mathcal{E}' - eU_D. \tag{3.147}$$

The integral equation (3.147) has "retarding" arguments.

Assuming as in the previous section that the electrons are reflected elastically without energy losses but can disappear on the wall, i.e.,

$$\eta(\mathcal{E}', \mathcal{E}_p'') = \delta(\mathcal{E}' - \mathcal{E}_p''), \quad \sigma = 1 - \nu,$$

we arrive at the equation

$$g(\mathcal{E}, z) = q(\mathcal{E}, z) + \sigma\, g(\mathcal{E} - W, z + l). \tag{3.148}$$

Assuming $g$ to be a smooth function of its arguments and $W$ and $l$ sufficiently small, we obtain at $\nu \ll 1$

$$-W\frac{\partial g(\mathcal{E}, z)}{\partial \mathcal{E}} + l\frac{\partial g(\mathcal{E}, z)}{\partial z} = \nu g(\mathcal{E}, z) - q(\mathcal{E}, z). \tag{3.149}$$

By setting

$$q = \delta(z - l)\, A(\mathcal{E}), \tag{3.150a}$$

the equations for the characteristics outside the original cross-section can be written in the form

$$\frac{dz}{l} = -\frac{d\mathcal{E}}{W}, \quad \frac{dg}{\nu g} = \frac{dz}{l}. \tag{3.150b}$$

Obviously, they have a solution

$$\mathcal{E} + \frac{zW}{l} = C_1, \quad g = C_2 \exp\left(\frac{\nu z}{l}\right). \tag{3.150c}$$

From here we derive the general expression for $g(\mathcal{E}, z)$, i.e., the distribution function of escaping electrons

$$g = \begin{cases} C_2\,(\mathcal{E} + Wz/l)\exp(\nu z/l), & 0 < z < L, \\ 0, & z > L. \end{cases} \tag{3.150d}$$

The function $C_2\left(\mathcal{E} + Wz/l\right)$ is uniquely determined by the initial value of the function $A(\mathcal{E})$, and a comparison of the expression obtained with experimental data (3.32) shows that our model equation well approximates the behavior of the escaping group of electrons.

Now consider the intermediate group of electrons which comprise inelastically reflected particles. The energy distribution $\eta(\mathcal{E}, \mathcal{E}_p)$ of the low-energy secondary particles is practically independent of $\mathcal{E}_p$. This fact allows us to write Eq. (3.147) (without taking into account escaping electrons) in the form

$$g(\mathcal{E}, z) = q(\mathcal{E}, z) + \eta(\mathcal{E} - W) \int \sigma(\mathcal{E}'_p)\, g(\mathcal{E}'_p, z - l)\, d\mathcal{E}'_p. \quad (3.151)$$

Assuming that the intermediate electrons carry the same current over some part of the channel, their distribution should not strongly depend on $z$, so that at $q = 0$ we obtain

$$g(\mathcal{E}, z) = \eta(\mathcal{E} - W)\, \nu_e^{(\mathrm{Int})}, \quad (3.152a)$$

$$\nu_e^{(\mathrm{Int})} = \int \sigma(\mathcal{E}'_p)\, g(\mathcal{E}'_p, z - l)\, d\mathcal{E}'_p. \quad (3.152b)$$

Here $\nu_e^{(\mathrm{Int})}$ is the intermediate electron flux on the wall. Equation (3.152a) implies that the energy distribution of the intermediate electrons is determined (under reasonable conditions) by the secondary electron distribution function. This result is in qualitative agreement with existing concepts. Another solution of the model kinetic equation using a "table"-like approximation for $\eta(\mathcal{E}, \mathcal{E}_p)$ can be found in [45].

## 3.5. UHF-oscillations in the SPT channel[1]

We have mainly considered above the stationary characteristics of the electron component. However, the studies of EDF behavior in the SPT channel using ordinary Langmuir probes averaging over space ($\delta \leq 1\,\mathrm{mm}$) and time ($\tau \leq 10^{-6}\,\mathrm{s}$) has shown (see Section 3.2) that a "mixing" of all three EDF components, including that coming from the outlet (i.e., from the cathode-compensator), occurs in the ionization zone. This can be explained only by assuming a build-up of strong high-frequency ($f \gg 10^6\,\mathrm{Hz}$) oscillations. UHF-oscillations are also revealed

[1] The authors acknowledge K. P. Kirdyashev for significant assistance in writing this section.

by features of the NWC process that point to the possibility of DL detachment. This indicates the major role of high-frequency processes, which are mainly connected with electrons. The actuality of studying UHF-processes in SPTs is not only due to their role in the device's performance. The determination of locations of generation of these oscillations and their amplitudes turns out to be an effective indicator of processes in the thruster channel. Finally, UHF-oscillations in plasma can also generate proper UHF-radiation of the plasma stream, which will affect the radio link between the spacecraft and a ground-based station.

We shall be interested in studying UHF-oscillations from the point of view of diagnostics of electron processes in the channel. Such studies have been carried out by K. P. Kirdyashev since 1972 ("Fakel" Enterprise [48]). Some important results were obtained later (1977, 1993 — MIREA [49, 50], 1992–1996 — NIITP [51]). Unfortunately, these studies, despite their importance, were episodic and "by-products." Although the picture obtained has many gaps, the results are of great interest.

Both longitudinal UHF-oscillations in plasma and generated (transverse) plasma waves have been studied.

Here we shall be concerned with longitudinal oscillations only. To study them a "two-wire" probe inductively connected to a measuring device was used. The distance between the conductors was taken as $\delta l \sim 0.08\,\text{mm}$. Naturally, the choice of this distance affects the amplitude of the registered signal depending on the value

$$\alpha = k\Delta l,$$

where $k$ is the wavenumber. The author corrected $\alpha$, however somewhat conditionally. Therefore, below we shall focus on the qualitative results, which are highly reliable.

### *3.5.1. Characteristic frequencies of UHF-oscillations*

The measurements were made in the frequency range

$$0.5\,\text{GHz} \leq f \leq 30\,\text{GHz}. \tag{3.153}$$

The electron Larmor frequencies for typical magnetic fields in SPT channels of $100\,\text{Oe} \leq H \leq 300\,\text{Oe}$ lie within the limits

$$280\,\text{MHz} \leq f \leq 840\,\text{MHz}. \tag{3.154}$$

Clearly, the intervals (3.153) and (3.154) do not fully overlap, and so an ultimate conclusion about the noise at Larmor frequencies cannot be made, but the probe cannot register electron-Larmor frequency oscillations in the overlapping region. Langmuir frequencies corresponding to the characteristic electron concentrations in the range $10^{11}\,\text{cm}^{-3} \leq n_e \leq 10^{12}\,\text{cm}^{-3}$ lie within the limits

$$2.5\,\text{GHz} \leq f \leq 8\,\text{GHz}$$

and clearly appear in the measurements.

### *3.5.2. Noise source localization*

Figure 3.12b shows the typical noise distributions measured in the M-70 model along the channel at two frequencies, $f_1 = 1.9\,\text{GHz}$ and $f_2 = 4.0\,\text{GHz}$. The noise amplitude sharply increases in the ionization zone and at the channel outlet [47].

Figure 3.12c displays similar noise amplitude distributions along the radius for frequencies $f_1 = 1.7\,\text{GHz}$ and $4.5\,\text{GHz}$ [48]. The latter distribution is measured at a distance of 5 mm from the outlet.

The noise level near the external insulator is much higher than near the internal one. The noise amplitude distributions and their maximum values vary in detail for different models and SPT regimes, but the qualitative shape does not change. The noise generation zones are schematically shaded in Fig. 3.12a. It is seen that they can be naturally connected with the places where electron groups with different velocities emerge [50]. Indeed, in the ionization zone the newborn electrons interact with those drifting radially "for a long time." Data about the discharge voltage and the rate effect on the noise level in the ionization zone can be found in [48]. It is seen that the noise

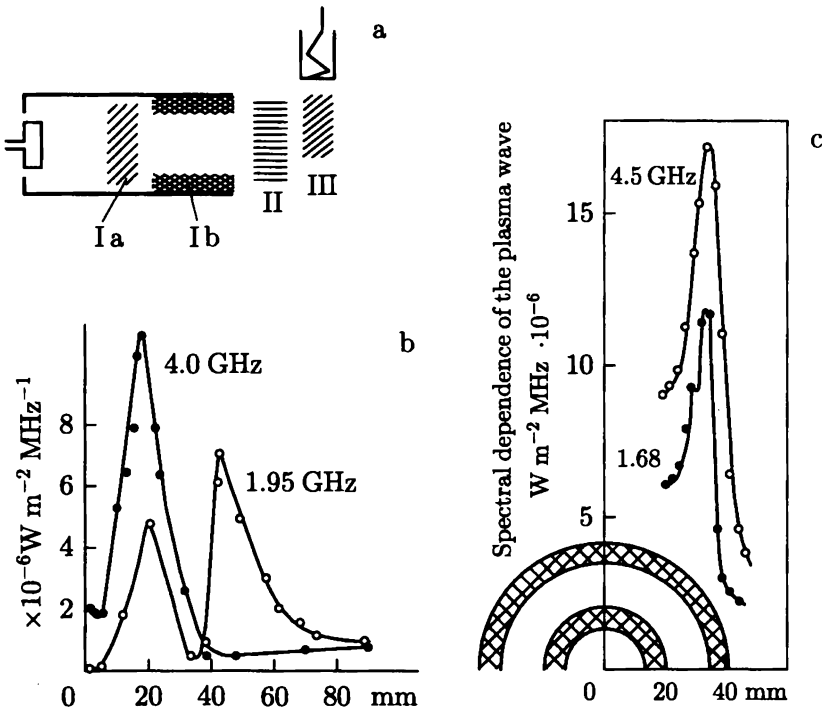


**Fig. 3.12.** UHF-oscillations in the SPT channel. (a) A priori regions of UHF-oscillations: Ia – the ionization zone, Ib – the near-wall zone, II – the electron input zone, III – the zone of electron capture by emerging ions. (b) The plasma wave intensity distribution along the channel (zones Ia, II, III). (c) The plasma wave intensity distribution along the radius (zone Ib).

intensity rapidly decreases here if the discharge voltage or the rate decreases. These facts have a simple explanation. It is known (Section 1, Fig. 1.1) that the volt-ampere characteristics of an SPT consists of two branches: "horizontal" and "vertical." Speaking of the ionization zone, we have in mind the working regimes located on the vertical branch. Then a sufficiently well-defined ionization zone with a thickness of $5-7$ mm exists. If, however, the voltage drops so that the discharge parameters fall

into the horizontal branch of the VAC, the discharge loses its azimuthal symmetry as a rule and a rotating "track" connecting the anode with the outlet emerges; the noise level sharply decreases. Now xenon ionization occurs throughout the entire channel space near this track and the electrons formed drift toward the anode under the action of the azimuthal component of the electric field.

Something like this occurs with a significant decrease in the rate and, hence, during the decrease in the electron concentration in the channel. As a result, the free-path length of an atom before ionization

$$\lambda = \frac{V_a}{\langle \sigma_{\text{ion}} V_e \rangle n_e}$$

increases monotonically and can comprise the whole channel.

Near the external insulator these azimuthally-drifting electrons "collide" with the braking flux coming outward from the wall. Moreover, as we have seen above (Section 3.3), a build-up of oscillations at Langmuir frequencies can also appear in the case where the temperature $T_e$ of electrons incident on the insulator approaches the first multiplication threshold $\mathcal{E}^*$.

A characteristic feature of the radial distribution of noise intensity (Fig. 3.12c) is a sharp asymmetry between the adjacent regions to the external and internal insulators. But this asymmetry is in good agreement with both the electron trajectory features and the DL characteristics.

Now we turn to the zone of the channel output. An interpretation of processes in this zone leading to noise generation at the channel output is much more complicated. In principle, two totally different processes take place here. One of them is a "quasi-ohmic" collisionless capture of electrons coming out from the cathode into the channel. Another is the capture of electrons from the same source into the escaping plasma stream. The first of these processes is mainly related to electron–ion interactions, and so it must operate at relatively low frequencies. Indeed, here the noises at frequencies $\sim 0.5-0.8$ GHz dominate. The second

process can be electron–electron interactions. Unfortunately, the existing experimental data do not allow us to separate these subzones.

### *3.5.3. Noise intensity*

The situation with noise intensity is very non-trivial. Not considering in detail the existing estimates of the oscillation power in different zones (see [50]), we note only that the ionization zone is the most noisy. In addition to this, it is necessary to consider two important observations concerning the intensity of UHF-oscillations.

*A hint of the possibility of DL breakdown.* DL breakdown or the absence of breakdown must have a strong effect on the UHF-oscillation character in the SPT channel. It is natural to expect that the DL breakdown must be somehow limited in time. However, at present we have no theoretical data on the DL evolution in real conditions, including the time of existence of the breakdown. A possible, although not wholly indubitable, hint as to the macrobehavior of the DL breakdown is the experimental data on the properties of the UHF-radiation coming from the channel at frequencies $\omega \sim \omega_{0e}$ and received by nearby antennas [49]. In that paper, it is shown that the envelope of the UHF-emission demonstrates chaotic overshoots with durations of up to $\sim 100\,\mu$s and spaced by time intervals of $\sim 100-500\,\mu$s (Fig. 3.13). The interpretation of the envelope overshoots as a result of the DL breakdown seems to be quite natural.

*The evolution of UHF-emission during resource tests.* A very well-defined correlation between the character of the insulator surface erosion during resource tests and the UHF-emission intensity has been found in [49]. This point will be further discussed in Section 4.3.

Broadly viewed, UHF-diagnostics is a very effective method of studying physical processes in the electron component. Even very simple considerations on the possibility of building-up beam-like oscillations allow us to understand qualitative features of the

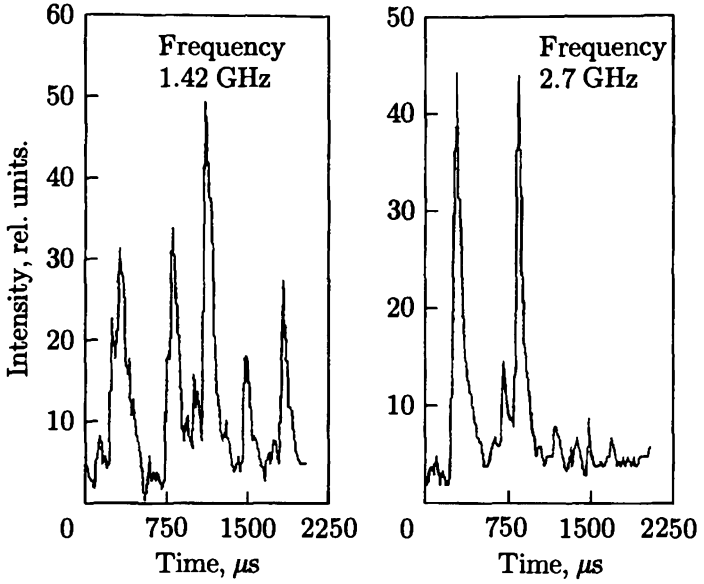


**Fig. 3.13.** Examples of realizations of HF-signal envelopes at the output of a measuring detector during the registration of electromagnetic radiation with a given frequency from the SPT channel.

UHF-oscillations. Naturally, understanding the mechanisms underlying these oscillations will provide a lot of useful information. However, here we shall not consider the specific mechanisms of these oscillations since presently there is no reasonably accurate theory for them in SPT conditions.

## 3.6. Some conclusions

The basic kinetic effects described above and mathematical models for them clearly indicate that at present we are unable to understand quantitatively the dynamics of the electron component and to calculate such characteristics as the conductivity, heat conductivity, energy losses on the wall, and radiation. Nevertheless, the qualitative picture of the physical processes is now

practically clear, and so we wish to list some conclusions with special attention to the conductivity in the channel.

In the SPT channel, the transport of electrons is done by all three mechanisms — spatial collisions (classical transport), scattering on the UHF-oscillations (anomalous transport), and collisions with the walls (quasi-classical near-wall conductivity). A different mechanism can dominate in different zones of the channel. Below we present estimates for the model A-4.

(a) The near-anode zone. Here the density of neutral particles is high ($n_0 \sim 2\times10^{13}\,\mathrm{cm}^{-3}$), the magnetic field strength and electron concentration are low ($H \sim 50\,\mathrm{Oe}$, $n_e \sim 10^{11}\,\mathrm{cm}^{-3}$); the electron temperature here is $T_e \sim 10\,\mathrm{eV}$. Nevertheless, for such parameters the NWC must prevail.

Indeed, considering that the cross-section of electron collisions with Xe atoms is $\sigma_{e0} \sim 2\times10^{-15}\,\mathrm{cm}^2$ and the Coulomb cross-section of electron collisions at this temperature is of the same order ($\sigma_{ei} \sim 10^{-15}\,\mathrm{cm}^2$) while the concentrations of atoms and ions are different by two orders of magnitude, collisions of electrons with neutral Xe atoms mainly contribute to the volume collisions. The free-path time is

$$\tau_{e0} \approx \frac{1}{n_0\sigma_{e0}V_e} \approx 10^{-7}\,\mathrm{s}.$$

Accordingly, the "non-magnetic" conductivity due to spatial collisions is

$$\sigma_0 = \frac{e^2 n_e \tau_{e0}}{m} \approx 2.5\cdot10^{12}\,\mathrm{s}$$

and across the magnetic field

$$\sigma_\perp \approx \frac{\sigma_0}{(\omega_{eH}\tau_{e0})^2} \approx 2.5\cdot10^{8}\,\mathrm{s}.$$

This is a rather small conductivity, since to provide an electron density current in the near-anode zone of $j \sim 0.1\,\mathrm{A\,cm}^{-2}$, an electric field strength of $E = j\sigma \sim 300\,\mathrm{Oe\,cm}^{-1}$ is required. Such a value is in dramatic disagreement with experiment. At

the same time, the level of UHF noise here is small, which appears, as experiment shows, in a clear subdivision of the EDF into three components. In principle, the development of asymmetric low-frequency waves is not excluded in this zone. But the latter do not ordinarily appear in working regimes. Thus, there are grounds to consider the electron transport in this zone to be predominantly due to the NWC.

Assuming that the potential jump on the DL is small and most electrons reach the wall, we find an effective value

$$\tau = \frac{b}{V_{Te}} \approx 10^{-8}\,\mathrm{s},$$

where $b$ is the channel width. Thus, we obtain an order of magnitude higher $\sigma_\perp$ and correspondingly an order of magnitude smaller $E$-field strength. Thus, the contribution of volume collisions in the near-anode zone is $\sim 10\%$ of the effective conductivity across the magnetic field.

(b) In the ionization zone, or more precisely, in the part that adjoins the acceleration zone, the anomalous conductivity due to UHF-oscillations prevails. This follows not as much from the presence of intense UHF-oscillations (we have no reliable data on their relation to the conductivity), but from the fact of "mixing" three components of the EDF, which come from the acceleration zone to the ionization zone and here "merge" to form a one-hump distribution. An estimate of the absolute value of the conductivity in this zone can be made using experimental data (Fig. 3.1c). It is seen that with a thickness of this zone of $\delta_{\mathrm{ion}} \sim 0.7\,\mathrm{cm}$ the potential difference is $\sim 90\,\mathrm{V}$. For the current density used above, this "experimental" conductivity $\sigma_\perp^{\mathrm{exp}} \sim 10^9\,\mathrm{s}$. It is seen that this value is close to the near-wall conductivity $\sigma_\perp^w$ calculated above. But the latter value has been found for $n_e \sim 10^{11}\,\mathrm{cm}^{-3}$ and $H \sim 50\,\mathrm{Oe}$. Obtaining the estimates for $\sigma_\perp^w$ at $n_e \sim 10^{12}\,\mathrm{cm}^{-3}$ and $H \sim 200\,\mathrm{Oe}$, we arrive at a value 1.5 times smaller than $\sigma_\perp^{\mathrm{exp}}$. This difference by itself when using averaged values lies within the accuracy of the estimates given above. Nevertheless, it represents an additional strong ar-

gument in favor of the anomalous character of this conductivity. Finally, a comparatively small thickness of the ionization zone with respect to the inter-wall distance ($b \sim 1.7\,\mathrm{cm}$) points once again to the correctness of our understanding of the transport in the ionization zone as being due to volume processes.

(c) In the acceleration zone, the near-wall conductivity clearly prevails in normal conditions. This is primarily due to the large sensitivity of the discharge characteristics of the SPT to the powdering of the channel walls in this zone.

## 4. Erosion of insulators in SPTs

### 4.1. The role and form of insulator erosion

In modern SPTs, the zones of ionization and acceleration of the propellant are not divided physically, so the ion flux focusing is far from ideal. Therefore, some fraction of the accelerated ions strike the walls, thus causing their sputtering. In addition, a near-wall electric current appears close to the walls due to the presence of crossed fields, and this, as was mentioned in Section 1, also leads to a very specific form of erosion, which has been called "anomalous." The erosion caused by ion bombardment will be referred to as "classical."

The erosion, however, does not simply "grind off" the outer parts of the insulators. It also forms a macrostructure on their surfaces, which affects the DL and NWC character. The structures caused by classical and anomalous erosion are entirely different. Ion bombardment in the SPT conditions forms, as a rule, a "pike's tongue"-like structure, which presents azimuthally oriented sharp prominences inclined to the incident flux. The distance between the prominences (along $z$) is of order $0.1-0.2\,\mathrm{mm}$. The appearance of this structure is visualized in the form of a "moiré" picture.

In the first-generation SPT models with a large divergence of the ion flux, only classical erosion appears during the first $\sim 500\,\mathrm{h}$. The material loss rate is $\sim 5\,\mu\mathrm{m\,h^{-1}}$. During this time

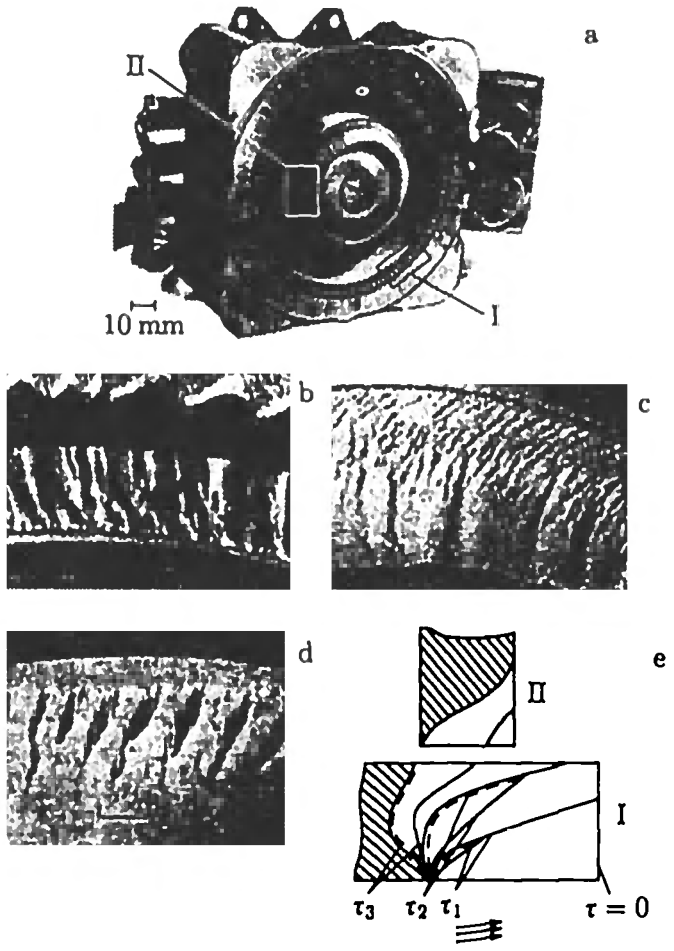


**Fig. 4.1.** Anomalous erosion of insulators in the SPT M-100. (a) The general shape of the SPT after 4000 h of operation with the location of fragments I and II marked. (b) The character of erosion of fragment I of the discharge chamber and the external pole of the accelerator. (c) The same, on the channel's interior wall (fragment II). (d) The view of the insulator's surface after 700 h of performance. (e) The evolution of the erosion zone profiles with time of performance $\tau$, *1* – 500, *2* – 1800, *3* – 3100 h (I – the external wall of the discharge chamber, II – the external pole).

$\sim 2.5-3$ mm of insulator is ground off and its profile (in the $r,z$-plane) is "adjusted" to that of the ion flux. As a result, the ion sputtering is notably reduced and the anomalous erosion begins [51]. It first appears as deep "scratches" oriented mostly along the channel. These "scratches" in the SPT M-100 become of $\sim 5$ mm in length, $\sim 1$ mm in width, and $\sim 1$ mm in depth $\sim 500$ h after their appearance. The side surfaces of the "scratches" are of a "torn" character; they are nearly equally spaced at a distance of $\sim 1-2$ mm. This is the scale of the electron Larmor radius. The picture changes in time and after about 1500 h takes its "ultimate" shape (Fig. 4.1). Now the erosion rate significantly slows down and stabilizes at a level of $2-3\,\mu\mathrm{m\,h^{-1}}$. The macrostructure set has some distinctive features. Firstly, an asymmetry in the erosion of the inner and outer insulator is seen. On the outer insulator the structures are "sharply" pronounced, while on the inner one erosion formations are much less pronounced, their forms being relatively smooth, or smudged, so to say. Another distinctive feature is the presence of traces of erosion in the parts of the insulator "screened" from direct ion bombardment. The period of anomalous erosion structure remains the same all the time, of the order of the electron Larmor radius $\rho_e$. It is surprising that the integral characteristics (such as the discharge current, thrust, and useful efficiency) at a constant rate $\dot{m}$ and discharge voltage $U_p$ hardly change over $\sim 7000$ h of operation in spite of the fact that the outer part of the insulator is fully "ground off" and the wearing of the magnetic poles begins. At the same time, the UHF-noise level behaves quite differently. At the first stage the level of UHF-radiation is comparable with the equilibrium radiation of a plasma with $T_e \sim 10$ eV. Then the UHF-radiation intensity rapidly increases and exceeds the thermal level by 2–4 orders of magnitude. This takes place over the entire stage of appearance of the "scratches." Finally, after 1000–1500 h of tests the radiation intensity decreases by 1–1.5 orders and stabilizes. These stages correlate with the presence of a steady "toothed" structure.

Although the details of particle detachment from the insulator are not fully clear, the anomalous erosion is clearly connected with the electron component. Therefore, below we shall show how the "kinematics" of this erosion can be modeled numerically. But from the very beginning the following are clear: (a) that the stronger erosion of the external insulator may be due to the "adhesion" of electron trajectories to the insulator; (b) the electron scale of the structure period; (c) the character of "excavations" that are oriented along the flux; and (d) the behavior of UHF-oscillations connected with the surface structure reorganization, etc. — all these facts clearly indicate the important role of electrons in this erosion.

One may say that it is hard to invent a clearer argument in favor of the important role of direct electron collisions with the wall than the anomalous erosion phenomenon.

Below, for completeness we consider first the formation of the surface structure by ion bombardment. We shall be interested in the kinematics of the surface structure formation developed in [52–54]. Here, in particular, we shall show how the "pike's tongue" is formed. In the second part of this section we consider a numerical model for the anomalous erosion "kinematics."

## 4.2. Ion sputtering

### *4.2.1. The basic equations of ion erosion and their general solutions [52, 53]*

The expressions for the $\dot{\delta}$-velocity of the movement of a plane surface along the normal due to sputtering (Fig. 4.2a) are fundamental:

$$\dot{\delta} = \dot{N}_n S_0(\mathcal{E})\, \Phi(\alpha, \mathcal{E}). \tag{4.1}$$

Here $\dot{N}_n$ is the normal density of the particle flux, $S_0$ is the sputtering coefficient for normal incidence, $\Phi(\alpha, \mathcal{E})$ is the angular distribution ($\Phi(0, \mathcal{E}) = 1$), and $\alpha$ is the incidence angle.

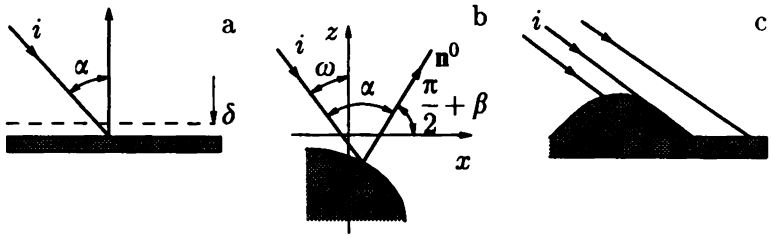


**Fig. 4.2.** Geometrical characteristics of ion sputtering. (a) The eroded layer thickness $\delta$. (b) The angles $\alpha$, $\omega$, $\Gamma$. (c) The shadow region is hatched.

Later we shall consider only the flat case, i.e., the profile will be assumed to depend on only one coordinate, $x$ (Fig. 4.2b):

$$z = z(x, t). \tag{4.2}$$

If $\omega$ is the incident angle of particles onto the plane $z =$ const, the incidence of particles onto the elementary surface will be

$$\alpha = \omega - \beta, \quad \tan\beta = \frac{\partial z}{\partial x} = z'. \tag{4.3}$$

With account of

$$\dot{\delta} = \frac{\partial z}{\partial t}\cos\beta \tag{4.4}$$

Eq. (4.1) takes the form

$$\dot{z} \equiv \frac{\partial z}{\partial t} = -\dot{N}_0 S_0 \frac{\cos(\omega - \beta)}{\cos\beta}\Phi(\omega - \beta). \tag{4.5}$$

Here $\dot{N}_0$ is the density of the particle flux on a unitary area normal to the flux. If $\dot{N}_0$, $S_0$, $\Phi$, $\omega$ do not depend on $x$, Eq. (4.5) can be simplified:

$$\dot{z} = F(z'). \tag{4.6}$$

Otherwise,

$$\dot{z} = F(x, z'). \tag{4.7}$$

Before solving Eqs. (4.6), (4.7), the possibility of existence of "screened" regions (Fig. 4.2c) should be noted. Clearly, the shadowing is generated by those points of the surface where the incident flux slides along the surface, in other words, where

$$\omega - \beta = \omega - \arctan z' = \pi/2. \tag{4.8}$$

For a given $\omega$, Eq. (4.8) determines the location of the "sliding points." However, here we consider only surfaces without shadowing.

Differentiation of Eq. (4.6) with respect to $x$ yields the well-known equation

$$\frac{\partial u}{\partial t} + \frac{\partial \varphi(u)}{\partial x} = 0. \tag{4.9}$$

Here $u \equiv \partial z/\partial x$. The simplest example of this equation is the equation of motion of a zero-temperature gas:

$$\frac{\partial V}{\partial t} + \frac{\partial}{\partial x}\frac{V^2}{2} = 0. \tag{4.10}$$

It is well known that the solution to this equation even for smooth initial conditions can have singularities (discontinuities), especially in view of the non-monotonic dependence $\Phi(u)$.

The general solution of Eq. (4.6) can be obtained using the method of characteristics which are determined by the equations [55]

$$\begin{aligned} &\frac{dx}{dt} = \frac{dF(q)}{dq}, \quad \frac{dz}{dt} = -F + q\frac{\partial F}{\partial q}, \\ &\frac{dq}{dt} = 0, \quad F(q) = F(z')\Big|_{z'=q}. \end{aligned} \tag{4.11}$$

After integrating system (4.11) we obtain

$$x = \frac{\partial F}{\partial q}t + x_0, \quad z = -\left(F - q\frac{\partial F}{\partial q}\right)t + z_0, \quad q = q_0. \tag{4.12}$$

Here $x_0$ and $z_0$ are interpreted as the surface coordinates at $t = 0$, and $q_0 \equiv z'(x_0)$. From Eq. (4.12) we find a parametric representation of the surface sought:

$$\begin{aligned} z &= -\left(F(q) - q\frac{\partial F(q)}{\partial q}\right)t + z_0\left(x - \frac{\partial F(q)}{\partial q}t\right), \\ q &= z_0'\left(x - \frac{\partial F(q)}{\partial q}\right)t. \end{aligned} \tag{4.13}$$

After having excluded $q$ from this system, we obtain the equation of the surface:

$$z = z(x, t).$$

Equation (4.13) implies that points of the profile move during the erosion with characteristic velocities

$$W_x = \frac{\partial F}{\partial q}, \quad W_z = -\left(F - q\frac{\partial F}{\partial q}\right). \tag{4.14}$$

In view of the complexity of the general solution, we shall restrict ourselves to a brief consideration of only two cases: (a) stationary processes with the particular case of "pike tongue" formation, and (b) self-similar unsteady structures.

### *4.2.2. Stationary structures*

Let us first better define the term. We shall call "stationary structures" such surface modifications that do not change form with time and only move as a whole.

Equation (4.13) means that different stationary changes of the surface are possible.

(a) The surface may homogeneously "descend." This case corresponds to $q = 0$, $z_0 = 0$, and so $z = F(0)t$. A more general solution of this type is the erosion of a homogeneously tilted surface:

$$z_0 = qx, \quad z_0' = q = \text{const}.$$

In this case,

$$z = \left(F - q\frac{\partial F}{\partial q}\right)t + q\left(x + \frac{\partial F}{\partial q}t\right) = qx + Ft. \tag{4.15}$$

(b) As seen from the general solution (4.13), for a non-trivial self-similar erosion surface to appear, several values of $q_k$ should exist satisfying the conditions

$$\left(\frac{\partial F}{\partial q}\right)_1 = \left(\frac{\partial F}{\partial q}\right)_2 = \cdots, \tag{4.16a}$$

$$\left(F - q\frac{\partial F}{\partial q}\right)_1 = \left(F - q\frac{\partial F}{\partial q}\right)_2 = \cdots. \tag{4.16b}$$

These conditions can be visually reformulated as a "tangent line rule." Namely, let the characteristic velocities at the points $q_k$ be the same. Then the condition for equality of the $x$-components of this velocity will be equivalent to condition (4.16a) of the equality of tangent angles to the curve $F(q)$ (Fig. 4.3a). Condition (4.16b) means that all values of $q_k$, corresponding to one characteristic velocity, are coordinates of those points $F_k$ on the curve $F(q)$ that lie on a straight line $\alpha$ tangential to $F(q)$ at all these points. This geometrical criterion, being equivalent to conditions (4.16), is referred to as the "tangent line rule."

Using this rule, it is easy to verify that for a two-hump angular function $\Phi(\alpha)$ (see Fig. 4.3b) the "pike's tongue" is the only steady periodical profile. Indeed, Eq. (4.5) is written for an arbitrary falling beam. If the $z$-axis is directed along this beam, Eq. (4.5) takes the form

$$\frac{\partial z}{\partial t} = -S_0\Phi(\beta).$$

In that case the function $F(q)$, to within a constant factor and choice of argument, coincides with the angular dependence of the sputtering coefficient $\Phi(\beta)$. Clearly, in the two-hump case

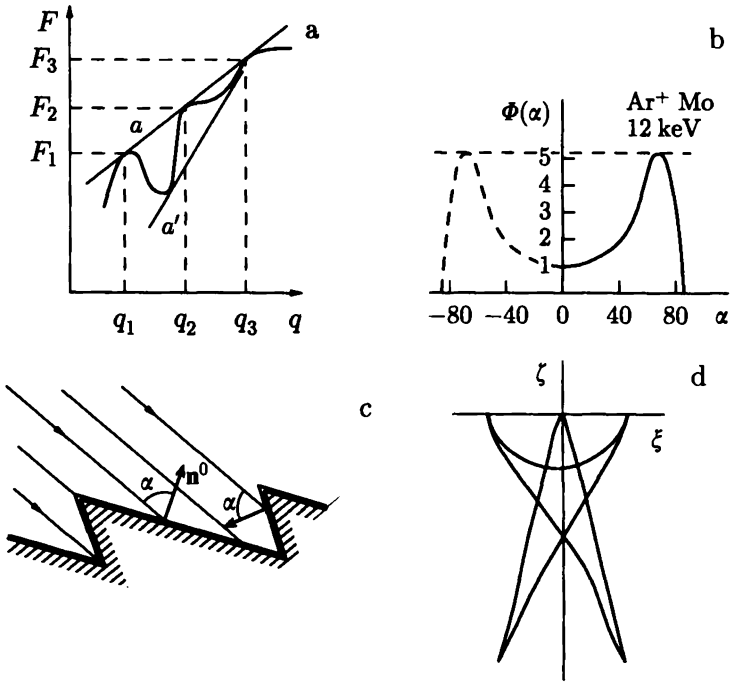


**Fig. 4.3.** Erosion profiles during ion bombardment. (a) The tangent line rule. (b) The tangent line on the two-hump angular dependence $\Phi(\alpha)$. (c) A "pike's tongue." (d) A "shaman-curve."

there are only two values of the incidence angle (they correspond to the horizontal tangent line parallel to the $x$-axis)

$$\beta_{1,2} = \pm\beta^*,$$

which determine the slope of the straight parts of the surface with one and the same characteristic velocity. At these points the function $\Phi(\beta)$ reaches a maximum. By knowing that in a steady configuration the angle between the planes is $2\beta^*$ and the beam direction coincides with the bisectrix, one can easily obtain a "pike's tongue" even in the case where the flux falls below some angle to the surface. If the incident angle of the flux is $\gamma$ and the "step" of the structure is $L$, the sides of the

prominence will be equal to (Fig. 4.3c)

$$a = L\frac{\sin\beta_2}{\cos 2\beta^*}, \quad b = L\frac{\sin\beta_1}{\cos 2\beta^*}, \qquad (4.17)$$
$$\beta_1 = \gamma - \beta^*, \quad \beta_2 = \pi - \gamma - \beta^*.$$

At this point we stop considering the analytical model for the "pike's tongue." However, some questions remain, which are connected with the presence of some "non-smoothness" in the profiles considered. In this respect, numerical calculations of the profile evolution have been made for some smooth connections between the planes [53]. As expected, if the inclination angles of the straight parts of the surface are taken in accordance with the "tangent line rule" and are, for example, $\beta_{1,2} = \pm 73°$, the transition zone width does not increase over a finite time interval.

The evolution of a saw-like surface which has tilts differing from $\pm\beta$ ($\beta_{1,2} = \pm 53°$) has also been calculated. These calculations, in complete agreement with the above considerations, have shown that a widening of the transition zones is observed over a finite time interval and a tendency to the disappearance of the initial structure is noted.

### *4.2.3. Self-similar structures*

We shall start from system (4.12)

$$x = W_x(q)\tau + x_0(q), \quad z = -W_z(q)\tau + z_0(q).$$

Here $\tau = \dot{N}_0 S_0 t$ is a "normalized" time.

The dependences $x_0(q)$ and $z_0(q)$ are sufficiently arbitrary initial functions subject only to the condition

$$\frac{dz_0}{dx_0} = q. \qquad (4.18)$$

The simplest class of non-stationary profiles can be obtained by setting at $\tau = 0$

$$x_0 = W_x(\tau_0), \quad z_0 = -W_z\tau_0, \quad \tau_0 = \text{const}. \qquad (4.19)$$

Using Eq. (4.14) it is easy to verify that condition (4.19) can be fulfilled. Substituting (4.19) into (4.14) we obtain

$$x = W_x(\tau + \tau_0), \quad z = -W_z(\tau + \tau_0),$$

or

$$\frac{z}{\tau + \tau_0} = G\left(\frac{x}{\tau + \tau_0}\right), \tag{4.20a}$$

i.e., the solution is self-similar. Without loss of generality, we can assume that $\tau \to 0$ and then

$$z/\tau = G\big(x/\tau\big). \tag{4.20b}$$

A notable feature of the profiles found is that their shape is mainly determined by the function $\Phi(q)$. However, self-similar profiles give rise to two interconnected difficulties. The first relates to the final size of these profiles: if $\Gamma$ is a self-similar profile, it is in contact with some "external" part of the surface $\Gamma^*$ whose evolution generally does not follow the self-similar evolution law $\Gamma$. The second difficulty relates to the function $\Phi(q)$ having a maximum. This results in function (4.20) turning out to be principally multi-valued. Therefore, the problem of "putting out additional branches" of the self-similar $z = \tau G\big(x/\tau\big)$ emerges.

Figure 4.3d displays a self-similar curve for this case:

$$\zeta = G(\xi), \quad \xi = x/\tau, \quad \zeta = z/\tau.$$

This curve has a very exotic shape (a "shaman-curve"), with one value of $\xi$ corresponding to one, two, or four values of $\zeta$. Thus, the self-similar curves prove to be multi-valued. The general form of the "shaman-curves" is independent of the specific shape of $\Phi(q)$ and is determined only by the presence of a maximum for $\Phi(q)$ and the vanishing of $\Phi$ with $q \to 0$.

A further analysis of the "shaman-curve" is presented in [54]; the general scheme is illustrated by the example $\Phi(q) = (1 + q^2)\exp\big(-\alpha q^2\big)$.

## 4.3. Mathematical modeling of the anomalous erosion

Above, we have described the character of the anomalous erosion. Here we consider a simple physical model for this phenomenon, a mathematical scheme for the calculations, and the results obtained.

### *4.3.1. Physical setting of the problem*

A totally adequate model of the anomalous erosion actually observed must take into account many factors such as the presence of a magnetic field that is inhomogeneous by $(r, z)$-coordinates, the presence of an inhomogeneous variable volume electric field $E(r, z, \theta, t)$, and the presence of a spatially and time-variable Debye potential jump near the wall $U_d(z, \theta, t)$. Here "breakdowns" of the Debye layers are possible. Also important are the presence of the ion flux onto the surface, the dependence of the sputtering coefficient of the insulator surface on the binding energy of its particles with the main body, and the possibility of "dissociation" of the insulator material (i.e., the total or partial disruption of insulator particle bonds with their ground) by the bombardment of high-energy electrons ($\sim 10-40\,\mathrm{eV}$).

In addition to these facts, one should take into account the inhomogeneity (polycrystallicity) of the insulator. Calculations showed that the surface evolution is significantly dependent on the initial geometry.

Naturally, accounting for these factors is a very complex and difficult (in the sense of numerical calculations) problem, especially considering the diffusive character of particle scattering by the insulator surface and random energy losses during this process.

Finally, also important is the fact that we neither know how $U_d(z, \theta, t)$ behaves nor the statistical characteristics of the dynamics of the $E$-field and particles. No data are available about the probability of "dissociation" of insulators by electron bombardment.

Under such conditions, we have to greatly simplify the problem and model only the "kinematics" of the process.

The general scheme of considerations is as follows. Electrons come out from a random point of the channel ionization zone with some initial velocities and start moving in the magnetic and electric fields. They are either reflected from the DL or pierce it. In the latter case, an elementary erosion act takes place and some "recess" is formed at this point of the surface. The depth of this recess is assumed to be known. The surface structure that appears on the insulator due to this erosion depends on the longitudinal coordinate $z$ and azimuth $\theta$ so that

$$r\big|_s = R_0 + \xi(\theta, z, t).$$

Here $s$ is the surface index, and $\xi$ is the surface shift. According to the classical model (3.51a), we have the equation for the Debye potential jump

$$j_{ni} = j_{ne} = j_{e0}(1 - \sigma)\exp\left(-e|U_d|/kT_e\right). \tag{4.21}$$

The electron flux incident on the surface will be considered isotropic and the ion flux directed strictly along the radius. Therefore,

$$j_{ni} = j_{i0}\frac{|\partial\xi/\partial r|}{|\nabla\xi|}. \tag{4.22}$$

From here the expression for the Debye layer variation $\delta U_d$ follows:

$$\frac{|\partial\xi/\partial r|}{|\nabla\xi|} = 1 - \frac{e}{kT_e}\left(|U_{d0} + \delta U_d| - |U_{d0}|\right). \tag{4.23}$$

We shall assume that the magnetic field has only a radial component $H_r$, the electric field has only a time-independent component $E_z$, and the near-wall (Debye) potential jump $U_d$ is infinitely thin and depends on the angle $\alpha$ between the radius and the normal to the insulator surface, $U_d = U_0 + U_1(1 - \cos\alpha)$.

Finally, we shall restrict ourselves to consideration of a comparatively narrow zone of insulator erosion along the $z$-axis

($\delta z \sim 5$ mm, which corresponds to real conditions), and assume that the "removal" of the insulator is constant. Such a model, in our opinion, must reflect such a significant property as the appearance of "slots" at the early stage of erosion structure formation and the emergence of profile modulations related to the electron Larmor radius.

At the first stage of study, it seems reasonable to restrict ourselves to consideration of a "sine-like" initial modulation of the cylindrical surface of the insulator.

### *4.3.2. Mathematical setting of the problem*

To be specific, we consider the inner surface of the external dielectric wall. Let at the initial time $t = 0$ be weakly modulated by the azimuthal angle $\theta$ profile $r = R(\theta)$, where $R(\theta)$ is a smooth function with period $\theta_{\text{mx}}$. The mean value $\langle R(\theta) \rangle$ is the external wall "radius." Two problems naturally appear. The first of them consists of studying distinctive features of the movement of individual electrons in the channel with a goffered outer wall. Due to a cork effect and the energy losses on the wall, an electron can be "captured" by individual "grooves" of the profile, i.e., the modulation of the profile by angle $\theta$ can break down the azimuthal drift of electrons. The second problem is to calculate a sufficiently large number of electron trajectories and, using some average characteristics, to try to understand the main tendencies of the evolution of the profile due to the bombardment by electrons passing through the Debye layer. As already said, here we shall start from the simplest and most naive assumption that the erosion of a surface element is proportional to the number of electron hits on the element.

An electron moves in the region $z_{\text{mn}} < z < z_{\text{mx}}$ ($z_{\text{mx}}$ is the channel outlet), $r_{\text{mn}} < r < R(\theta)$, $0 < \theta < \theta_{\text{mx}}$. The picture is assumed to be periodic with period $\theta_{\text{mx}}$: if one electron comes out of this region at $\theta = \theta_{\text{mx}}$, another with the same dynamical parameters enters the region at $\theta = 0$, and vice versa. The dynamics of electrons in an azimuthally symmetric magnetic

field $\Psi(r,z)$ ($\Psi$ is the magnetic flux function) and electric field $\Phi(r,z)$ ($\Phi$ is the electric potential) are described by Eqs. (3.22) with some random initial conditions. The functions $\Psi$ and $\Phi$ have the same form as in Eqs. (3.19) and (3.20).

On approaching the wall [either $r = r_{\mathrm{mn}}$ or $r = R(\theta)$] one of two events happens. If $mV_n^2/2 < U_d$ (where $V_n$ is the normal velocity component), the electron is reflected elastically (the incident angle is equal to the reflection angle and the electron energy is conserved). If $mV_n^2/2 > U_d$, the electron reaches the wall surface. The result of hitting the wall is random. The energy distribution of the reflected electrons is given by Eq. (3.25). The direction of electron motion after hitting the wall is also random and is determined as in Section 3.2. The electron trajectory can be calculated numerically, with the initial position and velocity of the electron being chosen at random.

The calculation and visualization of a large number of trajectories with different initial parameters of electrons allowed us to make some qualitative conclusions. The cork effect due to the magnetic field decrease near the external wall leads to electron collision, as a rule, with this wall much more frequently than with the internal one. The energy losses during the collisions and the azimuthal profile modulation often lead to "capture," i.e., the phase coordinate of the electron [the angle $\theta(t)$] changes weakly over relatively long time intervals.

Now we pass to a description of an algorithm for numerical study of the evolution of the external wall profile due to electron bombardment.

Let, at the initial time $t = 0$, there be a smooth profile $r = R_0(\theta)$ with period $\theta_{\mathrm{mx}}$ in the form

$$R_0(\theta) = \sum_0^7 a_j \cos(j\omega\theta) + \sum_1^7 b_j \sin(j\omega\theta),$$
$$\omega = \frac{2\pi}{\theta_{\mathrm{mx}}} n_p, \quad n_p = 1, 2, \ldots \tag{4.24}$$

This profile is characterized by the parameters $a_0, \ldots, a_7$, $b_1, \ldots, b_7$. We shall assume that the profile $r = R(\theta)$ always

has the form (4.24), but the parameters $a_0, \ldots, b_7$ change with "time." We suggest the following algorithm for passing from one set to another (at the next moment of "time"): (1) choose an integer number $N_d$ ($N_d \approx 20-50$); (2) calculate the length of the profile

$$l_0 = l\big[R_0(\theta)\big] = \int_0^{\theta_{\mathrm{mx}}} \sqrt{R_0^2 + (dR_0/d\theta)^2}\, d\theta;$$

(3) subdivide the profile into equal intervals in length for each $\Delta l = l/(N_d-1)$; (4) find the coordinates of the points of division $r_1, \ldots, r_N$, $\theta_1 = 0, \ldots, \theta_{N_d} = \theta_{\mathrm{mx}}$; (5) set an integer $N_p$ ($N_p \approx 100-1000$), and calculate the trajectories of $N_p$ electrons. For each of these trajectories we calculate the number of hits against the wall (the number of passages through the Debye layer) for each of $N_d - 1$ intervals. By summing the number of these hits over all $N_p$ trajectories we obtain the numbers $M_1, \ldots, M_{N_d-1}$. Then we determine the set of numbers

$$\delta_j = \frac{M_j}{\sum_i M_i}. \tag{4.25}$$

The next steps are as follows: (6) find the coordinates of the centers of the intervals $r_{s,i}$, $\theta_{s,i}$, $i = 1, \ldots, N_d - 1$; (7) find the outer normal to the profile $R_0(\theta)$ at these points; (8) shift these points along the outer normal by $\varepsilon\delta_j$, thus obtaining the set of points $r_{n,i}$, $\theta_{n,i}$, $i = 1, \ldots, N_d - 1$. Thus, $\varepsilon$ is some effective "sputtering coefficient"; (9) using the least-squares method, construct a function like (4.24) through the points $r_{n,i}$, $\theta_{n,i}$ so the new set of parameters is found from solving the extremum problem

$$\sum_{i=1}^{N_d-1} \Big| r_{n,i} - R_0(\theta_{n,i}) \Big|^2 \to \min, \tag{4.26}$$

thus giving the function $R_1(\theta)$. We have described only one "temporal" step. The sequence of functions $R_0(\theta)$, $R_1(\theta), \ldots$ yields the time evolution of the profile [56].

*4.3.3. Results of calculations*

Calculations of electron trajectories were carried out inside the region $r_{\text{mn}} = 1.7 < r < r = R(\theta)$ (below we use the dimensionless units introduced in Section 3.2), $0 < \theta < \theta_{\text{mx}} = 2\pi/n_w$ ($n_w = 40$), $z_{\text{mn}} = 2.7 < z < z_{\text{mx}} = 3$. At the "initial moment of time" the profile of the upper wall was taken in the form $R_0(\theta) = r_{\text{mx}} + l_s \sin(\omega\theta)$, where $\omega = 2\pi n_p/\theta_{\text{mx}}$, $r_{\text{mx}} = 2.0$, $n_p = 2$ (i.e., the two initial perturbation wavelengths are within the limits of the angle $\theta_{\text{mx}}$). The Debye jump was determined using the parameters $U_0 = 0$, $U_1 = 0.05$. At the initial moment the energy of the electrons was $\mathcal{E}_0 = 0.05$, the velocity was either directed along the radius toward the external wall or distributed isotropically, and the angle $\theta$ was taken to be uniformly distributed over the interval $[0, \theta_{\text{mx}}]$. In the calculations below we have assumed that $N_d = 40$, $N_p = 100-1000$, $\varepsilon = 0.03$.

Below, we shall characterize the initial perturbation amplitude not by the parameter $l_s$ but by a quantity $\alpha_s = l_s/\Lambda_{1/2}$ uniquely connected with it, where $\Lambda_{1/2}$ is the semi-period of the perturbation. The magnetic field amplitude (or correspondingly the degree of electron magnetization) will be determined by the value of the parameter $\beta = h/\Lambda_{1/2}$, where $h$ is the cycloid height ($h = 2mc^2E_0/(eH_0^2)$, $E_0$, $H_0$ are the electric and magnetic field strengths at the channel output).

As seen from the above, the model used is highly simplified. But even in such a simplified form this model is hard to realize. This, in particular, caused the choice of the reconstruction method — the least-squares method (4.25) with 15 Fourier harmonics. Here, naturally, it is impossible to "resolve" structures with a spatial scale of $l \leq \Lambda_{\text{mn}}$, where $\Lambda_{\text{mn}}$ is the wavelength corresponding to the most remote harmonics.

Figure 4.4a shows the results of calculations corresponding to three values of $\alpha_s$ (the initial amplitude) and to the parameter $\beta = 0.18$. It is seen that modulations with the same spatial period $\lambda_1 \approx 1.5\Lambda/N = \Lambda_{1/2}/5 \approx \beta\Lambda_{1/2}$, where $\Lambda$ stands for the wavelength and $N = 15$ is the number of valleys, increase

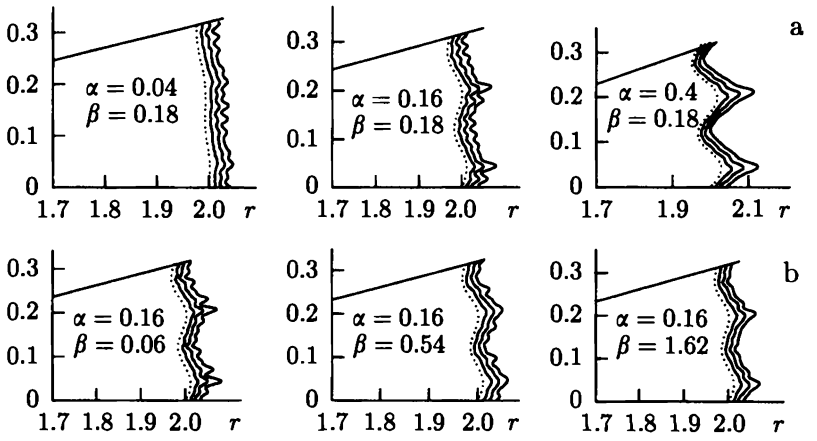


**Fig. 4.4.** Numerical modeling of the anomalous erosion kinematics. (a) The initial perturbation amplitude $\alpha$ at $\beta = 0.18$ is varied. (b) The effective cycloid height $\beta$ at $\alpha = 0.16$ is varied. The dashed line marks the initial perturbation.

in all three plots. Figure 4.4b shows the results of calculations at $\alpha_s = 0.16$ and different $\beta$. Here for $\beta = 0.54$ we obtain the period $\lambda_2 \approx 1.5\Lambda/6 = \Lambda_{1/2}/2 \approx \beta\Lambda_{1/2}$. For $\beta = 1.62$ we have $\lambda_3 \approx 3/2\Lambda_{1/2} \approx \beta\Lambda_{1/2}$. But for $\beta = 0.06$ we obtain the same scale $\approx\lambda_1$ as before.

The results of the calculations, although in the form of a rough model, appear to confirm the hypothesis on the electron mechanism of anomalous erosion structure formation [57].

## 5. Heavy particle dynamics in the SPT channel

In Section 3, we considered the "autonomous" dynamics of electrons. Now we turn to an "autonomous" description of the dynamics of heavy particles — atoms and ions. Unlike the electron component, whose properties only weakly depend on the specific characteristics of the heavy particle flux, the dynamics

of the latter are much more significantly connected with the electron component.

## 5.1. Dynamics of single heavy particles

### *5.1.1. Dynamics of single ions*

To calculate the dynamics of ions it is sufficient to know only the electric potential distribution inside the channel:

$$\Phi = \Phi(r, z). \tag{5.1}$$

The effect of the magnetic field on an ion is needed only to determine the azimuthal velocity component with which the ion leaves the channel. Clearly this value is

$$V_\theta|_\infty = \frac{e}{Mc}\Psi_*, \tag{5.2}$$

where $\Psi_*$ is a function of the magnetic flux at the ion birth point. The value of $V_{\theta\infty}$ is important to take into account the angular momentum that is carried away with the stream and thus is given with an opposite sign to that of the spacecraft. Calculations of ion motion in a field (5.1) are of major interest in the two-dimensional case in connection with the problem of preventing the ions from colliding with the channel walls.

In 1962–1963, the development of the SPT concept began with the calculation of the dynamics of single ions under two assumptions:

(1) Equipotentiality of the magnetic force lines. At that time, a linear connection between the electric potential $\Phi(r, z)$ and the magnetic flux function $\Psi(r, z)$ was considered for simplicity:

$$\Phi = \kappa\Psi. \tag{5.3}$$

This supposition, as is now well known, satisfies the experimental data to within the change of $\Phi$ by $\Phi_T$.

(2) The magnetic configuration must be chosen such that the ions do not collide with the walls. The simplest magnetic

configuration having such a property is described by a scalar potential:

$$\Psi_M = H_0 z \ln\left(r/r_0\right). \tag{5.4}$$

For fields such as (5.3), (5.4) the ion trajectories are calculated numerically. Later such calculations were carried out by many authors [58]. As a rule, the experimental distributions of the potential $\Phi$ were taken. Note that in some cases the calculation of ion trajectories can be done using the methods of ion optics [16].

### 5.1.2. *Dynamics of a single heavy particle with account of the ionization*

For this purpose, we need to know two parameters: the electric field $\Phi(r, z)$ and the ionization probability $w(r, z)$ :

$$w(r, z) = n_e \langle \sigma V_e \rangle\big|_{\text{ion}}, \tag{5.5}$$

which is fully determined by the electron density $n_e = n_e(r, z)$ and the ionization coefficient $\beta(r, z) \equiv \langle \sigma V_e \rangle\big|_{\text{ion}}$.

Thus, the "autonomous" calculation of the heavy particle dynamics with ionization requires the three functions $\Phi$, $n_e$, $\beta$ to be known throughout the channel volume. Naturally, these quantities must be taken from experiment. In comparison with calculation of the motion of "ready" ions, accounting for the ionization significantly complicates the problem, as here the event statistics are required. Namely, from the very beginning one should consider not one atom with some initial position $x_0$ and velocity $V_0$, but "streams" from particles with the same $(x_0, V_0)$ and, hence, following a common trajectory before ionization. The change of particle number in the "stream" is determined by the equation

$$\frac{dN}{dt} = -w(\mathbf{r})\, N. \tag{5.6}$$

After ionization each particle follows its own trajectory. But if a collision of an atom or ion with the wall occurs, not a single

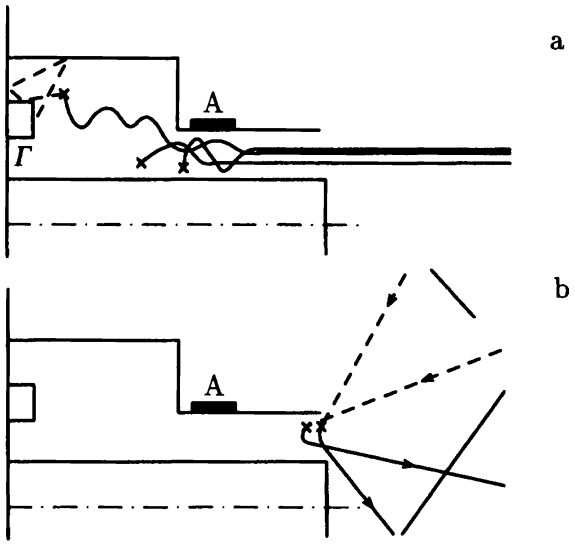


**Fig. 5.1.** The calculated trajectories of heavy particles ionized in the channel of the SPT-ATON ($\dot{m} = 4\,\mathrm{mg\,s^{-1}}$, $U_p = 300\,\mathrm{V}$). (a) The motion of particles supplied from the gas-distributor G into the buffer space and ionized there. The energy of the atoms corresponds to a temperature of $T_e = 700\,\mathrm{K}$. (b) The motion of particles injected into the SPT channel from a vacuum chamber. They are ionized in the channel and expelled from it. A – the anode, x – the ionization point, the dashed line is the trajectory of a neutral atom, and the solid line is the trajectory of an ion.

incident particle but the entire stream should again be considered at the collision point, since the scattering of particles by the wall is diffusive, ions can be neutralized, etc.

Despite of a certain awkwardness of such calculations and the need to use significant experimental data, they are often justified since they allow deeper analysis of the processes with heavy particles. A comparison of the characteristics (such as the energy spectrum and divergence) of the outgoing ion flux derived from experiment and calculated using the above method indicates their good correspondence. Figure 5.1 shows some ex-

amples of calculations described in [59] using the parameter distributions presented in Fig. 3.1.

## 5.2. A kinetic description of ionizing heavy particles

As we saw in the previous section, to calculate the dynamics of a single ionizing atom we need to formally specify two functions, $\Phi(\mathbf{r})$ and $w(\mathbf{r})$, which actually means three functions $(n_e, \Phi, \beta)$, since $w(\mathbf{r}) = n_e\beta$. However, the quantity $n_e(\mathbf{r})$ can be calculated using kinetic equations and assuming stationarity:

$$\begin{aligned} &\mathbf{v}\frac{\partial f_0}{\partial \mathbf{r}} = -\beta f_0 n_e, \quad n_e = \int f_i \, d\mathbf{v}, \\ &\mathbf{v}\frac{\partial f_i}{\partial \mathbf{r}} - \frac{e}{M}\nabla\Phi\frac{\partial f_i}{\partial \mathbf{v}} = \beta f_0 n_e. \end{aligned} \tag{5.7}$$

Here $f_0$ is the distribution function of neutral particles. In Eq. (5.7) we assume for simplicity that only singly ionized ions are present.

Calculations in the one-dimensional case in such a setting were carried out by I. V. Melikov and A. I. Morozov in 1974 [60]. As a result, the similarity laws of SPT performance with different propellants were established (see Section 5.3 below).

The calculation of the heavy component dynamics is further simplified if the thermalized potential

$$\Phi_T(\Psi) = \Phi - N(n)$$

can be introduced and the electron component can be considered isodrifting:

$$\Phi_T = \kappa\Psi.$$

In this case, to determine $f_0$ and $f_i$ only $\beta$ should be known. However, considering that

$$N(n) = \frac{1}{e}\int \frac{dP_e(n)}{n}$$

and the dependence $N(n)$ is known, one can estimate $T_e$ and thus $\beta$. For example, for a Maxwellian distribution,

$$N(n) = \frac{kT_{e0}}{e} \ln \frac{n}{n_0}, \quad T_{e0} = \text{const}.$$

In the adiabatic case, $P = P_0\left(n/n_0\right)^\gamma$ and

$$N = \frac{\gamma}{e(\gamma - 1)} kT_e.$$

Thus, with the assumptions made one can substitute into Eq. (5.7)

$$\Phi = \kappa\Psi + N\left(\int f_i \, d\mathbf{v}\right), \tag{5.8a}$$

and instead of $\beta(T)$ use

$$\beta = \beta\left(\frac{Ne(\gamma - 1)}{\gamma k}\right). \tag{5.8b}$$

Thus, we have a closed system of equations for $f_0$ and $f_1$ once the magnetic field $\Psi$ is known. Unfortunately, the thermalized potential in the form (5.8a) takes into account only the locked component and can be applied in zones without intensive ionization. The ionization can be accounted for with the use of a generalized thermalized potential. However, the problem of the intermediate component remains, since it can play an essential role in particle ionization. Apparently, it is not difficult to take it into account, as well as the exit of escaping particles, but this has not yet been done. So a quasi-autonomous description of the heavy component is possible but requires a more detailed experimental study of the electron distribution function in the SPT channel.

To conclude this section, we wish to mention an earlier study by S. A. Yakunin [61] in which the stationary kinetics of heavy particles with ionization was considered. This work was

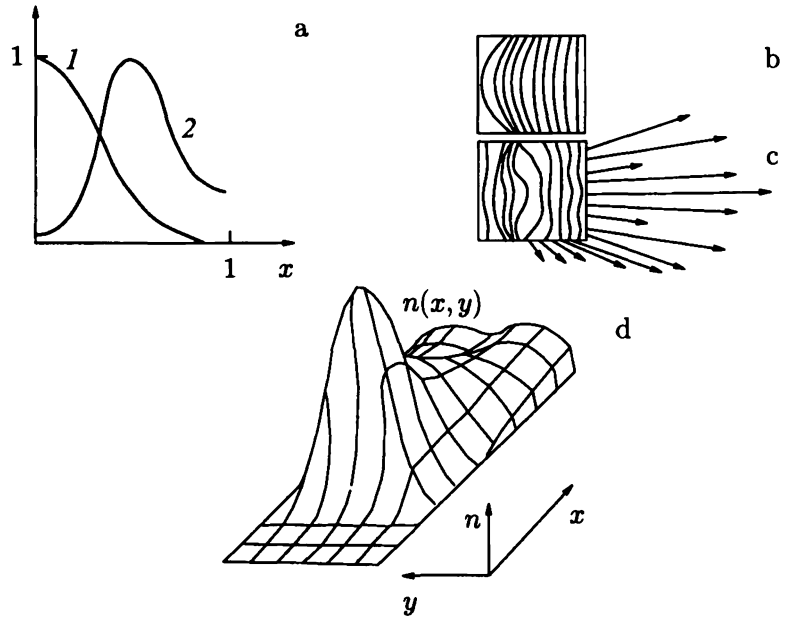


**Fig. 5.2.** The results of [61]. (a) The given normalized dependences, $\Phi_T(x)$ *(1)* and $T_e(x)$ *(2)*, in the middle plane of the channel. (b) Magnetic field force lines. (c) The equipotentials in the presence of the discharge and the velocity field of ions at the channel boundary. (d) The ion density distribution in the channel.

done before the EDF features in the SPT channel were revealed. Thus, the EDF was taken as a Maxwellian function

$$n = n_0 \exp\left\{-\frac{e\left[\Phi_T(\Psi) - \Phi(\mathbf{r})\right]}{kT_e(\Psi)}\right\}.$$

The functions $\Phi_T(\Psi)$ and $T_e(\Psi)$ were taken rather arbitrarily (Fig. 5.2a). The magnetic field lines were convex toward the anode. As result of the calculations, the electric potential distribution inside the channel, the changes in particle concentration with account of ionization, the ion distribution function, and the

ion flux field were found. The rate of insulator erosion was calculated as well. Some of these results are presented in Fig. 5.2b–e.

## 5.3. Similarity criteria for discharges in SPT

SPTs allow a large number of variants. They can have different sizes and work at different voltages and rates, as well as with different propellants. Thus it is natural to look for a criterion (or criteria) that would determine the similarity of working processes in different thrusters (SPTs).

Taking into account all that was said above, especially about the kinetics of electrons, one may suppose that "total" similarity of processes in two thrusters is possible only when a sufficiently large number of dimensionless similarity criteria coincide. The "total" set of similarity criteria has not been found thus far. However, one criterion has been found which has a strong effect on SPT characteristics. This is the Melikov–Morozov criterion [60], which was first introduced by these authors and has been checked many times. Basically, it is the ratio of the free-path-length scale before ionization $\lambda_{\text{ion}}$ to the working length of the channel $L$ :

$$S_i = \left\{\lambda_{\text{ion}}\right\}/L. \tag{5.9}$$

Here the curved brackets mean the scale of the corresponding quantity. The value of $\lambda_{\text{ion}}$ is determined by the characteristic velocity of neutrals $V_a$, the electron density $n_e$, and the ionization coefficient $\beta$:

$$\lambda_{\text{ion}} = \frac{V_e}{\beta n_e}; \tag{5.10}$$

$\lambda_{\text{ion}}$ can also be related to the scale of the velocity $V_{\text{ion}}$ acquired by ions in the electric field $E$ over the distance $\lambda_{\text{ion}}$ :

$$V_{\text{ion}} = \left(\frac{eE\lambda_{\text{ion}}}{M}\right)^{1/2}. \tag{5.11}$$

Clearly, the mean velocity of the ion flux coming out of the ionization zone is $\sim 0.5V_{\text{ion}}$. Combining these equations, we arrive at the relationship

$$\lambda_{\text{ion}} = \frac{eEV_a^2}{M\beta^2 n_e^2 V_{\text{ion}}^2}. \tag{5.12}$$

Further taking into account the condition of plasma quasi-neutrality $n_i \approx n_e$ and also bearing in mind that to an order of magnitude $n_i V_{\text{ion}} \sim q_0$, we obtain the final expression for the similarity criterion of ionization processes:

$$S_i \frac{\{\lambda_{\text{ion}}\}}{L} \propto \frac{eEV_a^2}{M\beta^2 q_0^2 L}. \tag{5.13}$$

The criterion $S_i$ was first derived from the analysis of a one-dimensional system of kinetic equations (5.7) in making them dimensionless. Indeed, using the channel length $L$, the density of the incoming gas $n_{a0}$, its velocity $V_{a0}$, $E_0 = U_p/L$, and the characteristic value $\beta_0$ as units for the length, density, velocity, electric field, and ionization coefficient, respectively, system (5.7) can be written in the form

$$\begin{aligned} V\frac{\partial f_i}{\partial x} + \frac{1}{\xi}E\frac{\partial f_i}{\partial V} &= \frac{1}{\zeta}\beta n_e f_0, \\ V\frac{\partial f_0}{\partial x} &= -\frac{1}{\zeta}\beta n_e f_0. \end{aligned} \tag{5.14}$$

Here dimensionless variables are denoted as before.

This system has two dimensionless similarity parameters: an analogue of the Froude number

$$\xi = \frac{MV_{a0}^2}{eU_p} \tag{5.15a}$$

and an analogue of the Knudsen number

$$\zeta = \frac{V_{a0}^2}{\beta_0 n_0 L}. \tag{5.15b}$$

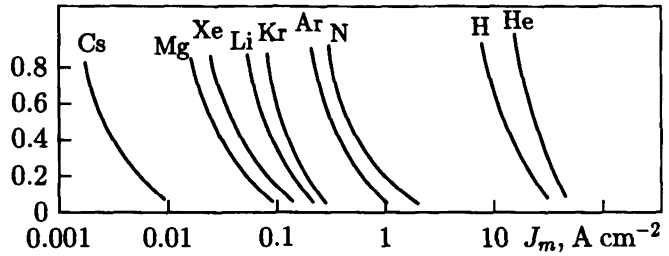


**Fig. 5.3.** The dependence of the degree of ionization of different materials on the consumption rate inside the SPT channel.

Now it is easy to verify the combination

$$\chi \equiv \frac{\zeta^2}{\xi} = \frac{eU_p V_{a0}^2}{M\beta_0^2 q_0^2 L^2} = S_i. \tag{5.16}$$

In [60], the system of equations (5.14) was calculated for constant $T_e = 10\,\text{eV}$, $E = 15\,\text{V cm}^{-1}$, $L = 4\,\text{cm}$, and $T_a = 600\,\text{K}$ for different gases. The degrees of ionization of the emerging flux were determined for different densities $q_0 = 1/ej_{\dot{m}}$ of the neutral particle flux at the entrance. The dependences $S_i(j_{\dot{m}})$ obtained are shown in Fig. 5.3. These values only slightly differ from those experimentally obtained (less than two times), and the correspondence of $j_{\dot{m}}$ necessary to obtain the same discharge characteristics was well confirmed experimentally for different gases (Xe, Ar, Ne, Kr, $H_2$, $N_2$).

We have briefly presented the results of a paper published in 1974. In 1989, N. A. Maslennikov published the results of systematization of a large number of experiments carried out in different laboratories with SPTs of various sizes, at different rates and voltages (these data were obtained on first-generation SPTs in which, in particular, the fraction of doubly ionized ions is small). This paper dealt with factors determining the integral characteristics, such as the discharge current, thrust, degree of ionization, etc. (Fig. 5.4a–c) [62].

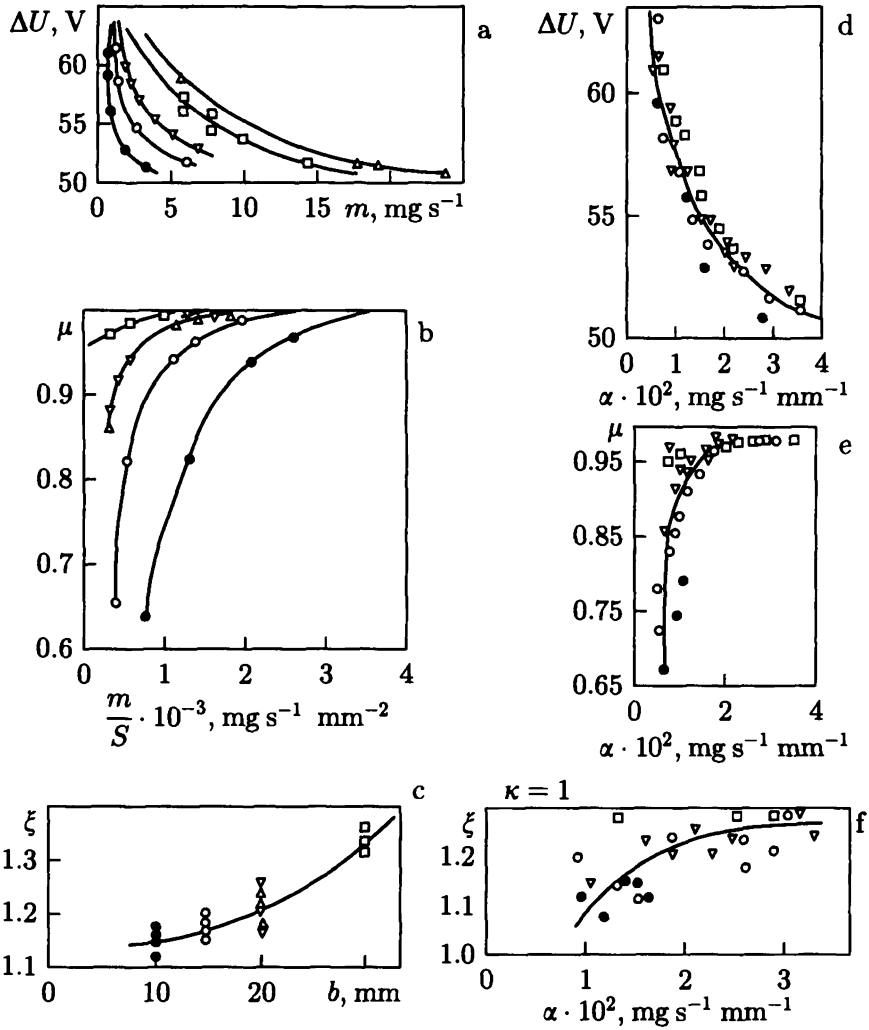


**Fig. 5.4.** (a) The change of the energy loss due to ionization and due to the propellant rate for different SPT models: • – M-50, ○ – M-70, ▽ – M-100, □ – P-130, △ – P-200. (b) The same for the change in the coefficient of usage of the propellant gas as a function of the specific rate. (c) The same for the exchange parameter as a function of the model's size. (d), (e), (f) Characteristics $\Delta U$, $\mu$, $\xi$ as functions of the parameter $\alpha$.

For this purpose, we consider three fundamental characteristics of the operational process in SPTs.

The dimensionless coefficient of voltage loss

$$\omega = \frac{\Delta U}{U_p}, \tag{5.17a}$$

where $\Delta U$ is the energy loss for ionization and other losses.

The coefficient of propellant usage

$$\mu = \frac{\dot{m}_i}{\dot{m}_0} = \frac{I_i}{I_{\dot{m}}}, \tag{5.17b}$$

where $\dot{m}_i$ is the mass of the ionized fraction of the propellant rate, $\dot{m}_0$ is the total propellant rate, $I_i$ is the current of ions emerging from the channel, and $I_{\dot{m}}$ is the rate expressed in current units. This coefficient characterizes the effective degree of ionization.

The parameter of exchange is the ratio of the discharge current to the mass ratio in current units:

$$\xi = \frac{I_p}{I_{\dot{m}}}. \tag{5.17c}$$

Knowledge of the dimensionless parameters $\omega$, $\mu$, and $\xi$ enables us to find the whole set of thruster characteristics. For example, the mean ion velocity

$$V = \sqrt{(1-\omega)2eU_p/M},$$

the accelerator thrust

$$F = \mu\dot{m}\sqrt{(1-\omega)2eU_p/M},$$

the power consumed

$$N = I_p U_p = \xi I_{\dot{m}} U_p,$$

etc.

Paper [63] tried to find the minimal number of parameters (ideally one, some $\alpha$) to reduce all the dependences shown in Fig. 5.4 to three functions, $\omega(\alpha)$, $\mu(\alpha)$, $\xi(\alpha)$, with a minimal dispersion.

Given the results (5.9) and (5.10), such a parameter $\alpha$ was taken in the form of a complex ($b$ is the channel width)

$$\alpha = \frac{\dot{m}}{2\pi r b} b^k = \tilde{m} b^{k-1}$$

with $k$ chosen such that the dispersion of points should be minimal for all three functions simultaneously; $k = 1$ is the most adequate for all three dependences. Although one cannot state *a priori* that these dependences must be a "strong" function of only one argument, our attempt to reduce everything to one parameter was successful enough and generally lies within the error of determination of individual values. At $k = 1$, the parameter $\alpha$ is in fact determined only by the total rate $\dot{m}$ and channel radius $r$ and is independent of $b$:

$$\alpha = \frac{\dot{m}}{2\pi r}. \tag{5.18}$$

The dimensional similarity parameter $\alpha$ can be naturally related to the parameter $S_i$ introduced earlier. As a result we obtain [63]

$$S_i = \theta \frac{eU_p k T_0}{\beta_0^2 \alpha^2} \frac{b^2}{L^2}. \tag{5.19}$$

Here $\theta \sim 1$ is a factor depending on the chosen scales for $\beta$, $L$, and $T_0$. Note that the length of the region with a strong magnetic field can be naturally taken for $L$, the wall temperature can be taken as a measure of $T_0$, and $\beta$ can be calculated using a linear spline (Fig. 3.6b) with a maximum energy equal to the first multiplication threshold $\mathcal{E}^*$.

A condition for the normal discharge glow can be taken in the form of the Bugrova–Maslennikov–Morozov criterion:

$$S_i < S_{i,\mathrm{cr}} = 1/3,$$

which means that the free-path length before ionization $L$ is at least three times smaller than the size of the strong $E$-field region.

Expression (5.19) can be simplified, making allowance for the fact that $b \approx L$. Then

$$S_i = \theta_1 \frac{eU_p k T_0}{\beta_0^2 \alpha^2}. \tag{5.20}$$

It is seen from here that the passage to the normal regime ($S_i < 1/3$) is determined, in the first approximation, by the mass rate independently of the propellant material. This result was first noted in [59] in the form of the so-called "Melikov's comb" (Fig. 5.3).

Substituting the characteristic parameters $U_p = 200\,\mathrm{V}$, $T_0 = 300^\circ\,\mathrm{C}$, and $\beta = 3 \times 10^{-8}\,\mathrm{cm^3\,s^{-1}}$ into Eq. (5.20), we obtain for Xe

$$\alpha = 0.15\sqrt{\theta_1/S_i}\,\mathrm{mg\,cm^{-1}\,s^{-1}}.$$

Further assuming $\theta_1 = 2/3$ and $S_1 = S_{1,\mathrm{cr}} = 1/3$, we have $\alpha_{\mathrm{cr}} \approx 0.2\,\mathrm{mg\,cm^{-1}\,s^{-1}}$, which is in good agreement with experiment. Of course, here some fine tuning is present for the choice of $\theta_1$. However, the coincidence to an order of magnitude is evident.

Now, using Fig. 5.4, we can write dimensionless expressions for $\omega_\varepsilon = \Delta U/\mathcal{E}$, $\mu$, and $\xi$ by assuming that these are functions of $S_i$ only. We get

$$\begin{aligned}
\omega_\varepsilon &= 1 + \sigma_1\sqrt{S_i}, \quad \sigma_1 \approx 1.2, \\
\mu &= 1 - \exp\left(-\frac{\sigma_2}{\sqrt{S_i}}\right), \quad \sigma_2 \approx 3, \\
\xi &= 1 + \frac{\sigma_3}{S_i}, \quad \sigma_3 \approx 0.03.
\end{aligned}$$

To conclude the discussion of SPT similarity, we note that the dependence of any output parameter $A$ on other characteristics (parameters) of the system can be represented in the form

$$A = A_0 f\big(P_1, P_2, \ldots, P_k\big),$$

where $A_0$ is some basic expression with the same dimension as $A$. The quantities $P_1, \ldots, P_k$ are dimensionless complexes. Generally, the function $f$ depends strongly on some of them and weakly on others. A strong parameter in our case is the dimensionless argument $P_1 = S_i$. The "dimensionless ion cost"

$$P_2 = \mathcal{E}/U_p$$

can also be of significance. However, the accuracy of the present data is still limited, and the final choice of the next most important dimensionless parameter is still to be made.

## 5.4. The "inverse" problem of heavy particle dynamics

In this section, by "inverse" problems we refer to the understanding of processes in the channel using integral parameters of the system $(\dot{m}, J_p, F)$ and properties of the flux emerging from the thruster.

### *5.4.1. An analysis of processes using integral flux characteristics*

During tests, the SPT-ATON demonstrated incredibly good characteristics (efficiency up to $\eta \sim 70\%$) with the exchange parameter (calculated for single ionization) $\xi \sim 1.15$ ($\xi = J_p/J_{\dot{m}}$, where $J_{\dot{m}} = e\dot{m}/M$ during single ionization). This discrepancy between $\eta$ and $\xi$ could be explained only by the fact that a comparatively large number of doubly ionized ions of $Xe^{++}$ are generated in the SPT. At that time no direct measurements of the $Xe^{++}$ concentration were available, so the following scheme was proposed to measure the fraction of $Xe^{++}$ using three integral parameters $(\dot{m}, J_p, F)$. The particle flux emerging from the channel is subdivided into three groups: $\dot{m}_1$ is the flux of singly charged ions, $\dot{m}_2$ is the flux of doubly charged ions, and $\dot{m}_3$ is the flux of particles that "fell out" of the normal acceleration process. The latter group $\dot{m}_3$ includes particles either not ionized at all or that underwent one or several $(\nu)$ collisions with

the wall. By simplifying the analysis (a more precise model, as shown by calculations and direct measurements, does not change the results significantly), we shall assume that both the first and second ionizations occur at practically the same place, i.e., with one potential $\Phi^*$. Then one may write the following three equalities [64]:

$$\begin{aligned} &\dot{m}_1 + \dot{m}_2 + \dot{m}_3 = \dot{m}, \\ &\dot{m}_1 + 2\dot{m}_2 + \nu\dot{m}_3 = \frac{MJ_p}{e}, \\ &\dot{m}_1 + \sqrt{2}\dot{m}_2 = MF\left(\frac{2e\Phi^*}{M}\right)^{-1/2} \end{aligned} \tag{5.21}$$

Here we have taken into account that an ion, after having collided with the wall, is most probably neutralized, so each of the collisions of the fallen-out ion with the wall contribute to the total discharge current. Consider an example. A first-generation SPT M-100 with Xe at $\dot{m} = 3\,\mathrm{mg\,s^{-1}}$, $U_p = 300\,\mathrm{V}$ has

$$\dot{m}_1 \approx 77\%, \quad \dot{m}_2 \approx 10\%, \quad \dot{m}_3 \approx 17\%.$$

A second-generation model SPT ATON(A-4) for $\dot{m} = 3\,\mathrm{mg\,s^{-1}}$, $U_p = 300\,\mathrm{V}$ has

$$\dot{m}_1 \approx 77\%, \quad \dot{m}_2 \approx 20\%, \quad \dot{m}_3 \approx 3\%.$$

Obviuosly, in the second case the number of "fallen-out" particles is strongly reduced and a notable ($\sim$20%) fraction of doubly ionized ions appear. A sharp decrease in the fallen-out particle number can be observed visually, in some sense. Namely, if M-70 yields a strongly divergent beam with a smeared-out outer boundary, A-4 in optimized regimes produces a flux like a weakly divergent cylinder with a sufficiently well-determined boundary.

Later, the $Xe^{++}$ ion concentrations were measured to be $\dot{m}_2 \sim 15\%$ by direct experimental methods.

## 5.5. An analysis of processes using the emerging flux characteristics

Here we only note the possibility of determining, using flux parameters, configurations and locations of equipotentials, as well as the spatial location of the ion birthrate density

$$q = n_e n_0 \langle \sigma V \rangle_{\text{ion}}.$$

The process is assumed to be strictly steady.

Under the assumptions made, the determination of $\Phi(\mathbf{r})$ and $q(\mathbf{r})$ can be made fully with the use of special energy analyzers.

First of all, to find the functions sought we choose some outlet $\Pi(z_0)$ of the flux coming out of the SPT. After having measured the energy ion distributions at different $r$, we obtain the relationship

$$Q(\Phi_*, r, z_0) = \frac{dJ_i}{2\pi r\, dr\, d\Phi}. \tag{5.22}$$

Here $\Phi_* = \mathcal{E}/e$ is the potential at the ion birth point $(z_1)$, which is uniquely related to the ion energy $\mathcal{E}$. The quantity $Q$ in turn is related to $q(\mathbf{r})$:

$$2\pi r_1 q(\mathbf{r})\, dr_1\, dz_1 = Q\, 2\pi r\, dr\, d\Phi_*,$$

or

$$q(r_1, z_1) = \frac{Q r\, dr}{r_1\, dr_1} \frac{d\Phi_*}{dz_1}. \tag{5.23}$$

To find $d\Phi/dz_1$, we need to determine the explicit dependence $\Phi(r_1, z_1)$. This can be done, thus far in principle, by measuring at the same point the azimuthal velocity of particles $V_\theta$ with the same energy. Since we suppose that oscillations are absent and the atomic temperature is small, $V_\theta$ uniquely determines the magnetic flux function $\Psi_*$ :

$$\Psi_*(r_1, z_1) = \frac{c}{e} M r V_\theta. \tag{5.24}$$

But since we know *a priori* the magnetic field, using Eq. (5.23) we can determine the magnetic surface near which the birth of a given group of particles with a given energy occurred. Thus, point by point, we can obtain the sets $(\Phi_*, \Psi_*, \alpha)$ at each point of the surface $\Pi$, where $\tan\alpha = r/z$. Thus, now we should construct equipotentials. This can be done by iterations using a computer.

After having determined the distribution $\Phi(r, z)$, we find the ion-birth density and thence the ion density distribution in the channel.

## 5.6. Estimate of energetic balance components in the SPT-ATON

One of the most important characteristics of any thruster is its efficiency coefficient. This can be determined by different means. In rocket technology, in particular, during SPT tests, one ordinarily uses a so-called "thrust" efficiency, which is determined as

$$\eta_T = \frac{F^2}{2\dot{m}U_p J_p}. \tag{5.25}$$

For our purposes, it is convenient to treat $\dot{m}$ as a mass rate supplied directly into the SPT channel, which does not include the propellant supply to the cathode $\dot{m}_K$, the latter being of order $\sim 0.1\dot{m}$. Neither shall we take into account the potential difference on the solenoids if they are connected consecutively with the discharge. Thus, formula (5.24) accounts for the voltage applied to the SPT channel ($U_\mathrm{A}$) and to the plasma bridge ($U_\mathrm{PB}$) between the channel outlet and emitting cathode-compensator (Fig. 1.2).

Let us evaluate the power loss in different processes occurring in the SPT-ATON (A-4) for $\dot{m} = 3\,\mathrm{mg\,s^{-1}}$, $U_p = 300\,\mathrm{V}$ in a well-optimized regime. In this case, $\eta_T \approx 67\%$ and the fraction of doubly ionized ions is $\alpha_2 \approx 15\%$; the discharge current is $J_p \approx 2.9\,\mathrm{A}$.

The total power $P_0 = U_p J_p = 870\,\mathrm{W}$ supplied to the thruster can be written as a sum of six terms: $P_0 = P_1 + \cdots + P_6$, where $P_1$ is the kinetic energy carried away by ions, $P_2$ is the energy brought by electrons to the cathode, $P_3$ are losses in the plasma bridge, $P_4$ are losses due to the "through" electron current, $P_5$ are ionization losses, and $P_6$ are losses on the walls.

(a) Before passing to estimating $P_1$, we should clarify the relationship between the efficiency coefficient, the thrust $F$, and the fraction of doubly ionized ions $\alpha_2$. Assuming that the ions $Xe^+$ and $Xe^{++}$ are born at one potential, the "thrust" kinetic energy of the stream is

$$W_K^F = \frac{F^2}{2\dot{m}} = \frac{\dot{m}}{2} V_z^2 \left[1 + \left(\sqrt{2} - 1\right)\alpha_2\right]^2.$$

At the same time, the actual kinetic energy carried away by ions $Xe^+$ and $Xe^{++}$ will be

$$W_K^R = \frac{\dot{m}}{2} V_z^2 (1 + \alpha_2).$$

The difference between these values at $\alpha_2 = 0.15$ is $\sim 2\%$. Taking into account that in this regime the divergence angle is $\sim \pm 10^\circ$ and the energetic ion spectrum has a width of $\sim 0.25 \mathcal{E}_{\max}$, the total kinetic energy carried away by the flux is $\approx 72\%$. Therefore, $P_1 \approx 627\,\mathrm{W}$.

(b) The electron enthalpy flux on the anode ignoring the DL is

$$P_2 = \frac{1}{e} \frac{5}{2} k T_e J_p. \tag{5.26}$$

(Accounting for the DL can appreciably reduce this value.) Assuming that $T_e = 10\,\mathrm{eV}$ near the anode, we get

$$P_2 \approx 72.5\,\mathrm{W}.$$

(c) The potential difference in the "plasma bridge" is usually $\delta U_{\mathrm{PB}} \sim 12\,\mathrm{V}$. Thence

$$P_3 \approx J_p \delta U_{\mathrm{PB}} \approx 35\,\mathrm{W}.$$

(d) Experiments show that a "through" electron current $J_t$ passes from the anode to the channel outlet. Apparently, it is needed for discharge stabilization. Its amplitude can be determined, under some assumptions, as

$$J_t = J_p - J_i^+ - J_i^{++} \approx 0.25\,\mathrm{A}. \tag{5.27}$$

This value is of the order of $\sim 9\%$ of the discharge current. The passage of this current, which is apparently transported by the intermediate EDF component, consumes a power of

$$P_4 \approx J_t U_p \approx 74\,\mathrm{W}. \tag{5.28}$$

This is naturally given to the channel walls.

(e) Ionization losses can be found assuming that the ionization is full. Accounting for the formation of two sorts of ions of $Xe^+$ (85%) and $Xe^{++}$ (15%), we obtain

$$P_5 = \frac{\dot{m}}{M} e(\zeta_1 + 0.15\zeta_2) = J_{\dot{m}}(\zeta_1 + 0.15\zeta_2). \tag{5.29}$$

Here $\zeta_1$ is the energetic cost of $Xe^+$, $\zeta_2$ is the cost of the second ionization, which is assumed to follow the first, $J_{\dot{m}} \equiv e\dot{m}/M = 2.3\,\mathrm{A}$ at $\dot{m} = 3\,\mathrm{mg\,s^{-1}}$. Since, as noted in Section 3.1, in the ionization zone the radiation of excited atoms can be considered mostly locked and, moreover, the electron temperature is high ($T_e \geq 15\,\mathrm{eV}$), $\zeta_1$ can be taken as 20 eV for estimates. We recall that the first ionization potential of Xe is $I_1 = 12.1\,\mathrm{eV}$, and the second is $I_2 = 21.2\,\mathrm{eV}$. The $Xe^+$ radiation is no longer locked, so to estimate $\zeta_2$ one can use the traditional rule of "three ionization potentials" $\zeta_2 \sim 60\,\mathrm{eV}$. As a result, we obtain

$$P_5 \approx 67\,\mathrm{W}.$$

Before passing to the estimation of $P_6$, the "secondary" energy fluxes on the walls, we note that the sum of the already evaluated five fluxes is 876 W. This value already exceeds $P_0 = 870\,\mathrm{W}$. Of course, the accuracy of these calculations is about $\pm 3-6\%$.

However, it is now difficult to point to which of the quantities used must be reduced first. It appears that they are losses on the anode and possibly in the plasma bridge.

(f) Now consider the flux $P_6$. In fact, it includes three different terms:

$$P_6 = P_6^i + P_6^e + P_6^\gamma. \tag{5.30}$$

The energy flux brought by ions in direct collisions with the wall can be roughly estimated using the insulator erosion value:

$$P_6^i = \theta J_i^F U_p, \tag{5.31}$$

where $J_i^F$ is the ion flux onto the part of the insulator being sputtered and $\theta \sim 0.5$ is a dimensionless factor characterizing the mean energy of the incident ions. In turn,

$$J_i^F \approx \dot{V}/S_V,$$

where $\dot{V}$ is the volume that is sputtered in unit time and $S_V$ is the bulk sputtering coefficient, which we take from Fig. 3.4 for ABN at $\mathcal{E}_i = 150\,\text{eV}$ :

$$S_V = 2 \cdot 10^{-2}\,\text{mm}^3\,\text{C}^{-1}.$$

This value is twice that given in the figure, thereby accounting for the dependence of $S_V$ on the incident angle.

As already noted, ion erosion is explicitly observed only in first-generation models, including M-70 with a strongly divergent beam, but only during the first 500–1000 h until the insulator profile is "adjusted" to the ion flux profile. Here the width (along the $z$-axis) of the zone being sputtered is $b \approx 7\,\text{mm}$ for both insulators, and the sputtering rate is $\delta \approx 5\,\mu\text{m}\,\text{h}^{-1} \sim 1.5 \times 10^{-6}\,\text{mm}\,\text{s}^{-1}$. It follows from here that

$$\dot{V} = 2\pi(R_1 + R_2)b\delta \approx 3 \cdot 10^{-3}\,\text{mm}^{-3}\,\text{s}^{-1}.$$

Here $R_1 + R_2$ is the sum of the insulator working surfaces. Given $S_V$ we find

$$J_i^F \approx 0.15\,\text{A}.$$

Substituting this value into Eq. (5.31), we obtain

$$P_6^i \approx 25\,\mathrm{W}.$$

It should be stressed that this estimate is very preliminary, since we have had to make a lot of assumptions to obtain it. It is not excluded that the real value of $P_6^i$ may differ from this estimate by a factor of two.

When the SPT passes into the anomalous erosion regime, the quantity $P_6^i$ can be neglected altogether. The second constituent of $P_6^e$, which is due to electrons, most likely contributes to the thermal flux related to the "through" electrons and can also be neglected. Finally, the third term $P_6^\gamma$, which is due to radiation of the accelerated stream and whose electron component is heated by the Joule heat, on the one hand is simply very small, and on the other hand is taken into account in losses related to the "through" electrons.

It is seen from the above that the characteristics of the SPT-ATON (A-4) are close to the limit. To increase the thrust efficiency by 3–4% in models working with the given parameters, a thorough study of electron kinetics over the entire channel space will be required. Thus, in the near future, improvement of SPT characteristics will probably be due to decreasing the propellant rate in the cathode-compensator.

## 6. Low-frequency oscillations in SPTs

As shown above, the quasi-autonomous consideration of the dynamics of electrons and ions enables us to understand most processes in SPTs and evaluate their quantitative characteristics as well. However, very important phenomena exist which mainly require a self-consistent consideration of the dynamics of all the plasma components: neutrals, ions, and electrons. This includes the ionization zone and oscillations inside the channel and at the output of the SPT at frequencies less than the electron Larmor frequency. Of course, a future "complete" theory of SPTs will be self-consistent.

In Section 4, we considered UHF-oscillations in the Langmuir frequency range (1 – 10 GHz), which can be studied using only one electron component. However, in addition there are oscillations at almost all frequencies from 1 kHz to hundreds of MHz. Of course, there are low-frequency (LF) oscillations in different frequency ranges with periods higher than or of the order of the flyby time across the thruster's channel:

$$\tau_0 \geq L/V_{iM},$$

where $V_{iM}$ is the velocity of ions at the channel output. This section and a part of the next one deal with some important properties of LF-oscillations.

## 6.1. Experimental data on LF-oscillations in the SPT channel

Figure 6.1a shows oscillograms of the discharge current and electron current to the probe for typical parameters $\dot{m} = 3\,\mathrm{mg\,s^{-1}}$, $U_p = 300\,\mathrm{V}$ for an optimal electric circuit [65].

It is seen that the oscillations at $H \sim H_{\mathrm{opt}}$ are very chaotic, but two characteristic frequency intervals can be clearly distinguished: (a) $\sim 20 \leq f \leq 50\,\mathrm{kHz}$, (b) $\sim 100 \leq f \leq 1000\,\mathrm{kHz}$.

In group (a), the oscillation periods are appreciably larger than the ion flyby time, but close to the atom flyby time $\tau_a = L/V_a \approx 10^{-4}\,\mathrm{s}$. Here $V_a$ is the thermal velocity of Xe atoms, which was taken to be $2 \times 10^4\,\mathrm{cm\,s^{-1}}$. Indeed, considering the numerical models below, we shall see that these oscillations are related to ionization. Thus, they are called ionization oscillations.

Oscillations of group (b) do not relate directly to ionization and are generally called "flyby" oscillations.

In addition to these two main types, oscillations at frequencies $\sim 5 - 20\,\mathrm{kHz}$ may be observed (usually when non-optimal parameters of the $R, L, C$-chain are chosen), which appear as a "singing" of the coil. They are called "contour" oscil-

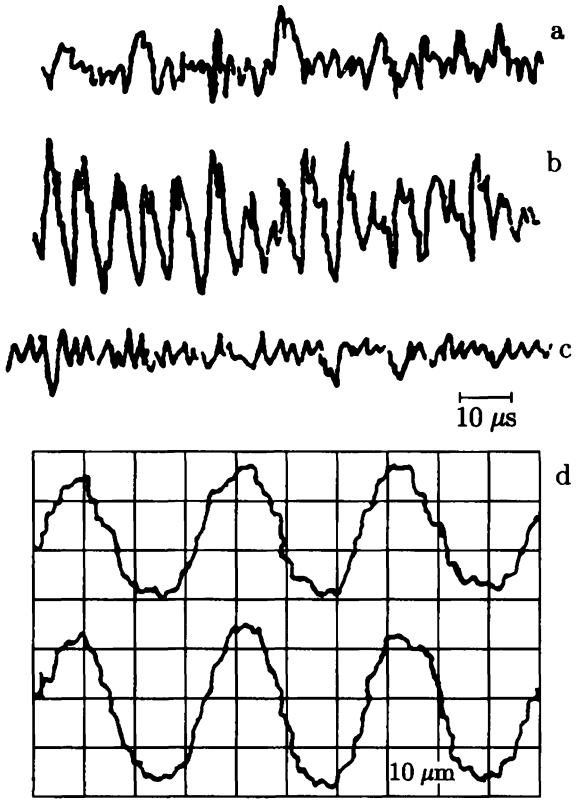


**Fig. 6.1.** Oscillograms of LF-oscillations ($f \leq 1\,\mathrm{MHz}$) in the SPT-ATON with non-dusty insulators. (a), (b), (c) Oscillations of the discharge current $J(t)$ at $\dot{m} = 3\,\mathrm{mg\,s^{-1}}$, $U_p = 300\,\mathrm{V}$, and for different magnetic configurations inside the channel (for different currents in the coils). Figure 6.1c corresponds to an "optimal" regime [oscillation amplitude $\sim 5\%$ of $J(t)$]. (d) The synchronicity of signals from two probes separated by 180° in azimuth.

lations. However, it is unclear at present whether they represent an autonomous oscillation group or are related to ionization oscillations.

Presently, there is no clear experimentally based picture of LF-oscillations. This is explained by their chaotic ("turbulent") shape and also by a strong dependence on various factors, in particular on the powdering of insulators.

Nevertheless, the LF-oscillations demonstrate two fundamental properties: (1) they are highly azimuthally symmetric and (2) they comparatively weakly affect the integral SPT characteristics.

### *6.1.1. Azimuthal symmetry of LF-oscillations*

At the very beginning of SPT studies, a correlation analysis of chaotic oscillations observed in the channel was made [66]. These data are of little interest now, since the organization of processes in the channel was comparatively poor. Nevertheless, the control of the azimuthal symmetry of LF-oscillations has been done many times and each time has given the same result. This is done using two probes separated by 180 degrees in azimuth. The two typical oscillograms obtained are presented in Fig. 6.1d. Such data enable us to consider the LF-oscillations to be azimuthally symmetrical. However, such a symmetry is realized only provided that

$$(\mathbf{v}_i, \nabla)\frac{H}{n} > 0,$$

i.e., for an increasing magnetic field and a sufficiently narrow ionization zone. If this condition is not met, the symmetrical plasma configuration in the channel is destroyed. Paper [67] describes experiments carried out at the AEI in 1971 using a laboratory SPT model with three solenoids allowing variation of the $z$-distribution of the magnetic field over a wide range and both $\partial H/\partial z > 0$ and $\partial H/\partial z < 0$ to be obtained (Fig. 6.2a). The experiments used Ar at a rate of $\dot{m} = 1.8\,\mathrm{mg\,s^{-1}}$. The change of the volt-ampere characteristics during variations of $H_r(z)$ (the magnetic force lines were symmetric with respect to the middle of the channel in all cases, as in the SPT-ATON) is shown in

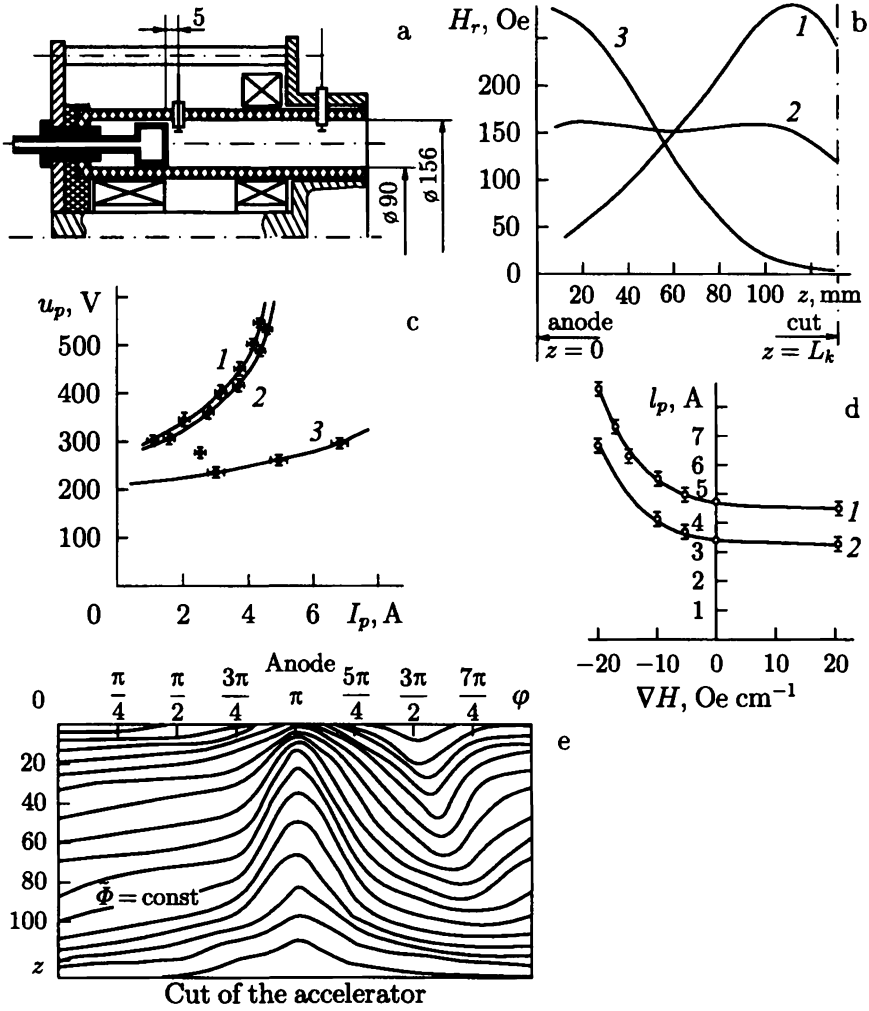


**Fig. 6.2.** The effect of $\nabla H$ on the SPT performance [67]. (a) The experimental model scheme. (b) The radial magnetic field component on the middle surface. (c) Volt-ampere characteristics: *1)* $\nabla H > 0$; *2)* $\nabla H \approx 0$; *3)* $\nabla H < 0$. (d) The dependence of the discharge current on $\nabla H$ for different voltages: *1* – 500 V, *2* – 400 V. (e) An instantaneous picture of equipotentials at $\nabla H < 0$.

Fig. 6.2c, d. At $\partial H/\partial z < 0$, the correlation measurements by probes of the potential distribution in time and space showed (Fig. 6.2e) that in a narrow region extending azimuthally from the outlet to the anode a gap in the equipotentials (magnetic drift surfaces) emerges, which rotates as a whole in the electron drift direction with a velocity of the order of 0.1 of the drift velocity $u_E = cE/H$. The appearance of an equipotential gap leads to the formation of an azimuthally running region of intense ionization where the gap approaches the anode. As a result, a "spike"-like ion flux rotating with a frequency of $\sim 25$ kHz arises. Unfortunately, such experiments using Xe have not yet been done, but undoubtedly the general properties of the process will remain the same.

Finally, we note that the azimuthal stability criteria contain not only $H$, but the plasma density $n$ as well. Thus, if $\partial H/\partial z > 0$, the plasma density increases quite rapidly along the channel length and the plasma configuration must be unstable with respect to the "spike" formation. This is actually observed in the "horizontal" part of the volt-ampere characteristic, when the ionization occurs inside the entire channel space. The conservation of the azimuthal symmetry in all regimes significantly facilitates their analysis. Under such conditions, only "longitudinal" (i.e., directed along the $z$-axis) and "membrane" (along the $r$-axis) oscillations of magnetic drift surfaces remain.

### *6.1.2. Membrane oscillations of the equipotential surfaces*

The equipotential surfaces can exhibit axially symmetric "membrane" oscillations accompanied by a curvature change, which leads to modulation of the flux divergence (Fig. 6.3a) [68]. Given the expression for a thermalized potential, we can write

$$\Phi(r, z) = \Phi_T(\Psi) + \frac{1}{e}\int \frac{dP_e}{n}.$$

It is seen from here that the equipotential curvature can vary due to the electron component enthalpy, i.e., its effective tem-

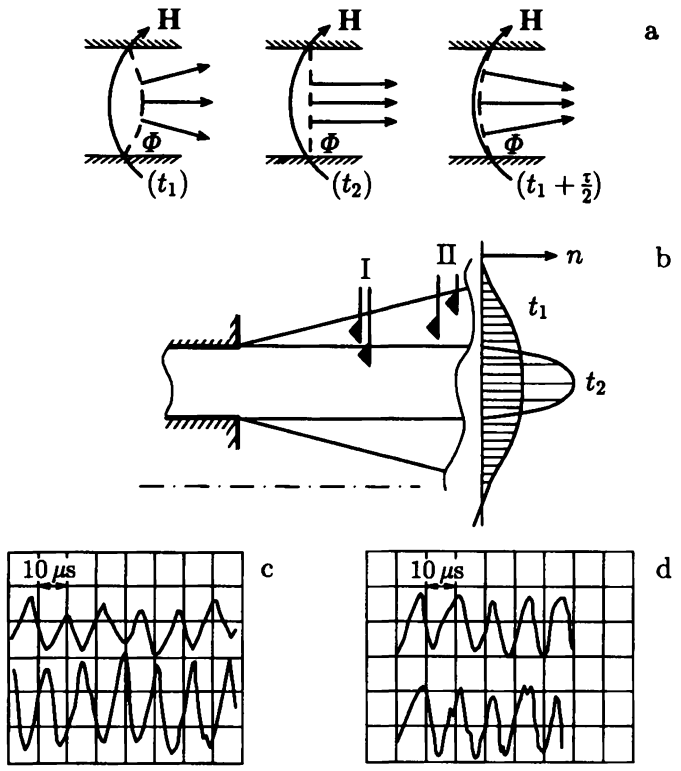


**Fig. 6.3.** Membrane oscillations of equipotentials. (a) The change of the equipotential forms during a half-period of oscillation $\tau/2$. (b) The location of pairs of probes on the "remote" (II) and "nearby" (I) parts of the flux. (c) Oscillograms of the ion current on the probes (I). (d) Oscillograms of the ion current on the probes (II).

perature. In particular, for a Maxwellian distribution

$$\Phi(r,z) = \Phi_T(\Psi) + \frac{kT_e}{e} \ln \frac{n}{n_0}.$$

The presence of such oscillations is clearly seen in experiment. They can be discovered primarily by counter-phase oscillations of ion signals at two probes, one of which is located closer to

the outcoming flux axis and the other closer to its periphery (Fig. 6.3c). By measuring electron temperature oscillations one can verify a correlation between these two signals and the oscillations in the flux divergence.

### *6.1.3. "Longitudinal" oscillations*

It is these oscillations, which are practically independent of the azimuth and weakly depend on the radius, that are primarily dealt with in experiments. It is these oscillations (on the probe oscillograms) or their consequences (on $U_p$ and $J_p$ oscillograms) that are presented in Fig. 6.1. Unfortunately, their analysis is far from completed. To conclude, we note that experimental attempts have been made to affect the longitudinal oscillations by a feedback system [69]. The development of an active system to handle the oscillations in the SPT channel seems to be very important and promising both in fundamental and applied aspects.

## 6.2. Linear oscillations in a one-dimensional flux model without ionization

### *6.2.1. Basic equations*

The complex picture of oscillations in SPTs revealed by experiments and numerically (see Section 7) makes us very cautious about constructing simple linear oscillation models. Nevertheless, such models seem to reflect some essential features of the flux perturbations.

Here we restrict ourselves to the simplest case of a one-dimensional flux streaming in a transversal magnetic field $H_z = H_0(x)$ and a longitudinal electric field $E_0(x)$. The channel is assumed to be narrow such that one may neglect the curvature of the magnetic lines and, correspondingly, the equipotential curvature. Near-wall plasma conductivity is assumed [70].

The initial system of equations reads ($\mathbf{u} \equiv \mathbf{V}_e$, $\mathbf{V} \equiv \mathbf{V}_i$)

$$\frac{\partial n}{\partial t} + \operatorname{div} n\mathbf{u} = 0, \quad 0 = -\nabla\Phi + \frac{1}{c}[\mathbf{u}, \mathbf{H}_0], \tag{6.1a}$$

$$\frac{\partial n}{\partial t} + \operatorname{div} n\mathbf{V} = 0, \quad M\frac{d\mathbf{V}}{dt} = -e\nabla\Phi, \tag{6.1b}$$

$$\mathbf{i}(x, y) = \lambda(x, y)\,\mathbf{E}(x, y). \tag{6.1c}$$

Here $\mathbf{i}(x, y)$ is the total near-wall current close to one insulator for given $(x, y, z = \pm z_0)$. Stationary solutions of this system satisfying the assumptions made are given by the following relationships:

$$\begin{gathered} n_0(x)V_0(x) \equiv \nu = \text{const}, \quad i_0 = \lambda E_0, \\ \frac{M}{e}\frac{V_0^2}{2} + e\Phi(x) \equiv \mathcal{E} = \text{const}, \\ \mathbf{u}(x) = \big(0, u_0 = -cE_0/H_0, 0\big). \end{gathered} \tag{6.2}$$

Below we restrict ourselves to considering only two-dimensional linear perturbations depending on $x$, $y$, and $t$. We set

$$\begin{aligned} n &= n_0(x) + n_1(x)e^{pt+qy}, & V_x &= V_0(x) + V_{1x}(x)e^{pt+qy}, \\ V_y &= V_{1y}(x)e^{pt+qy}, & V_z &= 0, \\ U_x &= U_{1x}(x)e^{pt+qy}, & U_y &= U_0(x) + U_{1y}(x)e^{pt+qy}, \\ U_z &= zS(x)e^{pt+qy}, & S &= S_1(x)e^{pt+qy}, \end{aligned} \tag{6.3}$$

The last equation suggests that an electron sink into the walls ($z = \pm z_0$), homogeneous over the plasma thickness is allowed.

Substituting Eq. (6.3) into Eq. (6.1), we obtain a system of linear equations with perturbation coefficients depending on $x$ :

$$u_{1x} = -\frac{c}{H_0(x)}q\Phi_1, \quad u_{1y} = \frac{c}{H_0(x)}\frac{\partial\Phi_1}{\partial x}, \tag{6.4a}$$

$$\big[p + u_0(x)q\big]\,n_1 - q\Phi_1\frac{\partial}{\partial x}\frac{n_0}{H_0} = -S_1 n_0, \tag{6.4b}$$

$$\left(p + \frac{\partial V_0}{\partial x}\right) V_{1x} + V_0 \frac{\partial V_{1x}}{\partial x} = -\frac{e}{M}\frac{\partial \Phi_1}{\partial x}, \tag{6.4c}$$

$$pV_{1y} + V_0 \frac{\partial V_{1y}}{\partial x} = -\frac{e}{M} q\Phi_1, \tag{6.4d}$$

$$\left(p + \frac{\partial V_0}{\partial x}\right) n_1 + V_0 \frac{\partial n_1}{\partial x} + V_{1x}\frac{\partial n_0}{\partial x} + n_0\left(\frac{\partial V_{1x}}{\partial x} + qV_{1y}\right) = 0. \tag{6.4e}$$

This system in some cases can be conveniently reduced to one linear equation. For this purpose, we introduce an independent variable $\tau$ instead of $x$, using the relation

$$d\tau = dx/V_0(x), \tag{6.5a}$$

and instead of the sought function $\Phi_1$, a new function ("velocity potential")

$$\theta(\tau) = \exp(-p\tau) \int_0^\tau \Phi_1 \exp(p\tau)\, d\tau. \tag{6.5b}$$

Given $\theta(\tau)$, we easily find

$$\Phi_1 = \frac{\partial \theta}{\partial \tau} + p\theta. \tag{6.6}$$

Now considering Eqs. (6.4c), (6.4d) as linear equations for $V_{1x}$ and $V_{1y}$, it is not difficult to express them as a function of $\theta$ :

$$\begin{aligned} V_{1x} &= -\frac{e}{MV_0}\left(\frac{\partial \theta}{\partial \tau} + C_1 e^{-p\tau}\right), \\ V_{1y} &= -\frac{e}{M} q\left(\theta + C_2 e^{-p\tau}\right). \end{aligned} \tag{6.7}$$

The constants $C_1$ and $C_2$ are determined by perturbations at boundaries ($x = 0$, $x = L$). Substituting Eq. (6.7) into (6.4e), we get

$$\begin{aligned} n_1 =& n_0 \frac{e}{M} e^{-p\tau} \int_0^\tau \Delta^* \theta e^{p\tau}\, d\tau + \frac{C_3}{V_0} e^{-p\tau} \\ &+ C_2 \frac{e}{M} n_0 q^2 \tau e^{-p\tau} - C_1 \frac{e}{M} n_0 p e^{-p\tau} \int_0^\tau \frac{d\tau}{V_0}. \end{aligned} \tag{6.8a}$$

Here

$$\Delta^*\theta = q^2\theta + \frac{1}{V_0^2}\frac{\partial^2\theta}{\partial\tau^2}, \tag{6.8b}$$

and $C_3$ is a constant of integration.

On the other hand, from Eq. (6.4b) it follows that

$$n_1 = \frac{1}{p+u_0q}\left[q\Phi_1\frac{1}{V_0}\frac{\partial}{\partial\tau}\frac{n_0}{H_0} - S_1n_0\right]. \tag{6.9}$$

Equating (6.8) to (6.9) yields an equation for $\theta$ :

$$\begin{aligned} n_0\frac{e}{M}e^{-p\tau}\int_0^\tau\left(q^2\theta + \frac{\partial}{\partial\tau}\frac{1}{V_0^2}\frac{\partial\theta}{\partial\tau}\right)e^{p\tau}d\tau \\ + Q(\tau,p,q,C_1,C_2,C_3) \\ = \frac{1}{p+u_0q}\left\{q\left[\left(p+\frac{\partial}{\partial\tau}\right)\theta\right]\frac{1}{V_0}\frac{\partial}{\partial\tau}\frac{n_0}{H_0} - S_1\right\} \end{aligned} \tag{6.10a}$$

This equation can be recast in a more compact form after dividing into $n_0$ taking into account that $n_0V_0 = \text{const}$, and then applying the operator $\left(p+\partial/\partial\tau\right)$. As a result, we arrive at the equation sought:

$$\begin{aligned} \left(q^2 + \frac{\partial}{\partial\tau}\frac{1}{V_0^2}\frac{\partial}{\partial\tau}\right)\theta = Q_1(\tau,p,q,C_1,C_2,C_3) \\ - \left(p+\frac{\partial}{\partial\tau}\right)\left[\frac{1}{p+u_0q}\frac{q}{\omega_H L}\left(p+\frac{\partial}{\partial\tau}\right)\theta - S_1\right], \\ L \equiv -\frac{\partial}{\partial x}\ln\frac{n}{H_0}. \end{aligned} \tag{6.10b}$$

To make this equation useful for calculations, it is necessary to express the "sink function" $S_1$ through the parameter $\lambda$ of the near-wall conductivity. This can be done using the continuity equation

$$\operatorname{div}_\perp \mathbf{i} = -enu_z\Big|_{z=z_0} = -enz_0S_1.$$

It follows from here that

$$\operatorname{div} \lambda \mathbf{E}_1 = -en_0 z_0 S_1$$

and

$$S_1 = \frac{1}{en_0 z_0}\left[\frac{1}{V_0}\frac{\partial}{\partial\tau}\frac{\lambda_x}{V_0}\frac{\partial}{\partial\tau} + \frac{\partial}{\partial y}\lambda_y\frac{\partial}{\partial y}\right]\left(p + \frac{\partial}{\partial\tau}\right)\theta. \qquad (6.11)$$

*6.2.2. Main types of perturbations*

*Static two-dimensional perturbations at $\lambda = 0$ and without perturbation at the input [more precisely, at $Q_1 = 0$ in Eq. (6.10)].* This case is of interest, in particular, in connection with probe measurements of the flux. The probe itself as a physical body and its electric potential perturb the flux, and it is important to know the character of these perturbations.

Assuming in Eq. (6.10) that $p = 0$, $Q_1 = 0$, and $S_1 = 0$, we can obtain the following equation for the potential perturbations:

$$\frac{\partial^2\Phi_1}{\partial y^2} - \frac{\partial^2}{\partial\tau^2}\left(\frac{M}{e}\frac{H_0'}{E_0 H_0}\Phi_1\right) = 0. \qquad (6.12)$$

It is clear that for $H_0' > 0$ the perturbations are hyperbolic, and for $H_0' < 0$ elliptical.

This prediction was checked at MIREA. The experimental scheme was as follows. The character of the potential perturbation in the channel was controlled by a "network" of near-wall probes. For different $H'(x)$ the lines of $\delta\Phi_1 = \text{const}$ obtained had different shapes in accordance with Eq. (6.12).

Let now $H = \text{const}$, $E = 0$, $V_0 = \text{const}$, $\lambda = \text{const}$. In this case, Eq. (6.10b) reduces to a simple equation:

$$\Delta\left[\left(\frac{\partial}{\partial t} + V_0\frac{\partial}{\partial x}\right)^2\Phi_1 + \frac{e^2 n_0 z_0}{\lambda M}\frac{\partial\Phi_1}{\partial t}\right] = 0. \qquad (6.13)$$

Clearly, it has two solutions: one Laplacian-like, with an arbitrary dependence of time

$$\Delta\Phi_1 = 0; \qquad (6.14a)$$

the second describes a flyby-dissipative instability

$$\left(\frac{\partial}{\partial t}+V_0\frac{\partial}{\partial x}\right)^2\Phi_1+\frac{e^2n_0z_0}{\lambda M}\frac{\partial\Phi_1}{\partial t}=0. \tag{6.14b}$$

Indeed, by setting $\Phi_1\sim\exp\bigl(-i\omega t+ikx\bigr)$, we find at $a\to 0$ and $a\to\infty$

$$\omega\cong kV_0\left(1\pm a\frac{1+i}{2}\right)\Big|_{a\to 0},\quad a^2\equiv\frac{e^2n_0z_0}{\lambda MkV_0},$$
$$\frac{\omega_1}{kV_0}\cong ia^2,\quad \frac{\omega^2}{kV_0}\cong -i\frac{1}{a^2}\Big|_{a\to\infty} \tag{6.15}$$

This instability can apparently be compared with flyby oscillations, which take the form of narrow solitary waves in the non-linear stage (see Section 7).

Properties of the flyby-dissipative instability do not change qualitatively in the case $E_0\neq 0$. This instability can be stabilized if the chamber's walls are covered with probes which are connected to Earth through a capacitor. In this case, the function $S$ describing the exchange of electrons between the plasma and the walls may be represented as a sum of two terms, one of which is due to the near-wall conductivity ($S_w$) and the other to emission from the probes ($S_p$) :

$$S=S_w+S_p,\quad S_p=-\frac{2C_1}{zen_0}\frac{\partial\Phi_1}{\partial t}. \tag{6.16}$$

Here $C_1$ is the capacity per $\mathrm{cm}^2$ of the wall. At $C_1\to\infty$ the instability stabilizes.

*The stability of the flux in SPTs relative to azimuthally asymmetric perturbations.* We have repeatedly stressed above that, as is clearly shown by experiment, these oscillations are stabilized if the freezing parameter $\kappa=n/H$ decreases toward the thruster's outlet.

In real conditions such a stabilization occurs in the presence of ionization, and it appears that it helps the stabilization

provided that $(\mathbf{v}, \nabla)\kappa < 0$. Here we restrict ourselves to a significantly simpler study of the stability of a one-dimensional fully ionized flux with respect to linear perturbations depending on the $y$ coordinate. In other words, we remain within the framework of Eq. (6.10b). However, taking into account that this equation contains the integration constants $C_2$ and $C_3$, which are dependent on the boundary conditions and in particular on the ionization zone, we consider the stability of small-scale perturbations. In this approximation, assuming $S_1 \to 0$, we get a linear equation with constant coefficients for $\Phi_1$:

$$\left(\frac{\partial}{\partial t} + u_0 \frac{\partial}{\partial y}\right)\left(\frac{\partial^2}{\partial y^2} + \frac{\partial^2}{\partial x^2}\right)\theta + \frac{1}{L\omega_H}\left(\frac{\partial}{\partial t} + V_0 \frac{\partial}{\partial x}\right)^2 \frac{\partial \theta}{\partial y} = 0. \tag{6.17}$$

Here the flux inhomogeneity is taken into account using a "locally constant" derivative of $n_0/H_0$, which enters $L$. Assuming $\Phi_1 \sim \exp\bigl(-i\omega t + ilx + imy\bigr)$, we obtain the dispersion equation

$$(-\omega + u_0 m)k^2 + \frac{1}{L\omega_H}(-\omega + V_0 l)^2 m = 0, \quad k^2 = l^2 + m^2. \tag{6.18}$$

From here we find the frequency

$$\omega = \frac{1}{2m}(2mlV_0 + k^2 L\omega_H) \pm \frac{1}{2m}\sqrt{(2mlV_0 + k^2 L\omega_H)^2 - 4m^2(l^2 V_0^2 + k^2 u_0^2 L\omega_H)} \tag{6.19a}$$

and thus the stability criterion

$$(2mlV_0 + k^2 L\omega_H)^2 \geq 4m^2(l^2 V_0^2 + k^2 u_0^2 L\omega_H). \tag{6.19b}$$

For this inequality to be satisfied at all $l, m$, it is sufficient that it have no real roots for the ratio $s = l/m$ when its lhs and rhs are equal. The roots $s_{1,2}$ are

$$s_{1,2} = -2\mu \pm \sqrt{4\mu^2 - (1 + 4\nu)}, \qquad \nu = \frac{|u_0|}{L\omega_H}, \quad \mu = \frac{V_0}{L\omega_H}, \tag{6.20}$$

and, hence, the stability criterion takes the form

$$1/4 + \nu > \mu^2. \tag{6.21}$$

Obviously, the criterion can be fulfilled only if

$$\frac{1}{L} = -\frac{H_0}{n_0}\frac{\partial}{\partial x}\left(\frac{n_0}{H_0}\right) > 0. \tag{6.22}$$

It should be noted that criterion (6.22) is met in real systems without a large margin. For example, for typical parameters of Xe thrusters $V_0 = 2 \times 10^6\,\mathrm{cm\,s^{-1}}$, $L = 2\,\mathrm{cm}$, $H = 200\,\mathrm{Oe}$, $E = 300\,\mathrm{V\,cm^{-1}}$, we obtain $\mu \sim 0.5 \times 10^2$, $\nu \sim 4 \times 10^3$.

The fact that the obtained stability reserve is small and, in addition, only estimates are available, indicates that the criterion of the flux stability with respect to an azimuthally asymmetric perturbation requires further study with explicit consideration of the ionization and final size of the channel. However, the conclusion implied by Eq. (6.21) that a decrease in $H$ toward the channel outlet leads to the instability is in perfect agreement with experiments.

# 7. One-dimensional self-consistent models for plasma flow in an SPT channel

## 7.1. Modeling an SPT in the one-dimensional hydrodynamic approximation

It is absolutely clear that a complete self-consistent model of the processes in SPTs would be very large and complicated. Thus, it seems reasonable to construct a sequence of comparatively simple models describing different aspects of the phenomena which in total would give a correct picture as a whole. The absence of azimuthally asymmetric oscillations in a working SPT helps construct such models for processes with the characteristic time-scales $\tau \geq \tau_0$ ($\tau_0$ is the flyby time). So we start with a one-dimensional hydrodynamic model for the dynamics of electrons,

atoms, and ions [71]. Single ionization will always be assumed. The behavior of the system in this model already appears very complex and nontrivial.

Let $x$ be the coordinate along the channel length, $x = 0$ being at the anode and $x = L$ at the channel's outlet (the cathode).

The principal entities in this model are $n(x,t)$ the ion concentration (and, by virtue of the quasi-neutrality, that of electrons), $V(x,t)$, the ion velocity, $n_a(x,t)$, the concentration of neutral particles, and $J(t)$, the electric current in the system. Then the model equations are: the continuity equation for ions

$$\frac{\partial n}{\partial t} + \frac{\partial nV}{\partial x} = \beta n n_a; \tag{7.1}$$

the equation of motion for ions:

$$\frac{\partial nV}{\partial t} + \frac{\partial nV^2}{\partial x} = \frac{en}{M}E + \beta n n_a V_a. \tag{7.2}$$

Considering the one-dimensionality of the model and the independence of the discharge current of $x$, we obtain Ohm's law in the form

$$E = \frac{J - enV}{\sigma(x)}. \tag{7.3}$$

Then the continuity equation for atoms is

$$\frac{\partial n_a}{\partial t} + V_a \frac{\partial n_a}{\partial x} = -\beta n n_a, \tag{7.4}$$

and the equation of the electric circuit is

$$L_c \frac{dJ}{dt} + RJ + \int_0^L E\,dx = U_0. \tag{7.5}$$

The rhs of Eq. (7.1) describes ionization by electron collisions, and $\beta$ is the coefficient of the ionization rate (below we shall

consider that $\beta = \text{const}$), $\sigma(x)$ is the plasma conductivity depending, in our model, only on the transversal magnetic field, which is considered as a parameter:

$$\sigma(x) = \sigma_0 \left[\frac{H_0}{H(x)}\right]^2, \quad \sigma_0 = \text{const}, \quad H_0 = \text{const}. \tag{7.6}$$

$H_0$ is the magnetic field at the channel's outlet, $H(x)$ is the profile of the transversal magnetic field. In Eq. (7.4), $V_a = \text{const} > 0$ is the velocity of atoms. In Eq. (7.5), $L_c$ is the inductance, $R$ is the active resistivity, and $U_0$ is the electromotive force in the chain.

System (7.1)–(7.5) is provided with sufficiently arbitrary initial data and the following boundary conditions at $x = 0$:

$$n(0,t) = n_0, \quad n_a(0,t) = n_{a0}, \quad V(0,t) = V_0 > 0. \tag{7.7}$$

For further study it is convenient to switch to new units. Let $L$ (the channel length) be a unit of length, $n_{a0}$ a unit of density, $E_0 = U_0/L$ a unit of electric field, $V_0$ a unit of velocity, $t_0 = L/V_0$ a unit of time, and $I_0 = U_0/R_{\text{ch}}$ a unit of electric current, where $R_{\text{ch}} = L/\sigma_0$ is the "resistivity" of the channel with a cross-section of $S = 1\,\text{cm}^2$. In the new units we get (we keep the same notation for basic quantities)

$$\begin{aligned}
\frac{\partial n}{\partial t} + \frac{\partial nV}{\partial x} &= \nu n n_a, \\
\frac{\partial nV}{\partial t} + \frac{\partial nV^2}{\partial x} &= \mu n E + \nu n n_a V_a, \\
\frac{\partial n_a}{\partial t} + V_a \frac{\partial n_a}{\partial x} &= -\nu n n_a, \\
l\frac{dJ}{dt} + rJ + \int_0^1 E\,dx &= 1, \quad E = h^2(x)\big(J - \chi n V\big),
\end{aligned} \tag{7.8}$$

and the boundary conditions (7.7) take the form

$$n(0,t) = n_0, \quad n_a(0,t) = 1, \quad V(0,t) = 1. \tag{7.9}$$

The basic dimensionless parameters are

$$\mu = \frac{eU_0}{MV_0^2}, \quad \nu = \frac{\beta n_{a0} L}{V_0},$$
$$\chi = \frac{e n_{a0} V_0 R_{ch}}{U_0}, \quad l = \frac{L_c V_0}{L R_{ch}}, \quad r = \frac{R}{R_{ch}}. \tag{7.10}$$

The magnetic field is taken in the form

$$h(x) = h_0 + (1 - h_0)x^2, \quad h_0 = H(0)/H_0. \tag{7.11}$$

The boundary problem for Eqs. (7.8) is strongly non-linear, containing a non-local term and many parameters. A complete study of this problem is impossible without involving modern numerical methods for solving equations in partial derivatives.

## 7.2. The results of calculations in the hydrodynamic model

### *7.2.1. Model parameter specification*

Consider a parameter range of practical interest for SPT operation when the rate is $\dot{m} = 2$–$4\,\mathrm{mg\,s^{-1}}$, the discharge voltage is $U_0 = 200-400\,\mathrm{V}$, and Xe is the propellant.

Let us estimate the main dimensionless parameters (7.10). Let $\dot{m}$ be $3\,\mathrm{mg\,s^{-1}}$. If the channel cross-section is $\cong 25\,\mathrm{cm^2}$, the atomic concentration at the anode is $n_{a0} \cong 3 \times 10^{13}\,\mathrm{cm^{-3}}$ (the velocity of atoms near the anode is $V_a \cong 2 \times 10^4\,\mathrm{cm\,s^{-1}}$). The velocity of ions at the anode is taken to be $V_0 \cong 2 \times 10^5\,\mathrm{cm\,s^{-1}}$ (the ion energy $\cong 3\,\mathrm{eV}$). For a channel length of $L \cong 3\,\mathrm{cm}$ we get $t_0 \cong 15\,\mu\mathrm{s}$. We assume that $\beta \cong 5 \times 10^{-8}\,\mathrm{cm^3\,s^{-1}}$. Then we obtain the following parameter estimates:

$$\mu = \frac{1}{6}U_0, \quad \nu = 20, \quad V_a = 0.1. \tag{7.12}$$

The evaluation of the "channel resistivity" $R_{ch}$ and the parameter $\chi$ are of a certain difficulty:

$$\chi = 0.9R_{ch}/U_0, \quad [R_{ch}] = \Omega\,\mathrm{cm^2} \tag{7.13}$$

The value of $R_{ch}$ can be estimated as follows. We find $R_{ch}$ such that at $U_0 = 300\,\mathrm{V}$ a stationary model (see below) would give a total discharge current of $J = 3\,\mathrm{A}$. As calculation showed, this requirement is met for $R_{ch} \cong 8 \times 10^4\,\Omega\,\mathrm{cm}^2$. Thus, we find

$$\chi = 7 \cdot 10^4 / U_0. \tag{7.14}$$

The parameters $l$, $r$, and $h_0$ are taken to be

$$l \cong 10^{-2}, \quad r \cong 10^{-3}, \quad h_0 = 0.1. \tag{7.15}$$

*A stationary model.* First, consider stationary solutions of (7.8) by setting $\partial/\partial t = 0$. We get

$$\frac{dnV}{dx} = \nu n n_a, \quad \frac{dn_a V_a}{dx} = -\nu n n_a, \tag{7.16a}$$

$$\frac{dnV^2}{dx} = \mu n h^2(x)(J - \chi nV) + \nu n n_a V_a, \tag{7.16b}$$

$$(r + r_0)J - \chi \int_0^1 h^2(x) nV\,dx = 1, \quad r_0 = \int_0^1 h^2(x)\,dx \tag{7.16c}$$

with the boundary conditions (7.7). The problem (7.16) is solved inside the range $0 \le x \le 1$. We have one obvious integral $nV + n_a V_a = n_0 V_0 + V_a$ that enables us to exclude $n_a$. The presence of the non-local term in Eq. (7.16c) gives the sense of an eigenvalue problem to system (7.16). Not going into detail, we only note that a solution exists and is unique in the parameter range of interest.

Calculations in the range 200–400 V gave the following results. The most rapid depletion of atoms occurs at $U_0 = 200\,\mathrm{V}$. The velocity of ions at the channel output grows with $U_0$ and at $U_0 = 400\,\mathrm{V}$ reaches $10V_0$ $(2 \times 10^6\,\mathrm{cm\,s^{-1}})$. Figure 7.1a demonstrates example profiles of $n$, $V$, and $n_a$ at $U_0 = 400\,\mathrm{V}$, $\dot{m} = 3\,\mathrm{mg\,s^{-1}}$.

Introduce the system's efficiency

$$\eta = \frac{\langle nV^2 \rangle_{X=L}^2}{2 n_{a0} V_a U_0 \langle J \rangle} = \frac{1}{2} \frac{\chi}{\mu V_a} \frac{\langle nV^2 \rangle_{X=1}}{\langle J \rangle}. \tag{7.17}$$

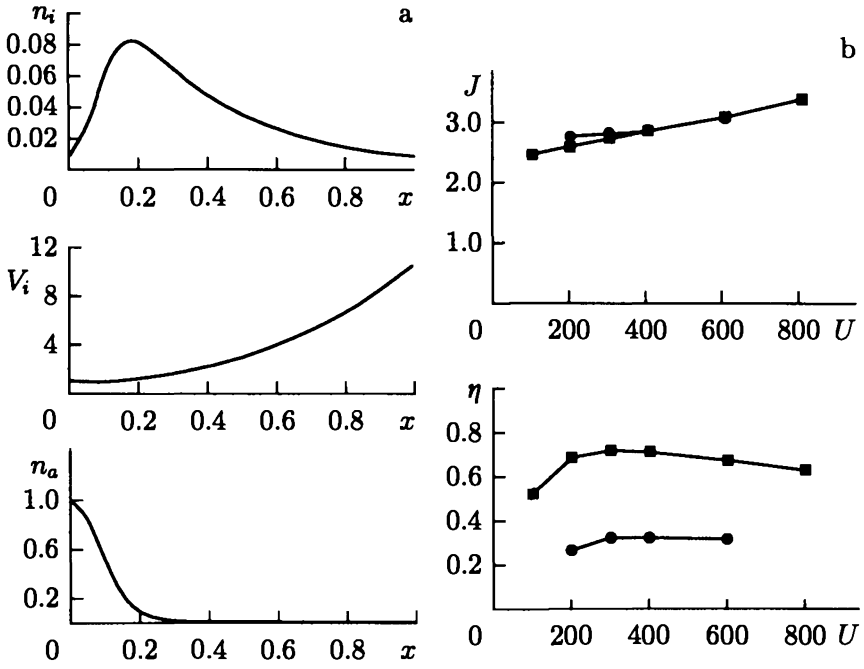


**Fig. 7.1.** Hydrodynamic model. (a) The ion density and velocity and neutral atom density distributions obtained in a stationary model with $\dot{m} = 3\,\mathrm{mg\,s^{-1}}$, $U_0 = 400\,\mathrm{V}$. (b) The volt-ampere characteristics $J(U)$ (dimensional units) and the efficiency $\eta(U)$ calculated in a stationary (squares) and a non-stationary (circles) model.

The angular brackets here indicate averaging over time (for steady regimes this is clearly unnecessary). Note here that if, when calculating $\eta$ (as is frequently done), one uses the voltage in the channel $U_p = \int E\,dx$ instead of $U_0$, a slightly higher efficiency is obtained since $U_p \leq U_0$.

Figure 7.1b shows the volt-ampere characteristics $J(U_0)$ and the efficiency $\eta(U_0)$ in the range $100 < U_0 < 800\,\mathrm{V}$ obtained on the basis of (7.16). The VAC is practically a straight line. The efficiency reaches a maximum $\eta_{\max} = 0.72$ at $U_0 = 350\,\mathrm{V}$

and slowly decreases with increasing $U_0$ and rapidly drops with decreasing voltage.

As an example we present below the simplest analytical solutions of Eqs. (7.16). Let the plasma be fully ionized ($\nu = 0$) and the magnetic field be homogeneous, $h(x) \equiv 1$. Then we have $nV \equiv 1$ and easily obtain

$$J = \frac{1+\chi}{1+r}, \quad E = \frac{1-r\chi}{1+r}, \quad V = \sqrt{1 + 2\mu \frac{1-r\chi}{1+r} x}. \qquad (7.18)$$

It is seen that there are three possibilities: (1) $r\chi < 1$, the velocity increases monotonically and the density decreases; (2) $r\chi = 1$; then $V \equiv n \equiv 1$; (3) $r\chi > 1$, the velocity decreases monotonically and the density increases. At the point $x^* = (1+r)/2(r\chi - 1)\mu$, $V = 0$, $n = \infty$. If $x^* < 1$, no solution to the problem exists. A similar situation applies in the general case.

*Non-stationary regimes.* Considering the steady solutions obtained as the initial conditions for Eqs. (7.8), we can study their stability. Calculations (over a wide parameter range) revealed the following fact. By varying the parameter $\chi$ (fixing all the rest), a stationary stable solution can be found for sufficiently small values of this parameter. On increasing $\chi$ the stationary steady solution disappears and a periodical solution emerges (Fig. 7.2a). Finally, on further increasing $\chi$, non-stationary non-periodic regimes set in (Fig. 7.2b). It turned out that in the parameter range of interest all the stationary solutions considered above are unstable. But this does not make them totally physically senseless, as they may be stable in other parameter ranges and, in addition, calculations of non-stationary solutions showed that some time-averaged quantities behave qualitatively as in the stationary regime.

Of practical interest is the case where all parameters but $\mu$ and $\chi$ are fixed and $\mu\chi = \text{const}$. Thus, we consider how the model properties change with the discharge voltage $U_0$ only. Such calculations in the range $200 < U_0 < 600\,\text{V}$ were carried out within the framework of model (7.8).

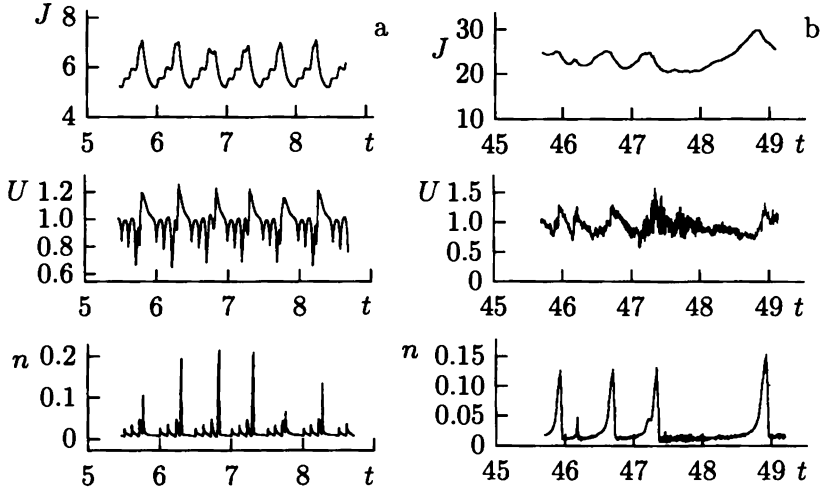


**Fig. 7.2.** Hydrodynamic model. An example of the construction of the temporal behavior of the calculated oscillograms of the discharge current, the channel voltage, and the ion density at the output, changing the parameter $\chi$. (a) Periodic oscillations ($\chi = 45$). (b) A non-periodic case ($\chi = 175$).

Figure 7.2b presents the time plots (oscillograms) of the discharge current $J(t)$, the channel voltage $U_p(t)$, and the ion density at the output ($x = 1$) for $U_0 = 400\,\mathrm{V}$ (we recall that the time unit here is $t_0 = 15\,\mu\mathrm{s}$). Calculations for other voltages show that the main (low-frequency) oscillation period $\tau_0$ increases with decreasing $U_0$: at $U_0 = 200$, $\tau \cong 170\,\mu\mathrm{s}$; at $U_0 = 600$, $\tau_0 \cong 45\,\mu\mathrm{s}$. The channel voltage oscillograms reveal the presence of high-frequency oscillations with a characteristic period $\tau_h$ of the order of a few microseconds, i.e., of the flyby time-scale. The low frequency apparently relates to the ionization oscillations. The flux parameter modulation then reaches 100%.

It is interesting to compare the VAC and efficiency with values obtained in a stationary model. Figure 7.1b gives the

plots $\langle J \rangle$ and $\eta$ as functions of $U_0$. It is seen that the discharge currents somewhat increase in the dynamical regimes. The efficiency in a non-stationary regime is smaller than in a stationary one, although the quantitative behavior of $\eta(U_0)$ does not change.

## 7.3. Dynamics of oscillations

Consider in more detail the results of calculations of the behavior of the flyby oscillation in the one-dimensional hydrodynamic model. The general character of these oscillations is much the same both with and without ionization. Thus, here we restrict ourselves to considering the case of "realistic" parameters with ionization ($\dot{m} = 3\,\mathrm{mg\,s^{-1}}$, $U_0 = 400\,\mathrm{V}$).

Figure 7.3 demonstrates the distribution of the values of $n$, $V$, and $E$ over the channel length at different times. It is seen that some density "bursts" are observed in the channel, which correspond to gaps in the velocity and the appearance of an electric field that brakes the ions. It is seen that the density bursts move along the channel approximately conserving their shape, and then their amplitude decreases. The bursts appear mainly near the outer (i.e., facing the channel's outlet) side of the ionization zone. Their amplitude rapidly attains the maximum, practically without shifting the burst. Ordinarily three bursts are observed in the channel; however, one or two bursts can appear. In that case it can emerge in the middle of the channel.

From these data we can estimate the velocity of the burst movement $V_b$ in the dimensionless units $V_b \sim 0.2-0.4$. At the same time, the mean velocity (starting from the ionization zone) is $\langle V_i \rangle \sim 2$. Thus, the flyby time for ions is $\tau_0 \sim 0.5$. Given that the distance between the bursts is $l_b \sim 0.2$, as follows from Fig. 7.3, the time interval $\tau_b$ between consecutive bursts at the channel outlet is $\tau_b \sim \tau_0$. This means that the term "flyby wave" reflects the burst frequency and not the net burst passage time over the channel length. The bursts behave as non-penetrable concentrations. On entering them the ion velocity decreases and

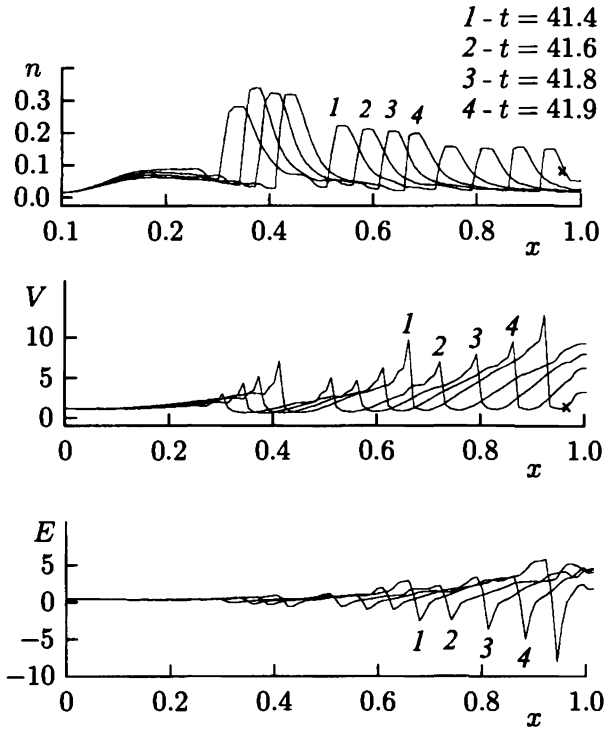


**Fig. 7.3.** Hydrodynamic model. Distributions along the channel of the ion density $n$, velocity $V$, and electric field $E$ at different moments of time ($\dot{m} = 3\,\mathrm{mg\,s^{-1}}$, $U_0 = 400\,\mathrm{V}$).

on leaving increases. The velocity of burst movement is close to that of the ions forming them.

## 7.4. A hybrid model for the plasma flow in an SPT [73]

In Section 7.1, we formulated a one-dimensional hydrodynamic model for the dynamics of ions and atoms in the SPT channel. This model gave a picture which in some respects is close to the experimental one over the parameter range of practical interest.

A more complete and adequate description of ions in the SPT conditions can be obtained using the kinetic equation and including an equation for the electron temperature. We call this model hybrid since the electrons here are described hydrodynamically as before.

As above, let $x$ be the longitudinal coordinate and $V$ be the longitudinal ion velocity. Then the main parameters of this model are: $f(x,V,t)$, the ion distribution function, $n_a$, the neutral atom concentration, $T(x,t)$, the electron temperature, and $J$ the discharge current. They are described by the following system of equations:

$$\frac{\partial f}{\partial t} + V\frac{\partial f}{\partial x} + \frac{e}{M}E\frac{\partial f}{\partial V} = \beta(T)nn_a\delta(V - V_a), \qquad n = \int_{-\infty}^{+\infty} f\,dV, \tag{7.19}$$

where $\beta(T)$ is the ionization rate constant depending on the electron temperature $T$,

$$\frac{\partial n_a}{\partial t} + V_a\frac{\partial n_a}{\partial x} = -\beta(T)nn_a, \tag{7.20}$$

$$\frac{3}{2}\left(\frac{\partial T}{\partial t} + V_e\frac{\partial T}{\partial x}\right) = -nT\frac{\partial V_e}{\partial x} + \frac{\partial}{\partial x}\left(\kappa_e\frac{\partial T}{\partial x}\right) + J_eE - \alpha\beta(T)nn_a, \tag{7.21}$$

$$V_e = -\frac{J_e}{en} = -\frac{J - J_i}{en}, \quad J_i = e\int_{-\infty}^{+\infty} VF(V)\,dV$$

Here, as before, the velocity of atoms along the $x$-axis, $V_a$, is assumed to be constant, $\kappa_e$ is the electron thermoconductivity across the magnetic field, and $\alpha$ is the ion cost. Finally, the equation of circuit and Ohm's law are

$$L_c\frac{dJ}{dt} + RJ + \int_0^L E\,dx = U_0, \quad E = \frac{J - J_i}{\sigma(x)}. \tag{7.22}$$

The notation of the basic quantities is the same as in Section 7.1.

The boundary conditions: at $x = 0$ (the anode), $n_a = n_{a0}$, $\partial T/\partial x = 0$, $f = f_0(V)$ for $V > 0$ are given; at $x = L$ (the channel's outlet), $T = T_0$. The function $f_0(V)$ was taken in the form

$$f_0(V) = \frac{\pi}{2}\frac{n_0}{V_0^2} V \exp\left\{-\frac{\pi}{4}\left(\frac{V}{V_0}\right)^2\right\}, \tag{7.23}$$

where $n_0$ and $V_0$ are this function's parameters (the density and the mean ion velocity at the anode, respectively). The function $\sigma(x)$ was determined in (7.6). We need to determine the functions $\beta(T)$ and $\kappa_e$. They were taken in the following form:

$$\beta = \begin{cases} 0, & T < T^* \\ \beta_0\,(T/T^* - 1), & T > T^*, \end{cases} \tag{7.24}$$

$$\kappa_e = \kappa_0 \frac{T}{H}, \quad \kappa_0 = \text{const}, \quad \beta_0 = \text{const}. \tag{7.25}$$

Expression (7.24) for $\beta$ was obtained by approximating the experimental and calculation results for Xe, with $\beta_0 = 2.2 \times 10^{-8}\,\text{cm}^3\,\text{s}^{-1}$. As for the thermal conductivity coefficient $\kappa_e$, taking its form to be like (7.25) is fairly arbitrary, since at present there are no theoretical or experimental data about this coefficient in real SPT conditions.

We use the same dimensionless units as in Section 7.1. Then, in addition to the already defined parameters (7.10), the following new parameters appear:

$$\alpha = \frac{\alpha}{T_0}, \quad \kappa_0 = \frac{\kappa_0}{LV_0 n_{a0}}, \quad \zeta = \frac{eU_0}{T_0}, \quad T^* = \frac{T^*}{T_0}. \tag{7.26}$$

In equalities (7.26), the dimensioned values are on the rhs and the dimensionless — on the lhs. The dimensionless quantities are often denoted by the same letter.

*A comparison of two models.* Of course, it was impossible to expect that in all cases the two different models should give

Table 7.1

| $\mu$ | $\langle J\rangle_H$ | $\langle J\rangle_G$ | $\langle U\rangle_H$ | $\langle U\rangle_G$ |
|---|---|---|---|---|
| 1.0 | 49.8 | 50.7 | 0.75 | 0.75 |
| 2.5 | 23.1 | 22.8 | 0.88 | 0.88 |
| 5.0 | 13.3 | 13.3 | 0.93 | 0.93 |
| 10.0 | 8.8 | 8.7 | 0.95 | 0.95 |

at least qualitatively similar results. However, it is clear that the mean values of different physical characteristics should be expected to be similar. Thus, we start discussing the hybrid model results with the case where both models have a stationary stable solution. Now we shall assume that $\beta = \text{const}$ and the equation for $T$ is not necessary.

Let us take $\mu = 10$, $\nu = 7$, $\chi = 15$, $V_{a0} = 0.3$, and $n_0 = 0.02$. In this case, both models yield a steady stable solution. The discharge currents in these models are 8.72 and 8.76, respectively. The channel voltages are $U_p = 0.95$. There is both good qualitative and quantitative agreement between the results even for the spatial distribution of the main quantities.

Compare now the VAC obtained within the framework of the two models. The results of the calculations are presented in Table 7.1.

In this table, $\langle \ldots \rangle$ means time-averaging, the indexes $H$, and $G$ denote the quantities obtained in the hydrodynamic and hybrid models, respectively. The volt-ampere characteristics (in our units this is the dependence of $\langle J\rangle$ on $\mu$) practically coincided. The closest were the channel voltages. With decreasing $\mu$ the stationary flows lose stability and the regime becomes periodical. In the hybrid model this occurs at a smaller $\mu$ than in the hydrodynamic one. With a further decrease in $\mu$ the solution becomes non-periodic, with this transition occurring earlier in hydrodynamics. Thus, the hybrid model proves to be "more stable."

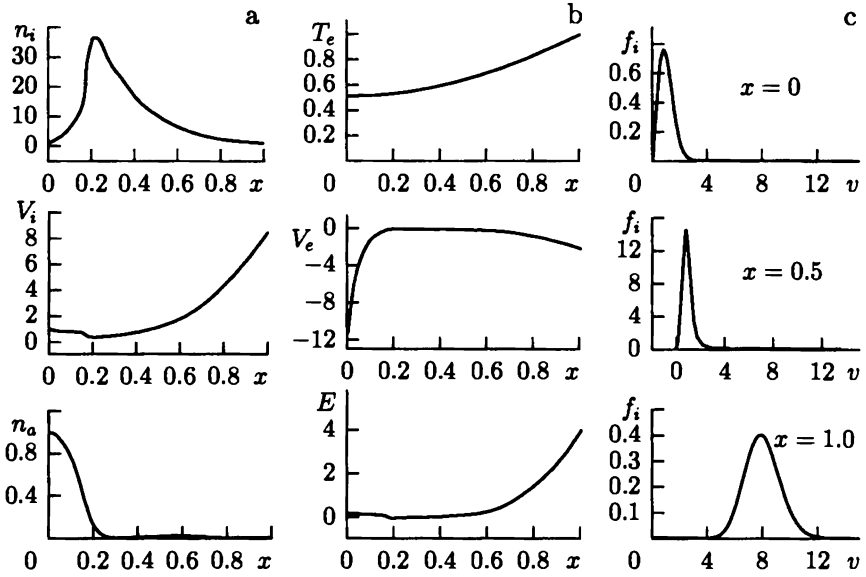


**Fig. 7.4.** Hybrid model with electron temperature. (a) Distributions of the ion density and velocity, and the neutral atom density along the channel length at $\dot{m} = 3\,\mathrm{mg\,s^{-1}}$, $U_0 = 300\,\mathrm{V}$; (b) the same for the electron temperature, electron velocity, and electric field; (c) the ion distribution function $f(V)$ in three different cross-sections.

The comparison of oscillograms in the two models results in the following observation. Although the time spectra of the two models are generally different, nevertheless a good correspondence is observed between their low-frequency components and the total oscillation amplitude.

*A hybrid model with electron temperature.* In what follows, we start from the "total" system of equations for the hybrid model (7.19)–(7.22). Let us determine the set of the main physical parameters at which the calculations were made: $\dot{m} = 3\,\mathrm{mg\,s^{-1}}$ (it is taken into account that the channel cross-section is $\sim 20\,\mathrm{cm^2}$), $V_a = 6\times10^4\,\mathrm{cm\,s^{-1}}$, $V_0 = 2\times10^5\,\mathrm{cm\,s^{-1}}$, $T_0 = 20\,\mathrm{eV}$, $T^* = 4\,\mathrm{eV}$, $\alpha = 40\,\mathrm{eV}$, $L = 3\,\mathrm{cm}$, $n_{a0} = 10^{13}\,\mathrm{cm^{-3}}$, $U_0 = 300\,\mathrm{V}$,

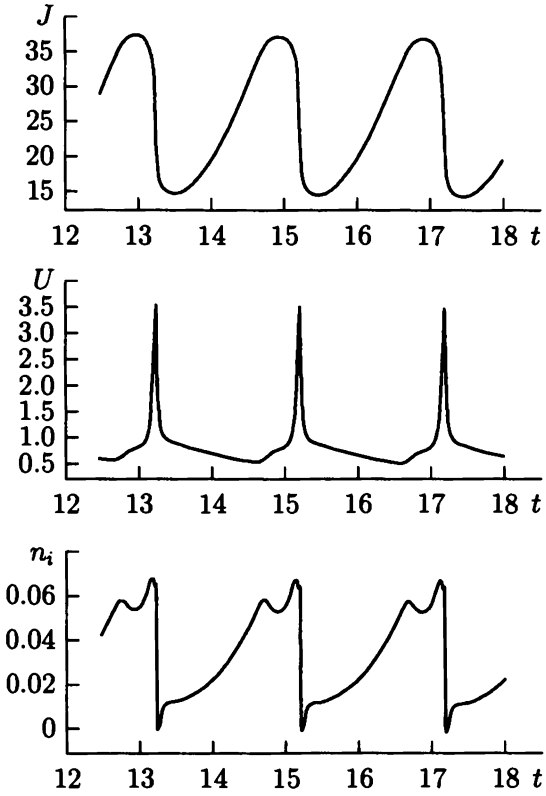


**Fig. 7.5.** Hybrid model with electron temperature. Oscillograms of the discharge current, the channel voltage, and the ion density at the output.

and the propellant is Xe. Then the dimensionless parameters take the following values: $\mu = 50$, $\nu = 9$, $\chi = 80$, $l = 10^{-2}$, $V_a = 0.3$, $\alpha = 2$, $\zeta = 15$, and $T^* = 0.2$. Let $h_0 = 0.1$ and $\kappa_0 = 1$.

Consider the results of calculations for these parameters. The flow proves to be non-stationary and $x$-distributions of the parameters below produce an instant but characteristic picture. Figure 7.4a shows the profiles of the density, ion velocity, and atom density. At $x = 0.2$, a practically complete ionization of

the flux occurs. Then the flux speeds up monotonically toward the channel's exit and its velocity reaches $8V_0 \approx 1.6 \times 10^6\,\mathrm{cm\,s^{-1}}$. Figure 7.4b shows the profiles of the electron temperature, electron velocity, and the electric field. $T_e$ varies weakly (this is due to the high electron thermoconductivity assumed in these calculations). The velocity of electrons rapidly increases at the anode and reaches $\approx 10V_0 = 2 \times 10^6\,\mathrm{cm\,s^{-1}}$. In Fig. 7.4c, we present the plots $f(V)$ for $x = 0,\ 0.5,\ 1$. The ion velocity at the output falls within the range $8 \times 10^5$–$2.4 \times 10^6\,\mathrm{cm\,s^{-1}}$. The oscillograms of the three quantities (the discharge current, channel voltages, the ion density at the output) are shown in Fig. 7.5. The mean current is about 24.2. The current and the voltage oscillate in counter-phase. The ion density shows the strongest modulation. The principal oscillation period is $\approx 2t_0 = 30\,\mu\mathrm{s}$.

## 8. SPTs in real conditions

In previous sections, we considered processes occurring inside the discharge chamber of the SPT. Of the external factors, only the propellant supply from the anode, the supply of a small fraction ($\sim 10\%$ of $J_p$) of electrons from the channel's outlet (from the cathode-compensator), and, of course, the potential difference between the cathode and anode were taken into account.

However, in addition to these factors, a plasma stream emerging from the thruster is present. Here we briefly consider the effects caused by the stream.

If the stream goes into an "ideal vacuum" (for example, when an SPT works outside the terrestrial magnetosphere), the back action of the stream on the processes in the channel is apparently insignificant, although oscillations in the stream may affect the oscillations in the channel. The stream itself comes out and permanently widens both due to the initial transverse velocities of ions and the electron pressure. Both the electron temperature and the potential in the stream decrease with dis-

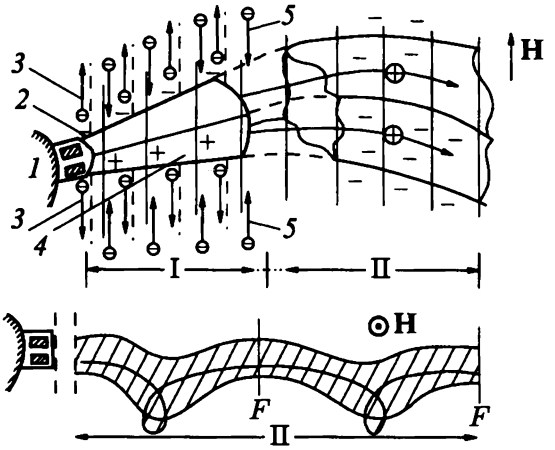


**Fig. 8.1.** Plasma stream from an SPT in the magnetic field of the ionosphere ($\mathbf{V} \perp \mathbf{H}$). I – the plasma stream (ion moves together with electrons coming out of the SPT). II – the compensated ion flux (electrons are practically not entrained by ions). (a) The processes near the thruster: *1* – the thruster on a spacecraft, *2* – the zone of negative polarization of the stream, *3* – electron fluxes into the ionosphere, *4* – the zone of positive polarization, *5* – electron fluxes from the ionosphere. (b) The focusing of the compensated ion flux by the ionospheric magnetic field. F – focal planes (the view along the plane perpendicular to **H**).

tance from the SPT. The potential difference both across and along the stream is

$$\delta\Phi \approx \frac{kT_e}{e}\Big|_{\text{outlet}} . \tag{8.1}$$

When a spacecraft with an SPT moves in the ionosphere, the situation is more complicated. This is most clearly seen during the injection of the stream across the magnetic field. In this case, a polarization of the flux occurs due to the Lorentz force (see Fig. 8.1a), which gives rise to an electric field providing particle drift (primarily, electrons) along the stream with a

velocity equal to the initial velocity of the plasma flow. At the same time, electrons from the "negative" side of the flux escape into the ionosphere along the magnetic lines, and ionospheric electrons, in contrast, are "attracted" by the "positive" side of the flux. These motions of electrons in the ionosphere result in the build-up of very intense oscillations. These oscillations were discovered during the first flight of an SPT onboard the "Meteor" satellite [74]. Later, all the processes of interaction of the plasma stream with the ionosphere were studied in a series of international experiments known as "Porcupine," in which the stream from the SPT was simultaneously measured at different distances using several probes [75]. In [76], A. I. Morozov and R. Z. Sagdeev noted that since the Larmor frequency does not depend on particle velocities, during the motion of a spacecraft across an **H**-field the ion tail (after the plasma stream spreading) represents a chain of condensations in a plane normal to **H**, which are spaced by a distance

$$\Lambda = V_A \frac{2\pi}{\omega_H}. \tag{8.2}$$

Here $V_A$ is the velocity of the apparatus (Fig. 8.1b). But all the above-mentioned effects seem to have no appreciable effect on the processes inside the SPT channel itself.

The situation really changes when the SPT works in a vacuum chamber (VC). Here the appearance of back relations between the SPT and VC becomes significant. The action of the VC on the SPT is mainly due to particles entering from the VC into the SPT channel. These are atoms of the residual gas, as well as products of the sputtering of the "target" (i.e., the plates upon which the flux falls), the chamber walls, and especially the coatings of sputtered target material settled on the walls.

## 8.1. The particle influx from the VC into the SPT

At the initial stage of EPT studies, it seemed that the lower the pressure in the VC, the better. However, this proved to

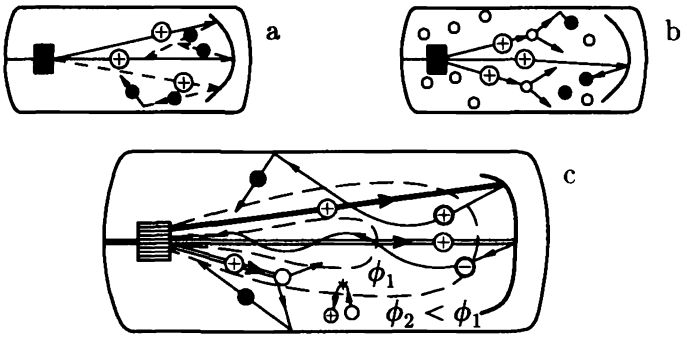


**Fig. 8.2.** SPT+vacuum chamber system. (a) Two particle sources during SPT performance in a high-vacuum chamber (the particle free path $\lambda \gg L$, where $L$ is the characteristic chamber size). (b) The regime with a "gaseous target" ($\lambda \ll L$). (c) The influence of the positive potential of the stream on the dynamics of particles flying into the stream. The "suction" of negative ions into the SPT channel.

be not the case, since for typical ion energies ($\mathcal{E}_i \sim 200$–$300\,\mathrm{eV}$), each ion knocks off $\sim 0.2-0.5$ particles on average. Thus, in a high vacuum there are not one but two particle sources in the VC: the SPT and the target, as well as the "side" sputtering from the wall (Fig. 8.2a). Thus a prerequisite appears for an intense flux of sputtered particles into the channel. This indeed clearly appears in the fact that in a thoroughly cleaned SPT, the near-anode surfaces, including (in the case of the SPT-ATON) the buffer, are rapidly powdered (become black in color). Only the external parts of the insulators remain "clean," being subjected to erosion due to the action of the plasma stream.

### *8.1.1. Negative ions*

Although the powdering of the internal parts of the channel seems to be quite natural, the situation is even more complicated. The fact is that the stream coming out of the SPT has

a positive potential and a comparatively high electron temperature. Figure 8.2b shows the lines of $n_e = \text{const}$ and $T_e = \text{const}$. Given the ionization cross-section of atoms of the target (usually it is stainless steel), it is easy to see that the plasma stream that already left the SPT (and thus the working channel) effectively ionizes comparatively slow sputtered atoms and thus prevents most metallic ions from entering the near-cathode zone and the buffer (Fig. 5.1b). So another factor should exist which, in contrast, helps particles penetrate into the SPT. Many experiments (most of them carried out at MIREA) compellingly showed that the powdering of the internal surfaces is due to the appearance, during the sputtering, of both positive and negative ions (Fig. 3.4). It is these ions that are not expelled but pulled into the channel and powder its internal parts (Fig. 8.2c). We note here one of the most compelling arguments favoring the proposed concept. It is known that the elements from the second group of Mendeleev's periodic table do not form stable negative ions. Thus it is natural to make the target of zinc, for example. The experimental result was as follows. Since Zn belongs to easily sputtered metals, very soon (in approximately 40 min) all the chamber's interior was covered with a clearly visible layer of sputtered zinc, while the SPT interior remained clean. Experiments analyzing the nature of the sputtering are described in detail in [77].

### *8.1.2. Effect of the VC properties on the SPT characteristics*

The flux of heavy particles coming out of the VC into the SPT gives rise to some effects that affect the exploitation characteristics. These effects can be subdivided into two groups: surface and volume. The former relate to a modification of the working surfaces (insulators, the anode), and the latter are connected with the ionization of injected atoms and their subsequent acceleration.

First we discuss surface processes. Above we described the penetration of sputtered particles into the near-anode zone and

the buffer. It turns out that if the particle beam in the VC strikes a non-metallic surface, for example, quartz walls, then particles flying into the channel can form non-conducting coatings on the anode, which notably worsens the characteristics. This is mainly due to the appearance of micro-arcs on the anode, which break the discharge symmetry.

The particles sputtered on the insulator's surface cannot lead to the characteristic fall if the surface is sufficiently effectively cleaned by the accelerated ion flux in the channel, which is mainly incident on the walls. It is this situation that was realized in the first SPT models constructed at the Kurchatov AEI (EOL-1, EOL-2). The modern models M-70 and M-100 work in this regime. Another situation is the case of the SPT ATON, in which the accelerated flux is well separated from the insulator's walls. Here metallic (or other) coatings with a thickness of a few atomic layers, which have a substantially higher multiplication threshold $\mathcal{E}^*$ (see Fig. 3.3), appear due to low sputtering. As a result, the NWC decreases and the acceleration zone shortens and shifts toward the outlet, which leads to a larger divergence of the flux, the growth of oscillations, and an appreciable worsening of the thruster's characteristics [78].

Not only the inflow of condensing particles can affect the SPT performance. It turns out that a small admixture of hydrogen that either enters with xenon ($\sim$1% by particle number) or flows into the channel from the VC working with cryogen pumps (the low temperature of hydrogen condensation produces, in the absence of additional turbomolecular pumps, a high partial pressure in the VC; this problem does not emerge when using oil pumps) gives rise to effects similar to the situation arising during the powdering of walls by metals. Apparently, when hydrogen is present on the walls, plasmo-chemical reactions occur that lead to the appearance of "metallic" (at least, by their secondary-emission characteristics) coatings because of different admixtures that are present in both the insulators and the incoming Xe.

In addition to the surface processes, the influx of particles into the channel can give rise to unfavorable volume processes.

Indeed, if an atom of the propellant has a large velocity along the direction toward the entry to the channel, it can penetrate the channel and be ionized there, slow down, and then accelerate and fly out of the channel. The appearance of the "second" ionization zone near the channel's output leads to a de-equipotentialization (due to $\nabla P_e$) and an increase in the flux divergence angle. It is easy to verify that depending on the mean potential $\Phi^{**}$ of the second ionization zone relative to the mean potential $\Phi^{*}$ of the first ionization zone, the efficiency coefficient can increase if

$$\Phi^{**}/\Phi^{*} > 1/4 \tag{8.3a}$$

and decrease if

$$\Phi^{**}/\Phi^{*} < 1/4. \tag{8.3b}$$

This is due to the fact that independently of where the ionization of an inflowing atom occurred, it (in the case of single ionization) extracts an energy $eU_p$ from the power source. This energy is shared between the ion ($\mathcal{E}_i = e\Phi^{*}$) and the electron [$\mathcal{E}_e = e(U_p - \Phi^{*})$] and, given the quadratic dependence of the efficiency on $F$, it is easy to obtain the above estimate. For more details about the pressure effects in the vacuum chamber on the SPT characteristics, see [77].

## 8.2. Preventing particle influx from the VC

A. I. Bugrova's laboratory at MIREA and A. I. Morozov have developed some methods preventing particle inflow from the VC into the channel.

First of all, it is necessary to work as much as possible in the "gaseous target" regime when the vast majority of the fast ions are braked in the gaseous cushion before the target. Then the choice of target material is of importance. Moreover, to intercept negative ions it is possible to create potential traps for ions. This can be done provided that an arc with an autonomous matter supply is ignited in an appropriate part of the plasma stream to increase the density and temperature of electrons. Thus, a

zone with a relatively high potential will be formed, which is capable of capturing negative ions. This idea has been very successfully realized in experiments. Finally, it is possible to weaken significantly the sputtered particle and propellant fluxes in SPTs by appropriately choosing the form, size, and materials for the VC and by installing screens.

Of course, the problems mentioned for an optimal VC require both experimental and theoretical studies. In particular, it is required to solve the system of kinetic equations for neutral particles and ions, as well as the hydrodynamic equations for electrons. One of the main difficulties of such modeling is in setting boundary conditions on the powdered walls of the vacuum chamber.

## 8.3. Supersynchronization phenomenon

We have considered above the dynamics of heavy particles in the VC. However, electrons can also produce specific effects. An example may be provided by a phenomenon called "supersynchronization." This was discovered at MIREA in an attempt to measure the velocity of flow in the VC with a simple probe. The supersynchronization appeared in the fact that the signals from probes located at different distances from the SPT outlet proved to be synchronized to within $\sim 1\,\mu$s. The essence of this phenomenon is apparently simple. It is similar to a phenomenon known in electrostatics, when a charge, inserted into a hollow metal body, practically instantaneously induces an equal charge on the body's surface.

A similar situation persists in the case of the SPT+VC system. Namely, let an "excessive" (with respect to the steady regime in the VC) charge begin entering the SPT from the VC. Since electrons inside the channel are magnetized, they do not "accompany" ions entering the VC. Therefore, due to the tendency to quasi-neutrality, these ions "attract" electrons from the VC plasma volume, induce an equal positive charge on the plasma volume surface, and thus change its potential with re-

spect to the earth. Later on, neutralization of the charge on the plasma volume surface occurs either due to an enhancement of emission from the cathode-compensator or due to cold emission from microedges on the surfaces. In very high-voltage cases, as was shown by the first experiments in 1962, near-wall arcs can be ignited on the chamber's surface for a significant increase in plasma potential.

## Conclusions

As seen from the above, the discharge in SPTs is unlike any other known discharge. It is characterized by the presence of the following factors: the spatial separation of the ionization and acceleration zones, the presence of crossed $(\mathbf{E}, \mathbf{H})$-fields, with the $\mathbf{H}$-field crossing the walls while the $\mathbf{E}$-field is tangential to them, a free-path length of charged particles much higher than the system's size, and the drift of electrons being closed. During this discharge, plasma is created with a very high (for electrode discharges) electron temperature ($T_e$ up to 20 eV), and most distinctive features of the EDF are determined by the interaction of electrons with the channel walls.

To date, SPTs with a narrow power range of $\sim 0.4-1$ kW and outflow velocities of $\sim 15$–$20\,\mathrm{km\,s^{-1}}$ have operated in space. However, laboratory SPT models with a power of $\sim 20-30$ kW and velocities of $\sim 30-40\,\mathrm{km\,s^{-1}}$ and higher have existed for a long time. SPTs may work with high characteristics using different gaseous propellants. SPTs serve as an effective technological tool to process and form surfaces and are used for such purposes in different countries using Ar, $O_2$, and other propellants.

The authors hope that the material presented in this review describes in detail the problems related to processes in SPTs and the VC. For many of them adequate models have been constructed.

However, at present we do not have a complete theory that would enable us to quantitatively calculate SPT characteristics

for their performance in space or, moreover, in a VC. It seems that one recent significant achievement is the understanding of the principal role of the SPT+VC system, and not simply the SPT, since the perfection of a thruster, as well as its exploitation for technological purposes, naturally requires using a VC.

The construction of a quantitative theory of SPTs and, especially, of the SPT+VC system requires numerous simultaneous theoretical and experimental studies of physical processes.

# Appendix

## A. The necessity of electric propulsion thrusters

The propulsion by a jet thruster is

$$F = \dot{m} V_M. \tag{A.1}$$

Here $\dot{m}$ is the mass rate, $V_M$ is the velocity of the mass outflow. It is seen from here that the higher $V_M$, the smaller $\dot{m}$. As was shown by K. E. Tsiolkovskii, integrally it follows from Eq. (A.1) that to make a maneuver, the initial mass of a spacecraft $M_0$ is connected with the final mass $M_1$ by the relationship

$$M_0 = M_1 \exp\left(V/V_M\right), \tag{A.2}$$

where $V$ is the so-called characteristic velocity of the maneuver, i.e., the velocity the spacecraft would attain moving in the absence of external forces with the same cyclogram of the thruster's performance. Thus, for the same values of $M_1$ and $V$, but with decreasing $V_M$, the starting mass increases exponentially.

The ordinary thermochemical thrusters of rocket carriers have a velocity of outflow of $\sim 3-5\,\mathrm{km\,s^{-1}}$. For satellites, the outflow velocities lie close to the lower limit or are even smaller.

At the same time, the characteristic velocities for many problems attain tens of kilometers per second, especially for flights to celestial bodies returning to the Earth.

But even for much more moderate problems where $V$ is about $1\,\mathrm{km\,s^{-1}}$, small $V_M$ lead to large mass consumption rates. It is clear from here that thrusters with outflow velocities of $\geq 10\,\mathrm{km\,s^{-1}}$ are needed in the future. However, the increase in $V_M$ is simultaneously accompanied by an increase in the "energetic cost" of the thrust $\gamma$. For example, for a thruster with 100% efficiency,

$$\gamma = \frac{N}{F} = \frac{1}{2}\frac{\dot{m}V_M^2}{\dot{m}V_M} = \frac{V_M}{2}. \tag{A.3}$$

But the "chemical" resources of the combustion itself are sufficient only to produce the above-mentioned outflow velocities. So to reach higher $V_M$ special energy sources are required. These may include nuclear reactors of different types (radio-isotopic, fusion or synthesis reactors). At present, the main energy source on spacecraft are solar photoelements. The electric power they supply is presently used for spacecraft operation, as a rule, but it can also supply the thruster. The power is usually 0.5–5 kW. Thus, thrusters with a high outflow velocity develop a small propulsion of the order of a few units or several tens of grams (for example, for 100% efficiency, as follows from Eq. (A.3), to provide a thrust of 1 g at $20\,\mathrm{km\,s^{-1}}$, a power of 100 W is required). It might seem that this thrust is too small for any reasonable problem. However, this is not the case. Small thrusters, in contrast to liquid-fuel ones, have a long lifetime of the order of many months and years. In particular, a thruster with a propulsion of 10 g provides a total momentum of $P = Ft = 3.6 \times 10^4\,\mathrm{kg\,s}$ over 1.5 months (1000 h). Such a momentum is sufficient for many tasks.

Large outflow velocities can be obtained with very different devices. The thrust density:

— in plasmotrons of different types using the gas heating is

$$f \sim \nabla P, \tag{A.4}$$

— in ion and colloid injectors (sources), in which only ions are present in the accelerating gap between electrodes or drops

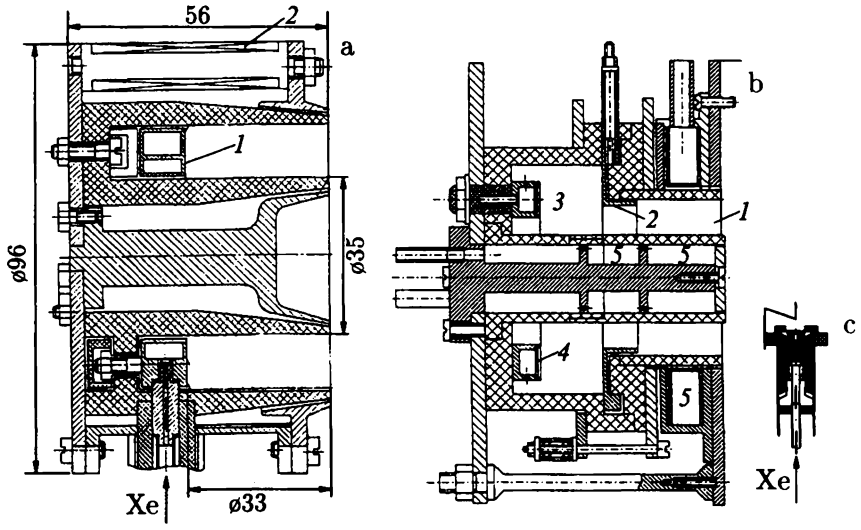


**Fig. A.1.** Constructive schemes of a real SPT. (a) The first SPT launched in space (EOL-1): *1* – the anode-gas-distributor, *2* – magnetic field coils (eight). (b) The SPT-ATON (A-4): *1* – the acceleration channel, *2* – the anode, *3* – the buffer capacity, *4* – the gas-distributor, *5* – the magnetic coils. (c) The cathode-compensator of the EOL-1.

with the same charge, is

$$f \sim qE \sim \nabla E^2/8\pi, \tag{A.5}$$

— in electromagnetic plasma accelerators in which the acceleration of quasi-neutral plasma occurs due to the Ampere force, is

$$f \sim jH \sim \nabla H^2/8\pi. \tag{A.6}$$

Thrusters with outflow velocities of $V_M \sim 10-25\,\mathrm{km\,s^{-1}}$ are the most urgent today. This range is overlapped only by plasma thrusters. Among them, SPTs are especially popular. Although this abbreviation simply means "stationary plasma thruster," it has come to be used for a certain class of plasma thrusters. The units of the first installation with an SPT launched in space (called EOL) are shown in Fig. A.1a.

## REFERENCES


1. A. I. Morozov, in: *Plazmennye Uskoriteli* (Plasma Thrusters) [in Russian, edited by L. A. Artsimovich], Mashinostroenie, Moscow (1973), pp. 5–15.
2. A. I. Bugrova and A. I. Morozov, in: *Ionnye Inzhektory i Plazmennye Uskoriteli* (Ion Injectors and Plasma Thrusters) [in Russian, edited by A. I. Morozov and N. N. Semashko], Energoatomizdat, Moscow (1990), pp. 42–55.
3. A. I. Morozov, A. I. Bugrova, et al., *Fiz. Plazmy*, **23**, 635–645 (1997).
4. L. A. Artsimovich, A. M. Andronov, A. I. Morozov, et al., *Kosm. Issled.*, **12**, No. 3, 451–468 (1974).
5. E. E. Yushmakov, in: *Fizika Plazmy i Problema Upravlyaemyh Termoyadernyh Reaktsiy* (Plasma Physics and Thermonuclear Reaction Control) [in Russian], Vol. 4, AN SSSR, Moscow (1958), pp. 235–257.
6. V. M. Bystritskii and A. N. Didenko, *Usp. Fiz. Nauk*, **132**, No. 1, 91–122 (1980).
7. A. V. Zharinov and Yu. S. Popov, Zh. Tekh. Fiz., **37**, No. 2, 126–130 (1967).
8. E. A. Lyapin and A. V. Semenkin, in: *Ionnye Inzhektory i Plazmennye Uskoriteli* (Ion Injectors and Plasma Thrusters) [in Russian, edited by A. I. Morozov and N. N. Semashko], Energoatomizdat, Moscow (1990), pp. 20–32.
9. S. D. Grishin, V. S. Eorofeev, and A. V. Zharinov, in: *Plazmennye Uskoriteli* (Plasma Thrusters) [in Russian, edited by L. A. Artsimovich], Mashinostroenie, Moscow (1973), pp. 54–61.
10. I. P. Zubkov, A. Ya. Kislov, and A. I. Morozov, *Zh. Tekh. Fiz.*, **41**, 526 (1971).
11. L. A. Kvasnikov, L. A. Latyshev, D. D. Sevruk, and V. B. Tikhonov, *Teoriya i Raschet Energosilovykh Ustanovok Kosmicheskih Apparatov* (Theory and Calculation of Energy Power Sources of Spacecraft) [in Russian], Mashinostroenie, Moscow (1984).
12. V. N. Dem'yanenko, *Zh. Tekh. Fiz.*, **48**, 634–636 (1978).
13. A. I. Morozov, *Dokl. Akad. Nauk SSSR*, **163**, No. 6, 1383 (1965).

14. A. I. Mororzov, in: *Plazmennye Uskoriteli* (Plasma Thrusters) [in Russian, edited by L. A. Artsimovich], Mashinostroenie, Moscow (1973), pp. 12–13.

15. S. I. Braginskii, in: *Reviews of Plasma Physics*, edited by M. A. Leontovich, Vol. 1, Consultants Bureau, New York (1965).

16. A. I. Morozov and S. V. Lebedev, in: *Reviews of Plasma Physics*, edited by M. A. Leontovich, Vol. 8, Consultants Bureau, New York (1980).

17. A. I. Morozov, *Fizicheskie Osnovy Kosmicheskih Elektroreaktivnyh Dvigateley* (Physical Grounds of Space Electric Propulsion Thrusters) [in Russian], Atomizdat, Moscow (1978).

18. S. K. Demitrov and V. A. Obukhov, in: *Ionnye Inzhektory i Plazmennye Uskoriteli* (Ion Injectors and Plasma Thrusters) [in Russian, edited by A. I. Morozov and N. N. Semashko], Energoatomizdat, Moscow (1990), pp. 193–219.

19. V. V. Zhukov, A. I. Morozov, and G. Ya. Shchepkin, *Pis'ma Zh. Eksp. Teor. Fiz.*, **9**, No. 1, 24, (1969).

20. V. V. Zhukov and A. I. Morozov, *Pis'ma Zh. Eksp. Teor. Fiz.*, **18**, No. 6, 373–376 (1973).

21. A. I. Morozov and V. V. Savel'ev, *Usp. Fiz. Nauk*, **138**, No. 11, 1153–1193 (1998).

22. *Fizicheskie Velichiny, Spravochnik* (Physical Quantities Handbook) [in Russian, edited by I. S. Grigor'ev and E. Z. Meilikhov], Energoatomizdat, Moscow (1991).

23. I. P. Zapesochnyi and P. V. Feltsman, *Opt. Spektrosk.*, **32**, 521–523 (1966).

24. I. M. Bronshtein and B. S. Fraiman, *Vtorichnaya Elektronnaya Emissiya* (Secondary Electron Emission) [in Russian], Nauka, Moscow (1969).

25. M. A. Kaminskii, *Atomnye i Ionnye Stolknoveniya na Poverkhnosti Metalla* (Atomic and Ion Collisions on the Metal Surface) [in Russian], Mir, Moscow (1967).

26. V. V. Egorov, V. Kim, A. A. Semenov, and I. I. Shkarban, in: *Ionnye Inzhektory i Plazmennye Uskoriteli* (Ion Injectors and Plasma Thrusters) [in Russian, edited by A. I. Morozov and N. N. Semashko], Energoatomizdat, Moscow (1990), pp. 56–61.

27. A. I. Morozov and L. S. Solov'ev, in: *Reviews of Plasma Physics*, edited by M. A. Leontovich, Vol. 2, Consultants Bureau, New York (1966).
28. A. I. Morozov and V. V. Savelyev, *Fiz. Plazmy*, **21**, 970–974 (1995).
29. A. I. Bugrova, V. S. Versotskii, L. E. Kalikhman, and A. I. Morozov, *Teplofiz. Vys. Temp.*, **16**, No. 5, 937–941 (1976).
30. A. I. Bugrova, *Zh. Tekh. Fiz.*, **57**, No. 9, 1852–1854 (1987).
31. A. I. Bugrova, A. V. Desyatskov, and A. I. Morozov, *Fiz. Plazmy*, **18**, No. 8, 963–975 (1992).
32. A. I. Morozov and G. B. Popkov, in: *Abstarcts 5th All-Union Conf. Plasma Thrusters and Ion Injectors*, Moscow (1982).
33. A. I. Morozov, *Fiz. Plazmy*, **17**, No. 6, 672–678 (1991).
34. I. B. Bernstein, J. M. Greene, and M. D. Kruscal, *Phys. Rev.*, **108**, No. 3, 546–550 (1957).
35. B. B. Kadomtsev, *Kollektivnye Yavleniya v Plazme* (Collective Phenomena in Plasma) [in Russian], Nauka, Moscow (1976).
36. L. A. Artsimovich and R. Z. Sagdeev, *Fizika Plazmy Dlya Fizikov* (Plasma Physics for Physicists) [in Russian], Atomizdat, Moscow (1979).
37. A. I. Morozov, *Appl. Mech. Tech. Phys.*, **3**, 19 (1968).
38. I. M. Lifshits, M. Ya. Azbel', and M. I. Kaganov, *Elektronnaya Teoriya Metallov* (Electron Theory of Metals) [in Russian], Nauka, Moscow (1971).
39. Yu. A. Volkov and A. I. Morozov, *Pis'ma Zh. Tekh. Fiz.*, **6**, No. 15, 909–911 (1981).
40. A. I. Bugrova, A. I. Morozov, and V. K. Kharchevnikov, *Fiz. Plazmy*, **18**, No. 6, 963–975 (1992).
41. A. I. Bugrova, *Zh. Tekh. Fiz.*, **17**, No. 9, 1852–1854 (1987).
42. A. I. Morozov and A. P. Shubin, *Pis'ma Zh. Tekh. Fiz.*, **10**, No. 1, 20–31 (1984).
43. A. I. Bugrova, V.A.Kurochkina, A. I. Morozov, and A. P. Shubin, *Ukr. Fiz. Zh.*, **10**, No. 1, 733–743 (1991).
44. V. A. Kurochkina and A. P. Shubin, *Fiz. Plazmy*, **10**, No. 4, 266–270 (1984).
45. A. I. Morozov, *Zh. Tekh. Fiz.*, **57**, No. 8, 1512–1514 (1987).

46. Yu. V. Esipchuk, K. P. Kirdyashev, and Yu. G. Kondakov, in: *Proc. 2nd All-Union Conf. Plasma Thrusters* [in Russian], Inst. of Physics, Minsk (1973), pp. 89–90.

47. A. I. Bugrova and K. P. Kirdyashev, in: *Abstracts 4th All-Union Conf. Plasma Thrusters and Ion Injectors* [in Russian], VNTNC GKNT, Moscow (1978), pp. 61–62.

48. K. P. Kirdyashev, *Pis'ma Zh. Tekh. Fiz.*, **23**, No. 10, 47–52 (1997).

49. V. I. Bukhtii and K. P. Kirdyashev, *Pis'ma Zh. Tekh. Fiz.*, **23**, No. 10, 37–41 (1997).

50. K. P. Kirdyashev and A. I. Morozov, *Fiz. Plazmy*, (in press).

51. B. A. Arkhipov, R. Yu. Gnizdor, N. A. Maslennikov, and A. I. Morozov, *Fiz. Plazmy*, **18**, No. 9, 1241–1244 (1992).

52. V. A. Kurochkina and A. I. Morozov, *Zh. Tekh. Fiz.*, **18**, No. 10, 1973–1978 (1988).

53. V. A. Kurochkina and A. I. Morozov, *Pis'ma Zh. Tekh. Fiz.*, **14**, No. 4, 368–374 (1988).

54. V. A. Kurochkina and A. I. Morozov, *Zh. Tekh. Fiz.*, **60**, No. 4, 77–82 (1990).

55. E. Kamke, *Handbook on First-Order Differential Equations in Partial Derivatives* [Russian translation], Nauka, Moscow (1966).

56. A. I. Morozov and V. V. Savel'ev, *Proc. 2nd German–Russian Conf. on Electric Propulsion and Appl.*, Moscow (1993).

57. A. I. Morozov and V. V. Savel'ev, *Pis'ma Zh. Tekh. Fiz.*, (in press).

58. Yu. A. Ermakov, in: *Proc. 31st AIAA-ASME-SAE-ASEE Joint Propulsion Conf.*, Report AIAA 95-2672, San Diego, California (1995).

59. Yu. A. Ermakov, in: *Proc. Joint Electro Propulsion Conf.*, Report 176, Moscow (1995), pp. 1204–1206.

60. A. I. Morozov and I. V. Melikov, *Zh. Tekh. Fiz.*, **44**, No. 3, 544 (1974).

61. S. A. Yakunin, *Vestn. MGU, Ser. Vychisl. Mat. Kibern.*, **4**, 20–27 (1977).

62. N. A. Maslennikov, in: *Ionno-Plazmennye Ustroystva v Tekhnike* (Ion-Plasma Devices in Technics) [in Russian], KhAI, Kharkov (1989), pp. 17–19.

63. A. I. Bugrova, N. A. Maslennikov, and A. I. Morozov, *Zh. Tekh. Fiz.*, **61**, No. 6, 45–51 (1991).

64. A. I. Morozov, A. I. Bugrova, et al., *Fiz. Plazmy*, **23**, 641 (1997).

65. A. I. Morozov, A. I. Bugrova, et al., *Fiz. Plazmy*, **23**, 639 (1997).

66. Yu. V. Esipchuk, in: *Plazmennye Uskoriteli* (Plasma Thrusters) [in Russian, edited by L. A. Artsimovich], Mashinostroenie, Moscow (1973), pp. 75–85.

67. A. I. Morozov, Yu. V. Esipchuk, A. M. Kapulkin, et. al., *Zh. Tekh. Fiz.*, **42**, No. 3, 612–619 (1972).

68. A. I. Bugrova, et al., *Fiz. Plazmy*, (in press).

69. A. I. Morozov, V. A. Nevrovskii, and V. A. Smirnov, *Zh. Tekh. Fiz.*, **43**, No. 3, 573 (1973).

70. A. I. Morozov, in: *Plazmennye Uskoriteli* (Plasma Thrusters) [in Russian, edited by L. A. Artsimovich], Mashinostroenie, Moscow (1973), pp. 85–92.

71. A. I. Morozov and V. V. Savel'ev, in: *Proc. 24th Int. Electric Propulsion Conf.*, Report IEPC-95-42, Moscow (1995).

72. A. I. Morozov and V. V. Savel'ev, *Pis'ma Zh. Tekh. Fiz.*, (in press).

73. A. I. Morozov and V. V. Savel'ev, in: *Proc. 24th Int. Electric Propulsion Conf.*, Report IEPC-95-161, Moscow (1995).

74. S. I. Avdyushin, I. M. Podgornyi, G. L. Popov, and A. A. Porotnikov, *Ionnye Inzhektory i Plazmennye Uskoriteli* (Ion Injectors and Plasma Thrusters) [in Russian], Nauka, Moscow (1984).

75. A. A. Galeev, V. S. Dokukin, V. A. Zhulin, et al., in: *Issledovaniya po Problemam Solnechno-Zemnoy Fiziki* (Solar-Terrestrial Physics Studies) [in Russian], Institute of Terrestrial Magnetism, Ionosphere, and Radiowave Propagation AN SSSR, Moscow (1977), pp. 152–160.

76. I. M. Podgornyi, *Fizika i Primenenie Plazmennyh Uskoriteley* (Physics of Plasma Thrusters and Their Applications) [in Russian, edited by A. I. Morozov], Nauka i Tekhnika, Minsk (1974).

77. A. I. Bugrova, A. S. Lipatov, and A. I. Morozov, *Fiz. Plazmy*, **21**, No. 7, 650–651 (1995).

78. A. I. Bugrova and A. I. Morozov, *Fiz. Plazmy*, **22**, No. 8, 701–706 (1996).